SYNTHESIS AND PHYSICO-CHEMICAL CHARACTERIZATION OF NOVEL CERIA BASED MATERIALS AND APPLICATION FOR LOW TEMPERATURE SOLID OXIDE FUEL CELLS

by

CHIMA BENJAMIN NJOKU

Submitted in fulfillment of the academic requirements for the degree of Doctor of Philosophy in the School of Chemistry and Physics,
University of KwaZulu-Natal, Durban

December 2015

As the candidate's supervisor, I have approved this thesis for submission.

Supervisor:

Signed: …….. Name: Patrick G. Ndungu Date: 10/12/2015

Co-Supervisor:

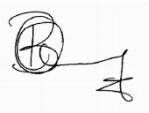

Signed: …….. Name: Bernard O. Owaga Date: 10/12/2015

ABSTRACT

The sol-gel technique is a simple method used to synthesize complex metal oxide formulations. This technique was used to synthesize all the perovskite material used in this research. The crystalline nano-structures and compositions were characterized by high resolution transmission electron microscopy and X-ray diffraction. The textural characteristics and particle morphology were respectively characterized by Nitrogen sorption at 77.5 K and scanning electron microscopy. The electrochemical properties were characterised by using a NUVANT^{TM} Powerstat 05 potentiostat/galvanostat and a Kittec Squadro muffle furnace to regulate the operating temperature, with air and hydrogen as the gases used.

Porous iridium oxide, with samarium doped ceria (SDC) material was synthesized withnon-ionic, anionic and cationic surfactant and calcined 950 °C for 4 hours. The study showed that the nature of the surfactant changed the particle morphology, pore diameter, pore size, crystallite size, surface area and electrochemical properties. Perovskite materials were made and applied as cathode materials for low temperature – intermediate temperature solid oxide fuel cells and the materials were calcined at temperatures of 800 °C, 900 °C, and 1000 °C. The performance of the perovskite materials was measured from 300 °C – 500 °C using the SOFC testing equipment. $Ce_{0.8}Sm_{0.2}Fe_{0.9}Ir_{0.03}Co_{0.07}O_{3-\delta}$ cathode showed promising performance, with maximum power density of 0.400 W/cm^2, and corresponding area specific resistance (ASR) of 0.247 Ω cm^2 at 500 °C for the sample calcined at 1000 °C.

In this study, the cathode $Ce_{0.8}Sr_{0.2}Fe_{0.9}Ir_{0.1}O_{3-\delta}$ perovskite exhibited a power density of 0.483 W/cm^2 and ASR of 0.342 Ω cm^2. The cathode $Ce_{0.8}Sr_{0.2}Fe_{0.9}Ir_{0.04}Co_{0.06}O_{3-\delta}$ perovskite produced a power density of 0.471 W/cm^2 and ASR value of 0.349 Ω cm^2. In this study, the adaptability of sol gel technique was employed to prepare the cathode $Ce_{0.8}Sm_{0.2}Ir_yCo_{1-y}O_{3-\delta}$ (y = 0.03 - 0.04) materials. The iridium nanoparticle was varied to test the performance of the perovskite. The cathode composition for y = 0.03 produced a maximum power density of 0.287 W/cm^2 when measured at 500 °C for the

perovskite calcined at 800 °C and y = 0.04 generated a power density of 0.222 W/cm^2 at 500 °C for the perovskite calcined at 1000 °C.

Finally, the structure directing properties of Pluronic F-127 was added in different masses to SDC electrolyte material. Results showed that the nature of surfactant influences the particle morphology, pore diameter, pore size, crystallite size, surface area and electrochemical properties. An investigative study was conducted on possible electrolytes for low temperature SOFCs to find the best. These are $Ce_{1-x}Sm_xO_2$ (x = 0.1 - 0.4) compositions, $Ce_{0.8}Sm_{0.2}O_2/Na_2CO_3$, $Ce_{0.8}Sm_{0.2}O_2/LiCO_3$ and $Ce_{0.8}Sm_{0.2}O_2/Na_2CO_3$ /$LiCO_3$ composite using sol-gel technique. It was discovered that $Ce_{0.8}Sm_{0.2}O_2/Na_2CO_3$/ $LiCO_3$ electrolyte composites generated the highest current density and power density of 0.249 W/cm^2, hence it can be said they perform better at low temperature conditions.

PREFACE

The experimental work described in this thesis was carried out in the School of Chemistry and Physics, University of KwaZulu-Natal, Durban, from February 2013 to June 2015, under the supervision of Professor Patrick G. Ndungu and co-supervisor Dr. Bernard Omondi Owaga.

These studies represent original work by the author and have not otherwise been submitted in any form for any degree or diploma to any tertiary institution. Where use has been made of the work of others it is duly acknowledged in the text.

DECLARATION 1 - PLAGIARISM

I, Njoku Chima Benjamin declare that

1. The research reported in this thesis, except where otherwise indicated is my original research.

2. This thesis has not been submitted for any degree or examination at any other university.

3. This thesis does not contain other persons' data, pictures, graphs or other information, unless specifically acknowledged as being sourced from other persons.

4. This thesis does not contain other persons' writing, unless specifically acknowledged as being sourced from other researchers. Where other written sources have been quoted, then:

    a. Their words have been re-written but the general information attributed to them has been referenced

    b. Where their exact words have been used, then their writing has been placed in italics and inside quotation marks, and referenced.

5. This thesis does not contain text, graphics or tables copied and pasted from the Internet, unless specifically acknowledged, and the source being detailed in the thesis and in the References sections.

Signed

.....

DECLARATION 2 - PUBLICATIONS

DETAILS OF CONTRIBUTION TO PUBLICATIONS that form part and/or include research presented in this thesis (include publications, submitted, *in press* and published and give details of the contributions of each author to the experimental work and writing of each publication)

Publication 1

Njoku, C.B, Ndungu, P.G, Effect of non-ionic, anionic and cationic surfactants on the sol gel synthesis of IrO/$Ce_{0.8}Sm_{0.2}O_2$ nanocomposite for solid oxide fuel cell application. Journal of Fuel Cell Science & Technology, 2014. DOI: 10.1115/1.4027366.

Contributions: I carried out the experimental work, characterized the perovskite materials, applied it as electrodes in LTSOFC and prepared the manuscript. These were achieved under the supervision of my supervisors (co-authors).

Publication 2

Njoku, C.B, Ndungu, P.G, Synthesis and characterization of novel $Ce_{0.8}Sm_{0.2}Fe_{0.9}Ir_{0.03}Co_{0.07}O_{3-\delta}$ perovskite material and possible application as a cathode for low – intermediate temperature SOFCs. Materials Research Bulletin, 2015, 68, 100-108,

Contributions: I carried out the experimental work, Characterizations and prepared the manuscript under the guidance of my supervisors (co-authors). My supervisors corrected, compiled and submitted the manuscript.

Publication 3

Njoku, C.B, Omondi, B, Ndungu, P.G, Characterization and electrochemical properties of $Ce_{0.8}Sr_{0.2}Fe_{0.9}Ir_{0.04}Co_{0.06}O_{3-\delta}$ (CSFIC) cathode material for application in low temperature SOFC. ECS Trans. 2015, 68 (1), 903-917.

Contributions: I carried out the experimental work, Characterizations and prepared the manuscript under the guidance of my supervisors (co-authors). My supervisors corrected, compiled and submitted the manuscript.

Publication 4

Njoku, C.B, Omondi, B, Ndungu, P.G, Physical chemical properties of $Ce_{0.8}Sm_{0.2}Ir_yCo_{1-y}O_{3-\delta}$ (y = 0.03 - 0.04) and preliminary testing as cathode material for low temperature SOFC. Materials Research Bulletin, *submitted.*

Contributions: I carried out the experimental work, characterizations and prepared the manuscript under the guidance of my supervisors (co-authors). My supervisors corrected, compiled and submitted the manuscript.

Publication 5

Njoku, C.B, Omondi, B, Ndungu, P.G, Evaluation of novel nanophase $Ce_{0.8}Sr_{0.2}Fe_{0.9}Ir_{0.1}O_{3-\delta}$ as cathode material for low temperature SOFC. Nanomaterials for Electrocatalysis and Electrochemical Energy Applications *accepted.*

Contributions: I carried out the experimental work, Characterizations and prepared the manuscript under the guidance of my supervisors (co-authors). My supervisors corrected, compiled and submitted the manuscript.

Signed:

……..

CONFERENCE CONTRIBUTIONS

1. POSTER PRESENTATION

Njoku, C.B, Omondi B, Ndungu, P.G, Characterization and electrochemical properties of $Ce_{0.8}Sr_{0.2}Fe_{0.9}Ir_{0.04}Co_{0.06}O_{3-\delta}$ (CSFIC) cathode material for application in low temperature SOFC (Presented at the South African Chemical Society (SACI) conference at Elangeli Sun Hotel, November 29 – December 4, 2015, Durban, South Africa).

2. POSTER PRESENTATION

Njoku, C.B, Omondi B, Ndungu, P.G, Characterization and electrochemical properties of $Ce_{0.8}Sr_{0.2}Fe_{0.9}Ir_{0.04}Co_{0.06}O_{3-\delta}$ (CSFIC) cathode material for application in low temperature SOFC (Presented at the ECS conference on Electrochemical Energy Conversion & Storage with SOFC-XIV, July 26 - 31, 2015, Glasgow, Scotland).

3. ORAL PRESENTATION

Njoku, C.B, Ndungu, P.G, Effects of surfactant on the sol gel formation of iridium oxide with samarium doped ceria for SOFC application (Presented at the College of Agriculture, Engineering and Science research day 2014, Westville Campus UKZN).

4. POSTER PRESENTATION

Njoku, C.B, Ndungu, P.G, Effects of surfactant on the sol gel formation of iridium oxide with samarium doped ceria for SOFC application (Presented at the Catalysis Society of South Africa (CATSA2013), 17^{th}- 20^{th} November, 2013, Wild Coast Sun Hotel, Durban South Africa).

TABLE OF CONTENTS

ACKNOWLEDGEMENTS

My profound gratitude goes to the Almighty God, for his protection, divine guidance and direction during the period of my research.

I also want to appreciate the School of Chemistry and Physics, College of Agriculture Engineering and Science, University of KwaZulu-Natal and staff for providing a comfortable environment, well equipped laboratories and state of the art instruments to carry out my research. I would like to thank the following organizations, ESKOM-TESP and NRF South Africa (Thuthuka Grant No: 76318) for their financial support.

I want to appreciate my supervisors Professor Patrick G. Ndungu, who has been a father, academic mentor and teacher. I have learnt a lot through his guidance and supervision and Dr. Bernard Omondi for his guidance and academic mentorship in making my study a success.

I want to thank my research group members namely Ekemena, Gumbi, Nteseng, Darrel, Tsithole, Tonde, Kudzai and all my friends for their contributions academically towards the progress of my research. I also want to appreciate Dr. Olushola Ogunnubi for introducing me to this university and for his brotherly support.

Finally, I want to appreciate my parents (Mr. & Mrs Obinna Njoku), my siblings (Adaku, Chukwudi, Prince and Chika), Mrs Christabel Babazim and Mrs Nkechi Onuorah for their financial, emotional support and encouragement towards my academic achievements.

ABBREVIATIONS

Abbreviations	Meanings
ASR	Area Specific resistance
CeO_2	Cerium Oxide
cm	Centimetres
D	Scherer Constant
E_a	Activation energy of conduction (eV)
FTIR	Fourier transform Infrared spectroscopy
FWHM	Full width at half maximum (degree)
GDC	Gadolina doped ceria
YDC	Yttria doped ceria
Hrs	Hours
HRTEM	High resolution transmission electron microscopy
IrO_2	Iridium oxide
ITSOFC	Intermediate temperature solid oxide fuel cell
k	Boltzmann constant ($J\ K^{-1}$)
kHz	KiloHertz
kV	KiloVolts
L	Electrolyte thickness (cm)
LSCF	$La_{0.6}Sr_{0.4}Co_{0.2}Fe_{0.8}O_3$
LTSOFC	Low temperature solid oxide fuel cell
M	Metal
mA	Milliamperes
mins	Minutes
ml	Millilitres
mW	Milliwatts
NANOCOFC	Multifunctional nanocomposites for advanced fuel cell technology
WGS	Water gas stream
LSGM	$La_{0.8}Sr_{0.2}Gd_{0.2}M_{0.8}$
NiO	Nickel Oxide
R	Cell resistance (Ω)
rpm	Rates per minutes
S	Electrode area of the electrolyte surface (cm^2)
SDC	Samarium doped ceria
SEM	Scanning electron microscopy
SOFC	Solid oxide fuel cell
$SrCoO_2$	Strontium cobalt oxide
T	Absolute temperature (K)

TEC	Thermal Expansion Coefficient
TGA	Thermogravimetric analysis
Ton	Tonnes
XRD	X- ray diffraction
YDC	Yttria doped ceria

CHAPTER 1

INTRODUCTION

1.0 Background of study

Solid oxide fuel cells (SOFCs) are electrochemical devices used to generate electricity and have been considered to be ideal as a future power source because of the overall high energy efficiency, potentially long operational lifetime and flexibility in the fuels they use [1]. SOFCs operating temperature has been a major interest for research in the last decade, the drive has been towards the reduction of its operating temperatures, cost and maintenance. High operating temperature limits certain properties of solid oxide fuel cells [2, 3]. A major limitation is the interdiffusion between the electrode and electrolyte boundaries causing separate layer formation within the cells. This causes strain and cracks to the cell because of the variation in the thermal expansion coefficient between the cells and densification of the electrodes.

Reducing the operating temperature of SOFCs has certain advantages. It broadens the choices for electrodes and electrolyte materials, reduces production and application cost and improves the overall lifetime and stability of the fuel cell. The reduction of the operating temperatures of fuel cells can be achieved either by reducing the electrolyte thickness or by using highly conductive electrolytes and electrodes such as perovskites.

Perovskite-type complex oxides are functional inorganic materials for application as electrode and electrolyte materials in SOFCs, gas sensors, memory devices (RAM), superconductors, and as catalysts. Perovskite materials possess excellent electromagnetic properties and can accommodate a large content of oxygen vacancies, which makes some of them good oxygen ionic conductors. Perovskite structures with the general formula ABX_3, contain A sites, B sites and the X sites. The A site usually contains metal ions (cations) that have larger sizes than the cations in the B site which can allow for first row transition elements to be introduced in the lattice. The X site is usually occupied by oxygen

anions. For the purpose of this study both the A and B cations adopt a trivalent state, with the A cations being restricted to rare earth metals. Metal like ceria can exist in the cerous, cerium (III), and ceric, cerium (IV), oxidation states [4]. Both oxidation states of cerium strongly absorb ultraviolet light and have two characteristic spectrophotometric absorbance peaks [5]. The unusual catalytic behaviour involved with nanoceria and other rare earth metals is believed to be due to oxygen vacancy sites on the lattice surface. These are characterized by cerium (III) atoms situatedat the center of the vacancy, surrounded by adjacent cerium (IV) atoms or the metals in tetravalent state [6].

1.1 Cations used in perovskite compositions

Perovskite compositions can contain different metal ions when used for SOFCs as shown in Figure 1 representing the schematic diagram of the metal ions used in this study for perovskite structures.

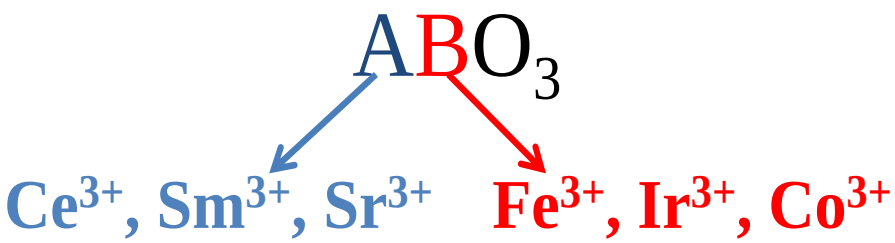

Figure 1: Schematics of compositions under study.

Cobalt containing compounds possess adequate linear thermal expansion coefficient, high electrical conductivity, magnetic and catalytic properties. Cobalt containing perovskites have the ability to adopt several oxidations and spin states, in various oxygen environments which accounts for the richness of their physical properties [2, 3]. When strontium fully occupies the A sub-lattice of perovskites, $SrCoO_3$ perovskite is formed which corresponds to a cubic perovskite. $SrCoO_{3-y}$ belongs to a family of non-stoichiometric perovskites with high oxygen mobility at room temperature [7, 8]. $SrCoO_{3-y}$ perovskites are used as cathodes

for SOFCs because of their high oxygen permeability values which have been shown to be greater than those of yttria stabilized zirconia (YSZ) [9].

Ceria has been effective in ceria based electrodes because of its high catalytic activity in oxygen combustion reactions [10 - 12], usually with the combination of samarium, gadolinium or any rare earth metals. For example, when ceria is doped samarium as SDC, they have been used as solid electrolytes because of their high ionic conductivity in low temperature SOFCs (LTSOFCs) [13 - 15]. Addition of sodium carbonates to SDC electrolyte increases the oxygen ion conductivity and improves the thermal stability of the nanostructure. The addition also improves the densification of the solid electrolyte layer to prevent any gas leakage and enhances its electrochemical performance at lower temperatures [16 - 18].

Ferrites provide stability in SOFCs cathodes and are also known to be substantially superior in electronic and ionic conductivity. Ferrites also have good thermal expansion coefficient under SOFC cathodic conditions whileiridium oxide can be reliable, for its electrocatalytic activities for oxygen reduction and when used in perovskites contributes to an increased conductivity of the material [19, 20].

1.2 Methods of improving the properties of Perovskites

1.2.1 Addition of Surfactant

Surfactants are compounds that lower the surface tension or interfacial tension between two liquids or between a liquid and a solid. Surfactants are classified according to their polar head groups.Polar heads with no charge groups are called non-ionic, while those that carry charge on their heads are called ionic surfactants. The ionic ones can be anionic when the polar heads are negatively chargedor cationic ifpositively charged.

During the formation of perovskites, the textural properties and morphology can be modulated by using surfactants while keeping the other processing parameters such as the solvents constant. Particle sizes for example can be controlled either by preventing or promoting coalescence of the droplets during their gelation which can be influenced by the

nature of the surfactant. There are no simple selection rules that can be applied to predict which surfactant will give a particular particle size, but research has proven that surfactant structure can provide better stabilization of the micelle walls, reduction in the inter-droplet exchange, resulting in the production of smaller particles and smaller crystals [21] and the avoidance of the aggregation of the metallic nanoparticles into matrices [22]. with appropriate pore diameter, high surface areas and a better access to the active sites [23 - 25]. These properties play a major role in determining the nature, number of active sites, and the activity of the perovskite.

1.2.2 The Sol-gel Method

Sol-gel method was utilised in this study. This technique is an adaptable and relatively simple method easily modified to synthesize complex metal oxide formulations (perovskites) with controlled structure [26, 27]. These materials are produced by two methods, the hydrolysis of the metal alkoxide precursor and its condensation [28] or by the aggregation of aqueous colloidal dispersions containing discrete sol particles. The mechanism of sol-gel transformation, structure and interactions in the colloidal gel state has led to the development of materials with tailored microstructure [29, 30].

1.3 Problem Statement

Solid oxide fuel cells offer more advantages than traditional energy conversion systems. The advantages include high efficiency, reliability, modularity, fuel adaptability, clean and minimal emission of pollutants, quiet and vibration-free operation eliminating noise. Although the originally developed SOFCs operated primarily in the temperature range of 900 to 1000 °C, it has been shown that at these temperatures they undergo high degradation especially of component materials, and slow start up and cool down times are observed. It is as such imperative that the fuel cell operation is optimized by reducing the SOFC operating temperature range between 300 – 600 °C. This would allow the use of a wide set of materials, that are less demanding on the seals and the balance of plant components, simplifies thermal management, helps in faster start up and cool down time, and results in less degradation of cell and stack material.

1.4 Hypothesis

In this study the hypothesis is made that perovskite materials fabricated, would exhibit high and promising performances as electrodes and electrolytes when applied to Low Temperature Solid Oxide Fuel Cells (LTSOFC) that work within 300 – 600 °C. These would be comparable to performances by perovskite materials recorded in the literature.

1.5 Aim & Objectives

The aim of this study is to develop novel nanocomposite approach to design and fabricate ceria based perovskite materials that can be applied as electrodes and electrolytes for Low temperature solid oxide fuel cells. This was achieved by the following objectives:

1. To synthesize IrO/$Ce_{0.8}Sm_{0.2}O_2$ perovskites with anionic, cationic and ionic surfactants as anodes for LTSOFC using sol gel technique.
2. To characterize the anode material using XRD, Raman spectroscopy, FTIR spectroscopy, SEM, HRTEM and Textural analysis (BET) and evaluate its electrochemical performance using SOFCs setup.
3. To synthesize novel $Ce_{0.8}Sm_{0.2}Ir_yCo_{1-y}O_{3-\delta}$ (0.03–0.04) and $Ce_{0.8}Sm_{0.2}Fe_{0.9}Ir_{0.03}Co_{0.07}O_{3-\delta}$ perovskites that would function as cathodes for LTSOFC and ITSOFC using sol-gel technique.
4. To characterize $Ce_{0.8}Sm_{0.2}Ir_yCo_{1-y}O_{3-\delta}$ (0.03 – 0.04) and $Ce_{0.8}Sm_{0.2}Fe_{0.9}Ir_{0.03}Co_{0.07}O_{3-\delta}$ materials using XRD, Raman spectroscopy, FTIR spectroscopy, SEM and HRTEM and to evaluate its electrochemical performances using SOFCs testing setup
5. To synthesize $Ce_{0.8}Sr_{0.2}Fe_{0.9}Ir_{0.1}O_{3-\delta}$ and $Ce_{0.8}Sr_{0.2}Fe_{0.9}Ir_{0.03}Co_{0.07}O_{3-\delta}$ perovskite that would function as cathodes for LTSOFC using sol gel technique.
6. To characterize $Ce_{0.8}Sr_{0.2}Fe_{0.9}Ir_{0.1}O_{3-\delta}$ and $Ce_{0.8}Sr_{0.2}Fe_{0.9}Ir_{0.03}Co_{0.07}O_{3-\delta}$ cathode materials using XRD, Raman spectroscopy, FTIR spectroscopy, SEM, HRTEM, Textural analysis (BET) and TGA and to evaluate the electrochemical performances of the cathode materials using SOFC setup.
7. To synthesize $Ce_{0.8}Sm_{0.2}O_2$ with pluronic F-127 surfactant that would function as electrolyte for LTSOFC using sol gel technique.

8. To characterize $Ce_{0.8}Sm_{0.2}O_2$ + pluronic F-127 nanomaterial using XRD, Raman spectroscopy, SEM, HRTEM and Textural analysis (BET) and to evaluate the electrochemical performance of the electrolytes using SOFC setup.
9. To synthesize $Ce_{0.8}Sm_{0.2}O_2$ (x = 0.1 – 0.4), $Ce_{0.8}Sm_{0.2}O_2/Na_2CO_3$, $Ce_{0.8}Sm_{0.2}O_2/LiCO_3$, $Ce_{0.8}Sm_{0.2}O_2/Na_2CO_3/LiCO_3$ that would function as cathodes for LTSOFC using sol gel technique.
10. To characterize $Ce_{0.8}Sm_{0.2}O_2$ (x = 0.1 – 0.4), $Ce_{0.8}Sm_{0.2}O_2/Na_2CO_3$, $Ce_{0.8}Sm_{0.2}O_2/LiCO_3$, $Ce_{0.8}Sm_{0.2}O_2/Na_2CO_3/LiCO_3$ electrolytes using XRD, Raman spectroscopy, FTIR spectroscopy, SEM, HRTEM and textural analysis (BET) and to evaluate the electrochemical performances of the electrolytes

1.6 Thesis Overview

This thesis consists of ten chapters which are discussed below. The novel part about this research is the synthesis of the electrode and electrolyte materials using sol gel synthesis that involves the integration of structure directing agents (surfactants), the aging and drying time and the solvent to metal oxide ratio. The study also integrated the use of a rare metal like Iridium in synthesizing the electrode materials forming a combination of perovskite structures that are novel, efficient and exhibited promising performance.

Chapter 1 covers the background of the study.

Chapter 2 covers the Literature review on the components of a SOFC, the mechanisms, types and the structures of the anode, cathode and electrolytes. It also includes other components like interconnectors and mathematical parameters used in SOFC models.

Chapter 3 describes the effects of the templating and structural directing properties of ionic, anionic and cationic surfactants on the perovskite materials made as electrodes. This work has been published.

Chapter 4 shows a study of the effects of varying the composition of iridium on the structural, textural, morphological and electrochemical properties of novel $Ce_{0.8}Sm_{0.2}Ir_yCo_{1-}$

$_yO_{3-\delta}$ (y = 0.03 - 0.04) perovskite that was applied as cathode in LTSOFC. This work is under review.

Chapter 5 integrates the synthesis, characterisation and electrochemical performances of novel $Ce_{0.8}Sm_{0.2}Fe_{0.9}Ir_{0.03}Co_{0.07}O_{3-\delta}$ perovskite material applied as cathode for LTSOFCs. This work has been published.

Chapter 6 covers the study on the structural, textural, morphological and electrochemical properties of a novel $Ce_{0.8}Sr_{0.2}Fe_{0.9}Ir_{0.1}O_{3-\delta}$ perovskite applied as cathode for LTSOFCs. This work has been published.

Chapter 7 includes the method of preparation, characterisation and electrochemical performance of novel $Ce_{0.8}Sr_{0.2}Fe_{0.9}Ir_{0.04}Co_{0.06}O_{3-\delta}$ (CSFIC) material applied as cathode for LTSOFCs. This work has been published.

Chapter 8 describes the effect of the structural directing properties of surfactant on the structural, textural, physical and morphological properties of samarium doped ceria ($Ce_{0.8}Sm_{0.2}O_2$) and to investigate, if the addition of surfactant improves the electrochemical performance of the electrolyte when applied in LTSOFCs.

Chapter 9 presents a comparative study of the different electrolytes that work best in LTSOFCs conditions and to investigate the electrolyte that exhibits the maximum electrochemical performance when tested.

Chapter 10 gives the conclusion, and further work that can be done following this study.

References

1. Hans-Rudolf, W., & Andrei, B. (2004). Minerals: Their Constitution and Origin. New York, NY: Cambridge University Press.
2. Li, Z. C., & Bergman, B. (2005). Electrical properties and ageing characteristics of $BaTiO_3$ ceramics doped by single dopants. *Journal of the European Ceramic Society*, *25*(4), 441- 445.
3. Luxová, J., Šulcová, P., & Trojan, M. (2008). Study of perovskite compounds. *Journal of Thermal Analysis and Calorimetry*, *93*(3), 823-827.
4. Jiang, L. Q., Guo, J. K., Liu, H. B., Zhu, M., Zhou, X., Wu, P., & Li, C. H. (2006). Prediction of lattice constant in cubic perovskites. *Journal of Physics and Chemistry of Solids*, *67*(7), 1531-1536.
5. Hu Z.Y., Haneklaus S., Sparovek G., Schnug E. (2006). Rare earth elements in soils. *Commun Soil Sci Plan*, *37* (9–10), 1381–1420.
6. Heckert, E. G., Karakoti, A. S., Seal, S., & Self, W. T. (2008). The role of cerium redox state in the SOD mimetic activity of nanoceria. *Biomaterials*, *29*(18), 2705-2709.
7. Esch, F., Fabris, S., Zhou, L., Montini, T., Africh, C., Fornasiero, P., & Rosei, R. (2005). Electron localization determines defect formation on ceria substrates. *Science*, *309*(5735), 752-755.
8. Zhu, W., Lü, Z., Li, S., Wei, B., Miao, J., Huang, X., Chen, K., Ai, N., & Su, W. (2008). Study on $Ba_{0.5}Sr_{0.5}Co_{0.8}Fe_{0.2}O_{3-\delta}$–$Sm_{0.5}Sr_{0.5}CoO_{3-\delta}$ composite cathode materials for IT-SOFCs. *Journal of Alloys and Compounds*, *465*(1), 274-279.
9. Njoku, C. B., & Ndungu, P. G. (2015). Synthesis and characterization of novel $Ce_{0.8}Sm_{0.2}Fe_{0.9}Ir_{0.03}Co_{0.07}O_{3-\delta}$ perovskite material and possible application as a cathode for low–intermediate temperature SOFCs. *Materials Research Bulletin*, *68*, 100-108.
10. Chen, D., & Jiao, X. (2000). Solvothermal synthesis and characterization of barium titanate powders. *Journal of the American Ceramic Society*, *83*(10), 2637-2639.

11. Zhang, L., Lan, R., Kraft, A., & Tao, S. (2011). A stable intermediate temperature fuel cell based on doped-ceria–carbonate composite electrolyte and perovskite cathode. *Electrochemistry Communications*, *13*(6), 582-585.
12. Goodenough, J. B., & Huang, Y. H. (2007). Alternative anode materials for solid oxide fuel cells. *Journal of Power Sources*, *173*(1), 1-10.
13. Beresnev, S. M., Kuzin, B. L., & Bronin, D. I. (2007). Nickel-cermet anode for fuel cells with the LSGM electrolyte. *Russian Journal of Electrochemistry*, *43*(8), 883-887.
14. Dalslet, B., Blennow, P., Hendriksen, P. V., Bonanos, N., Lybye, D., & Mogensen, M. (2006). Assessment of doped ceria as electrolyte. *Journal of Solid State Electrochemistry*, *10*(8), 547-561.
15. Tsipis, E. V., Kharton, V. V., & Frade, J. R. (2007). Electrochemical behavior of mixed-conducting oxide cathodes in contact with apatite-type $La_{10}Si_5AlO_{26.5}$ electrolyte. *Electrochimica acta*, *52*(13), 4428-4435.
16. Grgicak, C. M., Green, R. G., & Giorgi, J. B. (2008). SOFC anodes for direct oxidation of hydrogen and methane fuels containing H_2S. *Journal of Power Sources*, *179*(1), 317-328.
17. Steele, B. C. (1999). Fuel-cell technology: Running on natural gas. *Nature*, *400*(6745), 619-621.
18. Schober, T., & Ringel, H. (2004). Proton conducting ceramics: recent advances. *Ionics*, *10*(5-6), 391-395.
19. Schober, T. (2005). Composites of ceramic high-temperature proton conductors with inorganic compounds. *Electrochemical and Solid-State Letters*, *8*(4), A199-A200.
20. Uvarov, N. F., Ponomareva, V. G., & Lavrova, G. V. (2010). Composite solid electrolytes. *Russian Journal of Electrochemistry*, *46*(7), 722-733.
21. Adler, S. B. (2004). Factors governing oxygen reduction in solid oxide fuel cell cathodes. *Chemical Reviews*, *104*(10), 4791-4844.
22. Guo, W., Liu, J., Jin, C., Gao, H., & Zhang, Y. (2009). Electrochemical evaluation of $La_{0.6}Sr_{0.4}Co_{0.8}Fe_{0.2}O_{3-\delta}$–$La_{0.9}Sr_{0.1}Ga_{0.8}Mg_{0.2}O_{3-\delta}$ composite cathodes for $La_{0.9}Sr_{0.1}$

$Ga_{0.8}Mg_{0.2}O_{3-\delta}$ electrolyte SOFCs. *Journal of Alloys and Compounds*, *473*(1), 43-47.

23. Qiang, F., Sun, K., Zhang, N., Zhu, X., Le, S., & Zhou, D. (2007). Characterization of electrical properties of GDC doped A-site deficient LSCF based composite cathode using impedance spectroscopy. *Journal of Power Sources*, *168*(2), 338-345.
24. Blennow, P., Hjelm, J., Klemensø, T., Ramousse, S., Kromp, A., Leonide, A., & Weber, A. (2011). Manufacturing and characterization of metal-supported solid oxide fuel cells. *Journal of Power Sources*, *196*(17), 7117-7125.
25. Shen, C., & Shaw, L. L. (2010). FTIR analysis of the hydrolysis rate in the sol–gel formation of gadolinia-doped ceria with acetylacetonate precursors. *Journal of Sol-gel Science and Technology*, *53*(3), 571-577.
26. Brasil, M. C., Benvenutti, E. V., Gregório, J. R., & Gerbase, A. E. (2005). Iron acetylacetonate complex anchored on silica xerogel polymer. *Reactive and Functional Polymers*, *63*(2), 135-141.
27. Sharma, M., & Jeevanandam, P. (2011). Synthesis of magnesium oxide particles with stacks of plate's morphology. *Journal of Alloys and Compounds*, *509*(30), 7881-7885.
28. Mastuli, M. S., Ansari, N. S., Nawawi, M. A., & Mahat, A. M. (2012). Effects of cationic surfactant in sol-gel synthesis of nano sized magnesium oxide. *APCBEE Procedia*, *3*, 93-98.
29. Lou, Z., Peng, J., Dai, N., Qiao, J., Yan, Y., Wang, Z., Wang, J., & Sun, K. (2012). High performance $La_3Ni_2O_7$ cathode prepared by a facile sol–gel method for intermediate temperature solid oxide fuel cells. *Electrochemistry Communications*, 22, 97-100.
30. Ermokhina, N. I., Nevinskiy, V. A., Manorik, P. A., Ilyin, V. G., Shcherbatyuk, N. N., Klymchyuk, D. O., & Puziy, A. M. (2012). Synthesis of large-pore mesoporous nanocrystalline TiO_2 microspheres. *Materials Letters*, *75*, 68-70.

CHAPTER 2

Literature review

1.0 Introduction

Solid oxide Fuel cells are promising power generation systems of high efficiency through the conversion of fuel gases by electrochemical reactions. Electrical energy is produced in the process and steam and heatare giving off as byproducts [1, 2]. The general advantages of solid oxide fuel cells are reflected by the following desirable characteristics, high energy conversion efficiency, low emissions of pollutants, low noise or vibrations, efficient reduction of greenhouse gas (CO_2) formation at the source compared to low-efficiency devices; and provides simple conversion of chemical energy to electrical energy. Other advantages include fuel flexibility and existing infrastructure of hydrocarbon fuel supplies, co-generation ability [3 - 8].

SOFCs have been applied in auxiliary power units of vehicles, stationary power generation used to power homes, industries, offices and malls and in the production of heat engines that also act as power generating devices. The power generation outputs are within 100 W to 2 MW with high efficiency. For example, an Australian company, Ceramic Fuel Cell Ltd. in 2009 produced SOFCs that work with efficiency of 60 % [9]. SOFCs are used in the production of on-board auxiliary power units for heavy duty trucks, recreational vehicles and luxury automobiles that run on electrical power and vehicles that use pure hydrogen as fuel source. For example a 5 kW auxiliary power unit was successfully developed by Delphi Corporation, which runs on gasoline or diesel through its reformation by partial catalytic oxidation. Delphi worked on improving the auxiliary units over the years by reduction of its mass, volume and compatibility with automotive requirements, faster start up time and improved thermal cycling tolerance [10 - 12].

Over the years, the development of SOFCs has been within the operating temperature range of 900 to 1000 °C normally referred to as high temperature SOFCs (HTSOFCs). The

development of HTSOFCs is accompanied by the release of exhaust heat, which in turn can be used for cogeneration of energy when integrated with a gas turbine to increase the total efficiency of the engine capacity system [13]. However, SOFCs operating at these high temperatures come with disadvantages, which are highdegradation of fuel cell component materials, slow start up and cool down times and thermal compatibility of component materials [14, 15]. Based on these disadvantages studies on low temperature SOFCs (LTSOFCs) have become an area of intensive researchwith the focus on developing SOFCs that operate between 300 - 600 °C [16]. The advantages of reducing SOFCs temperature makes it possible to use less expensive materials, to suppress degradation caused by the high operating temperatures and by thermal cycling, to facilitate miniaturization, quicker start up and cool down time and to improve the efficiency of the SOFC system [17 - 19]. LTSOFCs have disadvantages which includes decrease in electrical conductivity and electrode kinetics during operation. One way to minimize these losses is using electrolytes with high ionic conductivity or by using thin electrolytes and alternative cell materials and designs, which are the main areas of current investigation [20]. SOFCs comprise of three key components, the electrolyte, cathode and anode, a schematic representation is shown in Figure 1.

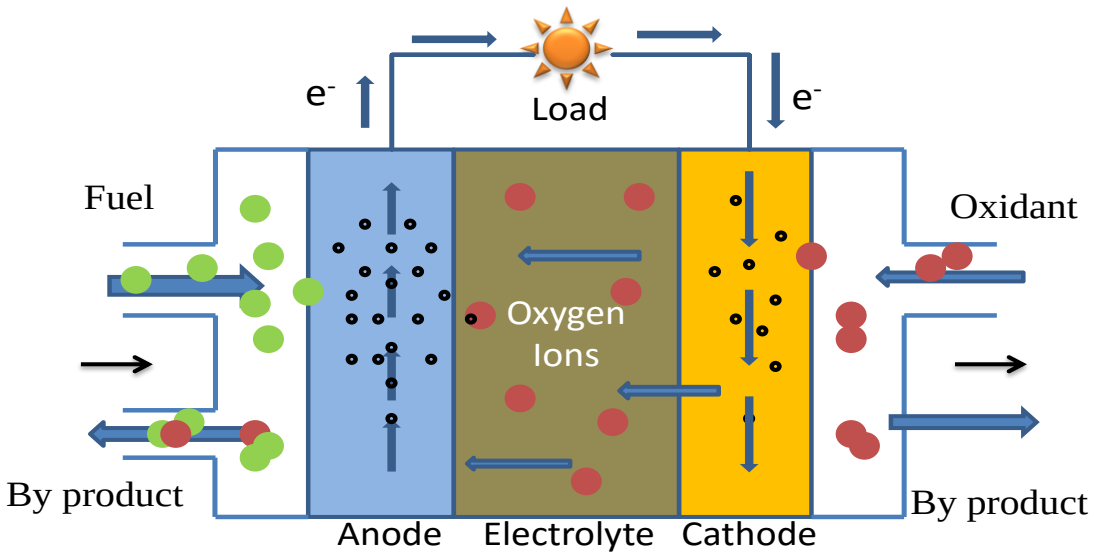

Figure 1: A Schematic diagram of an SOFC mechanism.

In SOFCs, the electrolyte layer is required to be compact while providing a pathway for ion transport. It is inserted between two porous electrodes called the anode and cathode, where the fuel oxidation reaction and the oxygen reduction reaction occur respectively. In SOFC device, hydrogen molecules (as fuel gas) dissociate and release electrons at the anode, these electrons migrate to the surface of the anode and move to the cathode along the external circuit, while the oxygen molecules from the cathode side are separated and ionized by the electrons to form oxygen ions. When the ions combine with the electrons, the oxygen ions are then transported to the cathode/electrolyte interfaces which are then incorporated into the electrolyte. They move continuously from the electrolyte to the anode/electrolyte interface, and then eventually to the reaction site. The half - cell reaction for the electrode processes are shown the equation below [21].

The half - cell oxidation reaction that occurs at the anode is:

$$2H_2 + 2O_2^- \leftrightarrow 2H_2O + 4_e^- \quad (1)$$

The half – cell reduction reaction that occurs at the cathode is:

$$O_2 + 4_e^- \rightarrow O_2^- \quad (2)$$

The reaction of these ions with the electrons generates electricity and produces water in the form of steam at the triple phase boundary (TPB) (where the ions, electrons and the gas phase meet). The water then flows to the surface of the anode and diffuses into the bulk gas of the exhausted fuel. The electron transport in the external circuit generates electricity and heat. Whereas for some composite electrolytes and perovskite electrode materials that exhibit mixed ionic and electronic conductivity in the fuel cell condition, water is produced both at the anode and cathode chambers of the cell [22, 23].

1.1 Types of SOFC

SOFCs are classified based on operating temperatures, electrolytes used, its combination with other components such as gas turbines and the electrochemical processes involved. SOFCs that operate at a temperature range, between 300 – 600 °C are called low

temperature SOFCs (LTSOFCs) [24]. Development of low temperature SOFCswould mitigate degradation, reduce sealing problems, encourage the use of less expensive materials, reduce production cost (e.g., ferritic stainless steels for interconnect), improve response to rapid start-up and repeat thermal cycling from ambient to operating temperatures [25 - 27].

SOFCs that operate between 600 and 800 °C are called Intermediate temperature SOFCs (ITSOFCs). The push for high performance ITSOFCs has been an area of focus in most research and development for the past decades. The electrodes used in ITSOFCs should possess adequate porosity for gas transport, high electrical conductivities, long-term stability and good compatibility with the electrolyte. There are factors that govern the electrode performance which includes the electronic resistivities of the electrocatalysts, overpotentials associated with charge-transfer at the electrocatalyst/electrolyte gas-phase boundaries, the ionic resistivity of the electrolyte, and rates of transport of gases through the porous electrodes. It has also been reported that slow interfacial (charge-transfer) reaction rate at the electrocatalyst/electrolyte interfaces often limits performance. One area of focus is the cathode material, it has been established that the oxygen reduction reaction is responsible for most of the limitation in performance, so the catalytic activity of the cathode is being studied and enhanced through various techniques, including catalyst impregnation to improve ITSOFCs [28 – 31].

SOFCs that operate in the temperature range of 800 to 1000 °C and above are called high temperature SOFCs (HTSOFCs). HTSOFCs exhibit high capabilities for the internal reformation of hydrocarbon fuels for example, natural gas. Such high temperature SOFCs also provide high quality exhaust heat for cogeneration, which when pressurized, can be integrated with a gas turbine to further increase the overall efficiency of the power system [32]. Fuel cells operating at high temperatures place considerable restrictions on the materials that can be used in both the cell construction and in the balance of plant materials, mismatch in thermal expansion coefficient (TEC) between the cell materials leading to cracking, slow startup and long cool down times.

Solid oxide fuel cell can also be combined with a gas turbine called SOFC-GT [33 - 37]. Such systems have been evaluated by Siemens Westinghouse and Rolls Royce as a means to achieve higher operating efficiencies by running the SOFC under pressure. SOFC - GT systems typically includes the anodic and cathodic atmosphere recirculation, thus increasing its efficiency. Theoretically, the combination of the SOFC and a gas turbine can produce overall results of high electrical and thermal efficiency. Palsson *et al*. [32] reported a maximum efficiency of 65 % lower heating value (LHV) obtained at a pressure ratio of 2, developed from a two dimensional, steady-state SOFC model and a combined system containing an external pre-reforming and recirculation of anode gases. GT–SOFC system comprises of six parts: air compressor, high temperature SOFC, combustor, recuperator, gas turbine and power turbine. Generally, SOFC can be attached to gas turbines in two different ways: indirect (Figure 2) and direct combinations. For indirect, the combustor of the gas turbine is substituted with a heat exchanger wherein air from the compressor is heated up by the fuel cell exhaust (Figure 2). Under the indirect SOFC–GT hybrid system, the SOFC can be operated at atmospheric conditions [38]. A schematic diagram is shown in Figure 2.

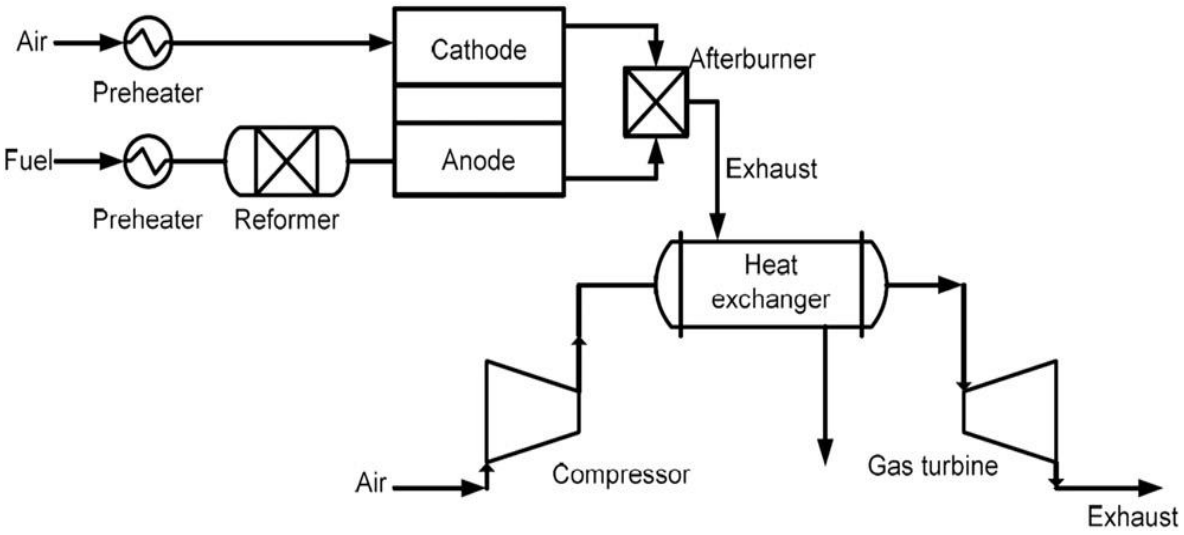

Figure 2: Schematics of combined gas turbine power plant with SOFC (Indirect).

Other types of SOFC are solid oxide electrolyser cells (SOEC) which are solid oxide fuel cells set in regenerative mode for the electrolysis of water with a solid oxide or ceramic electrolyte to produce oxygen and hydrogen gas. During this process vast amount of hydrogen carriers are produced, and they can operate at low temperatures and high temperature ranges. At low temperature range below 100 °C, alkaline water electrolysers are commercially available, and some work has been carried out to further improve the energy efficiency of the process at such temperatures. With conventional alkaline water electrolysers efficiencies can reach up to 65 %, but this efficiency can be improved to exceed 80 % by applying advanced technology with catalytically activated electrodes. High temperature electrolysers operate within the temperature range of 700 – 1000 °C and offers some added advantages compared to the low temperature techniques as shown in Figure 3. The higher operating temperature results in faster reaction kinetics thus enabling potentially high energy efficiency [39, 40].

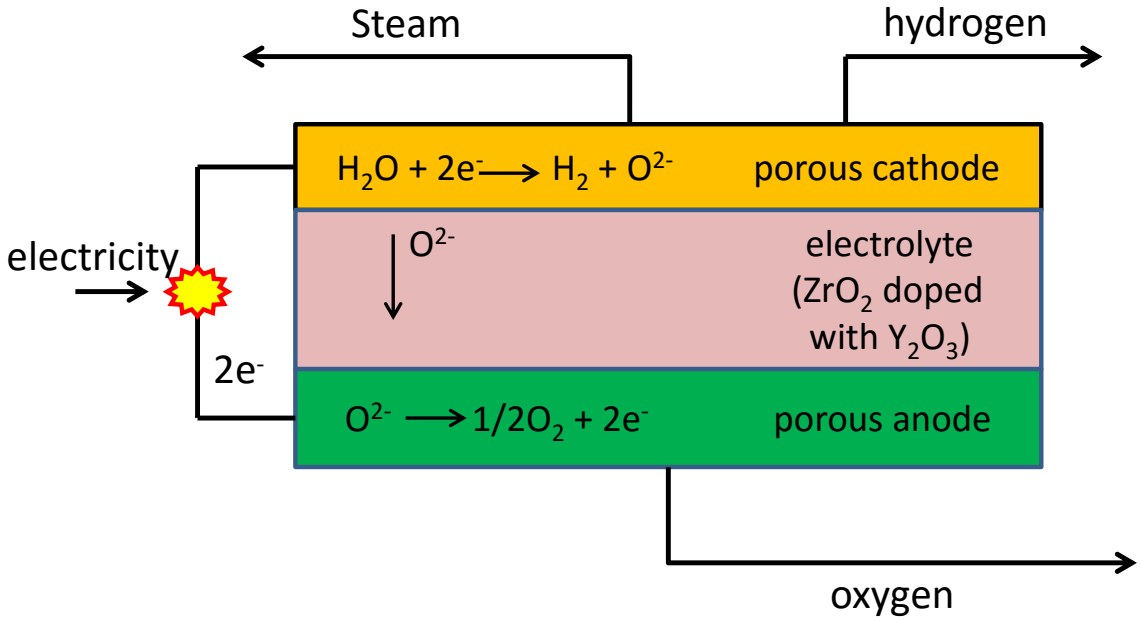

Figure 3: Schematics of a high temperature solid oxideelectrolyser cell.

1.2 Materials used for SOFC components

1.2.1 Anodes

SOFC anodes are generally porous ceramic-metallic (cermet) composites of an electrolyte (e.g. CeO_2) and a metal such as nickel (Ni). The metal acts as a catalyst to promote fuel oxidation, and serves as an electronic conductor, while CeO_2 acts as a conductor of O_2^- ions into the porous anode. This process extends the triple phase boundary (TPB) region, and provides a structural support to prevent the sintering of nickel [41, 42]. The electrolyte aids to balance the thermal-expansion coefficients of the anode and electrolyte, deterring cracking and leakage produced by thermal cycling [43]. An anode works as a catalyst for light hydrocarbon of fuels like methane (CH_4), pure hydrogen (H_2), mixture of carbon monoxide (CO), hydrogen, diesel, gasoline and the reformation of fuels into hydrogen. The electrochemical process at the anode comprises of the diffusion of oxygen ions through the electrolyte to oxidize the hydrogen fuel at the anode side, and produces heat, water and electricity in the process [44, 45]. The electrochemical reactions at the anode are shown in the equations below.

The overall anode half-cell oxidation reactions for four typical fuels are [45],

$$H_2(g) + O^{2-}(el) \leftrightarrow H_2O + 2e^-(a) \quad (3)$$

$$CO(g) + O^{2-}(el) \leftrightarrow CO_2(g) + 2e^-(a) \quad (4)$$

$$CH_4(g) + 4O^{2-}(el) \leftrightarrow CO_2(g) + 2H_2O + 8e^-(a) \quad (5)$$

$$C(s) + 2O^{2-} \leftrightarrow CO_2(g) + 4e^-(a) \quad (6)$$

where el = electrolyte, a = anode, g = gas.

The anode and materials must possess some distinguishable properties to be compatible with other components in an SOFC system. Anodes must have high electronic and ionic conductivity for improved transport of ions and electrons. They must possess reducing abilities for fuel oxidation and the porosity of the ceramic anode layer must be pronounced

for free flow of gases and electrons to the active sites [46 - 49]. The thermal expansion coefficient must be compatible with that of the cathode and electrolyte to avoid high polarisation loss and cracking of the cells.

1.2.2 Structure of Anodes

In recent years the development of anodes has focused on nickel because of its abundance and availability. The thermal expansion for nickel (13.3×10^{-6}/C) is higher than YSZ (10×10^{-6}/C) or doped ceria in it pure form, which makes it difficult to pair. Pairing them makes nickel to sinter and close off its porosity at high operating temperatures. This problem has been solved by making anode composites with electrolyte material. The electrolyte composites provide structural support for Ni-particles prevents closure of the pores and improves anode to electrolyte adhesion [43].

In addition, anode should be porous when fabricated. The microstructure must have lots of chemical and electrochemical reaction sites to promote charge transfer. They must also possess high solid-phase connectivity for electron, ion conduction and connected pore network to reduce limitations of mass transport [44 - 46]. SOFC anodes must also be chemically, mechanically compatible and stable under fabrication and operating conditions. They can be fabricated by impregnating the electrolyte with Ni or NiO e.g Ni-YSZ or Ni-GDC or SDC to extend the TPB into the bulk space of the anode. Another method is by infiltrating other electrolytes to the anode cermet e.g Ni-YSZ/SDC to improve the ionic and catalytic activities of the anode [50 - 55].

However, anodes can be applied to fuel cell by using powder technology processes. These techniques are used for the addition of Ni slurries over the cell and the electrolyte composite by electrochemical vapour deposition, or Ni - YSZ/SDC slurry is applied and sintered [56]. Another approach of using NiO - YSZ/SDC slurries is by freeze-drying approach to form porous structures without the use of fillers. Freeze dry process is done by applying the slurry through a dipping process and then freeze-dried which is then allowed to sublime. Due to the crystallization of water the resulting pore structures formed are neatly aligned allowing the passage of gases to and from the electrolyte/anode interface.

The fineness of the pore structure is easily controlled by adjusting the solid contents and water content of the slurry [57]. The anodes in powder form can also be applied unto the electrolyte by pellet formation. The anode powder is added unto the electrolyte in a pellet chamber and pressure is then exerted to form a disc. Moreover the thickness of the anode slurry depends on the structural configuration of the cell, for anode supported cells the anode cermet is thicker than that of electrolyte supported cells which is showed in Figure 5.

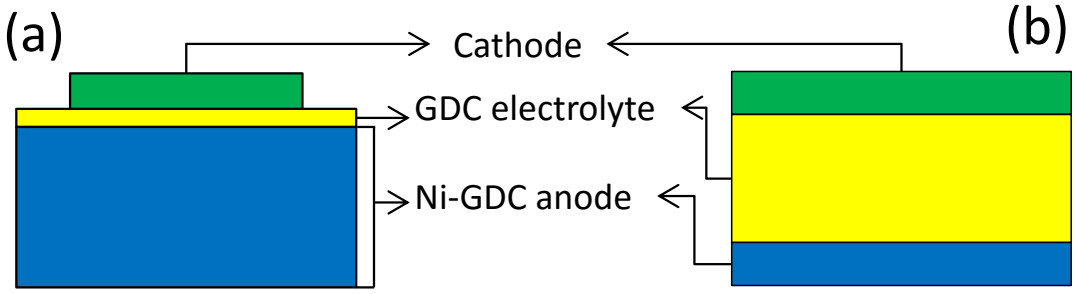

Figure 4: The schematics of (a) Anode supported cell configuration and (b) The electrolyte supported cell configuration.

1.2.3 Materials used as Anodes

1.2.3.1 Nickel based anodes

Nickel has been proven to be the best metallic conductor and is used as metallic anodes. Nickel is a superb catalyst for hydrocarbon fuel reforming, variability, and cracking, which causes rapid carbon deposition inside SOFC anodes, producing coking and deactivation at desired operating temperatures [58]. To some degree, the optimization of SOFC operating conditions can avoid carbon deposition. For instance, carbon deposition can be suppressed by increasing steam content through steam reforming and water gas stream (WGS) reactions. Likewise, carbon deposition on many oxides can also be prevented by reducing the operating temperature below 750 °C which helps to restrict CH_4 dissociation [59, 60].

Nickel combined with electrolytes to form anode cermet such as Ni-YSZ/SDC has been explored because of its advantage over other metal anode cermets. This is because during thermal cycling the porous layer of other metals detach from the electrolyte material due to

the disparity in their thermal expansion coefficient, leading to an increase in electrode resistance. This can be controlled by sintering fine grained metal/electrolyte cermet such as nickel based anodes, because, it is less volatile, chemically stable, affordable and has high catalytic activity [60]. For example Zhan *et al.* [61] reported a power density of 1.00 W/cm^2 for NiO-SDC anode, using H_2 + 3 % H_2O fuel composition at 600 °C and 0.60 W/cm^2 at 590 °C using 6 % iso-C_8H_{18} + 94 % air. Njoku *et al.* [62, 63] recorded a power density of 0.47 W/cm^2 at 500 °C for NiO-SDC anode and 0.40 W/cm^2 at 500 °C in pure hydrogen. Zha *et al.* [61] also investigated Ni-GDC anode at 600 °C and recorded a power density of 0.60 W/cm^2, 0.519 W/cm^2 and 0.433 W/cm^2 for H_2, CH_4 and C_3H_8 fuel gas respectively.

Further studies have also been done on infiltrating electrolytes into the anode cermets using Ni, Ru, Cu, YSZ, gadolinium doped ceria (CGO), on different fuel sources to improve its performance [61]. For example Hibino *et al.* [64] reported that Ru-Ni-GDC anode in Ru-Ni-GDC/GDC/SSC cell exhibited power densities of 0.769 W/cm^2 for H_2 gas, 0.750 W/cm^2 for Dry CH_4, 0.716 W/cm^2 for dry C_2H_6 and 0.648 W/cm^2 for dry C_3H_8 respectively at 600 °C. Also recent work done with nanostructured barium-oxide/nickel (BaO/Ni) anode interface produced by vapor deposition of BaO into Ni-YSZ has shown to be effective for carbon removal [65]. The BaO/Ni-YSZ anode exhibited stability during operation and high power density of 0.88 W/cm^2 for CO, 0.70 W/cm^2 C_3H_8 and gasified carbon fuels at temperatures below 750 °C, with no observable microstructural change and minimal carbon build up [65, 66].

Testing was also done for methane (CH_4) oxidation over the catalysts comprising of Cu, bimetallic Cu– Ni, and Ce (Ln)$O_{2-\delta}$, where (Ln = Gd or Tb), because copper is preferred for the conversion of hydrocarbon fuels, due to its resistance to carbon deposition. Ceria-based oxides ($Ce_{1-x}Gd_xO_{2-\delta}$ or GDC) are commonly used because ceria is a superb electrocatalyst for CH_4 and a good oxygen-ion conductor at reduced temperatures [60]. It was discovered that Ni-ceria cermets suffer from dimensional instabilities caused by the local oxygen partial pressure p(O_2) variations and minor TEC mismatch [61]. Therefore the combination of one redox-stable phase with moderate thermal expansion can be used to avoid the resultant increase in anodic polarization.

1.2.3.2 Ceria based anodes

Ceria-based anode materials were first tried out in SOFCs in the 1960s due to a number of reasons. They are known to have high catalytic activity in oxygen combustion reactions, especially in carbon oxidation which is beneficial to fuel cells which use biogas as fuel. In addition, the reduced form of $CeO_{2-\delta}$ and its derivatives have a substantial mixed oxygen ionic and electronic conductivity. The enhancement of its transport properties and reducibility can be made possible by acceptor-type doping (positive charge carriers that influence the properties of the material) [67, 68], which improve the electrode performance. For example, high power density was reported for $Ce_{1-x}Sm_xO_{2-\delta}$ (x = 0 – 0.4) anodes with YSZ electrolyte at 800 – 1000 °C in humidified hydrogen for x = 0.2 [69]. On the other hand, no carbon deposition was detected on $Ce_{0.6}Gd_{0.4}O_{2-\delta}$ electrode after testing the cell for 1,000 hrs at 1000°C. The steam to carbon ratio was 0.3. The electrocatalytic activity of gadolinium-doped ceria without extra additives was found to be insufficient to provide direct CH_4 oxidation [70].

Ohmic losses and current restriction is another phenomena of ceria solid solutions which can be solved by the introduction of additional metal components. Comparative tests carried out reported that electrode layers containing nickel and various mixed conducting components such as $Ni(Ca;Gd)(Co;Mg)O_{3-\delta}$ perovskites or $Gd_2Ti_2O_{7-\delta}$ pyrochlore exhibit a lower performance than those with ceria. For instance the overpotential of 95 wt % Ni – 5 wt % $Ce_{0.8}Ln_{0.2}O_{2-\delta}$ (Ln = Sm, Gd) anodes in contact with $La_{0.8}Sr_{0.2}Gd_{0.2}M_{0.8}$ (LSGM) were marginallylower for Ln = Sm. Through the test, conclusions were drawn on the role of ceria-based additives [71]. Ceria based components have increasing impacts with decreasing temperature which are crucial under the LT SOFC operating conditions [72]. Further improvement on ceria based components has been targeted at infiltrating nano-crystalline ceria onto the anode cermet surface. This combination can enhance the exchange rates between the solid electrolyte and electrode enlargement at the triple phase boundary (TPB), the surface area of the electrodes, provide a better contact between particle components and increase its tolerance towards sulphur poisoning [73, 74].

1.2.3.3 Alternative anode compositions

Recently, studies have been done on Cu-cerium oxide anode and discovered to be a possible alternative to nickel in LT SOFCs for the oxidation of hydrocarbons. It was discovered that copper is a superb current conductor but a weak catalyst for hydrocarbon reactions.Hence cerium oxide is added as a matrix to improve its hydrocarbon oxidation process. It has been reported that Cu-cerium oxide anodes are compatible with cerium oxide electrolytes in fuel cells andinitial results using a wide range of hydrocarbon fuels were promising [75]. For example He*et al.* [75] reported that Cu-$Ce_{0.8}Sm_{0.2}O_{2-\alpha}$ exhibited a maximum power density of 285 and 408 mW/cm^2 at 550 and 600 °C respectively. Zha *et al.* [76] examined CuO-GDC anode and reported power densities of 275 mW/cm^2, 200 mW/cm^2 and 175 mW/cm^2 at 600 °C in H_2, CH_4 and C_3H_8 fuel atmosphere. Ma *et al.* [77] reported a power density of 285 mW/cm^2 and 408 mW/cm^2 at 550 °C and 600 °C for CuO-SDC anode.

Researches have also shown that the addition of iridium to anode cermets enables internal reformation of hydrocarbons, and thus allows SOFCs to run on more conventional fuels [78 - 79]. For instance, Ir/CGO was used in reforming of ethanol, for CGO sample. Ethanol conversion remained constant at around 100 % during 25 hrs time of streaming (TOS). The main products formed were H_2, CO, CH_4, and CO_2. The addition of Ir to CGO enhances ethanol dehydrogenation rate, as observed for noble metal catalysts which promotes steam reformation of methane [80]. Other alternative anode cermets are shown in Table 2.

Perovskite related structures have also been used as alternative anode materials primarily because of its extensive cation substitution and good transport properties compared tospinel, fluorites, pyrochlores, C-type oxides, or garnets. The materials were compared during fabrication and SOFC operation, using the following conditions. Inspecting the O_2 partial pressure stability limits, by checking its electronic conduction and stability in oxidizing atmospheres which showed that the thermodynamic stability of magnetite, cobaltite, and ferrite based compounds were limited under anodic conditions. A variety of other compounds, such as rare earth vanadates and molybdates, displayed attractive

properties in reducing environments, but undergo phase changes leading to the formation of materials with low conductivity [81, 82].

Compounds of ternary oxides utilized as parent compositions in developing anodes are limited, especially those of Cr and Ti containing compounds. One good parent material, $LaCrO_3$ has been studied as alternative anodes in the reformation of hydrocarbon fuels and deposition of carbon as shown in Table 1 [83, 84]. For many other perovskites, the dominant p-type (positively charged) doping, electronic conductivity and electrocatalytic activity of lanthanum chromite has been enhanced by the substitution of La^{3+} with alkaline-earth cations. For example, (La, A) $CrO_{3-\delta}$ (A = Ca, Sr) anodes were reported to oxidize methane without coking at temperatures above 490 °C, showing promise as candidates for hydrocarbon fuelled SOFCs [85, 86].

Table 1: Alternative SOFC anode materials and their components.

Composition	Temperature T (K)	Conductivity α x 10^6 (K^{-1})	Reference
Ni	-	16.5	[87]
$Zr_{0.85}Y_{0.15}O_2$	303 – 1273	10.9	[87]
Ni-$Zr_{0.85}Y_{0.15}O_2$ (40 – 60 vol. %)	303 – 1273	12.6	[87]
$Zr_{0.94}Y_{0.06}O_2$	298 – 1273	10.5	[87]
Ni-$Zr_{0.94}Y_{0.06}O_2$ (30- 70 vol. %)	298 – 1273	12.7	[87]
Ni- $Zr_{0.94}Y_{0.06}O_2$ (40 – 60 vol.%)	298 – 1273	13.1	[87]
Ni-$Zr_{0.94}Y_{0.06}O_2$ (45-55 vol.%)	298 – 1273	13.3	[87]
$La_{0.9}Sr_{0.1}CrO_3$	303 – 1273	10.7	[88]
$La_{0.79}Sr_{0.20}CrO_3$	623 – 1273	11.1	[88]
$La_{0.7}Ca_{0.3}Cr_{0.5}Ti_{0.5}O_3$	303 – 1273	10.1	[88]
$[La_{0.75}Sr_{0.25}]_{0.95}Cr_{0.5}Mn_{0.5}O_3$	373 – 923	10.8	[89]
Nb-$SrTiO_3$	623 – 923	-	[90]

1.3 Electrolytes

Electrolytes are ceramics with a dense layer that promotes the conduction of oxygen ions. In high temperature SOFCs the transportation of oxygen ion is maintained sufficiently for a good performance [91]. When the operating temperature is lowered to about 600 °C, the

electrolyte begins to exhibit high resistances in its ionic transport and this affects the total performance [92, 93]. Standard electrolyte materials that have been used are yttria stabilized zirconia (YSZ) (often the 8 % form Y8SZ), scandia stabilized zirconia (ScSZ) (usually 9 mol % Sc_2O_3 – 9ScSZ) and doped ceria mixed with gadolinium or samarium (GDC/SDC) [88 - 90]. The electrolyte material has a vital effect on the cell performance. It has been discovered that unfavourable reactions occur between YSZ electrolytes and modern cathodes such as LSCF, which can be prevented by using ceria diffusion barriers that are <100 nm [94, 95].

Present endeavours are now geared towards maintaining a high level of oxygen ion conductivity in SOFCs at lower temperatures less than 500 °C which would broaden the material choices for SOFCs and solve many existing problems [96]. These problems can be solved by certain processing techniques which are thin film deposition, reduction in the electrolyte resistance and the migration distance of oxygen ions which produce grain structures that are less resistive, such as columnar grain structure. This micro-structure can be controlled by using nanocrystalline fine grains to achieve "fine-tuning" of the electrical properties and to build composites with large interfacial areas which have been reported to exhibit remarkable electrical properties.

1.3.1 Structure of Electrolytes

Electrolytes must be dense to avoid short circuiting of the reacting gases migrating through it. The thickness of the electrolyte should be ≤150 μm depending on the configuration of the cell, it can also be slim as possible to reduce resistive losses in the cell. Other materials used have to be thermally, chemically and structurally stable over a wide range of temperatures. The oxygen ions formed from the conversion of molecular oxygen migrates through the electrolyte to the anode side of the cell. This migration is encouraged by high ionic conductivity and no electrical conductivity possessed by the electrolyte. Electrolytes can also be mixed with two or more materials/phases called composite electrolytes or heterogeneous doped materials or dispersed electrolytes [97 – 99]. They are characterised by high conductivity and improved mechanical strength which occurs through interfaces

but at significantly lower temperatures [97 – 101]. The electrolyte properties can be controlled by varying the conductance type, which are very flexible.

1.3.2 Materials used as electrolyte

1.3.2.1 Ceria based electrolyte

Ceria based electrolyte exhibits high ionic conductivity at temperatures lower than 700 °C. The reduction in temperature has provided many options for combination and availability of materials used as electrolytes. The disadvantage is that electrolytes are susceptible to reduction at the anode (fuel) side, when operating at lower temperatures. The ionic conductivity is also hindered by the resistance within the grain boundaries. Several studies to develop compositions that solve these problems of resistance have been conducted [102 – 104].

1.3.2.2 Ceria based nanocomposite

Generally, the ionic conduction in single-phase electrolyte materials follows the oxygen vacancy mechanism. However, the limited oxygen vacancies (limited charge carriers) and the long transport ion distance (high activation energy) restrict the final ionic conductivity. Although the oxygen vacancy concentration can be enhanced with the increase of the doping content, there is an optimal value, above which the oxygen sublattice ordering caused by the defect association or interaction may reduce and subsequently affect the electrical conductivity.

In recent years, a series of functional two-phase ceria salts nanocomposite materials have been exploited to overcome the low ionic conductivity of the single-phase electrolyte materials [104, 105]. Two kinds of nanocomposites will be described in detail, one is the ceria carbonate nanocomposite electrolyte, and the other is ceria oxide nanocomposites. Ceria carbonate has been exploited for its properties and electrochemical performance, while the ceria-oxide composites need to be further developed for advanced applications.

1.3.2.3 Ceria oxide nanocomposites

The ceria oxides in composite electrolytes are SDC, GDC or YDC. The ionic conductivities of these composite electrolytes are much higher than those of the single-phase doped ceria or zirconia oxides. Taking the doped ceria - Na_2CO_3 as an example, its ionic conductivity can reach 0.1 S cm^{-1} around 300 °C, which is two orders of magnitude higher than that of single phase SDC material. The super ionic phase transition is highly dependent on the composition and the operational conditions, such as the temperature raising rate and the applied gas atmosphere. While Zajac *et al.* [105] reported Y_2O_3-SDC material displayed enhanced conductivity than SDC alone at all temperatures.

1.3.2.4 Ceria carbonate nanocomposite

Ceria-based nanocomposites have been developed as promising electrolyte candidates for LTSOFCs due to their enhanced ionic conductivity and fuel cell performance [106]. Among these composite electrolytes, doped ceria-carbonate shows the most promising potential compared with other doped ceria salt composites, and this has led to worldwide interest with great progress on both the ceria carbonate composite themselves, high performance fuel cells and electrode development [107, 108]. The composite designed and fabricated, uses the interface as an express path for ionic conduction. Recently, some new composite electrolytes with unique nanostructures, for example, core-shell SDC/Na_2CO_3 nanocomposite [109] and SDC nanowires have been designed by novel nanocomposite approach and are dominant factors for ion transport in these materials. Furthermore, it has been reported that the SDC-carbonate composites possess hybrid O^{2-}/H conduction property [110, 111].

The proton and oxygen ion conduction behaviours of SDC/Na_2CO_3 nanocomposite electrolyte conduction mechanism have been studied [109]. The result revealed that the proton conduction accounts for the notable ionic conductivity and fuel cell performance of SDC/Na_2CO_3 nanocomposite. This indicates that interface in the composite electrolyte, supplies high conductive paths for proton transport. An empirical “swing model” has been proposed for the mechanism of superior protonic conduction, as the secondary phase in

composite electrolyte, Na_2CO_3 performs several crucial functions in SDC/Na_2CO_3 nanocomposite. That enhance the ionic conductivity, thermal stability of the nanostructure, improves the densification of the solid electrolyte to prevent any gas leakage and supresses the electronic conductivity of the parent electrolyte material to improve the performance of single cells [112].

The above characteristics of the second phase require a homogeneous distribution of Na_2CO_3 inclusion in the composite. However, by the current use of dry mixing and wet mixing methods for composite fabrication, it is difficult to control the homogeneity of Na_2CO_3 phase in the SDC/Na_2CO_3 composite, since nucleation and crystal growth of Na_2CO_3 phase cannot be prevented. These drawbacks may be prevented by using techniques that has been advocated for chemical processes capable of producing pure, chemically homogeneous and ultrafine powders.

The electrolyte functions of ceria-carbonate nanocomposites have been demonstrated by many groups for low temperature SOFCs with excellent fuel cell performance. For example, fuel cells using Ni based electrodes and SDC $(Li/Na)_2CO_3$ composite electrolyte reached a power density of 1085 mW/cm^2 and an open circuit voltage (OCV) higher than 1.0 V using hydrogen as the fuel and air as the oxidant [113]. Higher performance of 1200 mW/cm^2 was also achieved when the air was replaced with the O_2/CO_2 mixed gas at 600 °C [114, 115]. More importantly, a recent work by Huang *et al.* [116] reported a high performance can be obtained with the nanocomposite homogeneous SDC/Na_2CO_3 prepared by a simple one-step co-precipitation method at low temperatures. The improved performance and the reduced material and system preparation process makes ceria carbonate nanocomposite more valuable for practical applications.

1.4 Cathodes

A Cathode is an electrode where reduction of oxygen occurs electrochemically and can be shown by an elementary reaction to SOFC cathode must possess the following: high catalytic activity for oxygen molecule dissociation and oxygen reduction, high electronic

conductivity, chemical and dimensional stability in environments encountered during cell fabrication and cell operation as shown in Equation 7. Thermal expansion compatibility with other cell components, and minimum reactivity with the electrolyte and inter connection are also considered. It must also be stable with porous microstructure so that gaseous oxygen can readily diffuse through it to the cathode/electrolyte interface [117, 118].

1.4.1 Structures of the Cathode

In cathodic environment oxygen diffuses from air toward the solid electrolyte near the triple phase boundary through the pores in the electrode structure which are not rate limiting in modern electrodes. During the diffusion process, impedance can occur but to reduce this impedance during gas diffusion, the outer layers must be made of coarse grains and large pores and close to the solid electrolyte finer grains and smaller pores. The reduction process in cathodes is characterized by the absorbance of oxygen molecules on the solid electrolyte, which are separated into two adsorbed atoms. These atoms diffuse on the solid electrolyte toward the metal and toward the triple phase boundary, where they combine with two electrons while entering the solid electrolyte [119 - 122]. The overall reaction can be described by Equation 7 [119];

The overall reaction is written in the kroger - vink notation. Kröger–Vink notation is a set of conventions that are used to describe electric charge and lattice position for point defect species in crystals. It is primarily used for ionic crystals and is particularly useful for describing various defect reactionssuch as:

$$\frac{1}{2}O_2 + 2e^- + V_O^{OO} \rightarrow O_O^X \quad (7)$$

where, V_o^{oo} and O_o^xrepresent an oxide ion vacancy and an oxide ion respectively. The rate of diffusion in the gas phase or along the grain boundaries depends on the morphology that might be different for different experiments and the charge transfer reaction rate which is dependent on the composition of the electrode. For LTSOFCs alternative cathode materials with high oxide ion diffusion rates and faster oxygen reduction kinetics at the cathode/electrolyte interface have been developed [121].

However, the thermal expansion coefficients for different cathode materials vary. For example TEC for cobaltites are much higher than that of electrolytes. This affects the electrical conductivities of the materials by lowering them. Nevertheless, promising results have been reported using these materials, though in many cases the improved cathodic performance is found to decrease during the cell lifetime as a result of chemical or microstructural instability [122]. The cathode materials used in LT SOFCs are discussed in the next section [119].

1.4.2 Materials used as cathode

1.4.2.1 Ferrites

These iron-containing oxide phases are stable under the SOFC cathodic conditions and display substantial electronic or mixed conductivity. These primarily include perovskites like $LnAFeO_{3-\alpha}$ and their derivatives existing as LnAFeO systems, $A_2Fe_2O_{5\pm\delta}$ brown millerites, $(Ln, A)_3Fe_5O_{12\pm\delta}$ garnets in the systems with relatively small Ln^{3+}cations [123, 124], Popper series like $(Ln, A)_{n+1}Fe_nO_3$, and a variety of other intergrowth compounds such as $Sr_4Fe_6O_{13\pm\delta}$ [125]. Cerium oxide pseudobinaries like $CoFe_2O_4$ comprising of (Ln, A)FeO_3 and (Ln, A)(Fe, M)O_3, is that derivatives which are characterized with large solid solution domains which facilitate cation interdiffusion. When compared to manganite electrode materials, one disadvantage of ferrites are they possess high chemical expansion. Chemical expansion is the spatial dilation of materials that occurs when their composition changes. When this dilation is caused by a gradual, iso-structural increase in the lattice parameter with composition, it is related to the composition change by stoichiometric expansion coefficient [126]. This results in increasing apparent thermal expansion coefficient (TECs) due to losses at elevated temperatures. This may lead to thermal and mechanical incompatibility with common solid electrolytes which can be reduced by using dopants like Ga, Al, Ti, Cr and Ni in La(Fe, Ni)O_3 based perovskites and $(La_{0.6}, A_{0.4})_{1-x}Fe_{0.8}M_{0.2}O_3$ where (A = Sr, Ca, M = Cr, Mn, Co, Ni) [126, 127, 103].

One attractive example of ferrites that has been widely used is $La_{1-x}Sr_xFe_{1-y}Co_yO_3$ (LSFC) where (x = 0.2 – 0.5 and y = 0.2) system [128, 129], where moderate dopant additions

provide a significant enhancement in the total conductivity and electrochemical properties of LSFCs. These are considered as good cathode materials for LT SOFCs with ceria based electrolytes. The cathodic overpotential of porous $La_{0.6}Sr_{0.4}Fe_{0.8}Co_{0.2}O_3$ layers in contact with $Ce_{0.8}Sm_{0.2}O_2$ is 10 – 40 times lower than those of $La_{0.82}Sr_{0.18}Fe_{0.8}MnO_3$/YSZ at 700 – 900 °C [128]. The difference increases with reducing temperature, while the polarization resistance of $La_{0.6}Sr_{0.4}Fe_{0.8}Co_{0.2}O_3$ double layer cathode comprising of a thick layer and a thin dense film, applied onto 10 and 20 mol % CGO was reported to exhibit values of 0.5 Ω cm^2 at 500 °C [130]. Other examples of ferrite cathodes reported with low area specific resistance (ASR) values at 600 °C is $La_{0.6}Sr_{0.4}Co_{0.8}Fe_{0.2}O_{3-\delta}$ reported ASR of 0.048 Ω cm^2, $La_{0.6}Sr_{0.4}Co_{0.2}$ $Fe_{0.8}O_{3-\delta}$ exhibited an ASR of 0.25 Ω cm^2, $Ba_{0.25}La_{0.25}Sr_{0.5}Co_{0.2}Fe_{0.8}O_{3-\delta}$ exhibited an ASR of 0.038 Ω cm^2, $La_{0.6}Sr_{0.4}Co_{0.2}Fe_{0.8}O_{3-\delta}$ + $Ce_{0.8}Gd_{0.2}O_{1.9}$ showed an ASR of 0.16 Ω cm^2 and $Ba_{0.25}La_{0.25}$ $Sr_{0.5}Co_{0.2}Fe_{0.8}O_{3-\delta}$ + $Ce_{0.8}Gd_{0.2}O_{1.9}$ exhibited an ASR of 0.076 Ω cm^2 [131, 132, 133].

1.4.2.2 Cobaltites

Cobaltite based perovskites, offer considerably better cathodic and transport properties, compared to higher thermal and chemical expansion which limits their compatibility with solid oxide electrolytes. These cobaltites include derivatives of $_{\delta}$-Bi_2O_3, $Bi_2VO_{5-\delta}$, and $La_2Mo_2O_{9-\delta}$ [134 – 137]. They also exhibit substantially lower TECs, relatively high mixed conductivity and fast exchange kinetics which has attracted significant interests in layered cobaltites such as perovskites like (Ln, Sr)$CoO_{3-\delta}$ and their solid solutions. The oxidation state of Co cations is often more stable when compared with disordered perovskite analogues such as ($LnBaCo_2O_5$) (Ln = Pr, Gd – Ho, Y), ($LnBaCo_4O_7$) (Ln = Dy – Yb, Y), and also Ruddlesden–Popper type (Ln, A)$_4Co_3O_{10}$ and (Ln,A)$_2CoO_{4-\delta}$ (Ln = La – Nd) existing at moderately reduced oxygen pressures [136 – 139].

Perovskite like (Ln; A)$CoO_{3-\delta}$ exhibit greater hole delocalization and ion mobility at low temperatures. Introduction of Ln-site vacancies in the composition leads to decrease in ionic and electronic transport [140]. These defects from the cation deficiency are governed by particular charge compensation mechanisms dependent on the Ln/A ratio, temperature,

and oxygen pressure. Cobaltite perovskite have a lower thermodynamic stability and are less tolerant to cation non-stoichiometry when compared to manganite and ferrites [141, 142]. For example $La_{2-x}Sr_xCoO_{4\pm\delta}$ (x = 0.7 – 1.0) composition, exhibited a total conductivity of 150 S cm^{-1} above 600 °C in air, which are comparable to that of K_2NiF_4 type nickelates which was 80 – 100 S cm^{-1} and the highest level of oxygen ionic transport was exhibited by $La_{1-x}Sr_xCoO_{3-\delta}$ composition when x = 0.65 – 0.70 [99,141,142]. Bi_2O_3containing materials for perovskite-type phases derived from A(Co, Fe)$O_{3-\delta}$ (A = Sr, Ba) also exhibit high electrical conductivity. They are associated with limitations experimentally and during partial conductivity measurements which arise from local vacancy ordering in the oxygen sublattice, cation demixing under non-equilibrium conditions and phase separation in low temperatures. These cobaltite compositions are affected by the cobaltite thermodynamic properties, the tolerance factors, the A-site cation radii and the materials microstructure [142], while Ba^{2+} doping has a positive impact on the oxygen reduction kinetics as established by numerous researchers [143 - 150].

Solid electrolyte additions comparable to the percolation threshold are hardly expected to decrease the average TECs down to any acceptable level [151, 152]. In cobaltites there are no direct correlations between the bulk transport properties and electrocatalytic behaviours of cobalt-containing electrodes, which are often visible when compared to other different groups of the electrode materials [153]. For instance, the maximum power density of LSGM based SOFCs with (La, Sr)$MO_{3-\delta}$ cathodes at 1000 °C increased in the sequence M = Cr<Mn<Fe<Co [154, 155] and similar trends are known for the electronic conductivity, oxygen ion diffusivity, and anion deficiency. On the contrary, the lowest polarization resistance in (Ln,Sr)CoO_3 based series was repeatedly found for the compositions where Ln^{3+}cation radius is smaller than that of La^{3+}, including Sm, Nd, or Pr [143, 144, 153, 155]. For $Y_{0:8}Ca_{0:2}Co_{1-x}Fe_xO_{3-\delta}$ perovskite that are stable in air at x = 0.1 – 0.7, the electrochemical activity is low comparable to manganite electrodes a poor performance was also reported for $Y_{0.9}Co_{0.5}Mn_{0.5}O_{3-\delta}$ [156]. The observed tendencies show that, in addition to the species occupying cobalt and oxygen sublattices, the cathodic kinetics are

significantly influenced by specific electrocatalytic properties of lanthanide cations or surface clusters comprising Ln^{3+}.

These conclusions are in agreement with numerous experimental and theoretical results demonstrating that the performance of cobaltite and ferrite electrodes are essentially governed by the exchange processes at the electrode and electrolyte surfaces and by ion transfer across the cathode/electrolyte interface [157, 158]. The role of bulk ionic transport in the electrode material crystal lattice seems important, but less critical with respect to these steps. Due to the very high electronic conductivity, the hole transport may not be rate limiting and exhibit no correlations with the electrochemical behaviour which makes it suitable for LTSOFCs. More examples of cobaltites with their power densities are shown in Table 2.

Table 2: Examples of the maximum power density in H_2 fuelled SOFC with cobaltite cathodes.

Cathodes	Electrolyte Thickness(μm)	Anode	Temperature (°C)	Max.Power Density(W/cm^2)	Reference
$\mathbf{La_{0.9}Sr_{0.1}CoO_3}$	YSZ/0.5	Ni	1000	0.39	[155]
$\mathbf{La_{0.9}Sr_{0.1}CoO_3}$	LSGM/0.5	Ni	1000	0.93	[155]
			800	0.38	[154]
$\mathbf{La_{0.6}Sr_{0.4}CoO_3}$	LSGM/0.5	Ni	1000	0.71	[155]
			800	0.21	
$\mathbf{La_{0.6}Sr_{0.4}CoO_3}$	LSGM/0.5	Co	1000	0.53	[155]
$\mathbf{La_{0.2}Sr_{0.8}CoO_3}$	LSGM/0.5	Ni	800	0.44	[159]
$\mathbf{La_{0.2}Ca_{0.8}CoO_3}$	LSGM/0.5	Ni	800	0.46	[159]
$\mathbf{La_{0.4}Ba_{0.6}CoO_3}$	LSGMC/0.4	Ni	600	0.12	[159]
$\mathbf{La_{0.2}Ba_{0.8}CoO_3}$	LSGM/0.5	Ni	800	0.52	[159]
$\mathbf{Sm_{0.6}Sr_{0.4}CoO_3}$	LSGM/0.5	Ni	800	0.44	[155]
$\mathbf{Sm_{0.5}Sr_{0.5}CoO_3}$	LSGM/0.5	Ni	800	0.53	[142]
			600	0.08	[154]
$\mathbf{Sm_{0.5}Sr_{0.5}CoO_3}$	CGO/0.03	Ni/CGO	600	0.27	[142]

1.4.2.3 Iridates

Iridates are reputed for high metallic conductivity and electrocatalytic activities [160, 161]. Iridium containing perovskites possess good chemical and physical properties such as high resistance to corrosion, solubility in mineral acids like aqua regia and resistance to other

molten metals and silicates at high temperatures. It also has a very high melting point, high modulus of elasticity, modulus of rigidity, good stability in air and a very low figure for Poisson's ratio (the relationship of longitudinal to lateral strain) which signifies a high degree of stiffness and resistance [162 - 166].

Iridates combine with perovskite ABO_3 and ABO_2 (where A = Ln (lanthanides) and B = Cu, Ni, Co, Fe, Mn, platinum metals (Pt, Ir). For example derivatives like $IrMnO_3$ are stable below 900 – 1100 °C operating temperatures. Lu *et al.* [167] reported that $Ir_{0.5}Mn_{0.5}O_2$ cathode material exhibited power densities of 43.2 and 80.7 mW/cm^2 at 600 °C and 700 °C respectively. IrO/YSZ has also been reported as suitable cathodes for SOFC applications within 300 – 600 °C [168]. IrO_2/YSZ composites are reported of single-phase particles, between 4 and 10 nm in size, with an excellent polarization resistance (Rp) of 21 – 968 Ω cm^2 at low temperatures within 300 – 500 °C. IrO_2/YSZ electrodes experience structural and morphological changes at high temperatures triggered by cathodic polarization above 500 °C. This behaviour could enhance the electrochemical performance of the electrode [169].

The extensive substitution of the Ir sublattice in Ln(Ce, Sm, Sr) (Ir, M)O_3 (M = Ti, Co, Ga, Fe, Ni) containing 5 – 10 % iridium forms the perovskite type $Ln_{1-x}A_xIr_{1-y}Fe_yO_{3-\delta}$ (x = 0.1 - 0.01). When iridates are doped with ceria there is a formation of ceria interlayer that helps to decrease cathodic polarization and makes it suitable for LTSOFCs. For example $Ce_{0.8}Sm_{0.2}Fe_{0.9}Ir_{0.03}Co_{0.07}O_{3-\delta}$ and $Ce_{0.8}Sr_{0.2}Fe_{0.9}Ir_{0.04}Co_{0.06}O_{3-\delta}$ exhibited ASR values of 0.247 Ω cm^2 and 0.349 Ω cm^2 at 500 °C [63, 64], $Ln_{2-x}A_xM_yIr_{1-y}O_4$ series (x = 0.1 – 1.4) where A = Sr, $x \leq 1.0$, A = Ba, $x \leq 0.5$, A = Sm, $y \leq 0.1$, M = Fe, x = 0.2 and Co at $y \geq 0.1$, where y = 0.1 – 1.0 for M = Cu at x = 0.1 [170 - 173]. Properties of iridates can also be improved by surface modification with metal oxides which improve surface oxygen exchange, for example in La_2IrO_4 where lanthanides determine its ionic conductivity. Substitution of iridium with higher valence cation in the sublattice increases interstitial concentration and ionic transport at low temperatures [173].

1.4.3 Composite cathodes used for LT SOFC

1.4.3.1 NANOCOFC approach

NANOCOFC are multifunctional nanocomposites for advanced fuel cell technology. Electrodes based on metal oxides (Ni- Cu-Zn- oxide) and samarium doped ceria (SDC) have been used as cathodes. Composites formed high homogeneous distribution of the particle material which enhances the catalytic properties, electronic conductivity and reduces the cathodic overpotential when applied in LTSOFC. For example LiNiCuZn-Oxides – NSDC reached a power output of 730 mW/cm^2 at 550 °C [174, 175].

Pr_2NiO_4-Ag composite based on ceria-carbonate composite electrolyte are nitrate compounds with doped silver metal. This composition displays acceptable electrocatalytic activity towards O_2 reduction reaction at a temperature of 500 – 600 °C [170, 176]. Lithiated NiO ($LiNiO_x$) has an electrocatalytic activity toward oxygen reduction reaction and $PrNiO_4$ possess high oxygen diffusion, surface exchange coefficient, and the largest amount of interstitial oxygen. The integration of these specific features to form LiNiOx – $PrNiO_4$ nanomaterial and the effective dissolution of Ni in the perovskite lattice gives rise to a high and stable performance. It has an improved maximum power density of 695 mW/cm^2 achieved at 600 °C [177]. Composite material of LiNiCuZn – Oxides, Gd_2O_3 and Sm doped CeO_2 composited with Na_2CO_3 (LiNiCuZn oxides-NGSDC), exhibit an OCV of 1.05 V and maximum power density of 800 mW/cm^2 [178, 179, 106]. LiNiOCuFeCo on ceria carbonate electrolyte gives maximum power density of 380 W/cm^2 at 560 °C [180]. The research to find suitable cathode materials for LTSOFCs still continues by the combination of the different materials and compounds of the groups of nickel, cobalt, copper and iron.

1.5 Mathematical models for Polarization

1.5.1 Polarizations

Polarization or overpotential, are irreversible losses in voltage due to imperfections in materials microstructure and design of the fuel cell. Polarization losses results from ohmic resistance of oxygen ions conducting through the electrolyte, electrochemical activation barriers at the anode and cathode. Finally concentration polarizations are due to inability of gases to diffuse at high rates through the porous anode and cathode (shown as ηA for the anode and ηC for cathode). The overall polarisation losses can be calculated using Equation [181].

$$V = E_o - IR_w - \eta_{cathode} - \eta_{anode} \quad (8)$$

where, E_o is the Nernst potential of the reactants, R_w is the Thevenin equivalent resistance value of the electrically conducting portions of the cell, $\eta_{cathode}$ and η_{anode} are the remaining difference between the actual cell voltage and the Nernst potential.

In SOFCs, it is often important to focus on the ohmic and concentration polarizations since high operating temperatures experience little activation polarization. However, as the lower limit of SOFC operating temperature approaches 600 °C, these polarizations do become important [182]. SOFC cell voltage can be calculated using the Equation itself. The results agree with particular experimental data where adequate factors are obtained and do not agree with original experimental working parameters [183]:

$$E_{sofc} = \frac{E_{max} + I_{max} \times \eta_f \times r_1}{\frac{r_1}{r_2}[1-\eta_f]+1} \quad (9)$$

where, E_{sofc} is the Cell voltage, E_{max} is the maximum voltage given by the Nernst equation I_{max} is the maximum current density (for given fuel flow), η_f is Fuel utilization factor, r_1 is the ionic specific resistance of the electrolyte and r_2 is the electric specific resistance of the electrolyte.

There are many parameters which impact cell working conditions, e.g. electrolyte material, electrolyte thickness, cell temperature, inlet and outlet gas compositions at anode and cathode, and electrode porosity. The flow in these systems is often calculated using the Navier-Stroke Equation.

1.5.1.1 Ohmic polarization

Ohmic losses in a SOFC results from ionic conductivity through the electrolyte which is a function of the crystal structure and atoms involved. However, to maximize the ionic conductivity, several methods were used when operating SOFCs, at high temperatures that can significantly decrease the ohmic losses. Substitution doping methods can also be used to improve the structure and control defect concentrations, which play a major role in increasing the conductivity. Another way to decrease ohmic resistance is to decrease the thickness of the electrolyte layer. The relationship between ohmic specific resistance of the electrolyte as a function of temperature can be described by this Equation [181]:

$$r_1 = \frac{\delta}{\sigma} \tag{10}$$

where, δ is electrolyte thickness and σ is ionic conductivity. The ionic conductivity of the solid oxide is defined by this Equation [181].

$$\sigma = \sigma_o \times e^{\frac{-E}{R.T}} \tag{11}$$

where, σ_o and E is the factors depended on electrolyte material, T is electrolyte temperature and R is the ideal gas constant.

1.5.1.2 Concentration polarization

The concentration polarization is the result of practical limitations on mass transport within the cell, and represents the voltage loss due to spatial variations in reactant concentration at the chemically active sites. This situation arises when the reactants in electrochemical reactions are consumed faster than the diffusion into the porous electrode, and can also be

caused by variation in bulk flow composition. This results from the consumption of reacting species causing a drop in the reactant concentration as it travels along the cell, which causes a drop in the local potential near the end of the cell.

The concentration polarization occurs in both the anode and cathode. The anode can be particularly problematic, as the oxidation of the hydrogen produces steam, which further dilutes the fuel stream as it travels along the length of the cell. This polarization can be mitigated by reducing the reactant utilization fraction or increasing the electrode porosity, but these approaches each have significant design trade-offs.

1.5.1.3 Activation polarization

Activation polarization results from the kinetics involved with the electrochemical reactions. Each reaction has a certain activation barrier that must be overcome in order to proceed and this barrier leads to the polarization. The activation barrier results from slow but complex electrochemical reaction at the electrode surface which is responsible for the polarization. Activation polarization is calculated using Butler-Volmer equation shown as Equation 12 [181]:

$$\eta_{act} = \frac{RT}{\beta_z F} \times In \frac{i}{i_o} \tag{12}$$

where, R is gas constant, T is operating temperature, β is electron transfer coefficient, z is electron associated with the electrochemical reaction, F is Faraday's constant, i is operating current density and i_o is the exchange current density. Activation polarizations can be modified by microstructural optimization, length of the triple phase boundary, which is the length where porous, ionic, electronic conducting pathways and gas phase meet. This directly relates to the electrochemically active length in the cell, the larger the length, the more the reactions can occur and thus reduces activation polarisation at TPB.

1.5.1.4 Open Circuit Voltage

Open-circuit voltage (abbreviated as OCV or V_{OC}) is the difference of electric potential between two terminals of a device when disconnected from any circuit. There is no external load connected. No external electric current flows between the terminals.

The Nernst open circuit cell voltage V_{OC} can be evaluated at a corrected average operating temperature T_{SOFC}, i.e. the average between the mixed anode and cathode inlet flow (~900 K) and the outlet of the SOFC at 1173 K. The OCV can be calculated using Equation (13).

$$V_{oc} = -\frac{\Delta G^0}{2.F} + \frac{R.T_{SOFC}}{2.F} . In \frac{P_{H_2}^{out} . (P_{O_2}^{out})^{\frac{1}{2}}}{P_{H_2O}^{out}} \quad (13)$$

where $F = 6.023 \times 10^{23} \times 1.602 \times 10^{-19}$ C mol^{-1} is the Faraday constant, 2 is the number of e^- produced per H_2 mole that reacts through reaction of which the molar Gibbs free energy change is expressed as $\Delta G^\circ = \Delta H^\circ - T_{SOFC}\,\Delta S^\circ$, calculated at T_{SOFC} and reference pressure. Finally, $P_{H_2}^{out}, P_{O_2}^{out}, P_{H_2O}^{out}$ are the SOFC exit partial pressures of the participating components in reaction [184]. Using the above partial pressures and temperature data, a FORTRAN calculator can be used to estimate the overpotentials due to ohmic (V_{OHM}), activation (V_{ACT}) and polarization (V_{PO}) losses.

1.6 Synthesis of perovskites

1.6.1 The Sol - gel method

Sol-gel technique is adopted because it is a less complicated synthesis procedure. It is cost effective and the synthesis can be carried out at room temperature. Also in this technique the synthesized perovskite are of high purity, homogenous and the size and morphology of the material can be regulated [185, 186].

The sol-gel technique involves two processes namely, hydrolysis and polycondensation reaction of the metal precursors, usually inorganic metal salts or metal organic compounds.

During hydrolysis, the gel is formed when there is a complete polymerization and loss of solvent from the reaction (sol) [187]. In a typical synthesis of perovskite material, the metal precursors, alcohol, acid/water, and surfactants are mixed together in a reactor and allowed to stir for a particular period of time depending on the material. A densely cross-linked three-dimensional structure forms a perovskite gel after stirring for a period varying from 30 mins to several hours depending on the sample.

Hydrolysis Reaction

$$M(OR)_n + H_2O \rightarrow M(OH)(OR)_{n-1} + ROH \quad (14)$$

$$M(OH)(OR)_{n-1} + H_2O \rightarrow M(OH)_2(OR)_{n-2} + ROH \quad (15)$$

The Reaction for equation 15 continues to form M (OH) $_n$

Polycondensation Reactions

$$-M-OH + HO-M- \rightarrow -M-O-M- + H_2O \quad (16)$$

$$-M-OR + HO-M- \rightarrow -M-O-M- + ROH \quad (17)$$

Where M represents the metal salts and ROH is the OH group. The reaction mechanism for the hydrolysis is illustrated by the flow diagram illustrating steps in the sol-gel technique is shown in Figure 6 [188, 189].

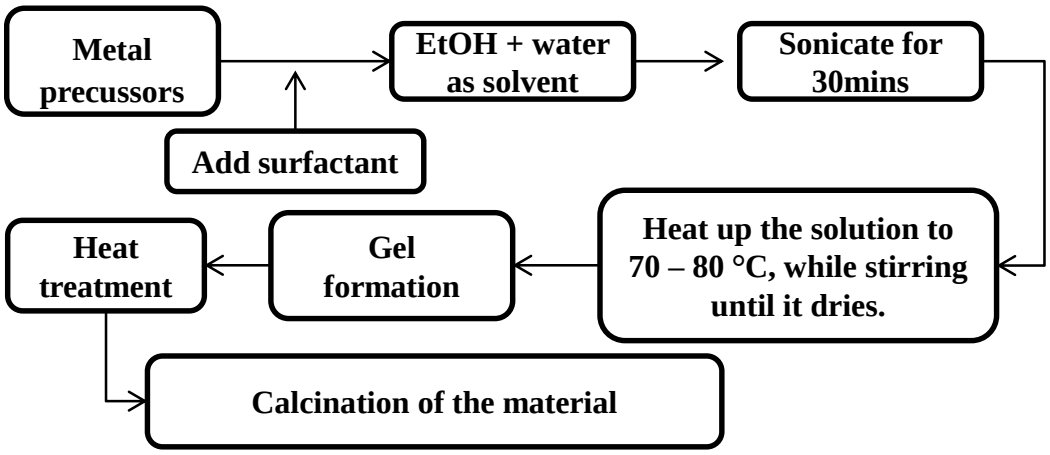

Figure 6: Flow diagram showing the synthesis route for Sol-gel technique.

1.6.2 Utilisation of Surfactants

Surfactants are compounds that lower the surface tension or interfacial tension between two liquids or between a liquid and a solid. In the formation of perovskites, particle size can be modulated by using surfactant while keeping the other processing parameters constant including the solvent. More importantly, emulsions are dynamic systems where droplets constantly coalesce, exchanging their cores which induces particle growth by a coalescence/ aggregation mechanism [190]. Thus, the size of the particles can be controlled by either preventing or promoting coalescence of the droplets during their gelation. The nature of the surfactant influences the particle morphology. There are no simple selection rule that can be applied to predict which surfactant will give a particular particle size, but research has proven that surfactant structure can provide better stabilization of the micelle walls, reduction in the inter-droplet exchange, resulting in the production of smaller particles and smaller crystals [191] and the avoidance of the aggregation of the metallic nanoparticles into matrices [192]. For this reason, it is believed that surfactant-assisted technique may provide materials with appropriate pore diameter, high surface areas and a better access to the active sites [193 - 195]. The surfactant has a fundamental role in determining the nature, number of active sites and the activity of the catalyst [196].

1.6.2.1 Types of surfactant

Surfactants are classified according to polar head groups. Surfactants with no charge group in its head are called non-ionic and surfactants that carry charge on its head are called ionic surfactants. The one with negative charge on its head is called anionic surfactant and if the charge is positive it is called cationic surfactant.

Anionic surfactant: They contain anionic functional groups at their head, such as sulfates and sulfonate, phosphate and carboxylate. Prominent alkyl sulfates include ammonium lauryl sulfate, sodium lauryl sulfate andsodium dodecyl sulfate (SDS).

Cationic surfactant: They are pH dependent primary, secondary or tertiary amines: Primary and secondary amines become positively charged at pH less than 10.For example, alkyltrimethylammonium salts, cetyl trimethylammonium bromide (CTAB), cetyl trimethyl ammonium chloride (CTAC), cetyl pyridinium chloride (CPC), benzalkonium chloride (BAC) and benzethonium chloride (BZT).

Nonionic surfactants: Many long chain alcohols exhibit some surfactant properties. Prominent surfactants among these are the fatty alcohols, cetyl alcohol, stearyl alcohol and cetostearyl alcohol and oleyl alcohol, polyoxyethylene glycol, polyoxypropylene glycol and glucosides.

1.7 Summary

In conclusion, to develop LTSOFCs there are several steps involved.Firstly you need to decrease the area specific resistance of the cells by using electrolyte materials with higher ionic conductivity and secondly to improve the electrode performance. The electrode performance can thus be enhanced by improving the architecture of the material, proper selection of the structural composition of the electrode material, the method of preparation and controlling the morphology of the material and the particle sizes by using surfactants. To further control the morphology and particle sizes, the nano size approach has been used to make nanoparticle sizes called nanomaterials.

The ionic conductivity of the electrolyte can be improved by two ways that follow the nanotechnology approach and composite approach. For nanostructured ionic conductors, grain growths are repressed effectively by integrating another phase into the interparticle region. For nanostructured composite materials, the grain boundary or interface conduction is dominant in overall transport, which contributes to an enhancement in conductivity. Thus the nanocomposite approach was introduced to fabricate the electrolyte and to further enhance the electrode performance, macroporous materials were fabricated.

References

1. Steele, B. C., & Heinzel, A. (2001). Materials for fuel-cell technologies. *Nature*, *414*(6861), 345-352.
2. Yang, L., Wang, S., Blinn, K., Liu, M., Liu, Z., Cheng, Z., & Liu, M. (2009). Enhanced sulfur and coking tolerance of a mixed ion conductor for SOFCs: $BaZr_{0.1}Ce_{0.7}Y_{0.2-x}Yb_xO_{3-\delta}$. Science, 326 (5949), 126-129.
3. Wolf, S., Adam, R., Fuhrmann, L., Ansar, S. A., & Friedrich, K. A. (2013). Characterization of electrolyte layers of plasma-sprayed metal supported solid oxide fuel cells. *Solid State Ionics*, *243*, 30-35.
4. Zuo, P., Fu, Z., & Yang, Z. (2013). First-principles study on the mechanism of coking inhibition by the Ni (111) surface doped with IB-group metals at the anode of solid oxide fuel cells. *Journal of Power Sources*, *242*, 762-767.
5. Hwang, C. S., Tsai, C. H., Yu, J. F., Chang, C. L., Lin, J. M., Shiu, Y. H., & Cheng, S. W. (2011). High performance metal-supported intermediate temperature solid oxide fuel cells fabricated by atmospheric plasma spraying. *Journal of Power Sources*, *196*(4), 1932-1939.
6. Singhal, S. C., & Kendall, K. (Eds.). (2003). High-temperature solid oxide fuel cells: fundamentals, design and applications: fundamentals, design and applications. *Elsevier*.
7. Williams, M. C., Strakey, J., & Sudoval, W. (2006). US DOE fossil energy fuel cells program. *Journal of Power Sources*, *159*(2), 1241-1247.

8. Lee, Y. C., Hung, I. M., Chang, S. L., Ciou, C. J., & Wu, J. S. (2011). The effects of doped Nd on conductivity and phase stability of $BaCe_{0.8}Y_{0.2}O_{3-\delta}$-based electrolyte for solid oxide fuel cell. *Journal of the European Ceramic Society*, *31*(16), 3137-3143.
9. Bhattacharyya, D., & Rengaswamy, R. (2009). A review of solid oxide fuel cell (SOFC) dynamic models. *Industrial & Engineering Chemistry Research*, *48*(13), 6068-6086.
10. Chen, H., Cong, T. N., Yang, W., Tan, C., Li, Y., & Ding, Y. (2009). Progress in electrical energy storage system: A critical review. *Progress in Natural Science*, *19*(3), 291-312.
11. Williams, M. C., Strakey, J. P., & Surdoval, W. A. (2005). The US department of energy, office of fossil energy stationary fuel cell program. *Journal of Power Sources*, *143*(1), 191-196.
12. Steinberger-Wilckens, R. (2011). European SOFC technology-status and trends. *ECS Transactions*, *35*(1), 19-29.
13. Stevenson, J. W., Armstrong, T. R., Carneim, R. D., Pederson, L. R., & Weber, W. J. (1996). Electrochemical Properties of Mixed Conducting Perovskites $La_{1-x}M_xCo_{1-y}Fe_yO_{3-\delta}$ (M= Sr, Ba, Ca). *Journal of the Electrochemical Society*, *143*(9), 2722-2729.
14. Sarasketa-Zabala, E., Otaegi, L., Rodriguez-Martinez, L. M., Alvarez, M. A., Burgos, N., Castro, F., & Villarreal, I. (2012). High temperature stability of porous metal substrates under highly humidified hydrogen conditions for metal supported Solid Oxide Fuel Cells. *Solid State Ionics*, *222*, 16-22.
15. Fan, L., Zhu, B., Chen, M., Wang, C., Raza, R., Qin, H., Wang, X., & Ma, Y. (2012). High performance transition metal oxide composite cathode for low temperature solid oxide fuel cells. *Journal of Power Sources*, *203*, 65-71.
16. Shao, Z., & Haile, S. M. (2004). A high-performance cathode for the next generation of solid-oxide fuel cells. *Nature*, *431*(7005), 170-173.
17. Park, S., Vohs, J. M., & Gorte, R. J. (2000). Direct oxidation of hydrocarbons in a solid-oxide fuel cell. *Nature*, *404*(6775), 265-267.

18. Moon, J. W., Hwang, H. J., Awano, M., & Maeda, K. (2003). Preparation of NiO–YSZ tubular support with radially aligned pore channels. *Materials letters*, *57*(8), 1428-1434.
19. Matsuzaki, Y., & Yasuda, I. (2001). Dependence of SOFC cathode degradation by chromium-containing alloy on compositions of electrodes and electrolytes. *Journal of the Electrochemical Society*, *148*(2), A126-A131.
20. Tucker, M. C. (2010). Progress in metal-supported solid oxide fuel cells: A review. *Journal of Power Sources*, *195*(15), 4570-4582.
21. Kuhn, M., & Napporn, T. W. (2010). Single-chamber solid oxide fuel cell technology from its origins to today's state of the art. *Energies*, 3(1), 57-134.
22. Yano, M., Kawai, T., Okamoto, K., Nagao, M., Sano, M., Tomita, A., & Hibino, T. (2007). Single-chamber SOFCs using dimethyl ether and ethanol. *Journal of the Electrochemical Society*, *154*(8), B865-B870.
23. Morel, B., Roberge, R., Savoie, S., Napporn, T. W., & Meunier, M. (2007). Catalytic activity and performance of LSM cathode materials in single chamber SOFC. *Applied Catalysis A: General*, *323*, 181-187.
24. Zhu, B., Fan, L., & Lund, P. (2013). Breakthrough fuel cell technology using ceria-based multi-functional nanocomposites. Applied Energy, 106, 163-175.
25. Liu, M., Lynch, M. E., Blinn, K., Alamgir, F. M., & Choi, Y. (2011). Rational SOFC material design: new advances and tools. *Materials today*, 14(11), 534-546.
26. Wachsman, E. D., & Lee, K. T. (2011). Lowering the temperature of solid oxide fuel cells. *Science*, 334(6058), 935-939.
27. Yamamoto, O. (2000). Solid oxide fuel cells: fundamental aspects and prospects. *Electrochimica Acta*, *45*(15), 2423-2435.
28. Steele, B. C., & Heinzel, A. (2001). Materials for fuel-cell technologies. *Nature*, *414*(6861), 345-352.
29. Adler, S. B. (2004). Factors governing oxygen reduction in solid oxide fuel cell cathodes. *Chemical reviews*, *104*(10), 4791-4844.
30. Sun, C., Hui, R., & Roller, J. (2009). Cathode materials for solid oxide fuel cells: a review. *J Solid State Electrochem*, *14*(7), 1125-1144.

31. Ding, D., Li, X., Lai, S. Y., Gerdes, K., & Liu, M. (2014). Enhancing SOFC cathode performance by surface modification through infiltration. *Energy & Environmental Science,* 7(2), 552-575.

32. Palsson, J., Selimovic, A., & Sjunnesson, L. (2000). Combined solid oxide fuel cell and gas turbine systems for efficient power and heat generation. *Journal of Power Sources*, *86*(1), 442-448.

33. Khandkar, A., Hartvigsen, J., & Elangovan, S. (2000). A techno-economic model for SOFC power systems. *Solid State Ionics*, *135*(1), 325-330.

34. Tanaka, K., Wen, C., & Yamada, K. (2000). Design and evaluation of combined cycle system with solid oxide fuel cell and gas turbine. *Fuel*, *79*(12), 1493-1507.

35. Riensche, E., Achenbach, E., Froning, D., Haines, M. R., Heidug, W. K., Lokurlu, A., & Von Andrian, S. (2000). Clean combined-cycle SOFC power plant—cell modelling and process analysis. *Journal of Power Sources*, *86*(1), 404-410.

36. Costamagna, P., Magistri, L., & Massardo, A. F. (2001). Design and part-load performance of a hybrid system based on a solid oxide fuel cell reactor and a micro gas turbine. *Journal of Power Sources*, *96*(2), 352-368.

37. Choudhury, A., Chandra, H., & Arora, A. (2013). Application of solid oxide fuel cell technology for power generation—A review. Renewable and Sustainable Energy Reviews, 20, 430-442.

38. Schiller, G., Ansar, A., Lang, M., & Patz, O. (2009). High temperature water electrolysis using metal supported solid oxide electrolyser cells (SOEC). *Journal of Applied Electrochemistry*, *39*(2), 293-301.

39. Janssen, H., Emonts, B., Groehn, H. G., Mai, H., Reichel, R., & Stolten, D. (2001). High-pressure electrolysis–the key technology for efficient H2 production. Hypothesis IV, proceedings, 1, 9-14.

40. Brandon, N. P., Skinner, S., & Steele, B. C. (2003). Recent advances in materials for fuel cells. *Annual Review of Materials Research*, *33*(1), 183-213.

41. Jasinski, P., Suzuki, T., Petrovsky, V., & Anderson, H. U. (2005). Nanocomposite nickel ceria cermet with low nickel content for anode-supported SOFCs. *Electrochemical and Solid-State Letters*, *8*(4), A219-A221.

42. Hao, X., Han, D., Wang, J., Liu, Y., Rooney, D., Sun, W., Qiao, J., Wang, Z., & Sun, K. (2015). Co-tape casting fabrication, field assistant sintering and evaluation of a coke resistant $La_{0.2}Sr_{0.7}TiO_3$–Ni/YSZ functional gradient anode supported solid oxide fuel cell. *International Journal of Hydrogen Energy*, *40*(37), 12790-12797.

43. Soltanzadeh, M. (2010). Modelling Triple Phase Boundary (TPB) in Solid Oxide Fuel Cell (SOFC) Anode.

44. Frandsen, H. L., Ramos, T., Faes, A., Pihlatie, M., & Brodersen, K. (2012). Optimization of the strength of SOFC anode supports. *Journal of the European Ceramic Society*, *32*(5), 1041-1052.

45. Hanna, J., Lee, W. Y., Shi, Y., & Ghoniem, A. F. (2014). Fundamentals of electro and thermochemistry in the anode of solid-oxide fuel cells with hydrocarbon and syngas fuels. *Progress in Energy and Combustion Science*, *40* 74 -111.

46. Fu, Q. X., Mi, S. B., Wessel, E., & Tietz, F. (2008). Influence of sintering conditions on microstructure and electrical conductivity of yttrium-substituted SrTiO 3. *Journal of the European Ceramic Society*, *28*(4), 811-820.

47. Gauckler, L. J., Beckel, D., Buergler, B. E., Jud, E., Muecke, U. P., Prestat, M., Rupp, M., & Richter, J. (2004). Solid oxide fuel cells: systems and materials. *CHIMIA International Journal for Chemistry*, *58*(12), 837-850.

48. Tao, S., & Irvine, J. T. (2004). Discovery and characterization of novel oxide anodes for solid oxide fuel cells. *The Chemical Record*, *4*(2), 83-95.

49. Gorte, R. J., Kim, H., & Vohs, J. M. (2002). Novel SOFC anodes for the direct electrochemical oxidation of hydrocarbon. *Journal of Power Sources*, *106*(1), 10-15.

50. Timurkutluk, B., Timurkutluk, C., Mat, M. D., & Kaplan, Y. (2011). Anode-supported solid oxide fuel cells with ion conductor infiltration. *International Journal of Energy Research*, *35*(12), 1048-1055.

51. Tsipis, E. V., Kharton, V. V., Bashmakov, I. A., Naumovich, E. N., & Frade, J. R. (2004). Cellulose-precursor synthesis of nanocrystalline $Ce_{0.8}Gd_{0.2}O_{2-\delta}$ for SOFC anodes. *Journal of Solid State Electrochemistry*, *8*(9), 674-680.

52. Hari, J., & Pukanzsky, B. (2011). *Nanocomposites: Preparation, structure, properties* (pp. 109-142). M. Kutz (Ed.). Elsevier Inc.: Waltham, MA, USA.

53. Sholklapper, T. Z., Kurokawa, H., Jacobson, C. P., Visco, S. J., & De Jonghe, L. C. (2007). Nanostructured solid oxide fuel cell electrodes. *Nanoletters*, *7*(7), 2136-2141.

54. Ding, D., Zhu, W., Gao, J., & Xia, C. (2008). High performance electrolyte-coated anodes for low-temperature solid oxide fuel cells: Model and Experiments. *Journal of Power Sources*, *179*(1), 177-185.

55. Liu, Z., Liu, B., Ding, D., Liu, M., Chen, F., & Xia, C. (2013). Fabrication and modification of solid oxide fuel cell anodes via wet impregnation/infiltration technique. *Journal of Power Sources*, *237*, 243-259.

56. Brinkman, H. W., Meijerink, J., De Vries, K. J., & Burggraaf, A. J. (1996). Kinetics and morphology of electrochemical vapour deposited thin zirconia/yttria layers on porous substrates. *Journal of the European Ceramic Society*, *16*(6), 587-600.

57. Van der Haar, L. M., & Verweij, H. (2000). Homogeneous porous perovskite supports for thin dense oxygen separation membranes. *Journal of Membrane Science*, *180*(1), 147-155.

58. Bouwmeester, H. J. M., & Burgraaf, A. J. Dense ceramic membranes for oxygen separation, Burggraaf AJ, Cot L., *Fundamentals of Inorganic Membrane Science and Technology*, 1996, 435-528.

59. Steele, B. C. H. (2000). Appraisal of $Ce_{1-y}Gd_yO_{2-y/2}$ electrolytes for IT-SOFC operation at 500 °C. *Solid State Ionics, 129*(1), 95-110.

60. Young, J. L., Molero, H., & Birss, V. I. (2014). The effect of pre-oxidation treatments on the oxidation tolerance of Ni-yttria-stabilized zirconia anodes in solid oxide fuel cells. *Journal of Power Sources, 271*, 538-547.

61. Zhan, Z., & Barnett, S. A. (2006). Operation of ceria-electrolyte solid oxide fuel cells on iso-octane–air fuel mixtures. *Journal of Power Sources*, *157*(1), 422-429.

62. Njoku, C. B., & Ndungu, P. G. (2015). Synthesis and characterization of novel $Ce_{0.8}Sm_{0.2}Fe_{0.9}Ir_{0.03}Co_{0.07}O_{3-\delta}$ perovskite material and possible application as a

cathode for low–intermediate temperature SOFCs. *Materials Research Bulletin*, *68*, 100-108.

63. Njoku, C., Omondi, B. O., & Ndungu, P. (2015). Characterisation and Electrochemical properties of $Ce_{0.8}Sr_{0.2}Fe_{0.9}Ir_{0.04}Co_{0.06}O_{3-\delta}$ (CSFIC) cathode material for Application in Low Temperature SOFC. *ECS Transactions, 68*(1), 903-917.

64. Hibino, T., Hashimoto, A., Yano, M., Suzuki, M., & Sano, M. (2003). Ru-catalyzed anode materials for direct hydrocarbon SOFCs. *Electrochimica Acta*, *48*(17), 2531-2537.

65. Yang, L., Choi, Y., Qin, W., Chen, H., Blinn, K., Liu, M., Liu, P., Bai, J., Tyson, T. A., & Liu, M. (2011). Promotion of water-mediated carbon removal by nanostructured barium oxide/nickel interfaces in solid oxide fuel cells. *Nature Communications*, *2*, 357.

66. Chiba, R., Yoshimura, F., & Sakurai, Y. (2002). Properties of $La_{1-y}Sr_yNi_{1-x}Fe_xO_3$ as a cathode material for a low-temperature operating SOFC. *Solid State Ionics*, *152*, 575-582.

67. Wilson, J. R., Kobsiriphat, W., Mendoza, R., Chen, H. Y., Hiller, J. M., Miller, D. J., Thornton,K., Voorhees, P. W., Adler, B. S., & Barnett, S. A. (2006). Three-dimensional reconstruction of a solid-oxide fuel-cell anode. *Nature Materials*, *5*(7), 541-544.

68. Uchida, H., Suzuki, H., & Watanabe, M. (1998). High-Performance Electrode for Medium-Temperature Solid Oxide Fuel Cells Effects of Composition and Microstructures on Performance of Ceria-Based Anodes. *Journal of the Electrochemical Society, 145*(2), 615-620.

69. Marina, O. A., Bagger, C., Primdahl, S., & Mogensen, M. (1999). A solid oxide fuel cell with a gadolinia-doped ceria anode: preparation and performance. *Solid State Ionics*, *123*(1), 199-208.

70. Tsipis, E. V., Kharton, V. V., Bashmakov, I. A., Naumovich, E. N., & Frade, J. R. (2004). Cellulose-precursor synthesis of nanocrystalline $Ce_{0.8}Gd_{0.2}O_{2-\delta}$ for SOFC anodes. *Journal of Solid State Electrochemistry*, *8*(9), 674-680.

71. Tsipis, E. V., Kharton, V. V., & Frade, J. R. (2005). Mixed conducting components of solid oxide fuel cell anodes. *Journal of the European Ceramic Society*, *25*(12), 2623-2626.

72. Kharton, V. V., Viskup, A. P., Naumovich, E. N., & Tikhonovich, V. N. (1999). Oxygen permeability of $LaFe_{1-x}Ni_xO_{3-\delta}$ solid solutions. *Materials Research Bulletin*, *34*(8), 1311-1317.

73. Kharton, V. V., Viskup, A. P., Figueiredo, F. M., Naumovich, E. N., Shaulo, A. L., & Marques, F. M. B. (2002). Electrochemical properties of Pr-doped $Ce(Gd)O_{2-\delta}$. *Materials Letters*, *53*(3), 160-164.

74. Park, S., Vohs, J. M., & Gorte, R. J. (2000). Direct oxidation of hydrocarbons in a solid-oxide fuel cell. *Nature*, *404*(6775), 265-267.

75. He, S., Li, R., Ge, L., Chen, H., & Guo, L. (2013). Preparation and characterization of Cu–SDC anodes for low-temperature solid oxide fuel cell. *Journal of Alloys and Compounds*, *576*, 242-246.

76. Zha, S., Moore, A., Abernathy, H., & Liu, M. (2004). GDC-based low-temperature SOFCs powered by hydrocarbon fuels. *Journal of the Electrochemical Society*, *151*(8), A1128-A1133.

77. Ma, Y., Wang, X., Li, S., Toprak, M. S., Zhu, B., & Muhammed, M. (2010). Samarium-Doped Ceria Nanowires: Novel Synthesis and Application in Low-Temperature Solid Oxide Fuel Cells. *Advanced Materials*, *22*(14), 1640-1644.

78. Skarmoutsos, D., Tsoga, A., Naoumidis, A., & Nikolopoulos, P. (2000). 5 mol % TiO_2-doped Ni–YSZ anode cermets for solid oxide fuel cells. *Solid State Ionics*, *135*(1), 439-444.

79. Tietz, F. (1999). Thermal expansion of SOFC materials. *Ionics*, *5*(1-2), 129-139.

80. Postole, G., Girona, K., Toyir, J., Kaddouri, A., & Gélin, P. (2012). Catalytic Steam Methane Reforming Over $Ir/Ce_{0.9}Gd_{0.1}O_{2-x}$: Resistance to Coke Formation and Sulfur Poisoning. *Fuel Cells*, *12*(2), 275-287.

81. Kharton, V. V., Naumovich, E. N., Tikhonovich, V. N., Bashmakov, I. A., Boginsky, L. S., & Kovalevsky, A. V. (1999). Testing tubular solid oxide fuel cells in nonsteady-state conditions. *Journal of Power Sources*, *79*(2), 242-249.

82. Gorte, R. J., Park, S., Vohs, J. M., & Wang, C. (2000). Anodes for direct oxidation of dry hydrocarbons in a solid-oxide fuel cell. *Advanced Materials*, *12*(19), 1465-1469.

83. Vernoux, P. (1997). Lanthanum chromite as an anode material for solid oxide fuel cells. *Ionics*, *3*(3-4), 270-276.

84. Tu, H. Y., Takeda, Y., Imanishi, N., & Yamamoto, O. (1999). $Ln_{0.4}Sr_{0.6}Co_{0.8}Fe_{0.2}O_{3-\delta}$ (Ln = La, Pr, Nd, Sm, Gd) for the electrode in solid oxide fuel cells. *Solid State Ionics*, *117*(3), 277-281.

85. Bronin, D. I., Kuzin, B. L., Yaroslavtsev, I. Y., & Bogdanovich, N. M. (2006). Behavior of manganite electrodes in contact with LSGM electrolyte: the nature of low electrochemical activity. *Journal of Solid State Electrochemistry*, *10*(8), 651-658.

86. Hussain, A. M., Høgh, J. V., Jacobsen, T., & Bonanos, N. (2012). Nickel-ceria infiltrated Nb-doped $SrTiO_3$ for low temperature SOFC anodes and analysis on gas diffusion impedance. *International Journal of Hydrogen Energy*, *37*(5), 4309-4318.

87. Wendy, L., (2009). Mechanical properties of $Sc_{0.1}Ce_{0.01}Zr_{0.89}O_2$ electrolyte material for intermediate temperature solid oxide fuel cells. Master's thesis, Texas A&M University.

88. Butz, B., Kruse, P., Störmer, H., Gerthsen, D., Müller, A., Weber, A., & Ivers-Tiffée, E. (2006). Correlation between microstructure and degradation in conductivity for cubic Y_2O_3-doped ZrO_2. *Solid State Ionics*, *177*(37), 3275-3284.

89. Zhang, S. L., Li, C. X., Li, C. J., Yang, G. J., & Han, Z. H. (2013). Scandia-stabilized zirconia electrolyte with improved interlamellar bonding by high-velocity plasma spraying for high performance solid oxide fuel cells. *Journal of Power Sources*, *232*, 123-131.

90. Wang, X., Ma, Y., Li, S., Kashyout, A. H., Zhu, B., & Muhammed, M. (2011). Ceria-based nanocomposite with simultaneous proton and oxygen ion conductivity for low-temperature solid oxide fuel cells. *Journal of Power Sources*, *196*(5), 2754-2758.

91. Fergus, J. W. (2006). Electrolytes for solid oxide fuel cells. *Journal of Power Sources*, *162*(1), 30-40.

92. Wang, S. F., Yeh, C. T., Wang, Y. R., & Wu, Y. C. (2013). Characterization of samarium-doped ceria powders prepared by hydrothermal synthesis for use in solid state oxide fuel cells. *Journal of Materials Research and Technology*, *2*(2), 141-148.

93. Xu, D., Liu, X., Wang, D., Yi, G., Gao, Y., Zhang, D., & Su, W. (2007). Fabrication and characterization of SDC–LSGM composite electrolytes material in IT-SOFCs. *Journal of Alloys and Compounds*, *429*(1), 292-295.

94. Singhal, S. C., & Kendall, K. (Eds.). (2003). High-temperature solid oxide fuel cells: fundamentals, design and applications: fundamentals, design and applications. *Elsevier.*

95. Rambabu, B., Ghosh, S., & Jena, H. (2006). Novel wet-chemical synthesis and characterization of nanocrystalline CeO_2 and $Ce_{0.8}Gd_{0.2}O_{1.9}$ as solid electrolyte for intermediate temperature solid oxide fuel cell (IT-SOFC) applications. *Journal of Materials Science*, *41*(22), 7530-7536.

96. Schober, T., & Ringel, H. (2004). Proton conducting ceramics: recent advances. *Ionics*, *10*(5-6), 391-395.

97. Schober, T. (2005). Composites of ceramic high-temperature proton conductors with inorganic compounds. *Electrochemical and Solid-State Letters*, *8*(4), A199-A200.

98. Uvarov, N. F., Ponomareva, V. G., & Lavrova, G. V. (2010). Composite solid electrolytes. *Russian Journal of Electrochemistry*, *46*(7), 722-733.

99. Murtanto, T. B., Natori, S., Nakamura, J., & Natori, A. (2006). Ac conductivity and dielectric constant of conductor-insulator composites. *Physical Review B*, *74*(11), 115-206.

100. Bhattacharyya, A. J., & Maier, J. (2004). Second Phase Effects on the Conductivity of Non-Aqueous Salt Solutions: “Soggy Sand Electrolytes”. *Advanced Materials*, *16*(9-10), 811-814.

101. Brett, D. J., Atkinson, A., Brandon, N. P., & Skinner, S. J. (2008). Intermediate temperature solid oxide fuel cells. *Chemical Society Reviews*, *37*(8), 1568-1578.

102. Ma, Y., Wang, X., Khalifa, H. A., Zhu, B., & Muhammed, M. (2012). Enhanced ionic conductivity in calcium doped ceria–carbonate electrolyte: a composite effect. *International Journal of Hydrogen Energy*, *37*(24), 19401-19406.

103. Wang, X., Ma, Y., Li, S., Zhu, B., & Muhammed, M. (2012). SDC/Na_2CO_3 nanocomposite: new freeze drying based synthesis and application as electrolyte in low-temperature solid oxide fuel cells. *International Journal of Hydrogen Energy*, *37*(24), 19380-19387.

104. Guo, M., Lu, J., Bi, Q., & Luo, M. (2010). Effect of Optical Absorbance on the Raman Spectra of $Ce_{0.9}Tb_{0.1}O_{2-\delta}$ Solid Solution. *ChemPhysChem*, *11*(8), 1693-1699.

105. Zając, W., Świerczek, K., & Molenda, J. (2007). Thermochemical compatibility between selected (La, Sr)(Co, Fe, Ni)O_3 cathodes and rare earth doped ceria electrolytes. *Journal of Power Sources*, *173*(2), 675-680.

106. Jing, Y., Ma, Y., Patakangas, J., Zhu, B., Johnsson, M., Cura, M. E., & Lund, P. (2014). Enhanced conductivity of SDC based nanocomposite electrolyte by spark plasma sintering. *International Journal of Hydrogen Energy*, *39*(26), 14391-14396.

107. Raza, R., Ma, Y., Wang, X., Liu, X., & Zhu, B. (2010). Study on nanocomposites based on carbonate @ ceria. *Journal of Nanoscience and Nanotechnology*, *10*(2), 1203-1207.

108. Lessing, P. A. (2007). A review of sealing technologies applicable to solid oxide electrolysis cells. *Journal of Materials Science*, *42*(10), 3465-3476.

109. Zhu, B., & Mat, M. D. (2006). Studies on dual phase ceria-based composites in electrochemistry. *International Journal of Electrochemical Sciences*, *1*(8), 383-402.

110. Rajesh, S., Macedo, D. A., & Nascimento, M. (2013). Composite Electrolytes and electrodes for Intermediate Temperature Hybrid Fuel Cells.

111. Wang, X., Ma, Y., Li, S., Zhu, B., & Muhammed, M. (2012). SDC/Na_2CO_3 nanocomposite: new freeze drying based synthesis and application as electrolyte in low-temperature solid oxide fuel cells. *International Journal of Hydrogen Energy*, *37*(24), 19380-19387.

112. Yin, S., Zeng, Y., Li, C., Chen, X., & Ye, Z. (2013). Investigation of $Sm_{0.2}Ce_{0.8}O_{1.9}/Na_2CO_3$ Nanocomposite electrolytes: Preparation, Interfacial Micro structures, and Ionic Conductivities. *ACS Applied Materials & Interfaces*, *5*(24), 12876 - 12886.

113. Yokokawa, H., Sakai, N., Horita, T., Yamaji, K., Brito, M. E., & Kishimoto, H. (2008). Thermodynamic and kinetic considerations on degradations in solid oxide fuel cell cathodes. *Journal of Alloys and Compounds*, *452*(1), 41-47.

114. Huang, J., Yang, L., Gao, R., Mao, Z., & Wang, C. (2006). A high-performance ceramic fuel cell with samarium doped ceria–carbonate composite electrolyte at low temperatures. *Electrochemistry Communications*, *8*(5), 785-789.

115. Zhu, B. (2011). Nanocomposites for advanced fuel cell technology. *Journal of Nanoscience and Nanotechnology*, *11*(10), 8873-8879.

116. Huang, J., Mao, Z., Liu, Z., & Wang, C. (2007). Development of novel low-temperature SOFCs with co-ionic conducting SDC-carbonate composite electrolytes. *Electrochemistry Communications*, *9*(10), 2601-2605.

117. Maguire, E., Gharbage, B., Marques, F. M. B., & Labrincha, J. A. (2000). Cathode materials for intermediate temperature SOFCs. *Solid State Ionics*, *127*(3), 329-335.

118. Gorte, R. J. (2005). Recent developments towards commercialization of solid oxide fuel cells. *AIChE Journal*, *51*(9), 2377-2381.

119. Yamamoto, O. (2000). Solid oxide fuel cells: fundamental aspects and prospects. *Electrochimica Acta*, *45*(15), 2423-2435.

120. Zhao, H., Huo, L., & Gao, S. (2004). Electrochemical properties of LSM–CBO composite cathode. *Journal of Power Sources*, *125*(2), 149-154.

121. Goodenough, J. B., & Cooper, S. L. (2001). Localized to itinerant electronic transition in perovskite oxides (Vol. 98). *Springer Science & Business Media.*

122. Fruth, V., Popa, M., Calderon-Moreno, J., Tenea, E., Anastasescu, M., Osiceanu, P., Anghel, E., Predoana, L., Malic, B., & Zaharescu, M. (2010). Perovskite type nanopowders and thin films obtained by chemical methods. *Processing and Application of Ceramics*, *4*(3), 167-182.

123. Kharton, V. V., Shaula, A. L., Naumovich, E. N., Vyshatko, N. P., Marozau, I. P., Viskup, A. P., & Marques, F. M. B. (2003). Ionic Transport in $Gd_3Fe_5O_{12}$-and $Y_3Fe_5O_{12}$-Based Garnets. *Journal of the Electrochemical Society*, *150*(7), J33-J42.

124. Patrakeev, M. V., Leonidov, I. A., Kozhevnikov, V. L., & Kharton, V. V. (2004). Ion–electron transport in strontium ferrites: relationships with structural features and stability. *Solid State Sciences*, *6*(9), 907-913.

125. Kharton, V. V., Kovalevsky, A. V., Avdeev, M., Tsipis, E. V., Patrakeev, M. V., Yaremchenko, A. A., Naumovich, E. N., & Frade, J. R. (2007). Chemically induced expansion of $La_2NiO_{4+\delta}$-based materials. *Chemistry of Materials*, *19*(8), 2027-2033.

126. Marrocchelli, D., Chatzichristodoulou, C., & Bishop, S. R. (2014). Defining chemical expansion: the choice of units for the stoichiometric expansion coefficient. *Physical Chemistry Chemical Physics*, 16(20), 9229-9232.

127. Tsipis, E. V., & Kharton, V. V. (2008). Electrode materials and reaction mechanisms in solid oxide fuel cells: a brief review. *Journal of Solid State Electrochemistry*, *12*(11), 1367-1391.

128. Kindermann, L., Das, D., Nickel, H., Hilpert, K., Appel, C. C., & Poulson, F. W. (1997). Chemical Compatibility of $(La_{0.6}Ca_{0.4})_xFe_{0.8}M_{0.2}O_3$ with Yttria-Stabilized Zirconia. *Journal of the Electrochemical Society*, *144*(2), 717-720.

129. Philippeau, B., Mauvy, F., Nicollet, C., Fourcade, S., & Grenier, J. C. (2015). Oxygen reduction reaction in $Pr_2NiO_{4+\delta}/Ce_{0.9}Gd_{0.1}O_{1.95}$ and $La_{0.6}Sr_{0.4}Co_{0.2}Fe_{0.8}O_{3-\delta}/La_{0.8}Sr_{0.2}Ga_{0.8}Mg_{0.2}O_{2.80}$ half cells: an electrochemical study. *Journal of Solid State Electrochemistry*, *19*(3), 871-882.

130. Riza, F., Ftikos, C., Tietz, F., & Fischer, W. (2001). Preparation and characterization of $Ln_{0.8}Sr_{0.2}Fe_{0.8}Co_{0.2}O_{3-x}$ (Ln= La, Pr, Nd, Sm, Eu, Gd). *Journal of the European Ceramic Society*, *21*(10), 1769-1773.

131. Marinha, D., Dessemond, L., Cronin, J. S., Wilson, J. R., Barnett, S. A., & Djurado, E. (2011). Microstructural 3D reconstruction and performance evaluation of LSCF cathodes obtained by electrostatic spray deposition. *Chemistry of Materials*, *23*(24), 5340-5348.

132. Ried, P. (2009). Development of Solid Oxide Fuel Cell cathodes for operation at 600° C.

133. Yin, J. W., Yin, Y. M., Lu, J., Zhang, C., Minh, N. Q., & Ma, Z. F. (2014). Structure and Properties of Novel Cobalt-Free Oxides $Nd_xSr_{1-x}Fe_{0.8}Cu_{0.2}O_{3-\delta}$ ($0.3 \leq x \leq 0.7$) as Cathodes of Intermediate Temperature Solid Oxide Fuel Cells. *The Journal of Physical Chemistry C*, *118*(25), 13357-13368.

134. Jiang, S. P. (2002). A comparison of O 2 reduction reactions on porous (La, Sr) MnO_3 and (La, Sr)(Co, Fe)O_3 electrodes. *Solid State Ionics*, *146*(1), 1-22.

135. Al Daroukh, M., Vashook, V. V., Ullmann, H., Tietz, F., & Raj, I. A. (2003). Oxides of the AMO_3 and A_2MO_4-type: structural stability, electrical conductivity and thermal expansion. *Solid State Ionics*, *158*(1), 141-150.

136. Kharton, V. V., Tsipis, E. V., Yaremchenko, A. A., Marozau, I. P., Viskup, A. P., Frade, J. R., & Naumovich, E. N. (2006). Oxygen permeability, electronic conductivity and stability of $La_{0.3}Sr_{0.7}CoO_3$-based perovskites. *Materials Science and Engineering: B*, *134*(1), 80-88.

137. Kostogloudis, G. C., Ftikos, C., Ahmad-Khanlou, A., Naoumidis, A., & Stöver, D. (2000). Chemical compatibility of alternative perovskite oxide SOFC cathodes with doped lanthanum gallate solid electrolyte. *Solid State Ionics*, *134*(1), 127-138.

138. Tsipis, E. V., Kharton, V. V., & Frade, J. R. (2006). Transport properties and electrochemical activity of YBa (Co, Fe)$_4O_7$ cathodes. *Solid State Ionics*, *177*(19), 1823-1826.

139. Barilo, S. N., Shiryaev, S. V., Bychkov, G. L., Shestak, A. S., Zhou, Z. X., Hinkov, V., Plakhty, V. P., Chernenkov, P. Y., Gavrilov, S. V., Baran, M.,

Szymczak, R., Sheptyakov, R., & Szymczak, H. (2006). Crystal growth and giant magnetoresistance of rare earth layered cobaltites. *Rev. Adv. Mater. Sci*, *12*, 33-45.

140. Raveau, B., & Seikh, M. (2012). Cobalt oxides: from crystal chemistry to physics. *John Wiley & Sons.*

141. Morin, F., Trudel, G., & Denos, Y. (1997). The phase stability of $La_{0.5}Sr_{0.5}CoO_{3-\delta}$. *Solid State Ionics*, *96*(3), 129-139.

142. Tsipis, E. V., & Kharton, V. V. (2008). Electrode materials and reaction mechanisms in solid oxide fuel cells: a brief review. *Journal of Solid State Electrochemistry*, *12*(11), 1367-1391.

143. Baumann, F. S., Fleig, J., Cristiani, G., Stuhlhofer, B., Habermeier, H. U., & Maier, J. (2007). Quantitative comparison of mixed conducting SOFC cathode materials by means of thin film model electrodes. *Journal of the Electrochemical Society*, *154*(9), B931-B941.

144. Peña-Martínez, J., Marrero-López, D., Pérez-Coll, D., Ruiz-Morales, J. C., & Núñez, P. (2007). Performance of XSCoF (X= Ba, La and Sm) and LSCrX′ (X′= Mn, Fe and Al) perovskite-structure materials on LSGM electrolyte for IT-SOFC. *Electrochimica acta*, *52*(9), 2950-2958.

145. Wan, J. H., Yan, J. Q., & Goodenough, J. B. (2005). LSGM-based solid oxide fuel cell with 1.4 W/cm^2 power density and 30 day long-term stability. *Journal of the Electrochemical Society*, *152*(8), A1511-A1515.

146. Uchida, H., Arisaka, S. I., & Watanabe, M. (2002). High Performance Electrode for Medium-Temperature Solid Oxide Fuel Cells: Control of Microstructure of La (Sr)CoO_3 Cathodes with Highly Dispersed Pt Electrocatalysts. *Journal of the Electrochemical Society*, *149*(1), A13-A18.

147. Simner, S. P., Shelton, J. P., Anderson, M. D., & Stevenson, J. W. (2003). Interaction between La(Sr)FeO_3 SOFC cathode and YSZ electrolyte. *Solid State Ionics*, *161*(1), 11-18.

148. Chen, Z., Ran, R., Zhou, W., Shao, Z., & Liu, S. (2007). Assessment of $Ba_{0.5}Sr_{0.5}Co_{1-y}Fe_yO_{3-\delta}$ (y = 0.0 – 1.0) for prospective application as cathode for

IT-SOFCs or oxygen permeating membrane. *Electrochimica Acta*, *52*(25), 7343-7351.

149. Bronin, D. I., Kuzin, B. L., Sokolova, Y. V., & Polyakova, N. V. (2000). Reaction of Cobalt-containing Materials with Solid Electrolyte Based on Lanthanum Gallate. *Russian journal of applied chemistry of zhurnal prikladnoi khimii*, *73*(9), 1557-1560.

150. Kuzin, B. L., Bogdanovich, N. M., Bronin, D. I., Yaroslavtsev, I. Y., Vdovin, G. K., Kotov, Y. A., Bagazeev, A. I.,Medvedev, A. I., Murzakaev, A. M., Timoshenkova, O. P., & Stol'Ts, A. K. (2007). Electrochemical properties of cathodes made of (La, Sr)(Fe, Co)O_3 containing admixtures of nanoparticles of cupric oxide and intended for fuel cells with a solid electrolyte based on ceric oxide. *Russian Journal of Electrochemistry*, *43*(8), 920-928.

151. Zhou, W., Shao, Z., Ran, R., Chen, Z., Zeng, P., Gu, H., Jin, W., & Xu, N. (2007). High performance electrode for electrochemical oxygen generator cell based on solid electrolyte ion transport membrane. *Electrochimica Acta*, *52*(22), 6297-6303.

152. Zhu, X. D., Sun, K. N., Zhang, N. Q., Chen, X. B., Wu, L. J., & Jia, D. C. (2007). Improved electrochemical performance of $SrCo_{0.8}Fe_{0.2}O_{3-\delta}$ – $La_{0.45}Ce_{0.55}O_{2-\delta}$ composite cathodes for IT-SOFC. *Electrochemistry Communications*, *9*(3), 431-435.

153. Serra, J. M., Vert, V. B., Betz, M., Haanappel, V. A. C., Meulenberg, W. A., & Tietz, F. (2008).Screening of A-Substitution in the System $A_{0.68}Sr_{0.3}Fe_{0.8}Co_{0.2}O_{3-\delta}$ for SOFC Cathodes. *Journal of the Electrochemical Society*, *155*(2), B207-B214.

154. Ishihara, T., Honda, M., Shibayama, T., Furutani, H., & Takita, Y. (1998). An intermediate temperature solid oxide fuel cell utilizing superior oxide ion conducting electrolyte, doubly doped $LaGaO_3$ perovskite. *Ionics*, *4*(5-6), 395-402.

155. Ishihara, T., Kilner, J. A., Honda, M., & Takita, Y. (1997). Oxygen surface exchange and diffusion in the new perovskite oxide ion conductor $LaGaO_3$. *Journal of the American Chemical Society*, *119*(11), 2747-2748.

156. Lee, H. Y., Jang, J. H., & Oh, S. M. (1999). Cathodic Activity and Interfacial Stability of $Y_{0.8}Ca_{0.2}Co_{1-x}Fe_xO_3$/YSZ Electrodes for Solid Oxide Fuel Cells. *Journal of the Electrochemical Society*, *146*(5), 1707-1711.

157. Steele, B. C. H. (1995). Interfacial reactions associated with ceramic ion transport membranes. *Solid State Ionics*, *75*, 157-165.

158. Fleig, J. (2002). On the width of the electrochemically active region in mixed conducting solid oxide fuel cell cathodes. *Journal of Power Sources*, *105*(2), 228-238.

159. Ishihara, T., Fukui, S., Nishiguchi, H., & Takita, Y. (2002). Mixed electronic-oxide ionic conductor of $BaCoO_3$ doped with La for cathode of intermediate-temperature-operating solid oxide fuel cell. *Solid State Ionics*, *152*, 609-613.

160. Kimura, T., & Goto, T. (2005). Ir –YSZ nano-composite electrodes for oxygen sensors. *Surface and Coatings Technology*, *198*(1), 36-39.

161. Musić, S., Popović, S., Maljković, M., Skoko, Z., Furić, K., & Gajović, A. (2003). Thermochemical formation of IrO_2 and Ir. *Materials letters*, *57*(29), 4509-4514.

162. Nakamura, T., Petzow, G., & Gauckler, L. J. (1979). Stability of the perovskite phase $LaBO_3$ (B = V, Cr, Mn, Fe, Co, Ni) in reducing atmosphere I. Experimental results. *Materials Research Bulletin*, *14*(5), 649-659.

163. Ai, N., Chen, K., & Jiang, S. P. (2013). A fundamental study of infiltrated CeO_2 and $(Gd,Ce)O_2$ nanoparticles on the electrocatalytic activity of Pt cathodes of solid oxide fuel cells. *Solid State Ionics*, *233*, 87-94.

164. Haanappel, V. A. C., Rutenbeck, D., Mai, A., Uhlenbruck, S., Sebold, D., Wesemeyer, H., Rowekamp, B., & Tietz, F. (2004). The influence of noble-metal-containing cathodes on the electrochemical performance of anode-supported SOFCs. *Journal of Power Sources*, *130*(1), 119-128.

165. Erning, J. W., Hauber, T., Stimming, U., & Wippermann, K. (1996). Catalysis of the electrochemical processes on solid oxide fuel cell cathodes. *Journal of Power Sources*, *61*(1), 205-211.

166. Babaei, A., Zhang, L., Liu, E., & Jiang, S. P. (2011). Performance and stability of $La_{0.8}Sr_{0.2}MnO_3$ cathode promoted with palladium based catalysts in solid oxide fuel cells. *Journal of Alloys and Compounds*, *509*(14), 4781- 4787.

167. Liu, B., Gu, Y., Kong, L., & Zhang, Y. (2008). Evaluation of nano-structured $Ir_{0.5}Mn_{0.5}O_2$ as a potential cathode for intermediate temperature solid oxide fuel cell. *Journal of Power Sources*, *185*(2), 946-951.

168. Wang, S., Kato, T., Nagata, S., Honda, T., Kaneko, T., Iwashita, N., & Dokiya, M. (2002). Performance of a $La_{0.6}Sr_{0.4}Co_{0.8}Fe_{0.2}O_3$ – $Ce_{0.8}Gd_{0.2}O_{1.9}$–Ag Cathode for Ceria Electrolyte SOFCs. *Solid State Ionics*, *146*(3), 203-210.

169. Torres-Huerta, A. M., Vargas-García, J. R., & Domínguez-Crespo, M. A. (2007). Preparation and characterization of IrO_2 –YSZ nanocomposite electrodes by MOCVD. *Solid State Ionics*, *178*(29), 1608-1616.

170. Fan, L., Chen, M., Wang, C., & Zhu, B. (2012). Pr_2NiO_4 – Ag composite cathode for low temperature solid oxide fuel cells with ceria-carbonate composite electrolyte. *International Journal of Hydrogen Energy*, *37*(24), 19388-19394.

171. Huang, J., Gao, R., Mao, Z., & Feng, J. (2010). Investigation of $La_2NiO_{4+\delta}$-based cathodes for SDC–carbonate composite electrolyte intermediate temperature fuel cells. *International Journal of Hydrogen Energy*, *35*(7), 2657-2662.

172. Gao, Z., Mao, Z., Wang, C., & Liu, Z. (2010). Preparation and characterization of $La_{1-x}Sr_xNi_yFe_{1-y}O_{3-\delta}$ cathodes for low-temperature solid oxide fuel cells. *International Journal of Hydrogen Energy*, *35*(23), 12905-12910.

173. Qin, H., Zhu, B., Raza, R., Singh, M., Fan, L., & Lund, P. (2012). Integration design of membrane electrode assemblies in low temperature solid oxide fuel cell. *International Journal of Hydrogen Energy*, *37*(24), 19365-19370.

174. Zhao, Y., He, J., Fan, L., Ran, W., Zhang, C., Gao, D., Wang, C., & Gao, F. (2013). Synthesis and characterization of hierarchical porous LiNiCuZn-oxides as potential electrode materials for low temperature solid oxide fuel cells. *International Journal of Hydrogen Energy*, *38*(36), 16558-16562.

175. Tan, W., Fan, L., Raza, R., Khan, M. A., & Zhu, B. (2013). Studies of modified lithiated NiO cathode for low temperature solid oxide fuel cell with ceria-

carbonate composite electrolyte. *International Journal of Hydrogen Energy*, *38*(1), 370-376.

176. Ahmad, S., Bakar, M. S. A., Rahman, H. A., & Muchtar, A. (2014). Brief Review: Electrochemical Performance of LSCF Composite Cathodes--Influence of Ceria-Electrolyte and Metals Element. *Applied Mechanics & Materials*, (695).

177. Kharton, V. V., Nikolaev, A. V., Naumovich, E. N., & Vecher, A. A. (1995). Oxygen ion transport and electrode properties of La(Sr)MnO_3. *Solid State Ionics*, *81*(3), 201-209.

178. Kharton, V. V., Yaremchenko, A. A., & Naumovich, E. N. (1999). Research on the electrochemistry of oxygen ion conductors in the former Soviet Union. II. Perovskite-related oxides. *Journal of Solid State Electrochemistry*, *3*(6), 303-326.

179. Plumejeau, S., Alauzun, J. G., & Boury, B. (2015). Hybrid metal oxide@ biopolymer materials precursors of metal oxides and metal oxide-carbon composites. *Journal of the Ceramic Society of Japan*, *123*(1441), 695-708.

180. Cheng, J., Navrotsky, A., Zhou, X. D., & Anderson, H. U. (2005). Enthalpies of Formation of $LaMO_3$ Perovskites (M = Cr, Fe, Co, and Ni). *Journal of Materials Research*, *20*(01), 191-200.

181. Milewski, J., & Miller, A. (2006). Influences of the type and thickness of electrolyte on solid oxide fuel cell hybrid system performance. *Journal of Fuel Cell Science and Technology*, *3*(4), 396-402.

182. Huo, H. B., Zhu, X. J., & Cao, G. Y. (2006). Nonlinear modelling of a SOFC stack based on a least squares support vector machine. *Journal of Power Sources*, *162*(2), 1220-1225.

183. Santarelli, M., Leone, P., Calì, M., & Orsello, G. (2007). Experimental evaluation of the sensitivity to fuel utilization and air management on a 100kW SOFC system. *Journal of Power Sources*, *171*(1), 155-168.

184. De Groot A., Advanced exergy analysis of high temperature fuel cell systems. PhD Thesis, Energy Research Centre of the Netherlands, Petten; 2004.

185. Yu, H., Ouyang, S., Yan, S., Li, Z., Yu, T., & Zou, Z. (2011). Sol–gel hydrothermal synthesis of visible-light-driven Cr-doped $SrTiO_3$ for efficient hydrogen production. *Journal of Materials Chemistry*, *21*(30), 11347-11351.

186. Amar, I. A., Lan, R., & Tao, S. (2015). Synthesis of ammonia directly from wet nitrogen using a redox stable $La_{0.75}Sr_{0.25}Cr_{0.5}Fe_{0.5}O_{3-\delta}$ – $Ce_{0.8}Gd_{0.18}Ca_{0.02}O_{2-\delta}$ composite cathode. *RSC Advances*, *5*(49), 38977-38983.

187. Ghosh, S., & Dasgupta, S. (2010). Synthesis, characterization and properties of nanocrystalline perovskite cathode materials. *Mater. Sci.-Poland*, *28*(2), 427-438.

188. Shimizu, Y., & Murata, T. (1997). Sol–Gel Synthesis of Perovskite-Type Lanthanum Manganite Thin Films and Fine Powders Using Metal Acetylacetonate and Poly (vinyl alcohol). *Journal of the American Ceramic Society*, *80*(10), 2702-2704.

189. Ahmad, A. L., Idrus, N. F., & Othman, M. R. (2005). Preparation of perovskite alumina ceramic membrane using sol–gel method. *Journal of Membrane Science*, *262*(1), 129-137.

190. Virkar, A. V., Chen, J., Tanner, C. W., & Kim, J. W. (2000). The role of electrode microstructure on activation and concentration polarizations in solid oxide fuel cells. *Solid State Ionics*, *131*(1), 189-198.

191. Murray, E. P., Sever, M. J., & Barnett, S. A. (2002). Electrochemical performance of (La, Sr)(Co, Fe)O_3 – (Ce, Gd)O_3 composite cathodes. *Solid State Ionics*, *148*(1), 27-34.

192. Keller, A. A., Wang, H., Zhou, D., Lenihan, H. S., Cherr, G., Cardinale, B. J., Miller, R., & Ji, Z. (2010). Stability and aggregation of metal oxide nanoparticles in natural aqueous matrices. *Environmental Science & Technology*, *44*(6), 1962-1967.

193. Lowe, A. B., Sumerlin, B. S., Donovan, M. S., & McCormick, C. L. (2002). Facile preparation of transition metal nanoparticles stabilized by well-defined (co) polymers synthesized via aqueous reversible addition-fragmentation chain transfer polymerization. *Journal of the American Chemical Society*, *124*(39), 11562-11563.

194. Xuan, W., Zhu, C., Liu, Y., & Cui, Y. (2012). Mesoporous metal–organic framework materials. *Chemical Society Reviews*, *41*(5), 1677-1695.

195. Chen, D., Cao, L., Huang, F., Imperia, P., Cheng, Y. B., & Caruso, R. A. (2010). Synthesis of monodisperse mesoporous titania beads with controllable diameter, high surface areas, and variable pore diameters (14−23 nm). *Journal of the American Chemical Society*, *132*(12), 4438-4444.

196. Frenzer, G., & Maier, W. F. (2006). Amorphous porous mixed oxides: Sol-gel ways to a highly versatile class of materials and catalysts. *Annu. Rev. Mater. Res.*, *36*, 281-331.

CHAPTER 3

Effect of non-ionic, anionic and cationic surfactantson the Sol gel synthesis of IrO/$Ce_{0.8}Sm_{0.2}O_{2-\delta}$ nanocomposite for SOFC application

Summary

This chapter has been published in the Journal of Fuel Cell Science & Technology and has been structured according to the journal's format. This chapter has also been reformatted to incorporate further comments and corrections by the examiners.

Abstract

The sol-gel technique is a versatile and relatively simple method easily adapted to synthesize complex metal oxide formulations. The sol-gel technique takes advantage of the structural directing properties and templating characteristics of non-ionic, anionic and cationic surfactant to produce porous Iridium oxide, with samarium doped ceria (SDC) nanoparticles. The nanopowders were calcined at a temperature of 950 °C, and the crystalline nanostructures and compositions were characterized by high resolution transmission electron microscopy and X-ray diffraction. Textural characteristics and particle morphology were respectively characterized by Nitrogen sorption at 77.5 K and scanning electron microscopy. The electrochemical properties were characterised by using a Kittec Squadro muffle furnace and SOFC testing equipment, with air and hydrogen as the gases used. The nature of the surfactant influenced particle morphology, pore diameter, pore size, crystallite size, surface area and electrochemical properties.

Keywords: Surfactant, Sol-gel technique, Nanoparticles, YSZ electrolyte, Samaria doped ceria, Iridium oxide, Electrochemical properties, Solid Oxide fuel cell, Anode and Perovskite.

1.0 Introduction

Sol-gel synthesis is a promising method toproduce oxide ceramic materials [1] with controlled structure and composition for many applications [2, 3]. This method is simple cost-effective, high yielding final product and has a low reaction temperature [3, 4]. It is an efficient way to prepare samarium doped ceria nanoparticles with Iridium oxide [5], because it synthesizes monodispersed particles, with controllable sizes in the nanometer scale. This method also regulates particle interactions at certain stages of material formation, and is necessary for the perfect structure of material [6].

The surfactant-assisted technique is thus suitable to provide materials with appropriate pore diameter, high surface areas and a better access to active sites [7 - 9]. The properties of surfactants influences particle morphology and no simple selection rule can be applied to predict which surfactant will give a particular particle size. Their structures, stabilization of the micelle walls and reduced inter-droplet exchange, produces smaller particles, crystals and prevents metallic nanoparticles aggregation into matrices [10].

The surfactants used in these methods are Pluronic P123 block copolymer, Pluronic F-127 block copolymer [11 - 14], Sodium dodecyl sulfate (SDS), Cetyltrimethyl ammonium bromide (CTAB) and Polyethylene glycol (PEG). The materials formed were used in low temperature solid oxide fuel cells application.

2.0 Materials and Method

Cerium (III) acetylacetonate hydrate ($Ce(acac)_3$) 99.9 % purity and Samarium (III) acetylacetonate hydrate ($Sm(acac)_2$) 99.9 % purity, were purchased from Aldrich Chemicals USA. Surfactants, Pluronic F-127 powder (bio reagent, suitable for cell culture), PEG, Pluronic P123, SDS and CTAB were purchased from Sigma Life Science Germany. Iridium (III) acetylacetonate ($Ir(acac)_3$) was purchased from Industrial Analytical Chemicals pty South Africa. These chemical reagents were used as acquired from their commercial sources without further purification.

2.1 $IrO/Ce_{0.8}Sm_{0.2}O_{2-\delta}$ Preparation

The materials and mass used are 0.724 g of $Ce(acac)_3$, 0.200 g of $Sm(acac)_2$, 0.021 g of Ir $(acac)_3$ and 5 wt % (2.5 g) of surfactants. These were added to 40 ml of ethanol and 10 ml of deionized water as solvents, the mixture was sonicated for 30 mins. This was then stirred on a hot plate for 30 mins at a temperature of 80 °C, to form a sol. The hydrolysis, condensation, solvent evaporation occurred rapidly and a collapse of the gel network followed. The sol was dried in an oven for 18 hrs and calcined in a Kittec Squadro muffle Furnace for 4 hrs at 950 °C. This method was applied to all the materials made with each surfactant.

2.2 $IrO/Ce_{0.8}Sm_{0.2}O_{2-\delta}$ without surfactant

The materials and mass used are 0.7240 g of Ce $(acac)_3$, 0.200 g of Sm $(acac)_2$ and 0.0218 g of Ir $(acac)_3$. These were added to 40 ml of ethanol and 10 ml of deionized water as solvents and the mixture was sonicated for 30 mins. The mixture was stirred on a hot plate for 2 hrs at a temperature of 80 °C. The hydrolysis, condensation and solvent evaporation was sluggish. The sample was dried in an oven for 18 hrs and then was calcined in a kittec squadro muffle furnace for 4 hrs at 950 °C. The summary and synthesis processes are shown in Table 1 below.

Table 1: The summary and processes used for synthesis conditions.

Sample ID	Mass of sample (5wt %)	Surfactant Name	Type
F-127	2.5g	Pluronic F-127	Non-IONIC
P123	2.5g	Pluronic P123	Non-IONIC
PEG	2.5g	PolyethyleneGlycol	Non-IONIC
SDS	2.5g	SodiumDodecylSulphate	ANIONIC
CTAB	2.5g	CetylTriammoniumBromide	CATIONIC
WS	Not added	No Surfactant	–

2.3 Characterization

The crystal structure, crystal size, lattice spacing and the phase present in the powder were analyzed with X-ray Diffraction (XRD). This instrument (Phillips PW3710) works with voltage and current settings of 30 kV and 35 mA respectively and uses Cu-Kα radiation (1.5406 Å) for qualitative analysis, the XRD diffractogram were recorded between the intervals of $5° \leq 2\theta \leq 90°$ at a scan speed of 2 °/min. The mean crystallite sizes 'D' were determined according to the Scherrer equation:

$$D = \frac{0.9\lambda}{\beta cos\theta} \quad (1)$$

Where λ is Xray wavelength (1.5406 Å), β is the full width at half maximum of the diffraction line and θ is the diffraction angle. The functional group analysis was performed by Fourier Transform Infrared Spectroscopy (FTIR). The Lattice Fringes and diffraction patterns were carried out by the High resolution transmission electron microscopy (HR-TEM). Scanning electron microscopy (SEMX130) was used to characterize the morphology and grain size of the powder; the samples were coated with gold before the examination.

N_2 adsorption- desorption, was done using the Tri-Star II3020 V1.03 to find the surface area, pore size, pore volume, and the pore size distribution of the different materials. The samples were degassed using the degassing instrument at 90 °C for 1 hr and 200 °C for 5 hrs. The samples were then analyzed with the Tristar II3020 V1.03 using Nitrogen at 77 K, to obtain the analysis. The kittec Squadro muffle furnace, a Powerstat 05 potentiostat and galvanostat were used to measure the current and voltage from the cell with a maximum voltage of 10 V and a current of 3 A. The ionic conductivity was calculated thus [15].

$$\sigma = \frac{l}{RS} \quad (2)$$

where, *l* is the electrolyte thickness, *S* is electrode area of the electrolyte surface and *R* is resistance in ohms (cell resistance). The activation energy was calculated using it in the Arrhenius plot, which is:

$$\sigma = \sigma^{o}\, exp\left[\frac{E_a}{kT}\right] \quad (3)$$

Where E_a is the activation energy of conduction, *T* is the absolute temperature, σ_o is the pre-exponential factor and *k* is the Boltzmann Constant. The galvanostatic and potentiostatic durability testing was carried out in order to assess the long - term static stability of the cell. Testing was carried out at low fuel consumption of (H_2 + 3 % H_2O) and an oxygen utilization of (<10 %), at 300 °C – 500 °C and at voltages within 0.1 – 1.2 V [16].

3.0 Results and Discussion

3.1 FTIR

Figure 1, shows the Infrared Spectroscopy investigation on the functionalization and vibration modes of IrO/$Ce_{0.8}Sm_{0.2}O_{2-\delta}$ nanocomposite produced and calcined at 950 ^{o}C. The surfactants were burnt off at this temperature leaving the metal composite. Surfactant addition caused shifts in the spectra peaks observed. The perovskite metals with F-127 showed absorbance peaks at 476.06 cm^{-1} indicates the formation of spinel metals and 1026.51 cm^{-1} are the M-O-M stretching vibrations of the metal oxide.

The absorbance peaks exhibited by P123 surfactant at 1526.95 cm^{-1} are H-O-H bending modes indicating the presence of absorbed water in the sample and the peak at 3421.10 cm^{-1} are M-OH stretching vibrations of the perovskites [17]. The perovskite metal formation from the PEG surfactant application displayed absorbance peaks at 1562.95 cm^{-1} and 3421.10 cm^{-1} also. The CTAB application revealed absorbance peaks at 471.86 cm^{-1} which is a characteristic band of spinel structures indicating the formation of a spinel metal. At 1054.82 cm^{-1} the absorbance band revealed the M-O-M stretching vibrations and at 3163.58 cm^{-1}, the M-OH stretching vibrations of the perovskite metals.

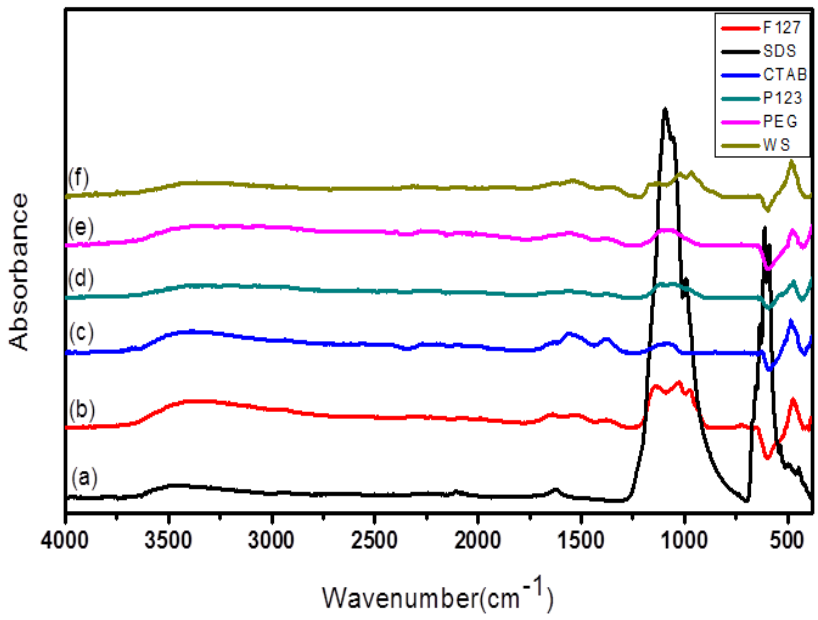

Figure 1: The FTIR spectra of (a) SDS (b) F127 (c) CTAB (d) P123 (e) PEG and (f) WS, surfactants added to $IrO/Ce_{0.8}Sm_{0.2}O_{2-\delta}$ calcined at 950 °C.

Absorbance peaks at 589.63 cm^{-1}, 610.96 cm^{-1}, 635.10 cm^{-1} and 992.03 cm^{-1} for the SDS application revealed characteristic absorbance bands of spinel structures which indicates the formation of spinel metals which are caused by vibrations of the tetrahedral sites of the metal – oxygen bond and absorption bands. The sample without surfactant showed absorbance peaks at 528.90 cm^{-1}, 926.67 cm^{-1}, 1017.54 cm^{-1}, 1258.47 cm^{-1}, 1375.10 cm^{-1}, 1513.09 cm^{-1}, 1579.09 cm^{-1} and 3151.99 cm^{-1}. The peaks displayed at 528.90 cm^{-1} are absorbance bands which are common characteristics of spinel structure representing the spinel metals formation, which are suspected bonds of iridium oxide metal, 926.67 cm^{-1}-1579.09 cm^{-1} absorbance peaks represents the M-O-M stretching vibrations of the enol and keto tautomer of SDC metals.

Metal acac consists of keto and enol tautomers and the replacement of the enolic hydrogen atom of acac by a metal cation, as shown in Figure 2. This produces a six membered metallocycle, shifting the keto–enol equilibrium in favor of the chelated enolate anion

formed in metal acetylacetonate complexes. The chelation of the acac ligands to transition metal ions as shown in Figure 2 will result in the displacement of the acac group carbonyl stretching bond. Many researchers have recorded this phenomenon with different transition metals, although the extent of shifting is different for different transition metals [17 - 19]. The characteristic absorbance of the metals shifts to the lower frequency region in all the cases is similar to what was observed in this study.

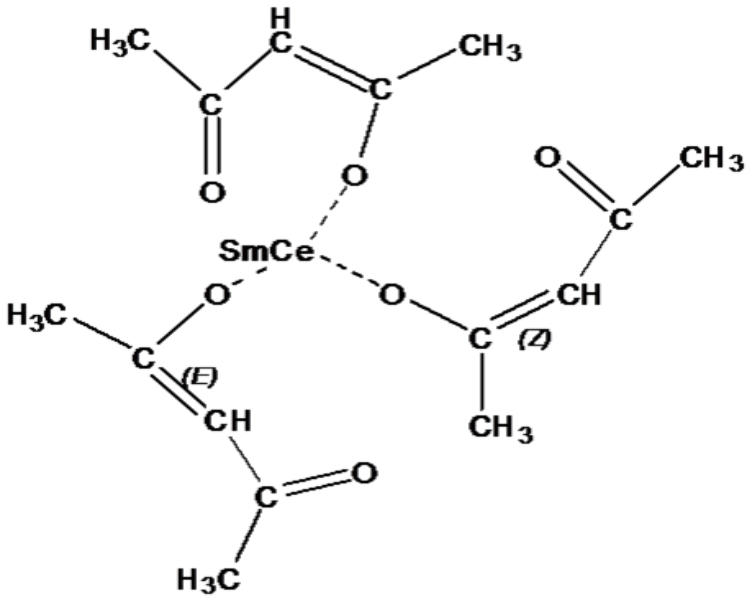

Figure 2: Schematic of the chelation of the acac ligands to transition metal ions

3.2 XRD

Figure 3 confirms the structural phase of Cerium oxide (CeO_2) peaks for the WS, PEG, F-127, P123 and CTAB. For SDS sample it revealed two phases namely CeO_2 and Sm_2O_3 peaks. The diffractogram showed the same structure, except that of the SDS surfactant, where the structure was not totally formed as a result of its effect on the materials. The structural pattern decreased in peak intensity from left to right as the angle 2θ increased, with very sharp peaks. The structure system was cubic that corresponds to an FCC lattice. The X-ray diffraction peaks were located at 2θ values of 28.50°, 34.67°, 40.12°, 47.19°, 53.92°, 58.63°, 65.89°, 69.17°, 76.25°, 78.61°, 83.32°, 87.87° and 94.48° which are

indexed respectively as (111), (200), (220), (311), (222), (400), (331), (420), (422) and (511).

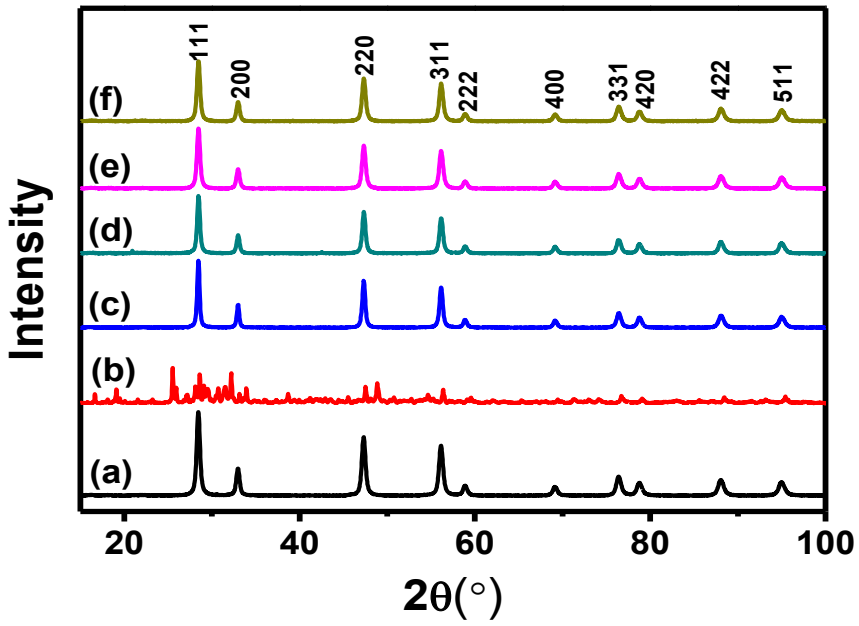

Figure 3: X-ray Diffraction pattern of (a) F127 (b) SDS (c) PEG (d) P123 (e) CTAB (f) WS, surfactants added to IrO/$Ce_{0.8}Sm_{0.2}O_{2-\delta}$ and calcined at 950 °C.

The average crystallite sizes are 30.96 nm for F127, 32.96 nm for P123, 36.66 nm for PEG, 43.11 nm for CTAB, 98.61 nm for SDS and 34.06 nm for the samples without surfactant (WS). The crystallite sizes were calculated from the Scherrer equation, using the most intense peak which confirmed the crystalline nature of the samples, because the peak intensities varied for the different surfactants. This was confirmed by the variance in the crystallite sizes, showing the effects of the surfactants on the sample. The crystallite sizes corresponded with the particle sizes from the HRTEM images, confirming the lateral relationship between the particle sizes of the sample and its crystallite size, confirming the surfactants effect.

3.3 HRTEM

Figure 4 shows the low magnification, lattice fringes and diffraction patterns of IrO/$Ce_{0.8}Sm_{0.2}O_{2-\delta}$ effects of the different surfactants on the sample. The low magnification of the image revealed the scattering, separation, shape, sizes of the particles and their formation.The uniformity of the spherical and rectangular shapes in the primary particles are evidence of surfactant effects. The sample particle sizes were in the range of 3.55 - 30.38 nm for F127; 2.63 - 30.49 nm for P123; 2.73 - 51.997 nm for PEG; 1.82 - 67.96 nm for CTAB; 1.73 - 79.59 nm for SDS and 3.42 - 66.56 nm for WS.

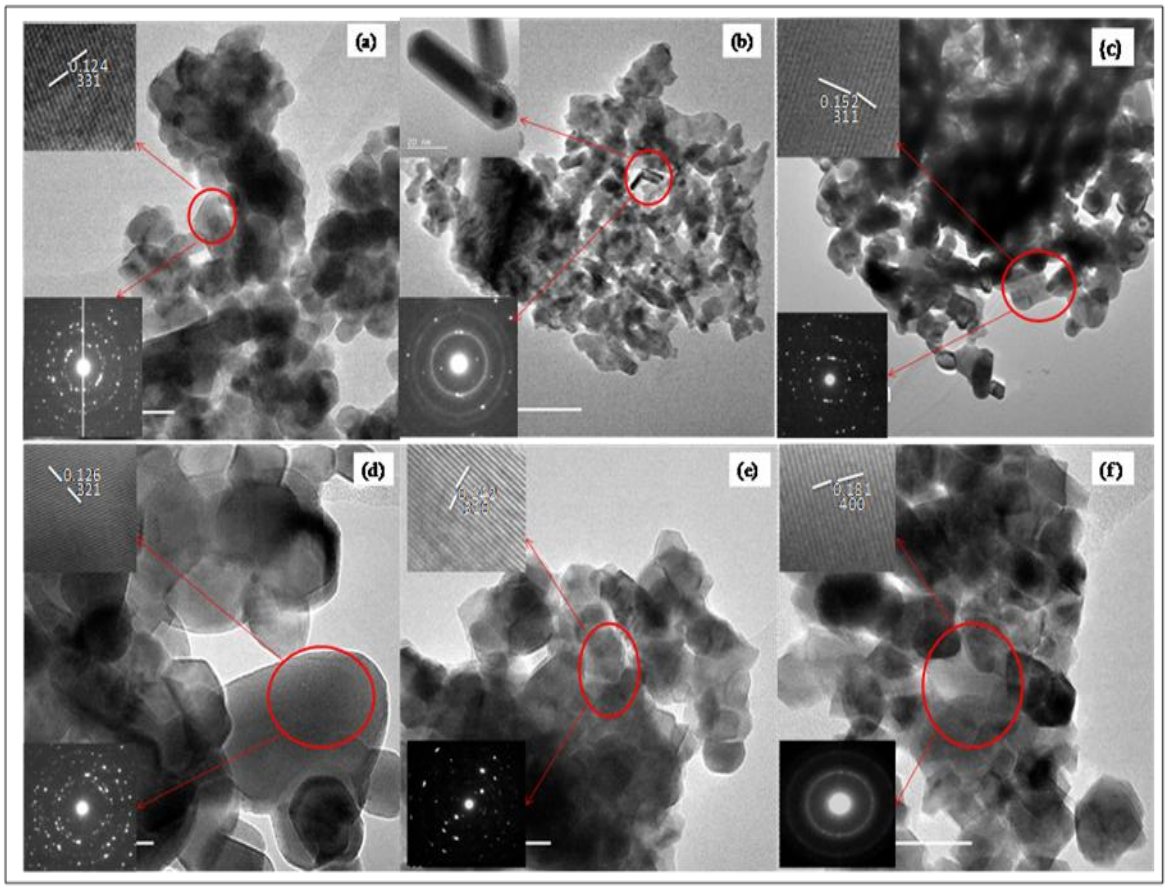

Figure 4: The Low magnification, Lattice fringes and diffraction patterns of (a) F127 (b) SDS(c) CTAB (d) PEG (e) P123 (f) WS, surfactants added toIrO/$Ce_{0.8}Sm_{0.2}O_{2-\delta}$and Calcined at 950 °C.

These correspond with the crystallite sizes in the XRD data and the varying particle sizes which confirm the effect of the surfactants. The lattice fringes also showed varying distances between the crystal layers, 0.126 nm (321) for PEG; 0.152 nm (311) for CTAB; 0.124 nm (331) for F127; 0.142 nm (310) for P123; 0.181 nm (400) for WS and the particles for SDS were rectangular. The values in brackets are the Miller indices for the crystal layer distance, as shown in Figure 4 below.

3.4 SEM

The morphology for F-127 surfactant as shown in Figure *5(a),* illustrated that the metals accumulated together in an agglomerate formation with large pore sizes in existence, between the particles. In Figure *5(b),* the effect of CTAB displayed morphology of a fine particle combination and agglomerate formation with pore spaces. Figure *5(c)* showed the effect of SDS on the sample, the morphology revealed large smooth aggregate surfaces with smaller loose particles.The morphology of PEG effects revealed a gel like structure with smooth surfaces separated by pores as shown in Figure *5(d).* The P123 effects illustrated, fine particles held together by strong and weak bonds in existence between the metal combination to form agglomerates and aggregates as shown in Figure *5(e).*

The image of the nanoparticles prepared without surfactants, revealed tiny particle separations to form bigger loosely packed particles, these particles bond and grew asymmetrically to form agglomerates as shown in Figure *5(f).*Surfactants addition produces particle separation and formation of loosely coherent secondary particles called agglomerates. Finely divided porous solids formed by this method are distinguished by large surface to volume ratios, enhanced chemical reactivity, higher adsorption capacity and lower sintering temperature. $IrO/Ce_{0.8}Sm_{0.2}O_{2-\delta}$ prepared using Pluronic F-127 and CTAB as surfactants observed from figure 5 revealed low conglomerations but a wide size distribution.

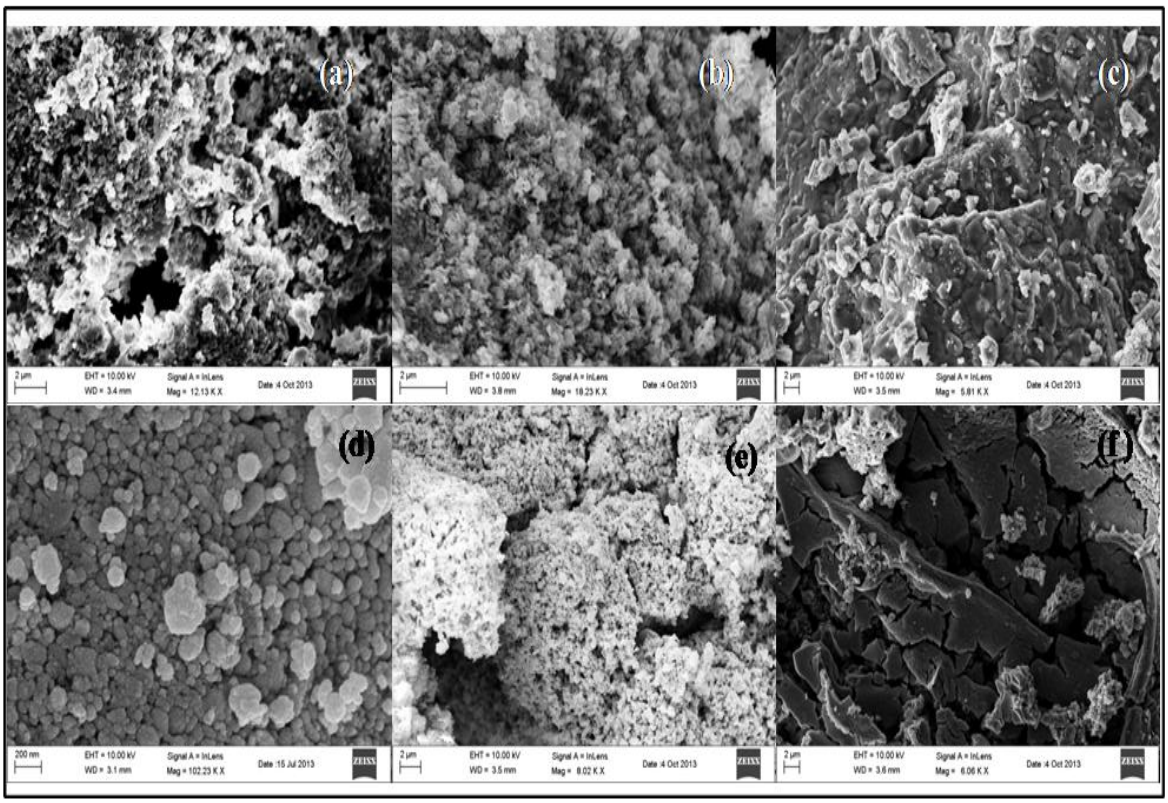

Figure 5: SEM morphology of (a) F127 (b) CTAB (c) SDS (d) WS (e) P123 and (f) PEG added to $IrO/Ce_{0.8}Sm_{0.2}O_{2-\delta}$ and calcined at 950 °C.

3.5 Nitrogen Adsorption/Desorption (BET)

In Figure 6, the isotherm plots confirmed the samples are macro porous materials, because the isotherm plots were type II. The surface area of F-127 prepared material, in comparison with the others, produced the highest surface area as shown in table 2. Surfactant addition increase or lower the material's surface area, affects particles sizes as shown in the HRTEM and crystallite sizes as seen in the XRD patterns. This also affected the materials pore sizes by the difference in pore sizes produced by the surfactants used, confirming its effects as shown in Figure 7.

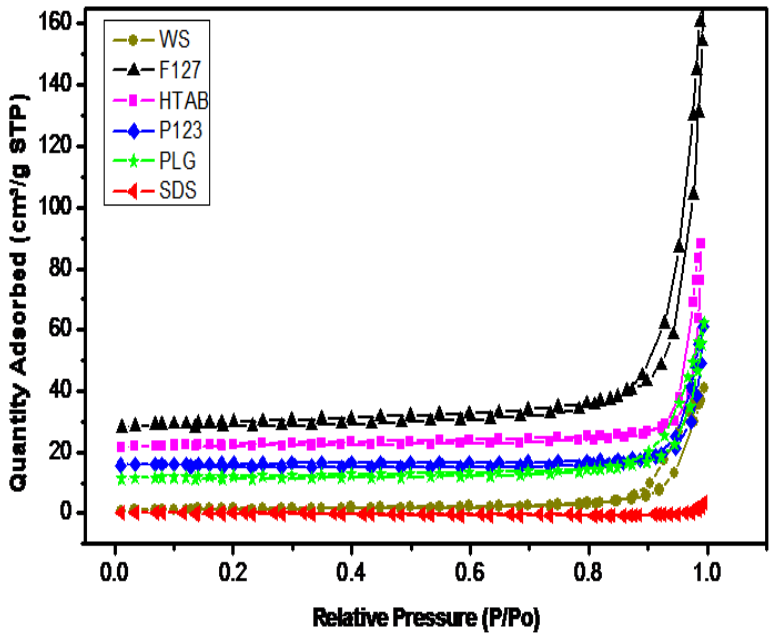

Figure 6: Isotherm plots for (a) WS (b) F127 (c) CTAB (d) P123 (e) PEG and (f) SDS added to $IrO/Ce_{0.8}Sm_{0.2}O_2$ and calcined at 950 °C.

Table 2: The Surface Area, Pore diameter, Pore volume and Crystallite size of (a) F127 (b) CTAB (c) PEG (d) WS (e) P123 and (f) SDS, added to $IrO/Ce_{0.8}Sm_{0.2}O_2$ and calcined at 950 °C.

Sample ID	Surface area (m^2/g)	Pore diameter (nm)	Pore volume (cm^3/g)	Crystallite size (nm)
F127	17.514	37.5	0.1641	33.87
CTAB	9.7064	27.8	0.0678	46.65
PEG	7.6359	29.5	0.0546	39.61
WS	5.5301	39.9	0.0552	43.85
P123	4.4621	32.5	0.0363	35.64
SDS	1.2478	18.58	0.0111	98.61

3.6 Electrochemical properties

The single cell was tested using Nuvant potentiostat and galvanostat connected to a Kittec Squadro muffle furnace device. Compressed air with flow rate of 50 m^3/min and humidified

hydrogen with a flow rate of 200 m^3/min was passed through pipes connected to the cell and the cell was tested for 6 hrs. The Single cell was prepared by brush-coating ink of $IrO/Ce_{0.8}Sm_{0.2}O_{2-\delta}$ anode material onto dense SDC electrolyte, which was bought commercially; these were sintered at 850 °C for 5 hrs. The cells with a foot print of 2 cm × 2 cm and 3.142 cm^2 active areas were tested electrochemically, with the active area being defined by the screen-printed anode.

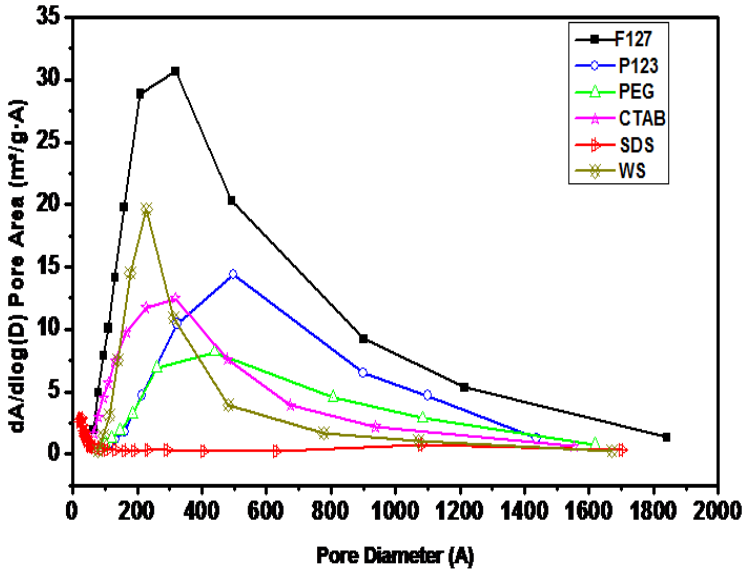

Figure 7: The Pore Size Distribution of (a) F127 (b) P123 (c) PEG (d) CTAB (e) SDS and (f) WS added to $IrO/Ce_{0.8}Sm_{0.2}O_{2-\delta}$ and calcined at 950 °C.

The cells were then tested in set-ups designed for the cell sizes and in this case, platinum (Pt) meshes were used as contact components. In the small set-up, rubber pipes were used to lead the gas flow perpendicular onto the 3.142 cm^2 cell and the corrugated Pt meshes acted as combined current collector and gas distributor. The polarization resistances for the single cell are shown in Figure 8 below showing the lowest polarization resistance obtained as 0.981 Ω cm^2, from the material synthesized with F-127.

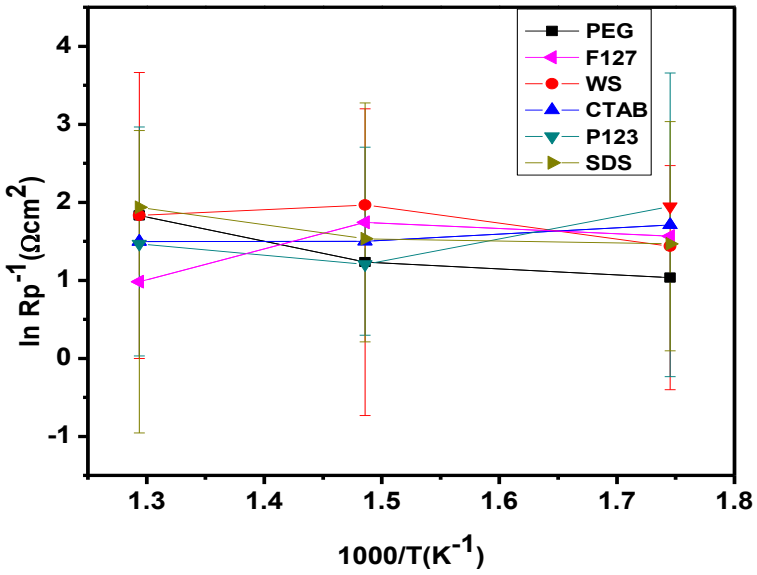

Figure 8: The Polarization resistance graph of (a) PEG (b) F127 (c) WS (d) CTAB (e) P123 and (f) SDS added to IrO/$Ce_{0.8}Sm_{0.2}O_{2-\delta}$ and calcined at 950 °C.

3.6.1 Polarization

The anodic polarization dependences for IrO/SDC synthesized with different surfactants are shown in Figures 9 - 14. These were obtained in humidified hydrogen and compressed air at the temperature intervals extending from 300 °C – 500 °C. At the cell temperature of 500 °C the current density was lower compared to the current density of 300 °C – 400 °C but produced a higher power density because of its low polarization losses and anodic overvoltage as shown in the graph. The ohmic overpotential is the internal resistance of the cell which can be estimated from the effective distance between the cells components coupled with the conductivity. The ohmic overpotential decreased, when the cell testing temperature increased from 300 - 500 °C, confirming a high resistance at lower temperature. The concentration overpotential are losses observed when current flows through the cell. This is more pronounced when fuel or oxidant gases with low purities are fed in to the cell. These losses were insignificant in this reaction, confirming high purity of the gases used and the concentration losses increased as the cell testing temperature increased as shown in Figures 9 - 14.

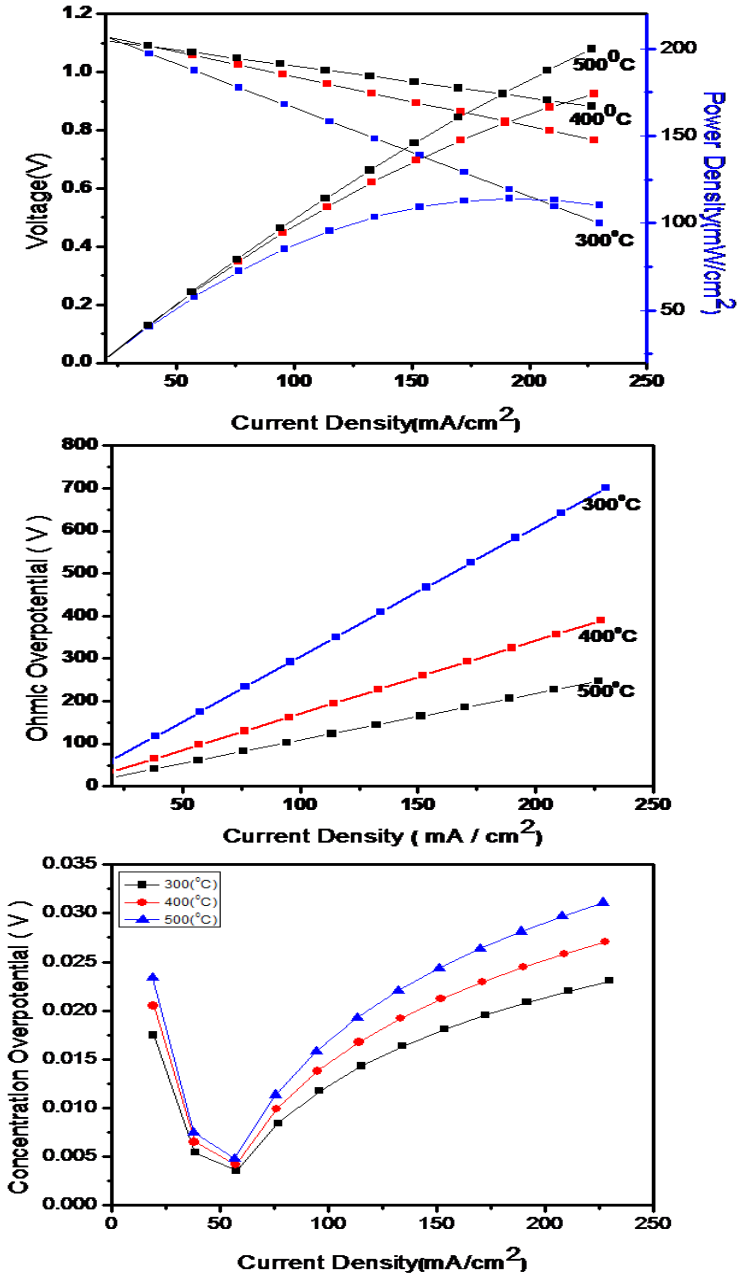

Figure 9: The polarisation curve, ohmic overpotential and concentration overpotential of PEG, added to IrO/$Ce_{0.8}Sm_{0.2}O_{2-\delta}$ and calcined at 950 °C.

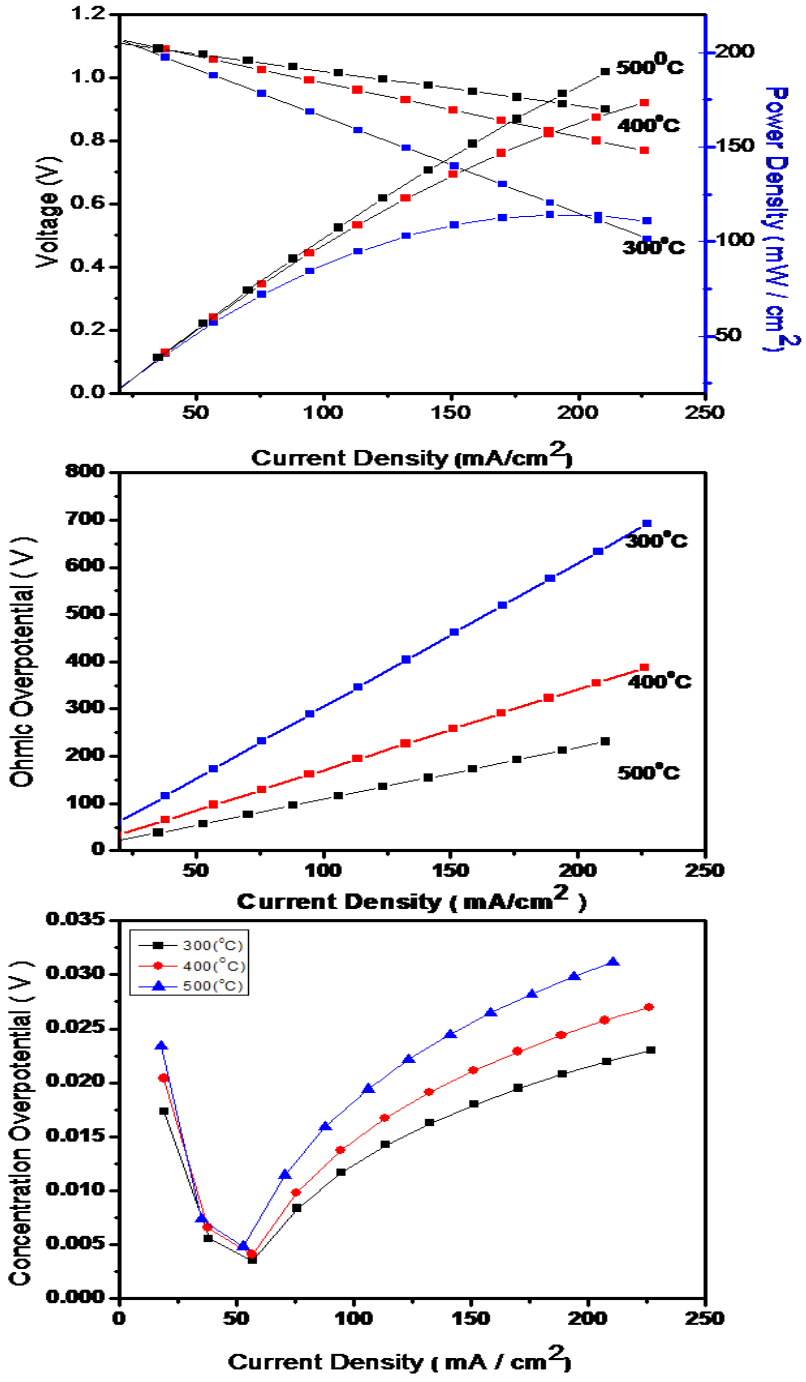

Figure 10: The polarization curve, ohmic overpotential and concentration overpotential of WS. Added to IrO/$Ce_{0.8}Sm_{0.2}O_{2-\delta}$ and calcined at 950 °C.

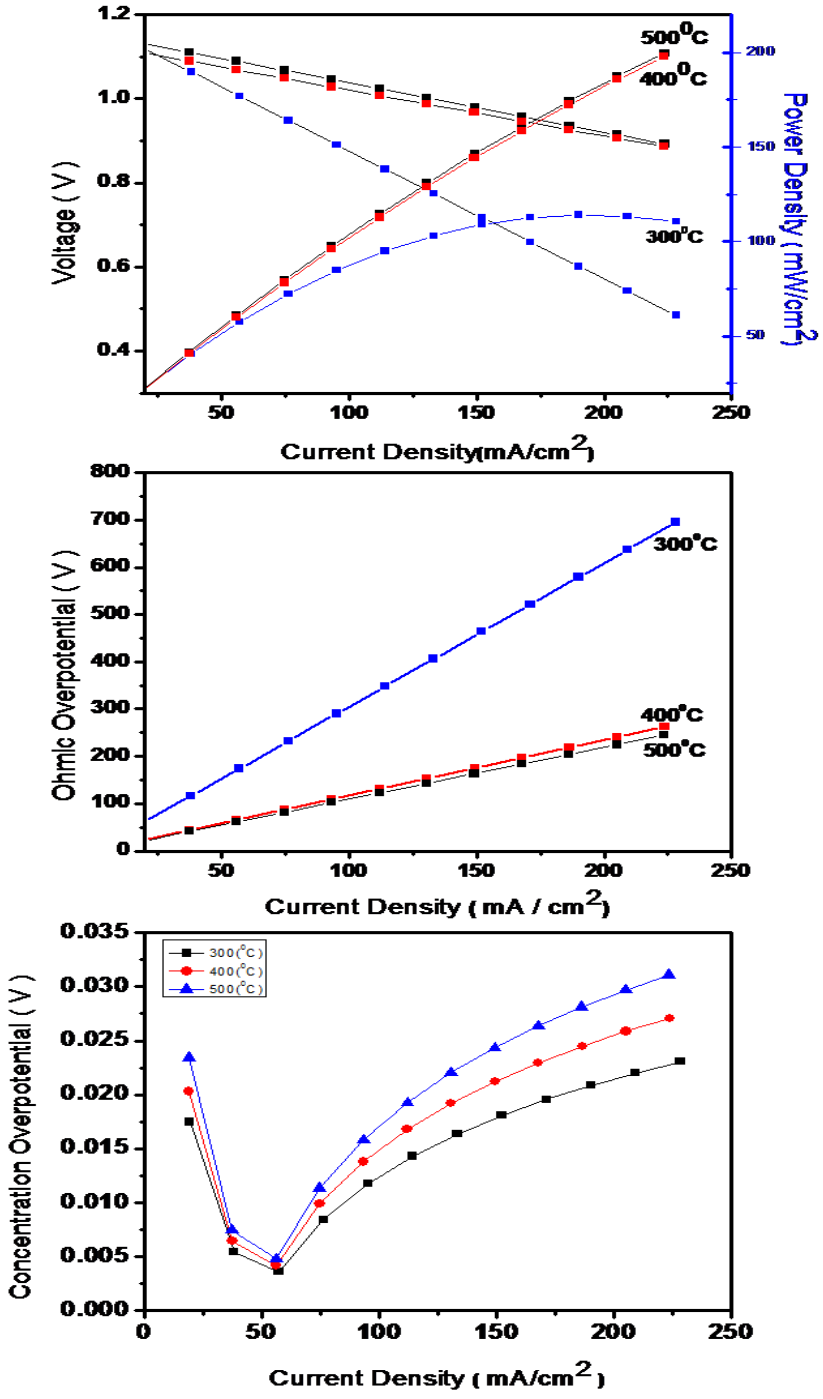

Figure11: The polarization curve, ohmic overpotential and concentration overpotential of CTAB added to IrO/$Ce_{0.8}Sm_{0.2}O_{2-\delta}$ and calcined at 950 °C.

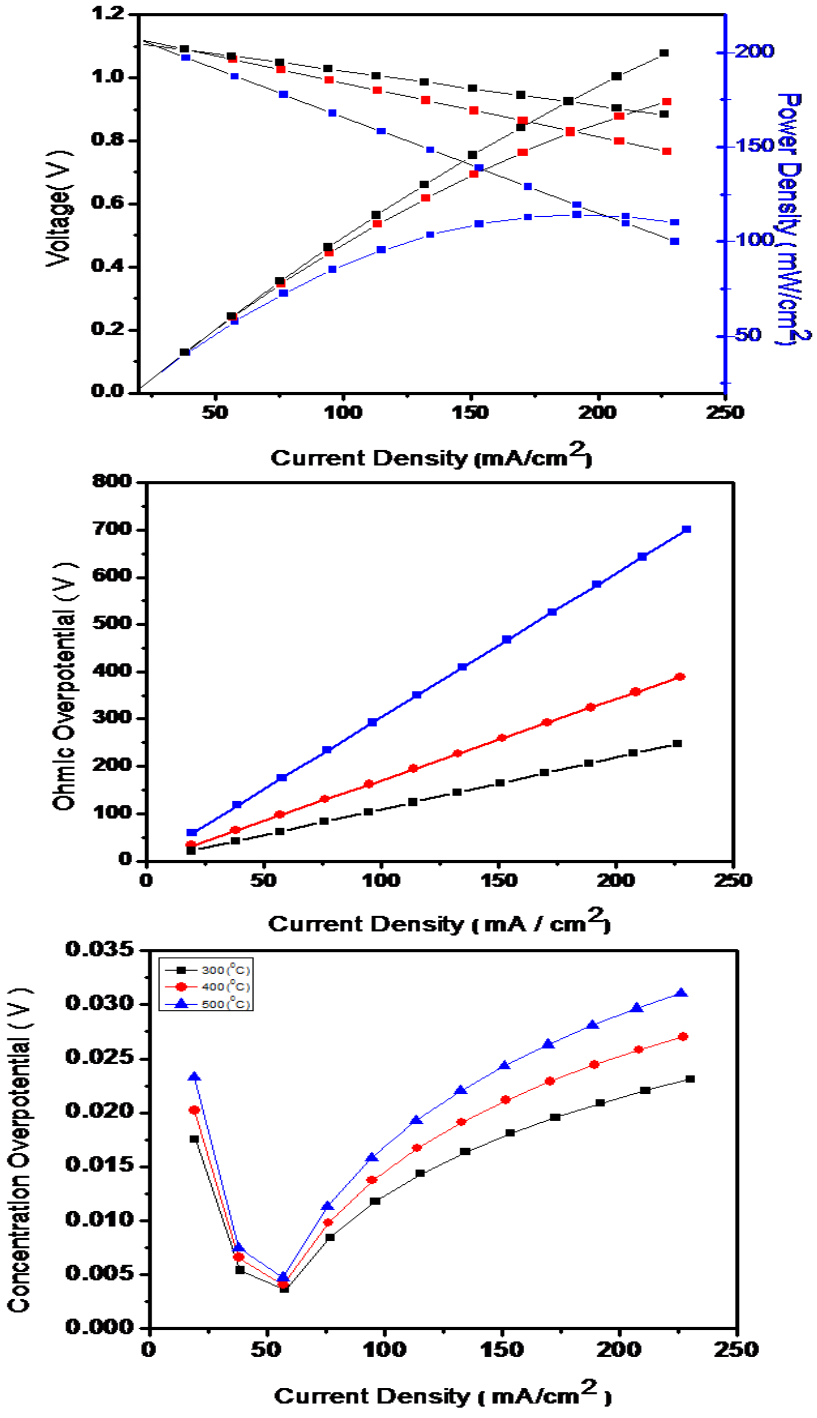

Figure 12: The polarization curve, ohmic overpotential and concentration overpotential of P123 added to IrO/$Ce_{0.8}Sm_{0.2}O_{2-\delta}$ and calcined at 950 °C.

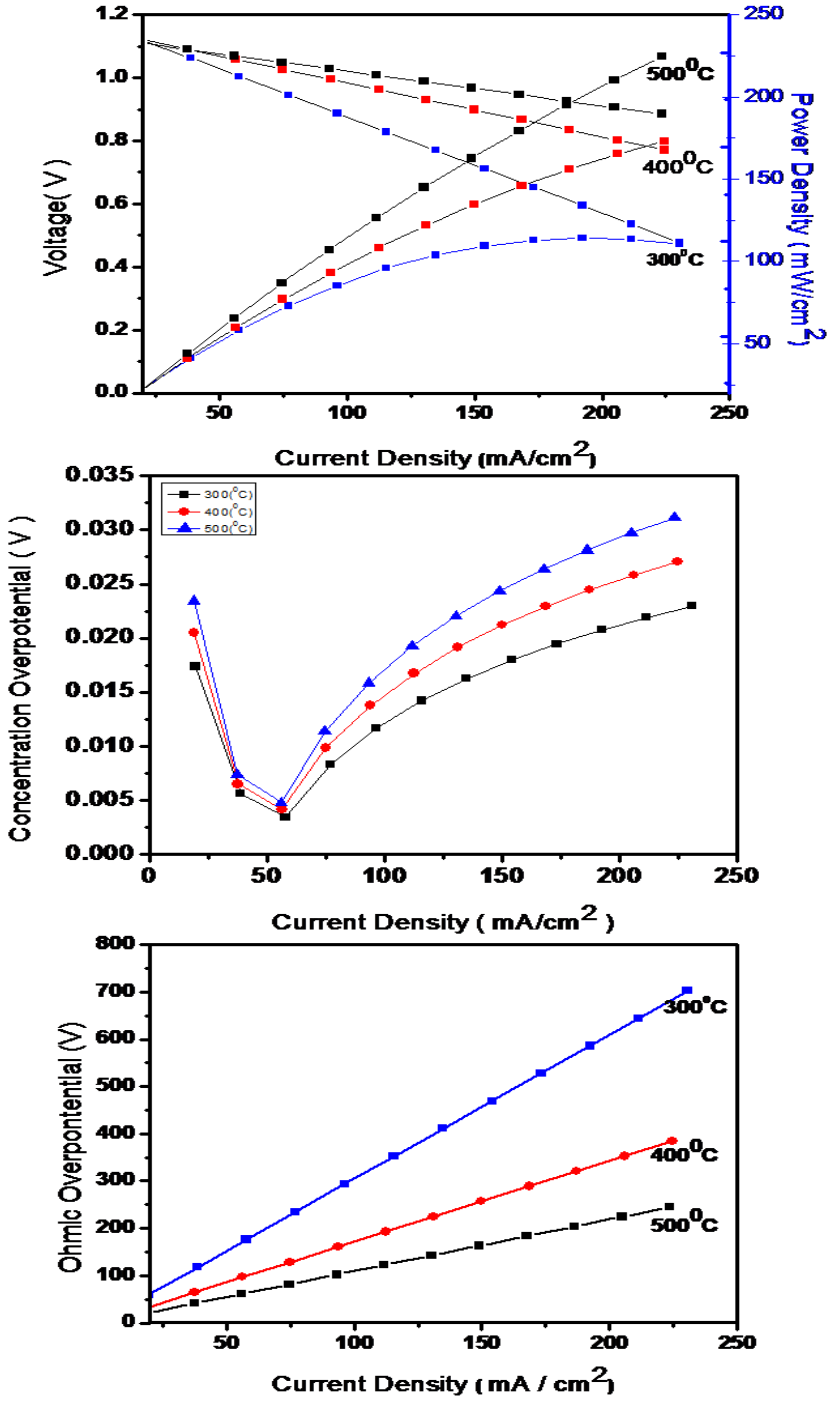

Figure 13: The polarization curve, ohmic overpotential and concentration overpotential of SDS added to IrO/$Ce_{0.8}Sm_{0.2}O_{2-\delta}$ and calcined at 950 °C.

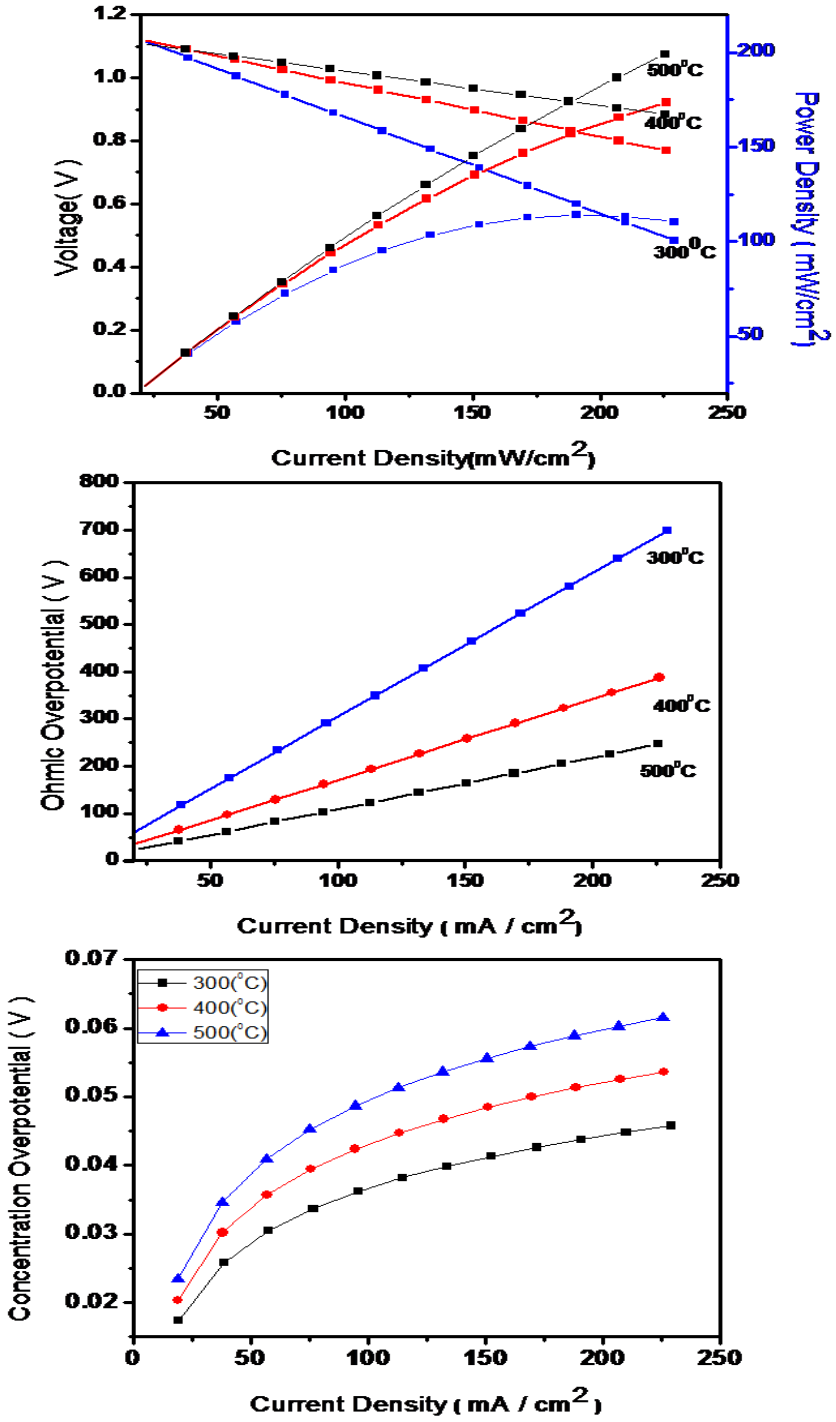

Figure 14: The polarization curve, ohmic overpotential and concentration overpotential of F-127 added to IrO/$Ce_{0.8}Sm_{0.2}O_{2-\delta}$ and calcined at 950 °C.

3.6.2 Power density

The power densities of the different samples are shown in Figure 15, extending from 300 °C – 500 °C. The maximum power densities were obtained at 500 ^{o}C with a maximum value of 199 mW/cm^2 obtained from the samples, which had F-127, CTAB and PEG added to it.

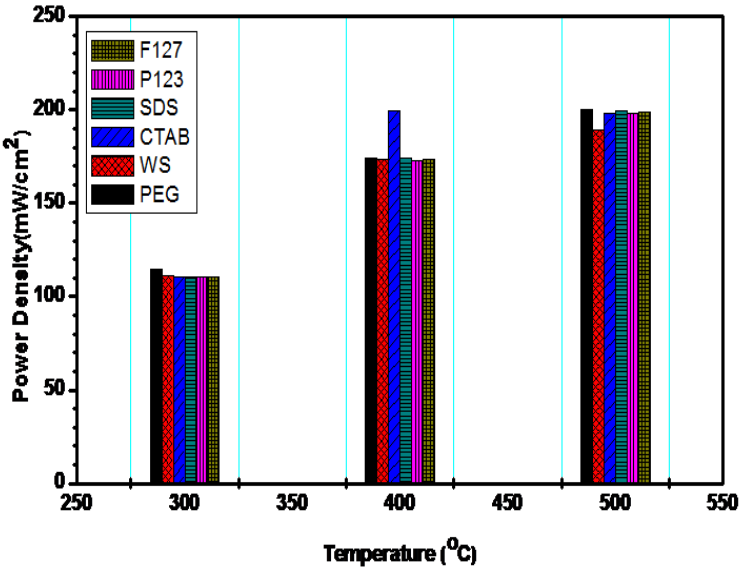

Figure 15: The Power Density graph of (a) F127 (b) P123 (c). SDS (d).CTAB (e).WS and (f).PEG added to IrO/$Ce_{0.8}Sm_{0.2}O_{2-\delta}$ and calcined at 950°C.

4.0 Conclusion

The nature of the surfactant influenced particle morphology, pore diameter, pore size, crystallite size, surface area and electrochemical properties. Surfactants addition caused a reduction in the crystallite sizes. This reduction was caused by an increase in the XRD peak intensities and a high, full width at half maximum value. Increase in the materials surface area was influenced by F127, CTAB, PEG and reduced by SDS and P123 compared with the sample without surfactant. The materials morphology changed from surfactant to

surfactant with varying porosity and particle sizes, resulting from a complete coalescing of the substituent materials.

The materials were tested as anodes and the electrochemical properties obtained. These properties are the power density, current density and polarization resistance. The results obtained, are shown in the figures above. F127 surfactant displayed the highest power density of 199 mW/cm^2, a current density of 226 mA/cm^2 and low polarization resistance of 0.981 Ω cm^2. Nonionic and cationic surfactants are good for our material, because of its surface area, low crystallite size, porous morphology and low polarization resistance. This research has revealed that surfactants are essential for material boosting and increased electrical performance in solid oxide fuel cell application.

Acknowledgement

The authors thank the University of KwaZulu-Natal, Westville campus for availability to research facilities used in this research.

References

[1.] Kalita, S. J., Abhilasha B., Himesh A. B.,2007 "Nanocrystalline calcium phosphate ceramics in biomedical engineering." Materials Science and Engineering: C 27.3: pp. 441-449.

[2.] Lou, Z., Peng, J., Dai, N.,Qiao, J., Yan,Y., Wang, Z., Wang, J., Sun, K., 2012, "High performance $La_3Ni_2O_7$ cathode prepared by a facile sol-gel method for intermediate temperature solid oxide fuel cells"Electrochem. Commun., 22: pp. 97–100.

[3.] Mastuli, M. S., Ansaria, N. S., Nawawia, M. A., Maria, A., 2012, "Effects of cat ionic surfactant in sol-gel synthesis of nano-sized Magnesium Oxide". APCBEE Procedia., 3: pp. 93 – 98.

[4.] Lou, Z., Qiao, J., Yan, Y., Peng, J., Wang, Z., Jiang, T., Sun, K., 2012, "Synthesis and characterization of aluminum-doped perovskites as cathode materials for intermediate temperature solid oxide fuel cells " Electrochem. Commun., 37: pp. 11345-11350.

[5.] Ermokhina, N. I., Nevinsky, V. A., Manorik, P. A., Ilyin, V. G., Shcherbatyuk, N. N., Klymchuk, D. O., Puziy, A. M., 2012, "Synthesis of large-pore mesoporous nano crystalline TiO_2 microspheres″ Materials Letters ., 75: pp. 68–70.

[6.] Parada, K. T., Aguilar, G. V., Mantilla, A.,Valenzuela, M. A., Hernández, E., 2013, "Synthesis and characterization of Ni/Ce–SiO_2 and Co/Ce–TiO_2 catalysts for methane decomposition.″ Fuel cell., 110 : pp. 70–75.

[7.] Chen, L. F., Wang, J. A., Norena, L. E., Aguilar, J., Navarrete, J., Salas, O., 2007, ″Synthesis and physicochemical properties of Zr–MCM-41 mesoporous molecular sieves and Pt/H3PW12O40/Zr–MCM- 41 catalysts.″ . J Solid State Chem., 180: pp. 2958–2972.

[8.] Gonzalez, O. A., Valenzuela, M. A., Wang, J. A., 2006, "Catalytic decomposition of methane over cerium-doped Ni catalysts, in the book ‘‘The hydrogen cycle generation, storage and Fuel cells″. Materials research society symposia proceedings. MRS., 885: pp. 223–238.

[9.] Schacht, P., Ramirez, S., Ancheyta, J., 2009, "CoMo/Ti–MCM-41/alumina catalysts: properties and activity in the hydrodesulfurization (HDS) of dibenzo thiophene (DBT)". Energy Fuels., 23: pp. 4860 – 4865.

[10.] Das, S. K., Bhunia, M. K., Sinha, A. K., Bhaumik, A., 2009, ″Self-assembled mesoporous zirconia and sulfated zirconia nanoparticles synthesized by triblock copolymer as template" . J. Phys. Chem., 113: pp. 8918–8923.

[11.] Liu, S. G., Wang, H., Li, J. P., Zhao, N., Wei, W., Sun, Y. H., 2007, "A facile route to synthesize mesoporous zirconia with ultra high thermal stability,". Mater. Res. Bull., 42: pp. 171–176.

[12.] Wang, K., Morris, M. A., Holmes, J. D., Yu, J., Xu, R., 2009, "Thermally stable nanocrystallised mesoporous zirconia thin films," Micropor. Mesopor. Mater., 117: pp. 161–164.

[13.] Duan, G., Zhang., C. A., Li, X., Yang, L., Lu, X., 2008, "Preparation and characterization of mesoporous zirconia made by using a poly (methylmethacrylate) template ". Nanoscale Res. Lett., 3: pp. 118–122.

[14.] Chen, Y., Lunsford, S. K., Song, Y., Ju, H., Falaras, P., likodimos, V., Kontos, A.G., Dionysiu, D. D., 2011, "Synthesis, characterization and electrochemical properties of mesoporous zirconia nanomaterials prepared by self-assembling sol–gel method with Tween 20 as a template", .Chem. Eng. J., 170: pp. 518–524.

[15.] Okkay, H., Bayramoglu, M., Öksüzömer, M. F, 2013, "$Ce_{0.8}Sm_{0.2}O_{1.9}$ synthesis for solid oxide fuel cell electrolyte by ultrasound assisted co-precipitation method." Ultrasonics Sonochemistry., 20: pp. 978–983.

[16.] Blennow, P., Hjelm, J. Klemens, T., Ramousse, S., Kromp, A., Leonide, A., Weber, A., 2011,"Manufacturing and characterization of metal-supported solid oxide fuel cells". Journal of Power Sources., 196: pp. 7117–7125.

[17.] Shen, C., Shaw, L. L., 2010, "FTIR analysis of the hydrolysis rate in the sol–gel formation of gadolinia-doped ceria with acetylacetonate precursors". J Sol-gel Sci Technol., 53: pp. 571–577.

[18.] Brasil, M. C., Benvenutti, E. V., Gregorio, J. R., Gerbase, A. E., 2005, "Iron acetylacetonate complex anchored on silica xerogel polymer". React Funct Polym., 63: pp. 135–141.

[19.] Krunks, M., Oja, I., Tonsuaadu, K., EsSouni, M., Gruselle, M., Niinisto, L., 2005, "Thermoanalytical study of acetaylacetonate-modified titanium (IV) isopropoxide as a precursor for TiO_2 films". J Therm Analysis Calorim., 80: pp. 483–488.

CHAPTER 4

Physical chemical properties of $Ce_{0.8}Sm_{0.2}Ir_yCo_{1-y}O_{3-\delta}$ (y = 0.03 - 0.04) and preliminary testing as cathode material for low temperature SOFC

Summary

This chapter has been submitted to Materials Research Bulletin and has been structured according to the journal's format. This chapter has also been reformatted to incorporate further comments and corrections by the examiners.

Abstract

A sol gel method was adapted to prepare $Ce_{0.8}Sm_{0.2}Ir_yCo_{1-y}O_{3-\delta}$ (y = 0.03 and 0.04). The materials were characterized using powder XRD, Raman and IR spectroscopy, high resolution transmission electron microscopy and scanning electron microscopy. The materials were then tested for applicability as a cathode in a solid oxide fuel cell. The XRD data showed distinct peaks for samarium doped ceria and iridium oxide, and Raman data confirmed there were perovskite and pyrochlore phases. When tested in a SOFC button cell, the materials calcined at 1000 °C had the highest power density of 0.287 W/cm^2 and 0.222 W/cm^2 at 500 °C for the materials with y = 0.03 and 0.04 respectively.

Key words: Solid Oxide Fuel Cell, Iridium Oxide, Samarium doped Ceria, Oxides; sol-gel chemistry; Raman Spectroscopy; X-Ray diffraction; electrochemical properties

1.0 Introduction

A Solid oxide fuel cell (SOFC) is an electrochemical device that generates electricity and gives off heat as a by-product. SOFCs, have attracted significant attention for several years, because of their high energy efficiency, excellent fuel flexibility, the growing global demand for non-polluting energy conversion systems, and a need for devices that can utilize renewable energy [1 - 4]. However SOFC systems, specifically those operating above 800 °C, also have some disadvantages which include longer start-up and cool down times, specialised and expensive balance of plant material, thermal management issues, and degradation of cell and stack components. Thus the reduction of SOFC operating temperature has become a key issue for the wide scale commercialization of these systems and an area of intensive research [5].

The improvement in the activity of SOFCs that can operate in the temperature range of 300 to 600 °C has increased dramatically in the last few years; however, at lower temperatures the electrolyte conductivity and electrode kinetics decrease significantly [6 - 8]. One way to overcome these drawbacks is to design and synthesize alternative cell materials based on cheaper precursors and using simpler methodologies [6, 8, 9]. In fact, the development of good cathode materials for low temperature SOFCs remains as one of the main challenges in this area, as its sensitivity affect the performance of low-temperature SOFCs.

The quest for low temperature SOFCs has led to the use of a mixture of electro-catalyst electrolyte composites as cathode material. Jiang *et al.* [10] reported that an anode supported fuel cell with a co-synthesized 70 wt. % $Sm_{0.5}Sr_{0.5}CoO_3$ – 30 wt. % $Sm_{0.2}Ce_{0.8}O_{1.9}$ (SSC – SDC 73) composite cathodes exhibited a peak power density of 924 mW/cm^2 at 800 °C. Li *et al.* [11] exploited the fabrication of a porous SDC/SSC composite cathode layer using environmentally friendly water-based ink. The results indicated that the cell with the inkjet printing cathode layer exhibited fantastic electrochemical performance, with a peak power density as high as 940 mW/cm^2 at 750 °C. Wu *et al.* [12] reported a minimum interfacial polarization resistance of 0.21 Ω cm^2 and a power density of 0.24 W/cm^2 at 700 °C for $Sm_{0.5}Sr_{0.5}CoO_{3-\delta}$ and $BaCe_{0.8}Sm_{0.2}O_{3-\delta}$ composites. Wang *et al.* [13] reported a peak

power density of 382 mW/cm^2 at 500 °C for $Ba_{0.5}Sr_{0.5}Co_{0.8}Fe_{0.2}O_{3-\delta}$ + $Sm_{0.2}Ce_{0.8}O_{1.9}$ (SDC) composites. Nie *et al.* [14] also recorded an interfacial resistance of 0.44 Ω cm^2 at 650 °C and a current density of 400 mA/cm^2 at 750 °C for $La_{0.6}Sr_{0.4}Co_{0.2}Fe_{0.8}O_{3-\delta}$ + SDC.

In this study, we synthesized a novel composite cathode material from iridium and cobalt oxide with Samaria-doped ceria (SDC) using a sol gel method. Samarium doped ceria tends to have promising oxygen ion conductivity and good electronic properties at low temperature [6, 9, 15 - 17]. Our previous work demonstrated the excellent potential that iridium, cobalt, iron, and SDC mixed phase materials have as low temperature SOFC materials [18]. In this work, the materials are iron free, and this is of interest since some reports in the literature have shown that cobalt, without the presence of iron, can improve the performance of mixed phase perovskite materials for low temperature SOFC applications [19, 20].

2.0 Experimental methods

2.1 Material synthesis

Cobalt (II) acetylacetonate hydrate, (99 % purity), Samarium (III) acetylacetonate hydrate (99.9 %), Cerium (III) acetylacetonate hydrate, (99.9 % purity), and Pluronic F-127 were purchased from Sigma-Aldrich (Pty) Ltd, South Africa. Iridium (III) acetylacetonate hydrate (98 % purity) was purchased from Alfa Aesar UK and these materials were used as received.

The materials were weighed out in various masses to make the different stoichiometry compositions. For the y = 0.04 composition, 0.0500 g iridium (III) acetylacetonate hydrate, 0.6481 g of Cerium (III) acetylacetonate hydrate, 0.2286 g of Samarium (III) acetyl acetonate hydrate and 0.0394 g of Cobalt (II) acetylacetonate hydrate were used. For the y = 0.03 composition, the masses were 0.0379 g of Iridium (III) acetylacetonate hydrate, 0.6551 g of Cerium (III) acetylacetonate hydrate, 0.2321 g of Samarium (III) acetylacetonate hydrate and 0.0465 g of Cobalt (II) acetylacetonate hydrate. The various perovskite nanocomposite compositions were prepared by weighing out the metal salts and adding a mixture of 50 ml

of ethanol and 15 ml of deionized water. The mixture was then placed in an ultrasound bath (UMC 20, 50 kHz) and sonicated for 30 mins to dissolve all the solids. The mixture was then heated up to 80 °C on a hot plate and stirred at 180 rpm for 30 mins, after which the solution was put in a convection oven for 18 hours at 200 °C to dry completely. Samples were made in triplicate. Samples were then calcined in a muffle furnace (Kittec Squadro 1350) at a heating rate 2 °C/min and a final hold time, at the final temperature for 10 hrs. The samples were calcined at 800 °C, 900 °C, and 1000 °C respectively. The samples were allowed to cool to ambient conditions and then used for further analysis.

The electrolyte (SDC) was synthesized by weighing out 0.200 g of samarium (III) acetyl acetonate and 0.534 g of cerium (III) acetylacetonate into 50 ml of ethanol and 15 ml of deionized water. The mixture was sonicated for 30 mins in an ultrasound bath (UMC 20, 50 kHz), and then placed on a hotplate and heated up to 80 °C at 120 rpm for 20 mins. The sample was then calcined at 850 °C for 5 hrs at a heating rate of 2 °C/min in a muffle furnace (Kittec Squadro 1350). The SDC material formed was then hand mixed with sodium carbonate (Na_2CO_3) in the ratio of 60:40 % before use.

2.2 Characterization

Characterization of the samples was done using powder X-ray Diffraction (XRD), High resolution transmission electron microscopy (HR-TEM), Raman spectroscopy and Fourier transform infrared spectroscopy (FTIR), Scanning electron microscopy (SEM). The powder patterns were recorded using Brucker D8 ADVANCE X-ray diffractometer equipped with a CuKα radiation source operating at 40 kV and a wavelength of 1.5406 Å. For HR-TEM small amounts of the samples were dispersed in ethanol and sonicated using an ultrasound bath, then drop-dried onto a carbon coated copper TEM grid, and examined using a JOEL 2100 HRTEM (200 kV accelerating voltage, beam current of 110 μA and a current density of 2.4 pA/cm^2). For SEM analysis, small amounts of the powders were placed onto double sided carbon tape that was firmly adhered to aluminium stubs and then the supported powder samples were coated with gold for SEM observations on a ZEISS FEGSEM Ultra Plus. For Raman analysis, the spectra were collected on a DeltaNu advantage 532™ Raman

Spectrometer (100 mWNd:YAG laser with an excitation wavelength of 532 nm). FTIR analysis of the samples was done by using an ATR accessory in a Perkin Elmer 1200 FTIR.

2.3 Button cell fabrication

Anode powder consisting of 60 wt % NiO and 40 wt % SDC were mixed and pressed using a 20 Ton press and a 13 mm die kit. The electrolyte powder (SDC + Na_2CO_3) was then added on top of the anode disc, and then the cathode powder was placed on top of the electrolyte powder and finally the materials were pressed together using 15 Ton pressure to form a trilayer structure. Thus the button cell consisted of NiO-SDC|SDC + Na_2CO_3| $Ce_{0.8}Sm_{0.2}Ir_yCo_{1-y}O_{3-\delta}$ and the single cell had an active surface area of 1.342 cm^2. The cell was then heated up to 500 °C for 2 hrs at a heating rate of 5 °C/min in air to densify the electrolyte. The sintering temperature was used because the addition of Na_2CO_3 to the electrolyte improves its densification at lower temperatures [21].

2.4 Electrochemical performance test

The fabricated cells were mounted in an open flange test set-up from Fiaxell SOFC Technologies™ with platinum mesh as the current collector and distributor connected to the cells. The test-bed was placed on a Kittec Squadro muffle furnace and connected to a steady flow of air on the cathode and humidified hydrogen gas on the anode side. Current and voltage from the cells were measured with a Nuvant™ Powerstat potentiostat and galvanostat. The measurements were taken between the temperatures of 300 °C - 500 °C and the ionic conductivity was calculated using the Equation [22].

$$\sigma = \frac{l}{RS} \tag{1}$$

where, l is the electrolyte thickness, S is electrode area of the electrolyte surface and R is resistance in ohms (cell resistance).

The activation energy and the Electrical conductivity were calculated using the Arrhenius relationship in Equation 2 [22].

$$\sigma = \sigma^{o}\, exp\left[\frac{E_a}{kT}\right] \quad (2)$$

where, E_a is activation energy of conduction, T is absolute temperature, σ^o is pre-exponential factor and k is the Boltzmann Constant. The Polarization curves were recorded between 300 –500 °C and the potentiostatic durability testing was carried out in order to assess long-term static stability of the cell.

3.0 Results and discussions

3.1 Powder X-ray diffraction analysis

Figure 1 shows representative XRD patterns of the perovskite material (y = 0.03 - 0.04) composition, calcined at 800 °C, 900 °C and 1000 °C. The XRD pattern displayed characteristic peaks for the cubic fluorite structure of SDC [22 - 24]. The SDC phases were observed at 2θ values of 28.44°, 47.33°, 56.19°, 88.22° and 95.20° indexed to (111), (220), (311), (422) and (511) respectively.

Iridium oxide structure peaks were noticed at 2θ values of 34.71°, 58.90°, 69.22° and 77.03° indexed to (101), (200), (301) and (310) respectively. For the CSIC samples after calcination, the average lattice parameter for CeO_2 phase and IrO_2 phase are shown in Table 1 using Rietveld, profile matching and integrated intensity refinement of X-ray diffraction data (Full Prof. 2k (Version 5.70)). The lattice parameter of the cathode material was different from the lattice parameter of CeO_2 (JCPDS file No. 00-034-0394) which confirms the formation of a new compound. There were no separate cobalt oxide peaks observed, and this could be due to the cobalt ion substituting into either the iridium oxide or the SDC phase. Previous work by Dreifus *et al* [26] has shown that Co^{2+} can substitute Ir^{4+} in the iridium oxide lattice and Yao *et al.* [27] reported on the formation of solid solution with cobalt and SDC [26]. The crystallite sizes for the composites with y = 0.03 were calculated to be 21.80 nm, 20.41 nm and 18.45 nm for the samples calcined at 1000 °C, 900 °C and 800 °C respectively. The composites with the y = 0.04 composition had crystallite sizes of 22.32 nm, 21.09 nm, and 14.92 nm for the samples calcined at 1000 °C, 900 °C and

800 °C. In general, the crystallite sizes increased as the calcination temperature was increased and is an expected result.

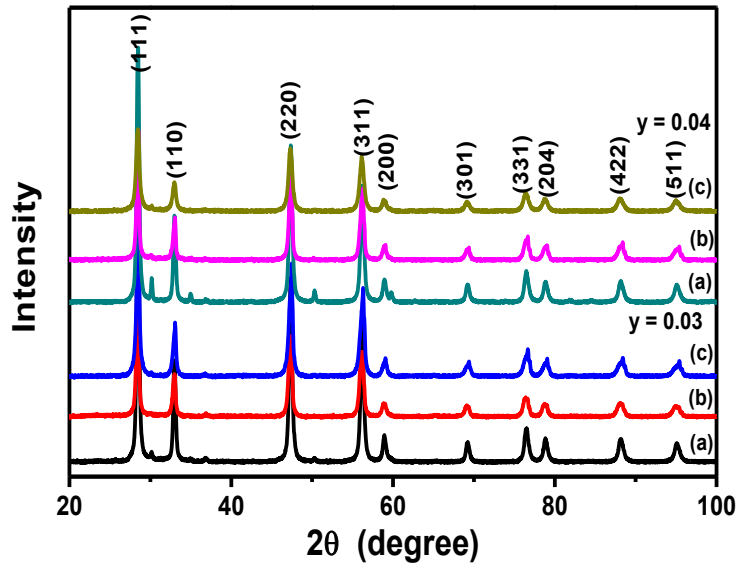

Figure 1: XRD patterns of the CSIC materials with y = 0.03 composition calcined at (i) 1000 °C (ii) 900 °C and (iii) 800 °C, and the y = 0.04 composition calcined at (iv) 1000 °C (v) 900 °C and (vi) 800 °C.

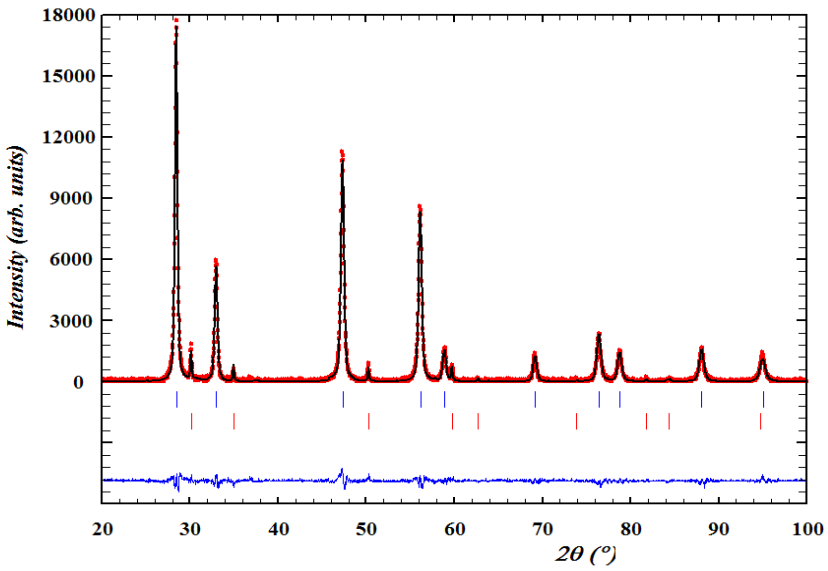

Figure 1b: The observed and calculated (Rietveld analysis) XRD patterns of A1 (y = 0.04) calcined at 1000 °C.

Table 1: The result of Rietveld refinement of XRD patterns of A1, B1, C1, A2, B2 and C2

	Phases	Y = 0.04			Y =0.03		
		(1000 °C)	(900 °C)	(800 °C)	(1000 °C)	(900 °C)	(800°C)
a **(Å)**	CeO_2	5.427	5.428	5.432	5.427	5.443	5.431
	IrO_2	5.128	5.135	5.130	5.129	5.128	5.131
Density (g/cm^3)	|CeO_2	7.131	7.330	7.114	7.133	7.070	7.050
	IrO_2	6.562	6.537	6.555	6.561	6.562	6.560
Cell volume (cm^3)	CeO_2	159.905	159.98	160.29	159.86	161.29	160.27
	IrO_2	134.905	135.42	135.05	134.93	134.91	134.90

3.2 FTIR analysis

Figure 2 shows the FTIR spectra of composites with (a) y = 0.03 and (b) y = 0.04 calcined at 800 °C, 900 °C and 1000 °C respectively. The stretching vibrations observed in the spectra between $1000cm^{-1}$ – $1100cm^{-1}$ were attributed to Ce-O-Ir or Sm-O-Co or Ce-O-Co (M-O-M) stretching vibrations. Samarium doped ceria, after calcination, does not typically display any FTIR peaks within the region 1000 – 1100 cm^{-1} [1]. The absorption bands ~470 – 680 cm^{-1} indicate the presence of metal oxides, these bands are usually observed with perovskite structure containing materials with metals such as doped ceria [28 - 30].

According to Waldron [31], the vibration of a unit cell of the cubic spinel can be constructed in the tetrahedral (A) sites and octahedral (B) sites. Therefore the absorption bands at 554 cm^{-1}, 672 cm^{-1}, 673 cm^{-1}, 675 cm^{-1}, 670 cm^{-1}, 670 cm^{-1} and 666 cm^{-1} are tentatively assigned to the vibrations of the tetrahedral metal – oxygen (M – O) bond and the absorption band at 472 cm^{-1}, 474 cm^{-1}, 478 cm^{-1}, 480 cm^{-1}, 482 cm^{-1} and 488 cm^{-1} are due to the metal–oxygen (M - O) vibrations in the octahedral sites. The change in band positions is expected because of the variation in the compositionsof the materials and the difference in the M^{+}– O_2^{-} distances in the tetrahedral and octahedral sites.

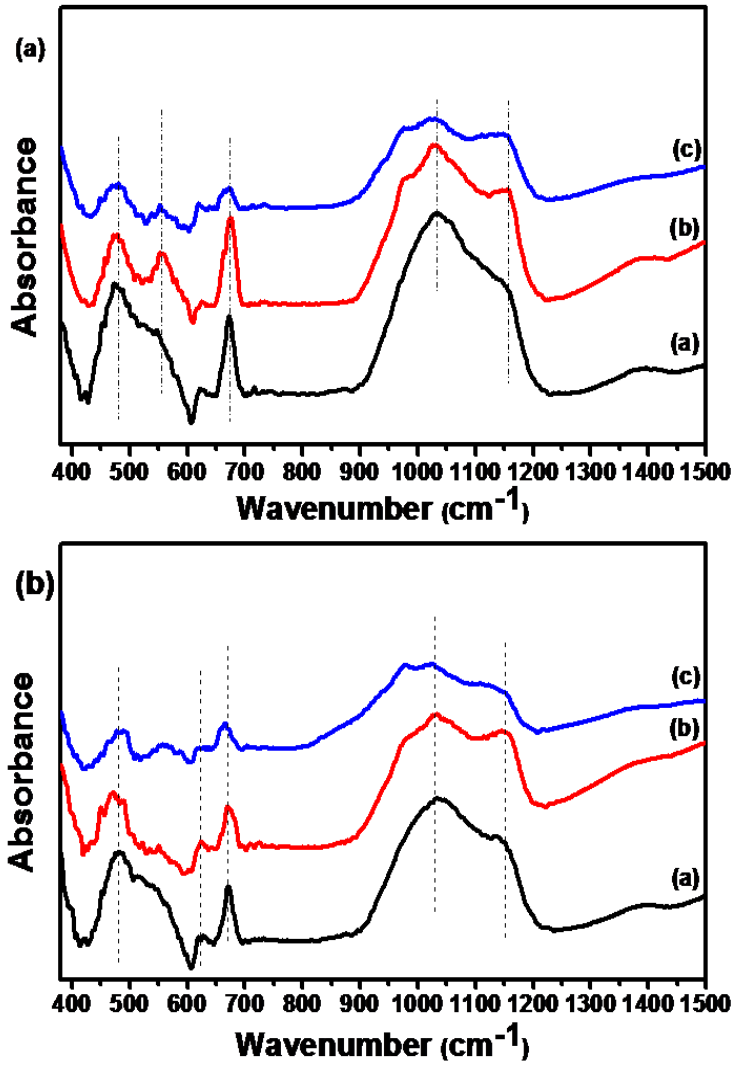

Figure 2: (A) presents the FTIR Spectra of the CSIC materials with the y= 0.03 composition calcined at (i) 1000 °C (ii) 900 °C and (iii) 800 °C) and (B) displays the FTIR spectra of the y = 0.04 composition calcined at (iv) 1000 °C (v) 900 °C and (vi) 800 °C.

3.3 Raman analysis

Figure 3 shows the Raman spectra of the composite with y = 0.03 calcined at (a) 1000 °C (b) 900 °C and (c) 800 °C. Samarium doped ceria has a main peak (F_{2g} vibration mode) at 460 cm^{-1}[23, 24], and the peak is present but shifted slightly at 800 °C (462 cm^{-1}), 900 °C

(459 cm^{-1}), and 1000 °C (465 cm^{-1}). The red shift is indicative of changes within the SDC fluorite structure; specifically, incorporation of Ce^{3+} cations and thus increase in oxygen vacancies and defects [32]. Co_3O_4 A_{1g} vibrational modes were observed at 686 cm^{-1} (800 °C), 691 cm^{-1} (900 °C), and 697 cm^{-1} (1000 °C).

These shifts with the Co_3O_4 A_{1g} mode are attributed to the different calcination temperatures. For the samples calcined at 800 °C, the minor peak at 314 cm^{-1} could indicate that some small amount of the iridium and samarium may have formed a pyrochlore phase [33], and the small peak at 818 cm^{-1} could be due to oxygen defects from the mixed phase metal oxides [34]. The disappearance of the peak at 314 cm^{-1} at higher calcination temperatures and the slight increase in the intensity of the peaks at 831 cm^{-1} (900 °C) and 826 cm^{-1} (1000 °C) are a further indication that the minor pyrochlore phase has transitioned to a defect fluorite structure. Several authors have reported on pyrochlore to defective fluorite transitions [34, 35].

The material with the composition y = 0.04 (Figure 3 (b)) showed similar peaks to the y = 0.03 composition at all temperatures except the sample calcined at 900 °C, which showed an interesting transition. The F_{2g} vibration mode around 460 cm^{-1} for samarium doped ceria decreases substantially, and a new peak at 552 cm^{-1} is observed, which indicates the new peak is not a simple substitution of the Ce^{4+} for trivalent cations in the SDC fluorite structure, as was the case reported by Luo *et al.* [24]. Instead, the appearance of the peaks at 552 and 831 cm^{-1} are indicative of pyrochlore phases due to the processing temperature and iridium content.

This result further supports the earlier discussions regarding the pyrochlore to a defect fluorite structure transition observed with the lower iridium content samples (y = 0.03). Finally, regarding the Raman spectra, a pure pyrochlore structure has six Raman active modes. These are, A_{1g}, E_g and $4T_{2g}$ [34, 35] and Hasegawa *et al.* [33] observed a weak T_{2g} Raman peak for $SmIr_2O_7$ pyrochlore at 549 cm^{-1}. The shift and increased intensity observed with the sample y = 0.04 calcined at 900 °C can be attributed to the presence of various other dopant ions [35] and the complexity of the different phases present.

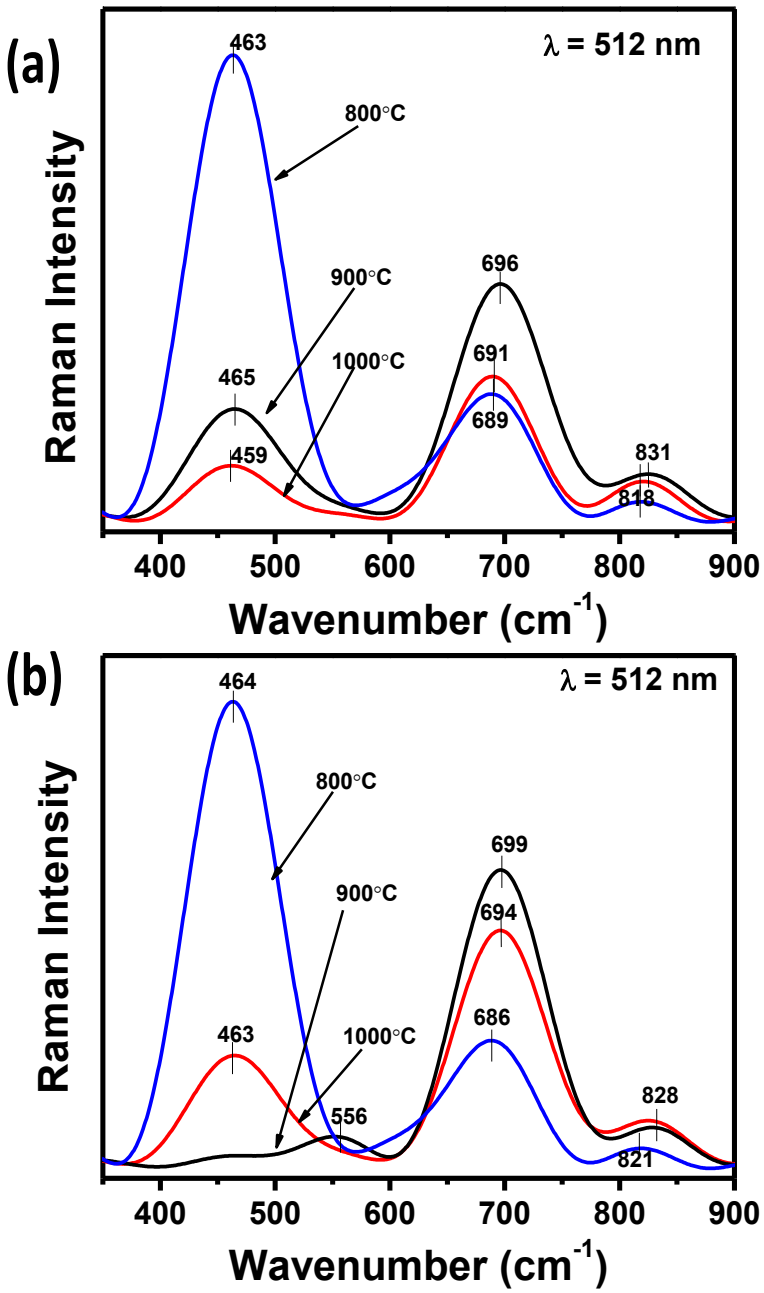

Figure 3: Panel (A) presents the Raman spectra for the CSIC materials with a composition of y = 0.03 calcined at 1000 °C, 900 °C and 800 °C. Panel (B) is the Raman spectra for the y = 0.04 composition calcined at 1000 °C, 900 °C and 800 °C.

3.4 HRTEM analysis

Figure 4 shows the HRTEM images for the various samples. The morphology for all the samples showed some differences in shape and sample contrast. Differences in contrast are indicative of changes in amorphous and crystalline regions within the sample and the differences seen with the HRTEM images as the samples are calcined form 800 - 1000 °C can be attributed to changes in the materials crystalline phases, which correlates with the phase changes noted and commented on in the Raman section.

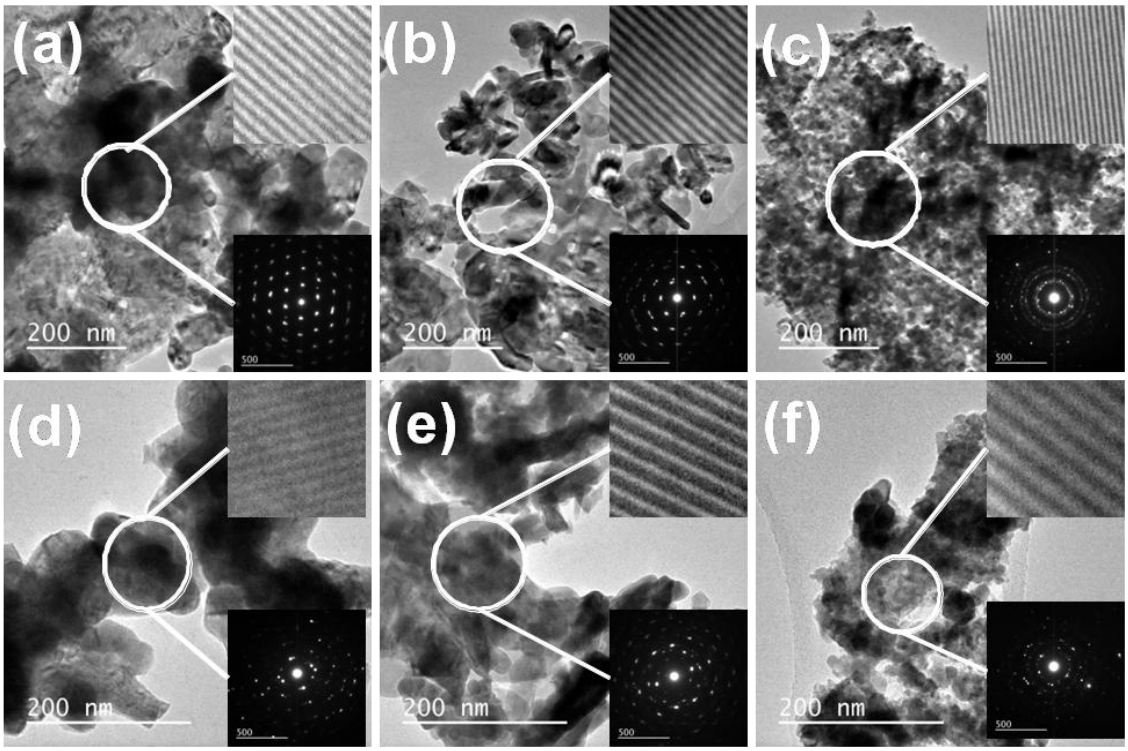

Figure 4: HRTEM images with the lattice fringes and selected area electron diffraction patterns for the CSIC materials with y = 0.03 calcined at (a) 1000 °C, (b) 900 °C, and (c) 800 °C. Images (d), (e), and (f) are for the y = 0.04 samples calcined at 1000, 900, and 800 °C respectively.

For Figure 4 (a) the measured distance between the fringes shown in the inset was 0.147 nm indexed to (310) plane, for Figure 4 (b) the fringes in the inset were 0.110 nm indexed to (422) plane, and in Figure 4 (c) the distance between the fringes were 0.091 nm and

indexed to (402) plane. The distance between the fringes shown in the inserts in Figure 4 (d), (e), and (f) were measured and found to be 0.200 nm indexed to (220), 0.254 nm indexed to (002) and 0.257 nm indexed to (002) planes. These correlates well with the XRD patterns presented and are identified as the SDCand IrO_2 structures. The selected area electron diffraction patterns are provided as a second inset within the HRTEM images and differ slightly in terms of the intensity of the rings and spots displaying a decrease in crystallinity as the calcination temperature decreases.

3.5 SEM Observations

The morphology of the materials synthesized are shown in Figure 5, and show that the metal oxides accumulated to form agglomerates with differing pore sizes, and spaces between the various particles.

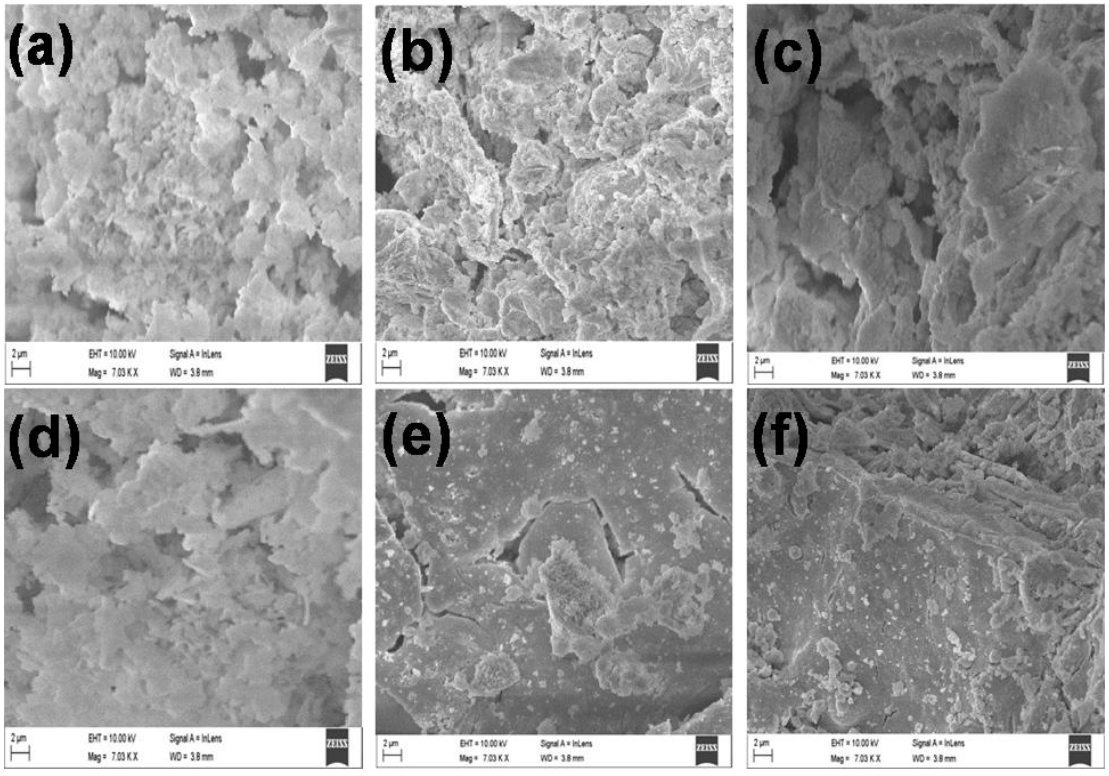

Figure 5: SEM images of the materials with y = 0.03 calcined at (a) 1000 °C, (b) 900 °C and (c) 800 °C. For y = 0.04, samples calcined at 1000 °C, 900 °C and 800 °C are presented in panels (d), (e), and (f) respectively.

The displayed morphology of the particles show a general trend where the samples with y = 0.03 composition displayed bigger pore spaces with the calcination temperature decreasing from 1000 °C (Figure 5 (a)), 800 °C (Figure 5 (c)). Whereas the y = 0.04 composition showed a different trend with the smallest spaces between agglomerates observed with the sample calcined at 900 °C (Figure 5 (e)), and the largest spaces seen with the sample calcined at 1000 °C (Figure 5 (d)). This observation can be attributed to the change in the materials phases as per the Raman observations and discussion.

3.6 Electrochemical properties

The materials electrochemical properties were then tested by using the NiO/SDC as the anode SDC/$NaCO_3$ as the electrolyte and CSIC as cathode in a SOFC button cell. The asymmetric cell was tested using a Kittec Squadro device. Compressed air with flow rate of 50 m^3/min and humidified hydrogen with a flow rate of 200 m^3/min was passed through the cell and the cell was tested for 14 hrs.

3.6.1 Polarization curve

Recently, Hanna *et al*. [4] reviewed in detail the current state of knowledge on the electrochemical characterizations and physical-chemical property relationships regarding SOFCs. One key aspect is polarization curves. Polarization curves provide crucial fundamental information on how a system deviates from ideal behaviour and the potential to utilize a material in a fuel cell. The polarization curves for the samples with y = 0.03 and y = 0.04 compositions calcined at 800 °C - 1000 °C are shown in Figures 6 and 7 respectively. These were obtained in humidified hydrogen and compressed air at temperature intervals of 300, 400 and 500 °C. From Figure 6 the values for the OCV dropped, as expected, as the button cell was tested at 300, 400 and 500 °C respectively.
The lowest OCV value observed was 0.81 V with the sample calcined at 1000 °C and tested at 500 °C (Figure 6), and the highest OCV value noted was 0.93 V with the sample calcined at 900 °C and tested at 300 °C (Figure 7).

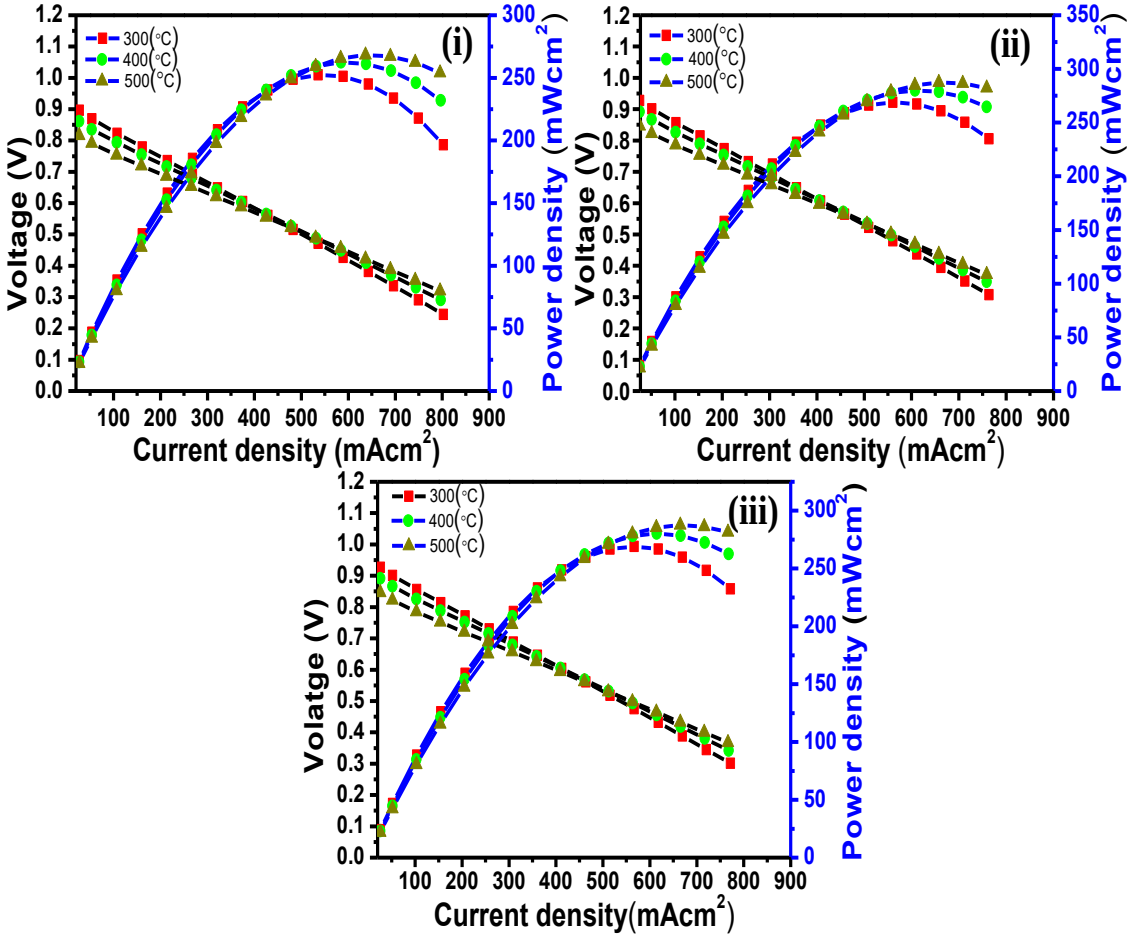

Figure 6: Polarisation curves for the y = 0.03 materials calcined at (a) 1000 °C, (b) 900 °C and (c) 800 °C all measured at 300 °C, 400 °C and 500 °C.

These values are below the theoretical Nernst potential, which can be attributed to either the non-optimal partial pressures of the gases on the electrodes [4], the presence of pinholes within the electrolyte or poorly formed electrolytes [11]. The polarization curves in Figure 6 show that the y = 0.03 compositions do not have any large differences in the gradients of the voltage-current density curves at the three temperatures. However, there are some differences at low current density, and since this the region of the polarization curve that is dominated by losses due to activation overpotentials [4], the differences are ascribed to the different temperatures.

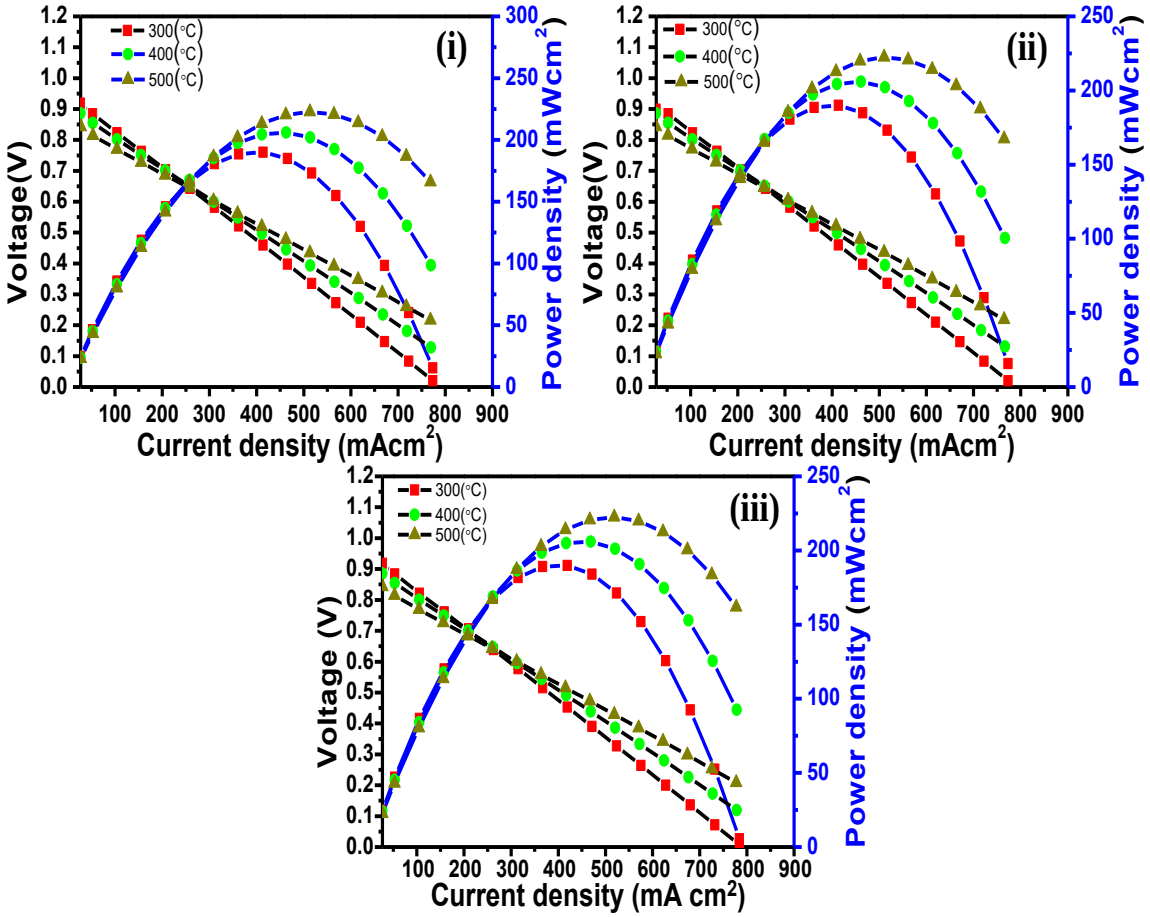

Figure 7: Polarisation curve for the y = 0.04 materials calcined at (a) 1000 °C, (b) 900 °C and (c) 800 °C all measured at 300 °C, 400 °C and 500 °C.

The maximum power densities for the y = 0.03 compositions were observed at 500 °C test temperature and the values were 268.2 mW/cm^2, 287.3 mW/cm^2, and 287.6 mW/cm^2 for samples calcined at 1000, 900 and 800 °C respectively. The samples did show relatively stable performance at 500 °C for 3600 mins. At low current densities, similar trends are seen with the composition y = 0.04 materials (Figure 7). However, overall the samples with y = 0.04 have a larger gradient with the voltage-current density curves. The decrease in the central part of the polarization curve is usually ascribed to Ohmic losses [4], and the two composition show some differences, with the y = 0.04 composition having larger differences with calcination temperature, when compared to the y = 0.03 composition.

The decreased concentration of cobalt in the y = 0.04 composition clearly has a slight detrimental effect on the performance of the SOFC electrode material. This is further highlighted by the drop to zero voltage at 300 °C with the y = 0.04 composition (Figure 7), and the non-zero value for the y = 0.03 materials. Furthermore, the observed power densities were lower for the y = 0.04 composition, with values of 222.8 mW/cm^2, 222.5 mW/cm^2 and 222.6 mW/cm^2, for the samples calcined at 1000, 900, and 800 °C respectively. Similar to the y = 0.03 composition, the samples with the y = 0.04 stoichiometry did show relatively stable performance for 3600 minutes.

However, it should be noted that a greater amount of cobalt, and less iridium, within these SDC materials seems to decrease concentration polarzation losses. Liu *et al.* [17] reported on micro-tubular SOFC systems with power densities of 50 mW/cm^2 at 500 °C. Although our current materials are a bit of an improvement on what has been reported, they still showed a lower performance than our previous report of 400 mW/cm^2 at 500 °C [18]. Thus it would seem the removal of iron from the materials actually decreases performance.

3.6.2 Area specific resistance

Figure 8 shows the normalized area specific resistance (ASR) of the single cells for the composites with y = 0.03 and 0.04. For each composition, the ASR decreased with an increase in the SOFC test temperature. The area specific resistance can be related to the material thickness and is a measure of the ionic and electronic conductivity [4]. The ASRs are calculated from the slope of the substantial linear portion (in the centre) of the I-V curve, where the Ohmic resistance is dominant [4]. The ASR is directly related to the design of the cell, anode, electrolyte and cathode properties and the assembly process used to make the single cell [4, 11]. The ASR values for the y = 0.03 (Figure 8 (A)) show some slight differences between 300 to 500 °C and this may imply the materials will have a similar operational profile in a fully functional SOFC system. The ASR for the y = 0.04 composition (Figure 8 (B)) display some interesting variations. At the highest operating temperatures, 500 °C, the sample calcined at 900 °C had the lowest ASR values. This can be attributed to the mixed perovskite pyrochlore phase observed with the Raman analysis.

At the mid operating temperature in this study, 400 °C, the mixed phase materials have the lower ASR, which are the materials with y = 0.04 calcined at 900 and 800 °C respectively. It is only at the lowest temperature used to test SOFC viability did the sample calcined at 1000 °C have the lowest ASR. These observations suggest that the mixed phase materials may have better oxygen ion conductivity at 500 °C, and 400 °C, and merits further investigation.

The ASR values obtained in this work are compared with selected examples from the literature, and the values are tabulated in Table 1. Using $PrBaCo_2O_{5+x}$ materials, Wang *et al.* [20] reported on slightly lower ASR and power density values than those in the current work, whereas Chen *et al.* [36] reported on a lower ASR, and a slightly lower power density when compared to the best cathode in this work.

The lower ASR value in the work by Chen *et al.* [36] *can* be ascribed to the impregnation technique used by the authors. Other examples with cobalt based cathode materials include work by Peters *et al.* [37], Wang *et al.* [38] and Hayd *et al.* [19]. The higher ASR with the work of Peters *et al.* is most likely due to the GCO/8YSZ electrolyte used, and the much lower value with the work with Hayd *et al.* [19] can be due to the optimized microstructure of the SOFC assembled in that body of work.

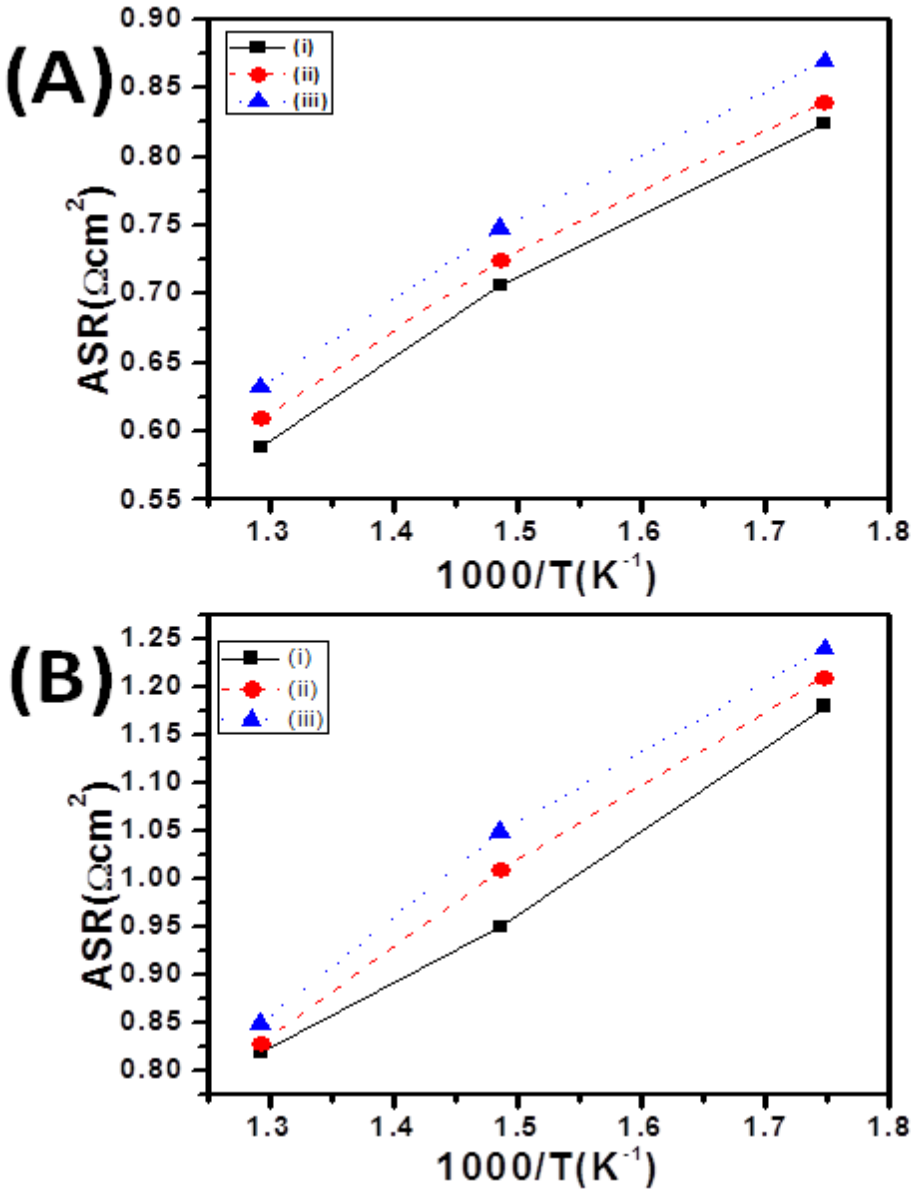

Figure 8: Panel (A) The Arrhenius plot of the ASR of the CSIC materials with y = 0.04 calcined at (i) 1000 °C, (ii) 900 °C, and (iii) 800 °C. Panel (B) is a similar plot for the y = 0.03 materials calcined at (i) 1000 °C, (ii) 900 °C, and (iii) 800 °C.

Figure 9 shows the SEM image of the button cell cross section before and after testing. The electrolyte does show some porosity and this correlates well with the low OCV values reported. However, one interesting aspect is the simple button cell assembly used in this

study produces comparable values, as shown in Table 1, and highlights that these cathode materials can be optimized further in the SOFC assembly process.

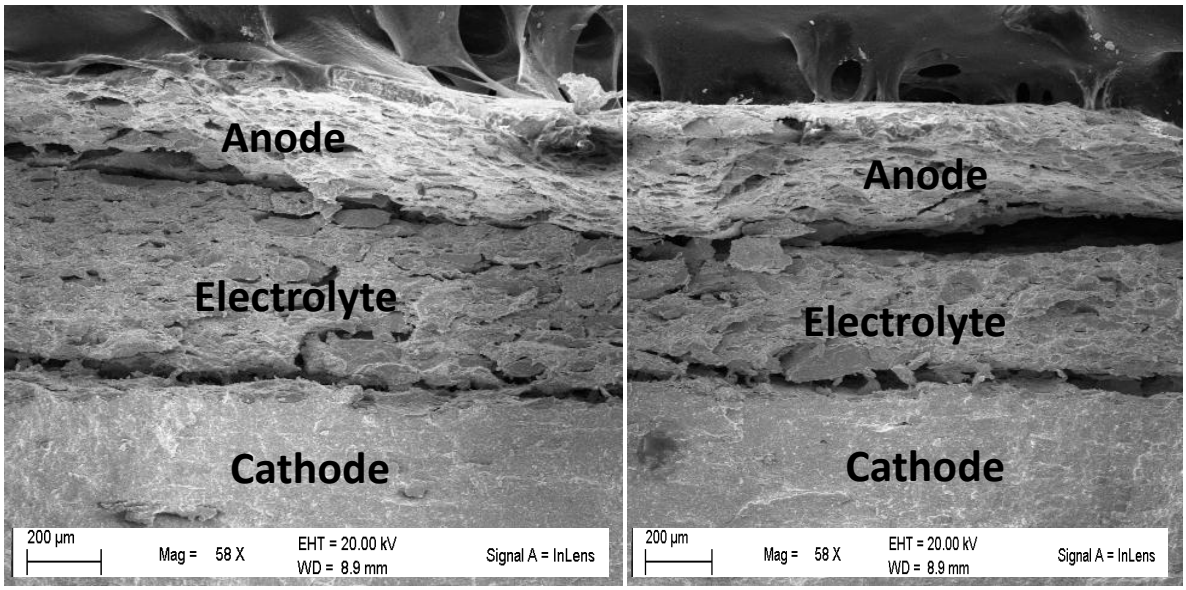

Figure 9: SEM micrographs of the single cell of the material calcined at a 1000 °C (x = 0.03) before (a) and after (a) cell testing at 500 °C.

Table 1: Comparison of the ASR values and power density obtained with the cathode materials tested at 500 °C with selected materials from the literature.

ASR (Ω cm^2)	Power Density (W/cm^2)	Cell Components			References
		Cathode	Electrolyte	Anode	
0.54	0.20	$PrBaCo_2O_{5+x}$	SDC	Ni-SDC	24
0.16	0.25	Impregnated $PrBaCo_2O_{5+x}$	SDC	Ni-SDC	40
1.10	-	$La_{0.5}Sr_{0.5}CoO_{3-\delta}$	GCO/8YSZ	Ni-SDC	41
0.60	-	$La_{0.5}Sr_{0.5}CoO_{3-\delta}$	GCO	Ni-SDC	42
0.25	-	$La_{0.6}Sr_{0.4}CoO_{3-\delta}$	GCO	Ni-SDC	23
0.79	0.24	Li-Ni-Co oxides	SDC/Na_2CO_3	NiO	43
0.58	0.28	CSIC (1000 °C) (y = 0.03)	SDC/Na_2CO_3	Ni-SDC	This work
0.82	0.22	CSIC (1000 °C) (y = 0.04)	SDC/Na_2CO_3	Ni-SDC	This work

4.0 Conclusions

Sol gel technique was successfully adapted to synthesize a samarium doped ceria with iridium and cobalt oxides. The powder XRD patterns did not show any distinct cobalt oxide phases, but only samarium doped ceria and iridium oxide. The Raman data revealed that these materials form complex oxide structures with perovskite, pyrochlore and defective fluorite phases. The initial electrochemical tests showed slight differences in the maximum power density for the different calcined samples. There were some small differences between the different compositions, with the sample with the y = 0.03 composition calcined at 800 °C having the highest power density of 287.6 mW/cm^2 at 500 °C, and the sample with y = 0.04 calcined at 1000 °C having a maximum power density of 222.7 mW/cm^2 at 500 °C. The materials merit further investigation and optimisation studies using plasma sintering, pore formers, thin electrolytes to improve the power density, and studies on their performance with hydrocarbon based fuels should be carried out.

Acknowledgements

The authors thank the University of KwaZulu-Natal for a partial bursary support, ESKOM - TESP and NRF South Africa (Thuthuka Grant No: 76318) for their support.

References

[1] A. Arabaci, Effect of Sm and Gd dopants on structural characteristics and ionic conductivity of ceria, Ceram. Int., 2015, **41**, 5836-5842.

[2] J. Liu, Z. Zhao, Y. Chen, C. Xu, A. Duan, G. Jiang, Different valent ions-doped cerium oxides and their catalytic performances for soot oxidation, Catal. Today, 2011, **175**, 117-123.

[3] S. Wolf, R. Adam, L. Fuhrmann, S. A. Ansar, K. A. Friedrich, Characterization of electrolyte layers of plasma-sprayed metal supported solid oxide fuel cells Solid State Ionics, 2013, **243**, 30-35.

[4] J. Hanna, W. Y. Lee, Y. Shi, A. F. Ghoniem, Fundamentals of electro-and thermochemistry in the anode of solid-oxide fuel cells with hydrocarbon and syngas fuels, Prog. Energy Combust. Sci., 2014, **40**, 74-111.

[5] E. D. Wachsman, S. C. Singhal, Solid Oxide Fuel Cell Commercialization, Research and Challenges, Electrochem. Soc. Interface, 2009, **18**, 38-43.

[6] W. Tan, L. Fan, R. Raza, M. Ajmal Khan, B. Zhu, Studies of modified lithiated NiO cathode for low temperature solid oxide fuel cell with ceria-carbonate composite electrolyte, Int. J. Hydrogen Energy, 2013, **38**, 370-376.

[7] Y. B. Go, A. J. Jacobson, Solid solution precursors to gadolinia-doped ceria prepared via a low-temperature solution route, Chem. Mater., 2007, **19**, 4702- 4709.

[8] K. T. Lee, E. D. Wachsman, Role of nanostructures on SOFC performance at reduced temperatures, Mater. Res. Bull., 2014, **39**, 783-791.

[9] C. Veranitisagul, A. Kaewvilai, W. Wattanathana, N. Koonsaeng, E. Traversa, A. Laobuthee, Electrolyte materials for solid oxide fuel cells derived from metal complexes: Gadolinia-doped ceria, Ceram. Int., 2012, **38**, 2403-2409.

[10] W. Jiang, B. Wei, Z. Lü, Z. H. Wang, X. B. Zhu, L. Zhu, Co-synthesis of $Sm_{0.5}Sr_{0.5}CoO_3$-$Sm_{0.2}Ce_{0.8}O_{1.9}$ composite cathode with enhanced electrochemical property for intermediate temperature SOFCs, Fuel Cells, 2014, **14**, 966-972.

[11] C. Li, H. Chen, H. Shi, M. O. Tade, Z. Shao, Green fabrication of composite cathode with attractive performance for solid oxide fuel cells through facile inkjet printing, J. Power Sources, 2015, **273**, 465-471.

[12] T. Wu, R. Peng, C. Xia,$Sm_{0.5}Sr_{0.5}CoO_{3-\delta}$–$BaCe_{0.8}Sm_{0.2}O_{3-\delta}$ composite cathodes for proton-conducting solid oxide fuel cells, Solid State Ionics, 2008, **179**, 1505-1508.

[13] K. Wang, R. Ran, W. Zhou, H. Gu, Z. Shao, J. Ahn, Properties and performance of $Ba_{0.5}Sr_{0.5}Co_{0.8}Fe_{0.2}O_{3-\delta}$+$Sm_{0.2}Ce_{0.8}O_{1.9}$ composite cathode, J. Power Sources, 2008,**179**, 60-68.

[14] L. Nie, M. Liu, Y. Zhang, M. Liu, $La_{0.6}Sr_{0.4}Co_{0.2}Fe_{0.8}O_{3-\delta}$ cathodes infiltrated with samarium-doped cerium oxide for solid oxide fuel cells, J. Power Sources, 2010, **195**, 4704-4708.

[15] V. Esposito, E. Traversa, Design of electroceramics for solid oxides fuel cell applications: playing with ceria, J. Am. Ceram. Soc., 2008, **91**, 1037-1051.

[16] N. Jaiswal, D. Kumar, O. Parkash, S. Upadhyay, Ca^{2+} and Sr^{2+} co-doped ceria/ carbonates nanocomposites for low temperature solid oxide fuel cells: Composite effect, Ceram. Int., 2015, **41**, 15162-15169.

[17] J. Xiao, W. Sun, Z. Tao, Z. Zhu, W. Liu, Fabrication and electrochemical characterization of anode-supported microtubular solid oxide fuel cells based on $Ce_{0.8}Sm_{0.2}O_{2-\delta}$ Electrolytes, Int. J. Appl. Ceram. Technol., 2012, **9**, 1064-1070.

[18] C. B. Njoku, P. G. Ndungu, Synthesis and characterization of novel $Ce_{0.8}Sm_{0.2}Fe_{0.9}Ir_{0.03}Co_{0.07}O_{3-\delta}$ perovskite material and possible application as a cathode for low–intermediate temperature SOFCs, Mater. Res. Bull., 2015, **68**, 100-108.

[19] J. Hayd, L. Dieterle, U. Guntow, D. Gerthsen, E. Ivers-Tiffée, Nanoscaled $La_{0.6}Sr_{0.4}CoO_{3-\delta}$ as intermediate temperature solid oxide fuel cell cathode: Microstructure and electrochemical performance, J. Power Sources, 2011, **196**, 7263-7270.

[20] Y. Wang, H. Zhang, F. Chen, C. Xia, Electrochemical characteristics of nano-structured $PrBaCo_2O_{5+x}$ cathodes fabricated with ion impregnation process, J. Power Sources, 2012, **203**, 34-41.

[21] L. Zhang, R. Lan, A. Kraft, S. Tao, A stable intermediate temperature fuel cell based on doped-ceria–carbonate composite electrolyte and perovskite cathode, Electrochem. Commun., 2011,**13**, 582-585.

[22] H. Okkay, M. Bayramoglu, M. Faruk Öksüzömer, $Ce_{0.8}Sm_{0.2}O_{1.9}$ synthesis for solid oxide fuel cell electrolyte by ultrasound assisted co-precipitation method, Ultrason. Sonochem., 2013, **20**, 978-983.

[23] M. Guo, J. Lu, Y. Wu, Y. Wang, M. Luo, UV and visible raman studies of oxygen vacancies in rare-earth-doped ceria, Langmuir, 2011, **27**, 3872-3877.

[24] L. Li, F. Chen, J. Q. Lu, M. F. Luo, Study of defect dites in $Ce_{1-x}M_xO_{2-\delta}$ (x = 0.2) solid solutions using raman spectroscopy, J. Phys. Chem. A , 2011, **115**, 7972-7977.

[25] M.Johnsson, P. Lemmens, Crystallography and chemistry of perovskites, Handbook of magnetism and advanced magnetic materials (2007).

[26] D. Von Dreifus, A. J. A. de Oliveira, A. V. do Rosario, E. C. Pereira,Magnetic and structural characterization of IrO_2 and Co: IrO_2 samples synthesized via pechini method, J Supercond Nov Magn, 2013, **26**, 2319-2321.

[27] H. C. Yao, X. L. Zhao, X. Chen, J. C. Wang, Q. Q. Ge, J. S. Wang, Z. J. Li, Processing and characterization of CoO and Sm_2O_3 codoped ceria solid solution electrolyte, J. Power Sources, 2012, **205**, 180-187.

[28] A. Arabaci, Ö. Serin,Characterization of Sm-doped ceria ceramics synthesized by two different methods, J. of Materi Eng and Perform, 2015, **24**, 2730-2737.

[29] Y. Tao, J. Shao, J. Wang, W.G. Wang,Morphology control of $Ce_{0.9}Gd_{0.1}O_{1.95}$ nanopowder synthesized by sol–gel method using PVP as a surfactant, J. Alloys Compd., 2009, **484**, 729-733.

[30] K. C. Anjaneya, G. P. Nayaka, J. Manjanna, G. Govindaraj, K. N. Ganesha, Preparation and characterization of $Ce_{1-x}Sm_xO_{2-\delta}$ (x= 0.1– 0.3) as electrolyte material for intermediate temperature SOFC, Solid State Sci., 2013, **26**, 89-96.

[31] R. D. Waldron,Infrared spectra of ferrites, Phys. Rev., 1955, **99**, 1727-1735.

[32] T. S. Nguyen, G. Postole, S. Loridant, F. Bosselet, L. Burel, M. Aouine, L. Massin, P. Gelin, F. Morfin, L. Piccolo, Ultrastable iridium–ceria nanopowders synthesized in one step by solution combustion for catalytic hydrogen production, J. Phys. Chem. A, 2014, **2**, 19822-19832.

[33] T. Hasegawa, N. Ogita, K. Matsuhira, S. Takagi, M. Wakeshima, Y. Hinatsu, M. Udagawa, Raman scattering study in iridium pyrochlore oxides, Journal of Physics: Conference Series, 2010, **200**, 012054.

[34] M. de los Reyes, K. R. Whittle, Z. Zhang, S. E. Ashbrook, M. R. Mitchell, L.Y. Jang, G. R. Lumpkin, The pyrochlore to defect fluorite phase transition in $Y_2Sn_{2-x}Zr_xO_7$, RSC Adv., 2013, **3**, 5090-5099.

[35] F. N. Sayed, V. Grover, K. Bhattacharyya, D. Jain, A. Arya, C. G. S. Pillai, A. K. Tyagi, $Sm_{2-x}Dy_xZr_2O_7$ pyrochlores: probing order−disorder dynamics and multifunctionality, Inorg. Chem., 2011, **50**, 2354-2365.

[36] D. Chen, R. Ran, K. Zhang, J. Wang, Z. Shao, Intermediate-temperature electrochemical performance of a polycrystalline $PrBaCo_2O_{5+\delta}$ cathode on samarium-doped ceria electrolyte. J. Power Sources, 2009, **188**, 96-105.

[37] C. Peters, A. Weber, E. Ivers-Tiffée,Nanoscaled $(La_{0.5}Sr_{0.5})CoO_{3-\delta}$ thin film cathodes for SOFC application at 500 °C< T< 700 °C, J. Electrochem. Soc., 2008, **155**, B730-B737.

[38] S. Wang, J. Yoon, G. Kim, D. Huang, H. Wang, A. J. Jacobson, Electrochemical properties of nanocrystalline $La_{0.5}Sr_{0.5}CoO_{3-x}$ thin films, Chem. Mater., 2010, **22**, 776-782.

CHAPTER 5

Synthesis and characterization of novel $Ce_{0.8}Sm_{0.2}Fe_{0.9}Ir_{0.03}Co_{0.07}O_{3-\delta}$ perovskite material and possible application as cathode for low-intermediate temperature SOFCs

Summary

This chapter has been published in Materials Research Bulletin and has been structured according to the journal's format. This chapter has also been reformatted to incorporate further comments and corrections by the examiners.

Abstract

A novel perovskite material, $Ce_{0.8}Sm_{0.2}Fe_{0.9}Ir_{0.03}Co_{0.07}O_{3-\delta}$ was synthesized using a sol-gel technique. The materials were calcined at temperatures of 800 °C, 900 °C, and 1000 °C. It was then characterized using X-ray diffraction, Raman and Infrared spectroscopy, high resolution transmission electron microscopy and scanning electron microscopy (SEM). The particle sizes and crystallite sizes increased with increasing calcination temperature and formed perovskite type materials with some separate Fe_2O_3, $FeSmO_2$ and iridium oxide phases. The powders were used to assemble button cells using samarium doped ceria as the electrolyte and NiO/SDC as the anode materials. The electrochemical properties were investigated using a Fiaxell open flanges test set-up and a Nuvant™ Powerstat-05 potentiostat/galvanostat. The $Ce_{0.8}Sm_{0.2}Fe_{0.9}Ir_{0.03}Co_{0.07}O_{3-\delta}$ cathode material calcined at 1000 °C exhibited the most promising performance, with a maximum power density of 0.400 W/cm^2, a current density of 0.8 A/cm^2, and a corresponding area specific resistance of 0.247 Ω cm^2 at 500 °C. The button cells were reasonably stable over 15 hours.

Key words: A. Oxides, B. Chemical synthesis, C. Raman spectroscopy, X-ray diffraction, D. Electrochemical properties.

1.0 Introduction

Solid oxide fuel cells (SOFCs) can be used as an alternative source of power generation. The technology has several interesting features; such as, low to zero deleterious emissions, proficient and adept generation processes. SOFCs have higher energy conversion efficiencies and can be used for co-generation of heat and electricity as an added benefit [1]. This has been drawing extensive attention for application in residential and commercial properties, large-size stationary power facilities for suburban neighborhoods, auxiliary power units for transportation vehicles [2 - 4] and with mobile applications where structural sturdiness, thermal shock resistance with low internal temperature are essential [5, 6]. Great efforts have been made in the past years to reduce the operational temperature, the cost of production and the plant component material hence the research drive to develop SOFCs technologies for low-intermediate temperatures between 300 - 600 °C.

Low temperature SOFC performance can be enhanced by reducing the electrolyte thickness and by developing new or alternative electrode materials with high ion and electronic conductivity under reducing and oxidative conditions, and high catalytic activity for fuel oxidation at relatively low temperatures [7 - 11] and to develop methods to minimize energy losses in the system [12]. Other areas of research in reducing SOFC operational temperatures includes the use of metal supported fuel cells and are beneficial due to its minimal cost, high power, improved feasibility, superior thermal conductivity and faster start-up time [13, 14].

In this study, porous composite of nickel oxide and samarium doped ceria was used as the cermet anode, which contained a high volume fraction of Ni oxide to form the electronic percolation path and expand the electrocatalytic active region in the electrode [15, 16]. Doped ceria was used as the electrolyte because of its compatibility with the cermet anode, its high conductivity, mixed proton and oxygen ionic conductivityat low temperature between (300 - 600 °C) [17 - 19]. Research reports on single cells using this electrolyte and optimized electrodes, presented stable performance in 100 hrs non-stop measurement [20].

This study includes the addition of platinum group metals specifically iridium, whose use as part of electrode materials are limited for example Huerta *et al.* [21], showed that the electrochemical properties of iridium oxide on yttrium stabilized zirconia (YSZ) were suitable for SOFC applications at the temperature range 573 – 873 K. In this study, a composite of doped ceria ($Ce_{0.8}Sm_{0.2}Fe_{0.9}Ir_{0.03}Co_{0.07}O_{3-\delta}$) was synthesized and tested as a potential cathode material for SOFC. The perovskite nanocomposites was prepared using a sol gel method, this technique is an adaptable and relatively simple method easily modified to synthesize complex metal oxide formulations. The perovskite were further calcined at 800 – 1000 °C and the electrochemical performance was investigated using humidified hydrogen and air as gases for the system.

2.0 Experimental Methods

2.1 Synthesis of Nanocrystalline Materials

Samarium (III) acetylacetonate hydrate (99.9 % purity), cobalt (II) acetylacetonate hydrate (99 % purity),cerium (III) acetylacetonate hydrate (99.9 % purity), iron(III) acetylacetonate (97 % purity) and Pluronic F-127 were purchased from Sigma-Aldrich (Pty) Ltd, South Africa. Iridium (III) acetylacetonate hydrate (99.9 % purity), was purchased from Alfa Aesar UK. These chemicals were used without further purification.

In a typical synthesis, 0.0758g of iridium (III) acetylacetonate hydrate (99.9 % purity), 1.3102 g of cerium (III) acetylacetonate hydrate (99.9 % purity), 1.1820 g of Iron (III) acetylacetonate (99.9 % purity), 0.0930 g of Cobalt (II) acetylacetonate hydrate (99.9 % purity), and 0.4640 g of samarium (III) acetylacetonate hydrate (99.9 % purity). Were weighed and added into a mixture of 50 ml of ethanol and 15 ml of deionized water. Then 4.00 g of Pluronic F-127 was added to the mixture, and then the mixture was sonicated for 30 mins in an ultrasound bath (UMC 20, 50 kHz). The solution formed was then placed on a hot plate and heated to 80 °C and stirred at 180 rpm for 30 minutes. The samples were then dried for 18 hours in an oven at 200 °C and then calcined in a muffle furnace (Kittec Squadro 1350) at a heating rate of 2 °C/min for 10 hours, to final temperatures of 800 °C,

900 °C, or 1000 °C. The $Ce_{0.8}Sm_{0.2}Fe_{0.9}Ir_{0.03}Co_{0.07}O_{3-\delta}$ (CSFIC) material formed was then characterised before further use.

To synthesize the electrolyte, 0.200 g of samarium (III) acetylacetonate and 0.534 g of cerium (III) acetylacetonate were mixed with a solution of ethanol (50 mL) and deionized water (15 ml) in an ultrasound bath. After 30 minutes, the solution was heated on a hotplate, while stirring, for 20 mins (120 rpm at 80 °C). Samples were then calcined at 850 °C for 5 hours at 2 °C/minute in a muffle furnace. The samarium doped ceria (SDC) material formed was hand mixed with sodium carbonate (Na_2CO_3) in a mass ratio of 60:40 % to form SDC/Na_2CO_3 electrolyte.

2.2 Characterization

The structural properties of the perovskite nanocomposite were characterized using powder X-ray diffraction (XRD), high resolution transmission electron microscopy (HR-TEM), infrared and Raman spectroscopy, while the morphology was characterized using scanning electron microscopy (SEM). The XRD patterns were obtained using Siemens D8 Advance diffractometer with a Cu Kα radiation source operating at 40 kV and a wavelength of 1.5406 Å. For HRTEM analysis, small amounts of the samples were dispersed in ethanol using an ultrasound bath, drop-dried onto a carbon coated copper TEM grid, and then examined on a JOEL 2100 HRTEM (200 kV accelerating voltage, beam current of 110 µA and a current density of 2.4 pA/cm^2).

The powders were pressed onto carbon tape coated aluminium stubs and gold coated for SEM observations on a ZEISS FEGSEM Ultra Plus. Infrared spectra were collected on a Perkin Elmer 1200 FTIR and Raman analysis was done on a DeltaNu advantage 532™ Raman Spectrometer (100 mW Nd:YAG laser with an excitation wavelength of 532 nm). The surface area, pore size, and pore volume were calculated from the nitrogen sorption isotherms collected at 77 K, using a Micrometrics Tri-Star II 3030. The calcined materials were degassed on a Micrometrics Flow Prep (060) under nitrogen flow at 90 °C for 1 hour and 200 °C for 4 hours before analysis.

2.3 Single Cell fabrication

The cells were prepared by moulding the materials using a 20 ton press and a 1.3 cm diameter die kit. The press was made from strong steel and the die kit was made from stainless steel. For the CSFIC material, 0.1535 g of the sample was placed into the die kit mould and 15 tons of pressure was then applied using the 20 ton press. A mass of 0.4500 g of NiO-SDC was used to make the anode and 0.2100 g of SDC/Na_2CO_3 was used to prepare the electrolyte using the same method. The discs had a total active area of 1.327 cm^2. The electrolyte and anode discs were then heat treated to 1050 °C for 2 hours at a heating rate of 5 °C/min, and the cathode materials to the sintering temperature used during synthesis (e.g. materials calcined at 800 °C, were sintered at 800 °C), all without binders. The electrolyte was estimated to be 0.03 mm thick, the cathode was 0.02 mm thick and the anode was 0.045 mm thick.

2.4 Electrochemical Performance test

To test the electrochemical properties, the electrolyte disc was positioned between the anode and cathode discs, and then placed in the open flange test set-up from Fiaxell SOFC Technologies™. This set-up was designed for the cell sizes, and platinum meshes were used as contact components, with the cell, to act as combined current collector and gas distributor.The test-bed was placed in a Kittec Squadro muffle furnace and linked to appropriate gas tight fittings for the delivery of humidified air and hydrogen gas to the cell. The current and the voltage from the cells were measured with a Nuvant™ Powerstat 05 potentiostat and galvanostat. Polarization curves were recorded between 300 °C - 500 °C with a fuel consisting of humidified hydrogen (4 – 20 % water) on the anode side and air on the cathode side.

3.0 Results and Discussion

3.1 Raman Characterizations

The Raman spectra of the CSFIC perovskite material are shown in Figure 1 and have four active Raman modes for the samples calcined at 1000 °C. The peak at 325 cm^{-1} is attributed

to an iron oxide vibration [22] and may indicate a solid solution was not formed with this sample. The F_{2g} vibration mode of cerium oxide fluorite structure was observed at 466 cm^{-1} [23 - 25], and the peak at 680 cm^{-1} is typically seen with iron oxides, however when considering the peak at 325 cm^{-1}, it suggests that the iron oxide has formed the magnetite phase [22]. The peak at 820 cm^{-1} is tentatively assigned to the A_{1g} mode of iridium oxide, typically the peak occurs at ~ 750 cm^{-1} [26]; however the blue-shift to 800 cm^{-1} could be due to iridium oxide distributed as nanocrystallites within the samarium doped ceria matrix.

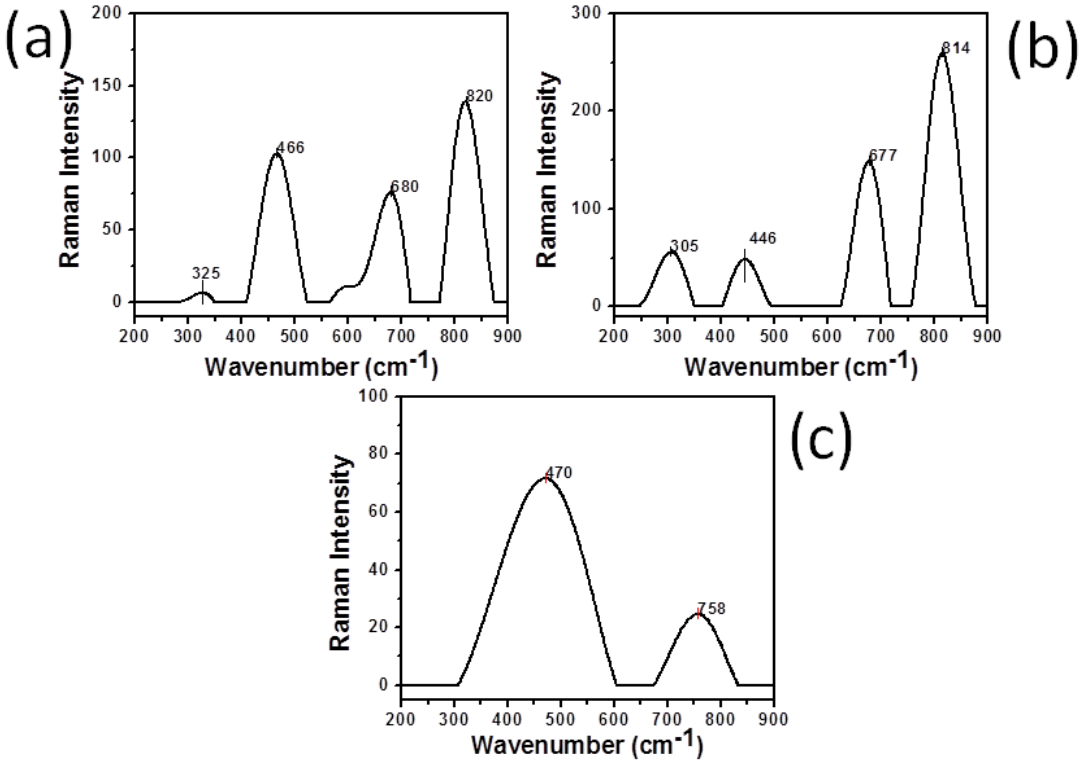

Figure 1: Raman spectra of $Ce_{0.8}Sm_{0.2}Fe_{0.9}Ir_{0.03}Co_{0.07}O_{3-\delta}$ calcined at (a) 1000 °C (b) 900 °C and (c) 800 °C.

Four active Raman modes were observed in the spectra for the sample calcined at 900 °C. The two peaks at 305 cm^{-1} and 677 cm^{-1} correspond to vibrationalactive modes of iron oxide that formed the magnetite crystal structure. The $F_{2g,}$ active modes of the ceriafluorite structure were observed at 446 cm^{-1}, and the A_{1g} mode of iridium oxide was observed at

814 cm^{-1}. All the peaks at 900 °C are red-shifted when compared to the samples calcined at 1000 °C.

The perovskite material calcined at 800 °C exhibited two active bands at 472 cm^{-1} and 754 cm^{-1} which correspond to F_{2g} active modes of ceria and the A_{1g} mode of iridium oxide. There was an observed shift in the Raman peaks of the materials, as the calcination temperature increased, which corresponds to changes in the metal to oxygen bonds. Some authors have noted when a larger ion like samarium substitutes for Ce^{4+}, the F_{2g} active modes of ceria will shift to lower values [24], and with our samples this is likely the case with the samples calcined at 900 °C. At 800 °C and 1000 °C the Raman shifts to higher values may indicate substitution of Ce^{4+} with smaller atomic mass cations (iron, cobalt, or iridium) or some of the cerium in the +3 oxidation state. Further comments and correlations on these observations are provided in the XRD section.

3.2 FTIR Analysis

Figure 2 shows the FTIR spectra of the CSFIC perovskite samples calcined at 800 °C, 900 °C, and 1000 °C. Absorbance peaks at 1508 cm^{-1} are attributed to C=O bonds from carbonate impurities. Such residual carbon species have been observed before with samarium doped ceria [27]. The peak at 1508 cm^{-1} was not present at higher calcination temperatures (1000 °C) as a result of complete combustion. At all calcination temperatures, the absorbance bands between 1000 - 1200 cm^{-1} are tentatively assigned to M-O-M bond vibrations due to Ce-O-Fe, Ce-O-Co, Sm-O-Fe, or Sm-O-Co; however, previous work by other authors has shown these bands can be due to M-OH bonds on the surface of iron ceria oxide materials calcined at 673 K [28].

There was also a shift observed from 1021cm^{-1} – 1102 cm^{-1} for 800 °C to 1000 °C caused by the M-O-M stretching vibration and the difference in the $M^{+}– O_2^{-}– M^{+}$ distances. The peak observed at 972 cm^{-1} for samples calcined at 800 °C, 965 cm^{-1} for samples calcined at 900 and 1000 °C may be due to separate iron oxide phases dispersed in a ceramic matrix, similar peaks have been observed in glasses containing iron and ceria [29].

Below 600 cm^{-1}, peaks were evident at 522 cm^{-1}, and 455 cm^{-1} for samples calcined at 800 °C, and at 521 cm^{-1} and 464 cm^{-1} for samples calcined at 900 °C, and at 457 cm^{-1} for the samples calcined at 1000 °C. For ABO_3 perovskites, the B-site cations (iron and cobalt with the current samples) will vibrate in the 500 – 700 cm^{-1} region [30], thus the peaks at 522/521 cm^{-1} with the samples calcined between 800 – 1000 °C are due to iron or cobalt oxide bonds.

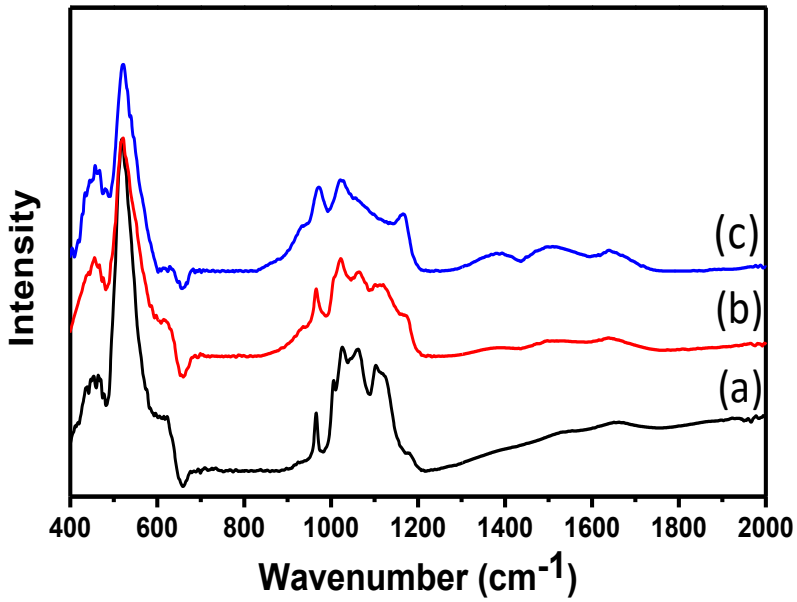

Figure 2: FTIR spectra of $Ce_{0.8}Sm_{0.2}Fe_{0.9}Ir_{0.03}Co_{0.07}O_{3-\delta}$ calcined at (a) 1000 °C (b) 900 °C and (c) 800 °C.

3.3 XRD Analysis

Figure 3 shows representative XRD patterns of the samples calcined at 800 °C, 900 °C, and 1000 °C. Cerium oxide, (fluorite) structure peaks observed at 2θ values of 28.59°, 33.08°, 47.41°, 56.16°, 69.30°, 76.67°, and 88.19° are indexed to (111), (200), (220), (311), (400), (331), (420), (331), and (422) respectively. These intense peaks are indicative of the material forming has a single phase solid solution [24, 25]. However, the large mole ratio of iron in the samples resulted in some low intensity peaks in the XRD at 2θ values of 35.66°, 49.55°, 62.57° and 95.15° are indexed to (110), (024), (214), and (511) for Fe_2O_3 in the

magnetite crystal phase. This observation correlates with the Raman and FTIR observations. Separate iron samarium oxide structure peaks were also noticed at *2θ* values of 40.89°, 58.93°, and 79.12° indexed to (022), (123), and (252) Miller indices.

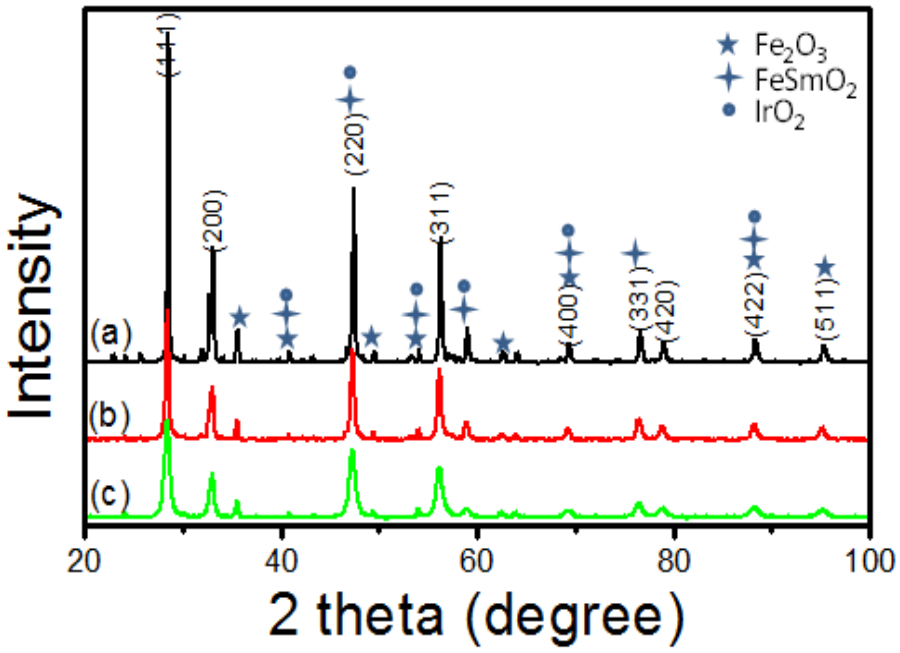

Figure 3: The XRD diffractograms of$Ce_{0.8}Sm_{0.2}$ $Fe_{0.9}Ir_{0.03}Co_{0.07}O_{3-\delta}$ calcined at (a) 1000 °C (b) 900 °C and (c) 800 °C.

Iridium oxide peaks were not clearly identified since the peaks positions overlap with the other phases identified, and the low stoichiometry used would imply a relatively low intensity or formation of a solid solution with the samarium doped ceria. However, the Raman peaks from 754 – 820 cm^{-1} did imply that the iridium oxide formed some separate phases in the material.

For the CSFIC samples after calcination, the average lattice parameter for the predominant CeO_2 phase *a* is 5.372 ± 0.44 Å, and the material is cubic was calculated by using the equation:

$$a = \frac{\lambda}{2} \times \sin\theta \times \sqrt{h^2 + k^2 + l^2} \quad (3)$$

where, λ is the average X-ray wavelength, θ is 2θ value/2, *h,k,l* are Miller indices of particular planes in crystal. The mass of the unit cell for all samples was 1.1557 x 10^{-27} g, and this was calculated using the equation.

$$\text{Mass of Unit Cell (M)} = \frac{(4atoms)(MolarMass)}{6.02\times10^{23}atoms/mol}\left[\frac{10^{-6}Mg}{g}\right] \quad (4)$$

The density of the unit cell is 7.454 g/cm^3, and the following equation was used to calculate this value.

$$\text{Density} = \frac{mass(unit\ cell)}{Volume(unit\ cell)} \quad (5)$$

Volume of unit cell was calculated to be 1.5503 x 10^{-28} cm^3 (from $v = a^3$ where a =$4R/\sqrt{2}$).

The lattice parameter of the cathode material was different from the lattice parameter of CeO_2 (JCPDS file NO. 00-034-0394) which confirms the formation of a new compound. In addition, several authors have reported that the changes in the lattice parameters are closely related to the substitution of the Ce^{4+} ion with smaller or larger ions, and changes in the oxygen vacancy concentration [24, 25, 31]. Earlier work by various authors has shown the importance of the (111) planes and the expansion of the lattice parameters as an indication of the presence of Ce^{3+} in such materials [32, 33]. Furthermore, the presence of Ce^{3+} in thefluorite ceria structure will produce oxygen vacancies to sustain electrostatic stability according to the equation [33]:

$$4Ce^{4+} + O^{2-} \longrightarrow 4Ce^{4+} + 2e^-/\boxdot + \frac{1}{2}O_2 \longrightarrow 2Ce^{4+} + 2Ce^{3+} + \boxdot + \frac{1}{2}O_2 \quad (6)$$

where □ represents an empty position (anion-vacant site) originating from the removal of O^{2-} from the lattice.

3.4 Thermogravimetric Analysis

Figure 4 shows the thermogravimetric analysis of the cathode material composite when heated in air at 30 mL/min from 30 °C to 1000 °C at 10 °C/min. In the profile there was a slow weight loss from 35 °C to 250 °C for the sample calcined at 1000 °C due to desorption of carbon dioxide and a gradual weight loss from 250 °C to 900 °C. For the samples calcined at 800 °C to 900 °C there was a gradual weight loss from 35 °C to 1000 °C throughout the process. The weight changes of the samples were assumed to be mainly due to the behaviour of lattice oxygen [34, 35], which can be represented by the equations [35]:

$$2Fe_{fe}^{\bullet} + O_o^x \rightarrow 2Fe_{fe}^{\bullet} + V_o^{\bullet\bullet} + \frac{1}{2}O_2 \quad (7)$$

$$2Co_{co}^{\bullet} + O_o^x \rightarrow 2Co_{co}^{\bullet} + V_o^{\bullet\bullet} + \frac{1}{2}O_2 \quad (8)$$

where $V_o^{\bullet\bullet}$ and O_o^x represent an oxide ion vacancy and an oxide ion, respectively. In the thermal profile the reactions of Co^{4+}, Fe^{3+} and Ir^{4+} were more dominant in the sample [35, 36], because of the gradual weight loss. The weight losses were thermally induced by loss of lattice oxygen which caused the formation of more oxygen vacancies. Furthermore, the onset temperature of the lattice oxygen loss for the samples calcined at 800 °C and 900 °C were lower than the samples calcined at 1000 °C and the weight loss of the samples calcined at 800 °C and 900 °C were more than that calcined at 1000 °C. This could indicate that the calcination temperature affects how the lattice oxygen can become more active at lower process temperatures. Raman results did not reveal any magnetite peaks at 800 °C, although XRD did show some phases at all calcination temperatures, thus the samples at 800 °C most likely had a significant amount of iron and cobalt substituted into the samarium doped cerium lattice. Recent theoretical studies by Li *et al.* [37], showed that more divalent ions substituted within the lattice of cerium oxide will reduce the mobility of oxygen vacancies within the material.

At higher calcination temperatures the Raman and FTIR results clearly indicated separate iron oxide phases and this would imply that the trivalent iron species is no longer within the SDC lattice and the cobalt has remained substituted within the perovskite. As a result the

divalent cobalt species plays a more dominant role with our samples at higher calcination temperatures and thus indicated change in oxygen vacancy behaviour revealed by the thermal analysis.

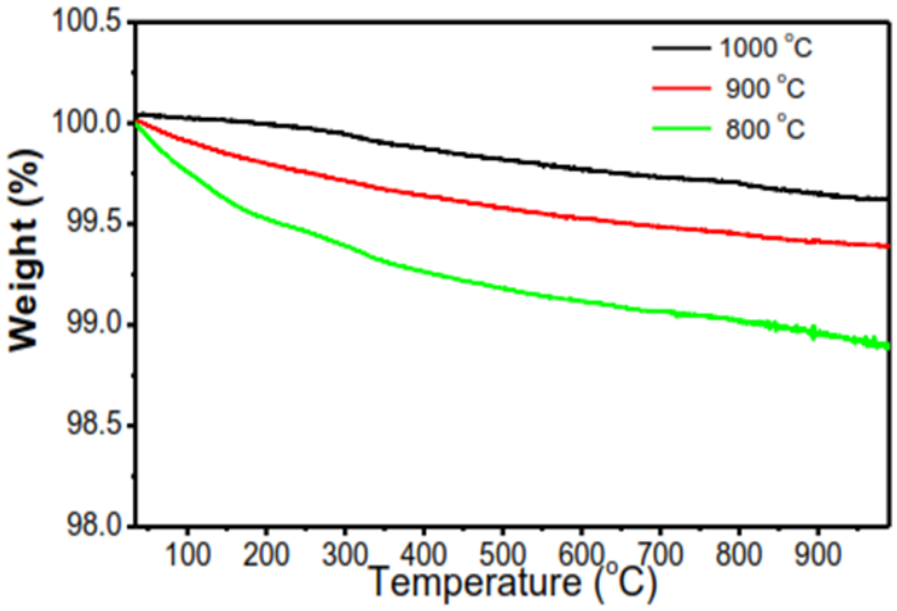

Figure 4: The thermogravimetric analysis of $Ce_{0.8}Sm_{0.2}Fe_{0.9}Ir_{0.03}Co_{0.07}O_{3-\delta}$ calcined at (a) 1000 °C (b) 900 °C and (c) 800 °C.

3.5 SEM Observations

The morphology of $Ce_{0.8}Sm_{0.2}Fe_{0.9}Ir_{0.03}Co_{0.07}O_{3-\delta}$ as shown in Figure 5 shows the materials accumulated together in an agglomerate formation with large pore sizes between the particles. These displayed morphology of fine particle combination and agglomerate formation with pore spaces that decreased as the calcination temperature decreased from 1000 °C to 800 °C. This is in agreement with the HRTEM micrograph which showed a particle size decrease as the calcination temperature decreased.

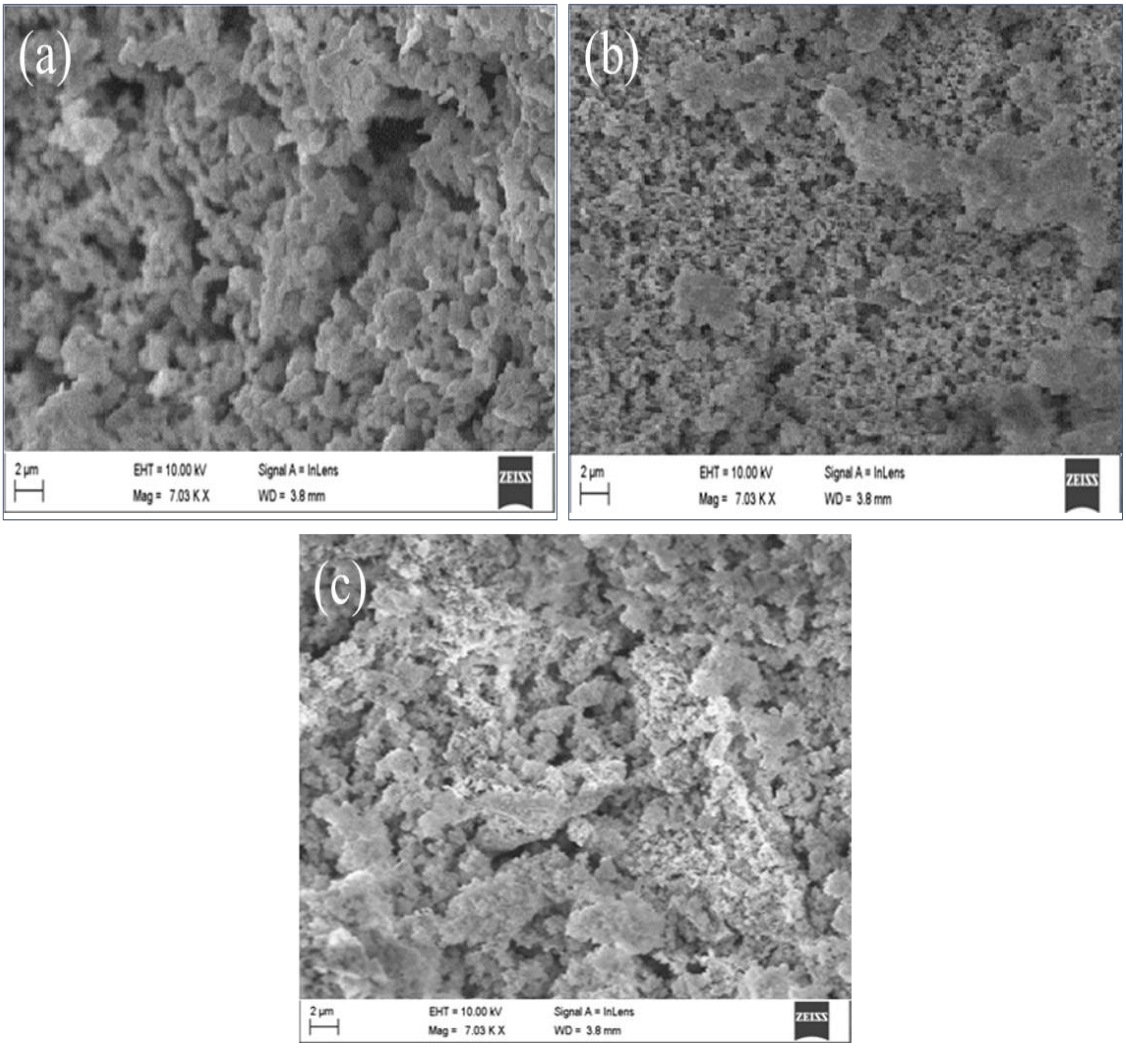

Figure 5: SEM morphology of $Ce_{0.8}Sm_{0.2}Fe_{0.9}Ir_{0.03}Co_{0.07}O_{3-\delta}$ calcined at (a) 1000 °C (b) 900 °C and (c) 800 °C.

The energy-dispersive X-ray spectroscopy (EDX) analysis on the powders, Figure 6, identified the individual metals within the samples. The false colour maps was done using EDX mapping. From the elemental mapping a uniform distribution of the metals was indicated and it did not show any obvious concentration of a particular metal within a specific area. The corresponding weight percentage analysis using SEM-EDX is presented in Table 1. This confirmed that the metals were present and the ratios were within reasonable and expected ranges, as seen by the small deviations.

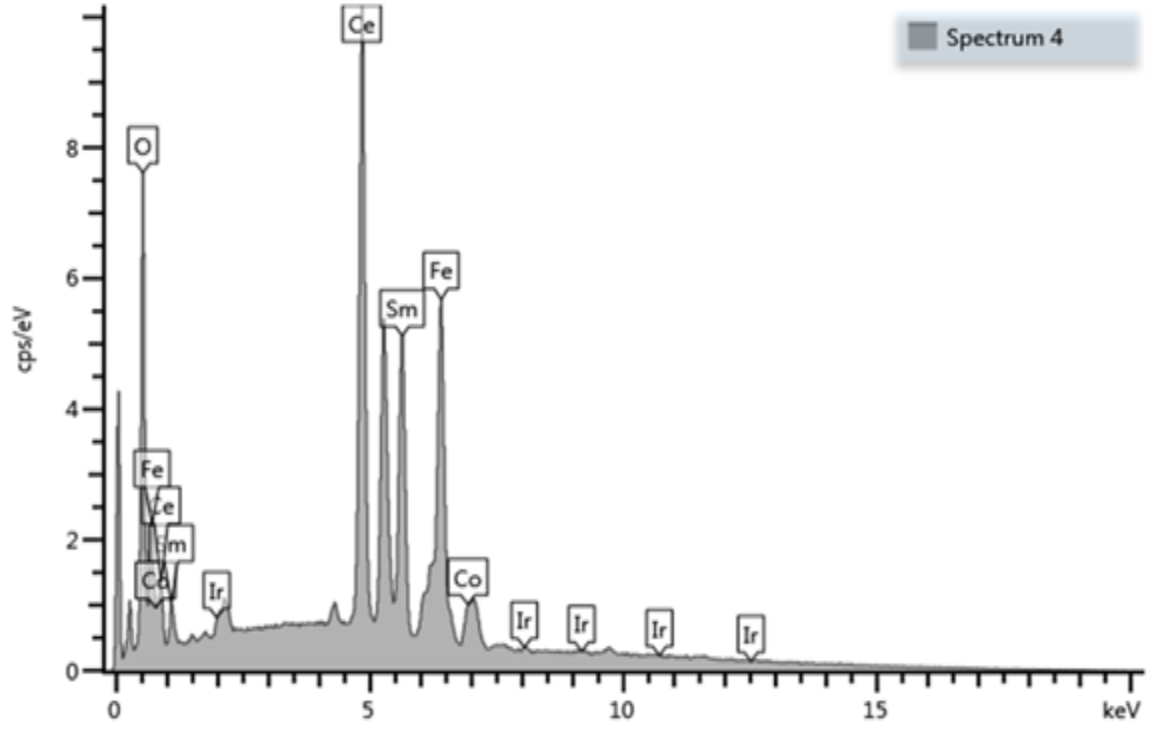

Figure 6 : The EDX analysis of the representative sample calcined at 1000 °C.

Table 1: The SEM-EDX analysis results from a representative sample calcined at 1000 °C.

Element	Measured (Wt %)	Theoretical (Wt %)
Ce	46.38	44.78
Sm	17.85	12.01
Fe	17.00	20.08
Ir	1.26	1.65
Co	2.32	2.30
O	15.18	19.18

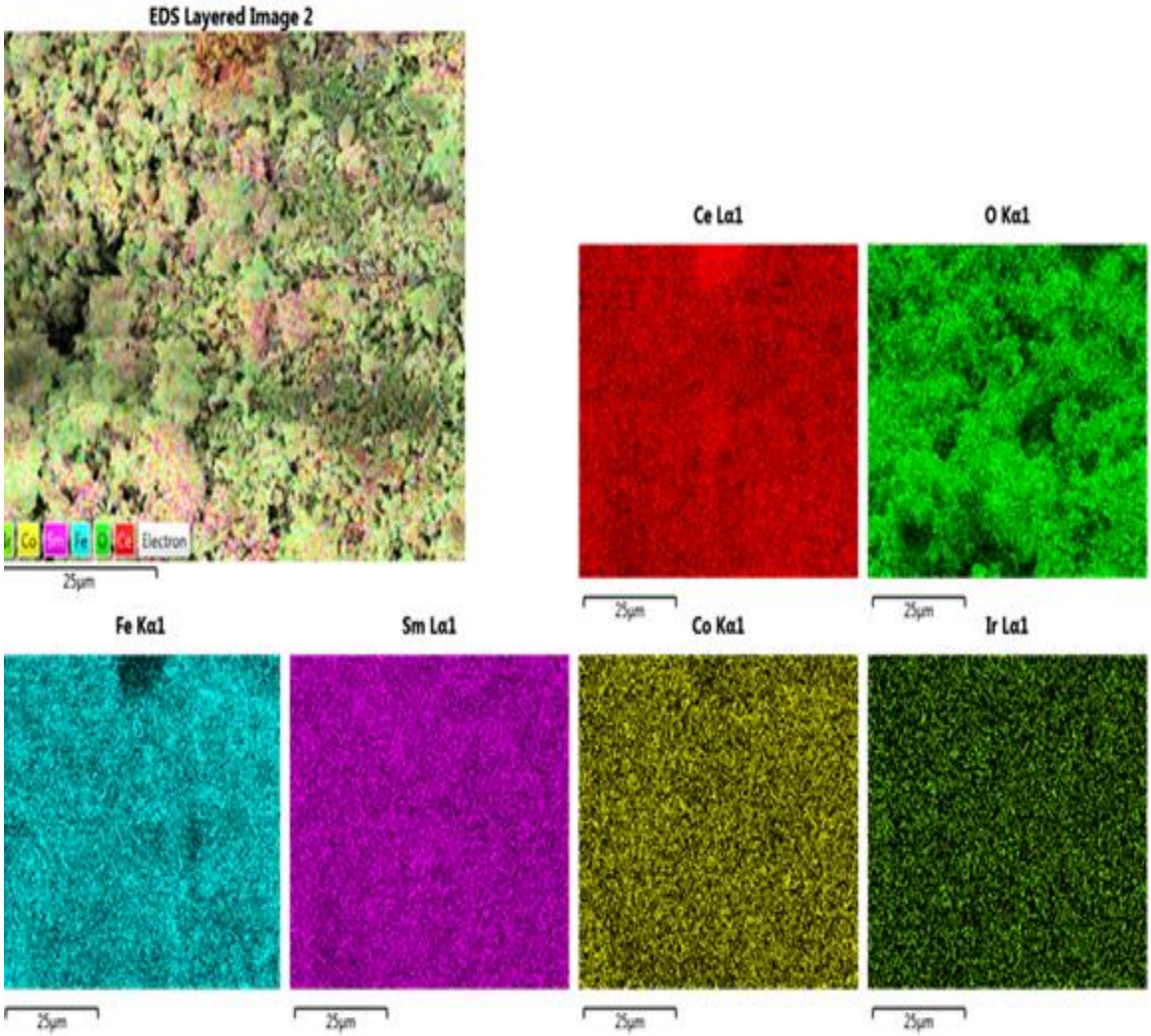

Figure 7: Imaging of $Ce_{0.8}Sm_{0.2}Fe_{0.9}Ir_{0.03}Co_{0.07}O_{3-\delta}$ calcined at 1000 °C by EDX mapping.

3.6 HRTEM Observations

The various powders were examined by HRTEM, and representative images are presented in Figures 8. The morphology for all the samples showed slight differences, specifically, irregular shaped powders, especially, the samples calcined at 800 °C showed smaller crystalline shapes. It was noted that the difference in the crystallite sizes were observed in the XRD data which confirmed a decrease in crystal sizes as the calcination temperature decreased from 1000 °C to 800 °C.

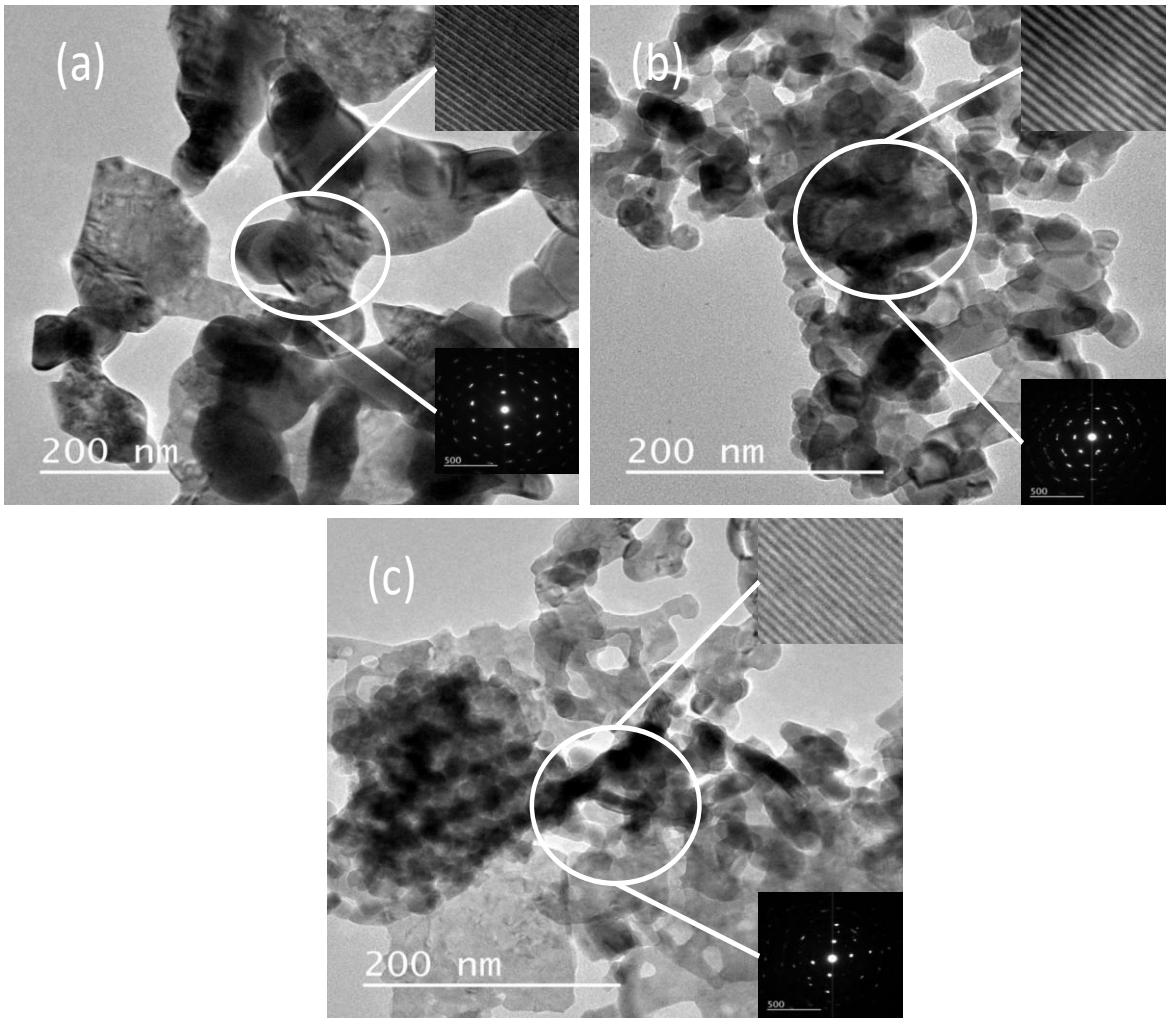

Figure 8: HRTEM Micrograph of $Ce_{0.8}Sm_{0.2}Fe_{0.9}Ir_{0.03}Co_{0.07}O_{3-\delta}$ calcined at (a) 1000 °C (b) 900 °C and (c) 800 °C.

The measured lattice distance between the fringes (inserted in Figure 8) were 0.134 nm indexed to (400), 0.380 nm indexed to (211) and 0.125 nm indexed to (331) for 800 °C – 1000 °C samples respectively. These are linked to the XRD as Fe_2O_3 (magnetite) and CeO_2 (fluorite) structures. The presence of CeO_2 fluorite structure with the HRTEM observations, correlate with the XRD analysis and indicates the samples have some concentration of oxygen vacancies on the surface. The presence of oxygen vacanciesinfluences oxygen ion diffusion paths through the electrode. The selected area electron diffraction patterns did not show too much significant differences between the samples.

3.7 Textural Characterizations of the calcined Materials

The nitrogen sorption isotherm analysis on the samples at 800 °C, 900 °C and 1000 °C are shown in Figure 9. The sample calcined at 1000 °C had the lowest surface area of 3.06 m^2/g, the lowest average pore size (27.4 nm) and a low pore volume of 0.015 cm^3/g. The surface area for the 900 °C calcined samples was 6.56 m^2/g, with an average pore size of 50.8 nm, and a pore volume of 0.068 cm^3/g.

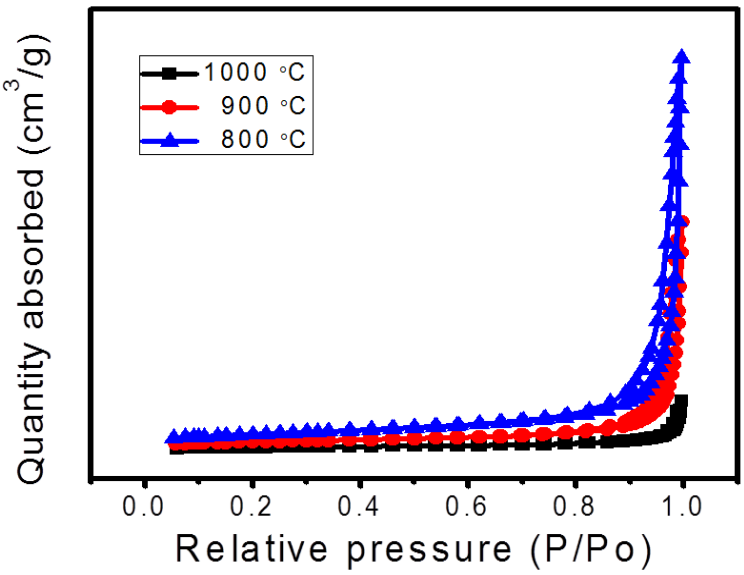

Figure 9: The thermogravimetric analysis of $Ce_{0.8}Sm_{0.2}Fe_{0.9}Ir_{0.03}Co_{0.07}O_{3-\delta}$ calcined at (a) 1000 °C (b) 900 °C and (c) 800 °C.

The materials observed in general, showed a decrease in the surface area as the calcination temperature increased, the pore volume and pore size also increased. This is attributed to the fact that the higher the calcination temperature the more compact the material becomes hence the reduction of surface area with higher calcination temperature. Also heating to high temperature might be too fast which causes agglomeration of the particles. In this case it can be improved by changing the heating conditions.

3.8 Electrochemical Properties

3.8.1 Polarization Curves

The polarization curves for $Ce_{0.8}Sm_{0.2}$ $Fe_{0.9}Ir_{0.03}Co_{0.07}O_{3-\delta}$ calcined at 800 °C- 1000 °C are shown in Figure 10. These were obtained in humidified hydrogen and compressed air in the temperature interval of 300°C - 500°C.

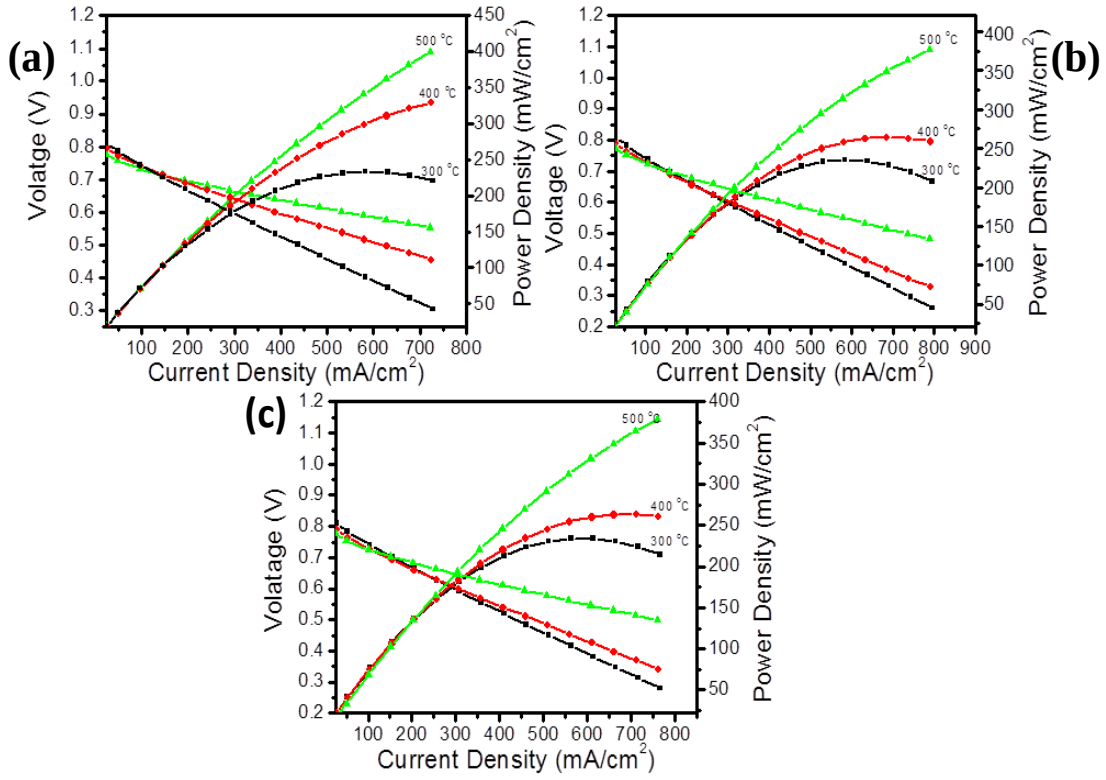

Figure 10: The polarization curve of $Ce_{0.8}Sm_{0.2}$ $Fe_{0.9}Ir_{0.03}Co_{0.07}O_{3-\delta}$ calcined at (a) 1000 °C (b) 900 °C and (c) 800 °C.

The OCV values of the tested cells, as shown in Figure 10, decreased when measured from 300 – 500 °C and were stable at 0.87 V for more than 15 hours at 500 °C for all calcined samples. This value is lower than the thermodynamic values calculated using the Nernst equation, which can be attributed to the assembly and structure of the cell.

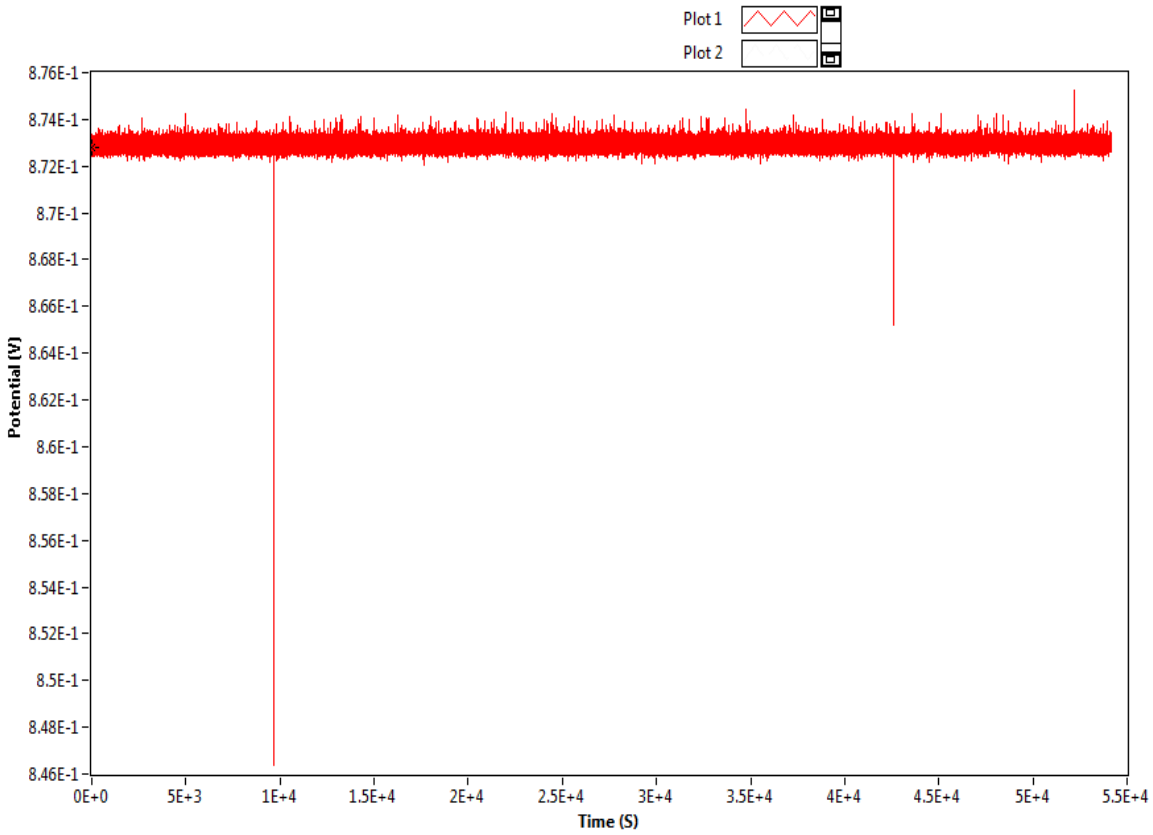

Figure 11: The Open Cell Voltage of $Ce_{0.8}Sm_{0.2}Fe_{0.9}Ir_{0.03}Co_{0.07}O_{3-\delta}$ calcined at 800 °C measured at 500 °C for 15 hours.

Gas crossover through the electrolyte can account for the lower OCV, and this can be due to the cold powder compacting temperature used, which could leave residual pores and result in leakage through any connected pores present. The polarization curves showed slight changes for the different calcination temperatures and displayed a linear fall in the voltage as the current densities increased. This is due to resistance to current flow within the button cell. When current increases, the voltage drop increases as a result of kinetic and ohmic losses within the cell. The power density increased with calcination temperatures. This can be linked to the structural differences determined by XRD, HRTEM and Raman spectroscopy. The presence of greater amount of oxygen vacancies, and Ce^{3+} within the material framework can allow for improved oxygen reduction kinetics and maybe one of the main reasons for the improved power density at 1000 °C.

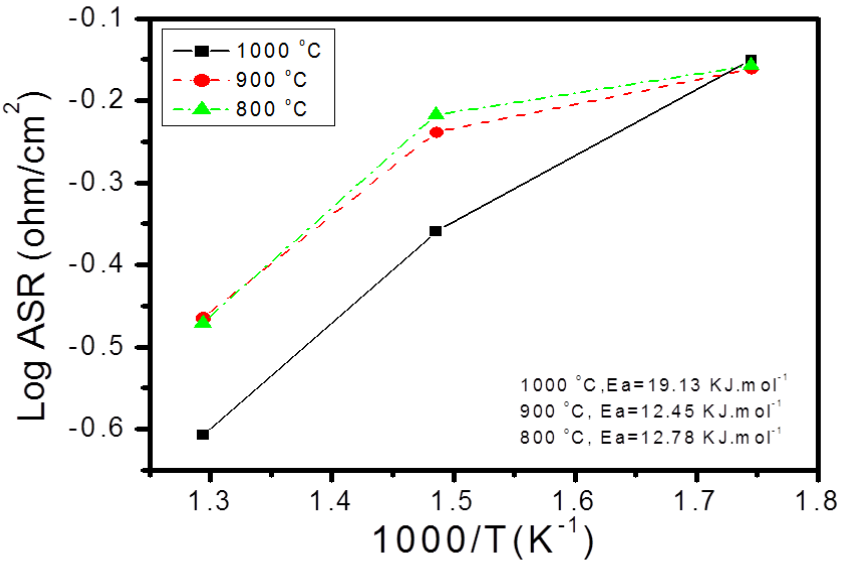

Figure 12: The Log Area Specific Resistance (ASR) against temperature of $Ce_{0.8}Sm_{0.2}Fe_{0.9}Ir_{0.03}Co_{0.07}O_{3-\delta}$ calcined at (a) 1000 °C (b) 900 °C and (c) 800 °C.

Figure 12 shows the normalized area specific resistance (ASR) of the single cell calculated from the slope of the substantial linear portion (in the centre) of the I-V curve, where the Ohmic resistance is dominant. The ASR is directly related to the design of the cell, anode, electrolyte and cathode properties and the assembly process used to make the single cell [38]. The ASR reduced when measured at 300, 400 and 500 °C. At 300 °C there was very little difference between the samples calcined at the three different temperatures.However at 400 °C there was a notable difference between the sample calcined at 1000 °C and those calcined at 800 and 900 °C and a similar trend at 500 °C between the 1000 °C sample and the two at lower temperatures. It is interesting to note that the calcination temperatures used have no effect at 300 °C. This can be attributed to the electrolyte and may suggest at 300 °C, SDC may not be a suitable electrolyte.

Additionally, the differences in the ASR can be linked to changes in the material properties and could indicate an increased oxygen loss from the lattice. As mixed ionic conductors, oxygen reduction occurs in the triple phase boundary and on the surface of electrodes in

this system which results from the increase in ionic conductivity of the electrodes. The Oxygen absorbed is reduced to O_2 ions and diffuses faster towards the electrode/electrolyte and electrolyte interface as influenced by increase in O_2 vacancies. The increase in the oxygen diffusion leads to a reduction in ASR [39]. The change in porosity, surface area, and pore volume with calcination temperature, and the overall morphology of the materials will affect transport properties at the phase boundary. In this regard, the 1000 °C calcination temperature is optimum for the materials reported here, and reduces the ASR slightly when compared to the other calcination temperatures. Shin *et al.* [40], reported on similar results, and found that with their samarium based materials for IT-SOFCs, the triple phase boundary and necking structure was optimal at 1000 °C.

3.8.2 Power Density

The maximum power density for $Ce_{0.8}Sm_{0.2}Fe_{0.9}Ir_{0.03}\ Co_{0.07}O_{3-\delta}$ samples calcined at 800°C, 900 °C and 1000 °C are shown in Table 2. The power density resultswere taken from 300 °C-500 °C. The maximum Power densities at 300 °C was 221.22 mW/cm^2 and at 400 °C was 330.16 mW/cm^2 and 500 °C was 400.15 mW/cm^2. The highest power density was exhibited by $Ce_{0.8}Sm_{0.2}Fe_{0.9}Ir_{0.03}Co_{0.07}O_{3-\delta}$ perovskite calcined at 1000 °C, when measured at 500 °C and it portrayed a low area specific resistance.

At each test temperature, the samples calcined at 1000 °C had the largest power density. However there was a marginal difference at 300 °C, a larger difference at 400 °C, and a small difference at 500 °C. These results could have some implications for applications at 300 or 500 °C, were the calcination of the materials can be done at somewhat reduced temperatures of 800 °C instead of 1000 °C using organic-metallic precursors in a sol-gel process.

Another key implication from our results is the moderate power output from a non-ideal single cell. Improvements can be achieved by using thin electrolyte and cathode layers and using tape casting or dip coating methodologies to control and optimise adhesion between the layers.

Table 2: The Area Specific Resistance and Maximum Power Density of $Ce_{0.8}Sm_{0.2}Fe_{0.9}Ir_{0.03}Co_{0.07}O_{3-\delta}$ calcined at (a) 800 °C (b) 900 °C and (c) 1000 °C.

Calcination Temperature (°C)	Measuring Temperature (°C)	Area Specific Resistance (Ω cm^2)	Max.Power Density (mW/cm^2)
800	300	0.695	214.01
	400	0.606	260.55
	500	0.338	379.36
900	300	0.689	207.15
	400	0.577	259.04
	500	0.342	380.58
1000	300	0.700	221.22
	400	0.436	330.16
	500	0.247	400.15

4.0 Conclusions

A new cathode material, $Ce_{0.8}Sm_{0.2}Fe_{0.9}Ir_{0.03}Co_{0.07}O_{3-\delta}$ was synthesized and characterised using vibrational spectroscopy, XRD, electron microscopy, TGA, and tested as an SOFC electrode. Raman spectroscopy revealed that the different calcination temperatures used produced materials with the characteristic vibration modes indicative of samarium doped ceria and iridium oxide at all calcination temperatures. Magnetite vibrational modes were observed at 900 and 1000 °C only, with the Raman spectra. FTIR spectra revealed that the 800 °C calcination temperature did not completely remove carbon impurities. The increase in calcination temperature resulted in shifts with the mid-range FTIR peaks indicating changes in the metal – oxygen – metal bonds. XRD analysis confirmed the existence of minor phases of iridium and iron oxides, and confirmed the Raman results and supported the notion concerning the presence of Ce^{3+} and oxygen vacancies within the samples. TGA analysis further confirmed that the concentration of oxygen vacancies differed with calcination temperatures. HRTEM analysis revealed the samples had irregular shaped crystallites with differing phase structures as the calcination temperature was increased. SEM observations showed all samples consisted of porous agglomerates.

Polarization curves for the various samples revealed that the sample calcined at 1000 °C produced the maximum power density of 400.15 mW/cm^2 at 500 °C and had an area specific resistance of 0.247 Ω cm^2. The results show that this can be a very promising material for SOFC cathodes operating at low – intermediate temperatures. Further improvement in terms of electrochemical performance can be achieved using advanced assembly processes such as spark sintering techniques or conventional tape casting methodologies.

Acknowledgements

The authors thank the University of KwaZulu-Natal, for providing access to research facilities used in this research. ESKOM-TESP and NRF of South Africa (Thuthuka programme, Grant No: 76318) for research funds.

References

[1] P. Pramote, M. Hiroki, M. Toshiaki, E. Koichi, Journal of Power Sources, 204 (2012) 67 - 73.

[2] F. Liangdong, Z. Bin, C. Mingming, W. Chengyang, R. Rizwan, Q. Haiying, W. Xuetao, W. Xiaodi, M. Ying, Journal of Power Sources, 203 (2012) 65 - 71.

[3] A. Atkinson, S. Barnett, R.J. Gorte, J.T.S. Irvine, A.J. McEvoy, M. Mogensen, S.C. Singhal, J. Vohs, Nat Mater, 3 (2004) 17 - 27.

[4] W. Sea-Fue, H. Yung-Fu, L. Wan-Ju, K. Kiyoshi, Solid State Ionics, 247 – 248 (2013) 48 - 55.

[5] T. Chun-Huang, H. Chang-sing, C. Chun-Liang, Y. Jen-Feng, N. Sheng-Hui, Journal of Power Sources, 197 (2012) 145 - 153.

[6] H. Rob, B. Jörg Oberste, D. P. Cyrille, Q. Wei, Y. Sing, L. Jean-Gabriel, M. Christian, Journal of Power Sources, 191 (2009) 371 - 376.

[7] J. Jiangwei, C. Fanglin, X. Changrong, Electrochimica Acta, 136 (2014) 422 - 429.

[8] J. D. Nicholas, S. A. Barnett, Journal of the Electrochemical Society, 157 (2010) B536 - B541.

[9] J. C. Ruiz-Morales, J. Canales-Vázquez, D. Marrero-López, J. T. S. Irvine, P. Núñez, Electrochimica Acta, 52 (2007) 7217 - 7225.

[10] T. Ikebe, H. Muroyama, T. Matsui, K. Eguchi, Journal of the Electrochemical Society, 157 (2010) B970 - B974.

[11] J. T. Vaughey, J. R. Mawdsley, T. R. Krause, Materials Research Bulletin, 42 (2007) 1963 - 1968.

[12] R. Vaßen, D. Hathiramani, J. Mertens, V.A.C. Haanappel, I.C. Vinke, Surface and Coatings Technology, 202 (2007) 499 - 508.

[13] W. Zhenwei, B. Jörg Oberste, Y. Sing, D. P. Cyrille, Q. Wei, H. Rob, M. Radenka, G. Dave, Journal of Power Sources, 176 (2008) 90 - 95.

[14] C.T. Michael, Y.L. Grace, P.J. Craig, C.D. Lutgard, J.V. Steven, Journal of Power Sources, 175 (2008) 447 - 451.

[15] F. P. R. Nielson, M. V. M. S. Mariana, R. M. N. Octávio, M. R. V. Sônia, S. Martin, Applied Catalysis A: General, 353 (2009) 305 - 309.

[16] H. Kishimoto, Y. P. Xiong, K. Yamaji, T. Horita, N. Sakai, M.E. Brito, H. Yokokawa, Journal of Chemical Engineering of Japan, 40 (2007) 1178 - 1182.

[17] F. Liangdong, W. Chengyang, C. Mingming, D. Jing, Z. Jiaming, Z. Bin, International Journal of Hydrogen Energy, 36 (2011) 9987 - 9993.

[18] W. Xiaodi, M. Ying, R. Rizwan, M. Mamoun, Z. Bin, Electrochemistry Communications, 10 (2008) 1617 - 1620.

[19] L. Seung-Hwan, K. Hong-Ki, K. Seung-Hyun, L. Sung-Gap, L. Young-Hie, Materials Research Bulletin, 58 (2014) 195 - 198.

[20] Z. Lei, L. Rong, K. Arno, T. Shanwen, Electrochemistry Communications, 13 (2011) 582 - 585.

[21] A. M. Torres-Huerta, J. R. Vargas-García, M. A. Domínguez-Crespo, Solid State Ionics, 178 (2007) 1608 - 1616.

[22] M. Hanesch, Geophysical Journal International, 177 (2009) 941 - 948.

[23] N. Chaubey, B. N. Wani, S. R. Bharadwaj, M. C. Chattopadhyaya, Solid State Sciences, 20 (2013) 135-141.

[24] K. Kuntaiah, P. Sudarsanam, B. M. Reddy, A. Vinu, RSC Advances, 3 (2013) 7953 - 7962.

[25] L. Li, F. Chen, J. Q. Lu, M. F. Luo, The Journal of Physical Chemistry A, 115 (2011) 7972 - 7977.

[26] A. V. Korotcov, Y. S. Huang, K. K. Tiong, D. S. Tsai, Journal of Raman Spectro scopy, 38 (2007) 737 - 749.

[27] A. Kaddouri, S. Bassil, B. Béguin, P. Gélin, Journal of Sol-gel Science & Technology, 67 (2013) 175 - 181.

[28] B. Chen, Z. Zhu, Y. Guo, Y. Qiu, J. Zhao, Journal of Colloid and Interface Science, 398 (2013) 142-151.

[29] D. P. Singh, G. Pal Singh, Journal of Alloys and Compounds, 546 (2013) 224 - 228.

[30] C. Zeng, Y. He, C. Li, Y. Xu, Ceramics International, 39 (2013) 5765 - 5769.

[31] M. Guo, J. Lu, Y. Wu, Y. Wang, M. Luo, Langmuir, 27 (2011) 3872 - 3877.

[32] L. Chen, P. Fleming, V. Morris, J. D. Holmes, M. A. Morris, The Journal of Physical Chemistry C, 114 (2010) 12909-12919.

[33] X. Liu, K. Zhou, L. Wang, B. Wang, Y. Li, Journal of the American Chemical Society, 131 (2009) 3140 - 3141.

[34] A. Botea-Petcu, S. Tanasescu, V. Varazashvili, N. Lejava, T. Machaladze, M. Khundadze, F. Maxim, F. Teodorescu, J. Martynczuk, Z. Yáng, L. J. Gauckler, Materials Research Bulletin, 57 (2014) 184 - 189.

[35] L. Shuyan, L. Zhe, H. Xiqiang, W. Bo, S. Wenhui, Solid State Ionics, 178 (2007) 417 - 422.

[36] S. Zongping, X. Guoxing, T. Jianghua, D. Hui, Y. Weishen, Separation and Purification Technology, 25 (2001) 419 - 429.

[37] Z. P. Li, T. Mori, J. Zou, J. Drennan, Materials Research Bulletin, 48 (2013) 807 - 812.

[38] U.F.C. Council, in: U.F.C.C.s.S.O.F.C.F. Group (Ed.), Washington DC, 2007.

[39] Z. Wenxia, L. Zhe, L. Shuyan, W. Bo, M. Jipeng, H. Xiqiang, C. Kongfa, A. Na, S. Wenhui, Journal of Alloys and Compounds, 465 (2008) 274 - 279.

[40] I. Park, J. Choi, H. Lee, D. Shin, Ceramics International, 39 (2013) 5561 - 5569.

CHAPTER 6

Evaluation of novel nanophase $Ce_{0.8}Sr_{0.2}Fe_{0.9}Ir_{0.1}O_{3-\delta}$ as cathode material for low temperature SOFC

Summary

This chapter has been accepted by "Nanomaterials for Electrocatalysis and Electrochemical Energy Applications" and has been structured according to the journal's format. This chapter has also been reformatted to incorporate further comments and corrections by the examiners

Abstract

In this study, $Ce_{0.8}Sr_{0.2}Fe_{0.9}Ir_{0.1}O_{3-\delta}$ (CSFI) perovskite type material was prepared by sol-gel technique, characterised, and then tested as a cathode material for solid oxide fuel cells operating between 300 – 500 °C. The materials were studied using X-ray diffraction, Raman spectroscopy, Fourier transform infrared spectroscopy and thermogravimetric analysis. The morphology was examined using scanning electron microscopy and high resolution transmission electron microscopy. Samples showed changes in the overall structure and defect chemistry with an increase in calcination temperature. When tested as cathode materials, the material calcined at 1000 °C had the greatest performance at a test temperature of 500 °C, with a current density of 774.47 mA/cm^2, a power density of 483.07 mW/cm^2 and an area specific resistance (ASR) of 0.342 $\Omega\ cm^2$.

Keywords: Solid Oxide Fuel Cell, cerium oxide, Iridium oxide, perovskites, nano-composites.

1.0 Introduction

Reduction in the operating temperature of Solid Oxide Fuel Cells (SOFCs) has been an important area of research for a long time, because operating at high temperatures, over 800 °C, limits the use of SOFCs [1 - 4]. The advantages of operating SOFCs at low temperatures include the reduction in cost, extension in the range of material selection and a significant improvement in the operational lifespan of the system.

Various researchers have used mixed ionic and electronic conductors (MIECS) type materials to reduce the operating temperature of SOFCs. The utilization of MIECs expands the active electrochemical reaction sites from the traditional triple phase boundary (TPB) at the solid electrolyte and electronic conductor electrode interface to the entire MIEC gas interface [5]. One major perovskite and MIEC combination, is $(LaSr)(CoFe)O_{3-\delta}$ (LSCF) perovskite, which has been investigated as a cathode material operating at intermediate temperatures with high catalytic activity promoted by rapid surface exchange kinetics [6]. Shao and Halle et al used strontium and iron in $Ba_{0.5}Sr_{0.5}Co_{0.8}Fe_{0.2}O_{3-\delta}$ (BSCF) cathode material at low temperature and it exhibited a high power output because of its high rate of oxygen diffusion [7]. Zhu *et al.* [8] made composite cathodes of $Ba_{0.5}Sr_{0.5}Co_{0.8}Fe_{0.2}O_{3-\delta}$–$x$ $Sm_{0.5}Sr_{0.5}CoO_{3-\delta}$ and tested them with samarium doped ceria electrolytes, and found the performance was excellent at 550 °C due to excellent electronic conductivity and a high concentration of oxygen vacancies. Colomer *et al.* [9] substituted cerium to make $Sr_{0.8}Ce_{0.2}$ $Fe_{0.7}Co_{0.3}O_{3-\delta}$ cathode materials which showed enhanced oxygen ion diffusion and better cathodic performance when compared with LSCF at 700 °C.

In this study, sol-gel method was developed to synthesize the cathode perovskite material $Ce_{0.8}Sr_{0.2}Fe_{0.9}Ir_{0.1}O_{3-\delta}$ (CSFI). Sol-gel processes are reliable techniques that are recurrently used to produce oxide ceramic materials with controlled structure and composition for SOFC application. This technique was also applied in the fabrication of the anode and electrolyte used in this study. Porous composite of nickel oxide and samarium doped ceria (NiO/SDC) was used as the anode, this contained a high volume fraction of nickel oxide to SDC in the ratio 60:40 %. This aids in the formation of electronic percolation pathways and

expansion of the electrocatalytic active region in the electrode [10, 11]. The electrolyte used was doped ceria because of its compatibility with the cermet anode, mixed proton and oxygen ionic conductivity and its high conductivity [12] at low temperatures between 300 - 600 °C [13-18].

2.0 Experimental Methods

2.1 Powder synthesis

The starting materials used were Strontium (III) acetylacetonate hydrate, (99.9 % purity), Cerium (III) acetylacetonate hydrate (99.9 % purity), Iron (III) acetylacetonate (97 % purity) and Pluronic F-127 were purchased from Sigma-Aldrich (Pty) Ltd, South Africa. Iridium (III) acetylacetonate hydrate was purchased from Alfa Aesar UK. These chemicals were used without further purification.

A mass of 0.0758 g of iridium (III) acetylacetonate hydrate, 1.3102 g of cerium (III) acetylacetonate hydrate, 1.1820 g of Iron (III) acetylacetonate, 0.0930 g of cobalt (II) acetylacetonate hydrate, and 0.4640 g of samarium (III) acetylacetonate hydrate were used. The preparation of the perovskite nanocomposite was synthesized by sol-gel technique. The metal salts were weighed into a mixture of 50 mL of ethanol and 15 mL of deionized water, and then 4.00 g of Pluronic F-127 was added to it. The mixture was sonicated for 30 minutes in an ultrasound bath (UMC 20, 50 kHz). The mixture was placed on a hot plate and heated upto 80 °C for 30 minutes stirring at 180 rpm. The samples were oven dried for 18 hours at 200 °C, and then calcined in a muffle furnace (Kittec Squadro 1350) for 10 hours at a ramping rate of 2 °C/minute, to final temperatures of 800 °C, 900 °C and 1000 °C.

The electrolyte was also synthesized by sol-gel technique, by weighing 0.200 g of samarium (III) acetylacetonate and 0.534 g of cerium (III) acetylacetonate into 40 mL of ethanol and 15 mL of deionized water. The mixture was sonicated for 30 mins in an ultrasound bath (UMC 20, 50 kHz), then placed on a hotplate, heated up to 80 °C for 20 minutes while stirring at 120 rpm. The sample was further calcined at 850 °C for 5 hours at

a heating rate of 2 °C/minute in a muffle furnace (Kittec Squadro 1350). The SDC material formed was hand mixed with sodium carbonate (Na_2CO_3) in the ratio of 60:40 %.

2.2 Characterization

The structural characteristics of the perovskite nanocomposite were characterized using high resolution transmission electron microscopy, powder X-ray diffraction (XRD), infrared and Raman spectroscopy, while the morphology was characterized using scanning electron microscopy. Small amount of the samples for the HR-TEM analysis, were poured in ethanol and sonicated for 5 minutes. It was then drop-dried onto a carbon coated copper TEM grid and then examined on a JOEL 2100 HRTEM (200kV accelerating voltage, beam current of 110 µA and a current density of 2.4 pA/cm^2). The XRD patterns were obtained using Siemens D8 Advance diffractometer with a Cu Kα radiation source operating at 40 kV and a wavelength of 1.5406 Å. Powders were pressed onto carbon tape placed onto aluminium stubs and then gold coated for SEM observations on a ZEISS FEGSEM Ultra Plus. The infrared spectra were collected on a Perkin Elmer 1200 FTIR and the Raman analysis was done on a DeltaNu advantage 532™ Raman spectrometer (100 mW Nd:YAG laser with an excitation wavelength of 532 nm). The thermogravimetric analysis (TGA) was done using a Perkin Elmer simultaneous thermal analyser STA 6000.

2.3 Button cell fabrication

The asymmetric cell was prepared by weighing out 0.1535 g of the cathode material, and 0.2100 g of SDC/Na_2CO_3 into a 1.3 cm die kit, and then applying 15 Ton pressure. The cylindrical pellet disc had a diameter of approximately 13 mm and 300 micrometre thickness (100 micrometre cathode and 200 micrometer electrolyte). It was then heated gently at 300 °C for 2 hrs at 5 °C/min to densify the cell.

2.4 Electrochemical performance test

The cell was tested in a Kittec Squadro muffle furnace from Fiaxell SOFC technologies. In this set-up, platinum meshes were used as contacts, with the cell, to act as combined current

collector and gas distributor. Humidified hydrogen and compressed air were passed through gas tight fittings, attached to the set up for the delivery of the gases to the cell. The current and the voltage from the cells were then measured with a Nuvant™ Powerstat 05 potentiostat and galvanostat. The measurements were carried out at temperatures between 300 - 500 °C. The ionic conductivity was calculated using the following equations [19]:

$$\sigma = \frac{l}{RS} \quad (1)$$

where, l is the electrolyte thickness, S is electrode area of the electrolyte surface and R is resistance in ohms (cell resistance).

$$R = \frac{l}{kA} \quad (2)$$

where, R is the resistance (ASR), k is conductivity, l is the electrolyte thickness and A is surface area [19].

$$\sigma \, T = \sigma^{o} \, exp\left[\frac{E_a}{kT}\right] \quad (3)$$

where, E_a is activation energy of conduction, T is absolute temperature, σ^{o} is pre-exponential factor and k is the Boltzmann Constant [19]. The Polarization curves were recorded between 300 - 500 °C with a fuel consisting of hydrogen and 4 - 20 % of water on the anode side and air on the cathode side. The long-time durability test was carried out in order to assess long-term static stability of the cell for 15 hrs.

3.0 Results and Discussions

3.1 FTIR analysis

Figure 1 shows the FTIR spectra for the sample calcined at 800 °C. This showed absorbance peaks at 425 cm^{-1}, 524 cm^{-1}, 588 cm^{-1}, 1023 cm^{-1}, 1072 cm^{-1} and 1448 cm^{-1}. The spectra for the samples calcined at 900 °C displayed peaks at 425 cm^{-1}, 534 cm^{-1}, 592 cm^{-1}, 1031 cm^{-1}, 1074 cm^{-1} and 1448 cm^{-1}. Absorbance peaks for the samples calcined at

1000 °C were noted at 421 cm^{-1}, 539 cm^{-1}, 619 cm^{-1}, 1031 cm^{-1}, 1074 cm^{-1} and 1454 cm^{-1}. The absorbance peaks generally for all the samples showed slight shifts to the right as the calcination temperature increased. The representative peaks at 1448 -1454 cm^{-1} are attributed to the C = O bonds from carbonate impurities from the precursor salts. The peaks between 1072 – 1074 cm^{-1} and at 1023 – 1031 cm^{-1} are attributed to M-O-M stretching vibrations.

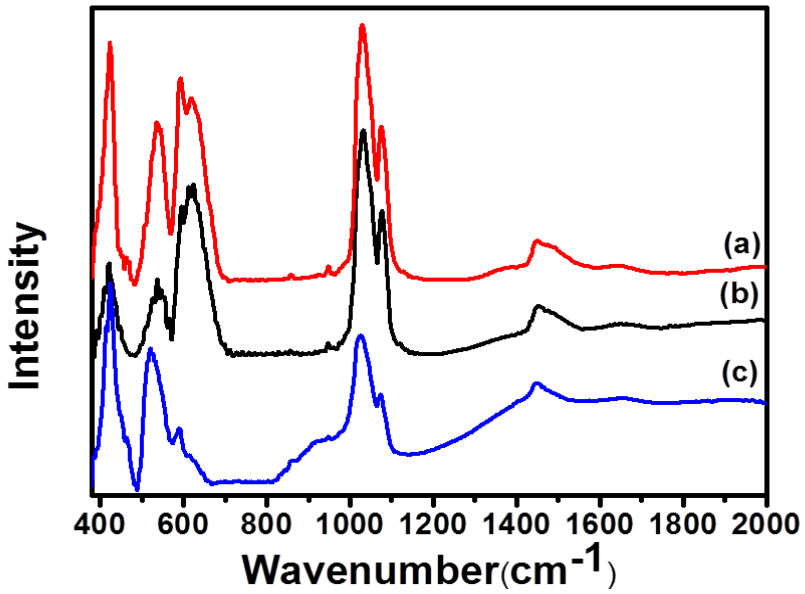

Figure 1: The FTIR spectra of CSFI samples calcined at (a) 1000 °C (b) 900 °C and (c) 800 °C.

The peaks seen from 588 – 619 cm^{-1} are caused by the metal-oxygen vibrations in the octahedral sites typically observed with spinel metals. Peaks indicative of the formation of metal oxides were also observed between 524 – 539 cm^{-1} and 421 – 425 cm^{-1}caused by the metal-oxygen bond vibrations of spinel structures in the tetrahedral sites. Similar observations have been reported in the literature [20].

3.2 Raman analysis

The Raman spectra of the cathode material are presented in Figure 2. The sample calcined at 800 °C had peaks at 255, 400, 508, 662, and 800 cm^{-1}. The peak at 255 cm^{-1} is attributed

to E_g active modes of Fe-O stretching mode of magnetite structure [21], the peak at 400 represents the F_{2g} active modes of CeO_2 fluorite structure and the peak at 508 cm^{-1} is indicative of Ce^{4+} substituted by larger cations such as Ce^{3+} [22]. The peaks at 662 cm^{-1} and 800 cm^{-1} are attributed to A_{1g} mode of Fe-O stretching modes of magnetite structure [21] and A_{1g} mode of iridium oxide [23, 24]. Peak shifts from those reported in the literature can be attributed to the materials forming defective fluorite phases [25].

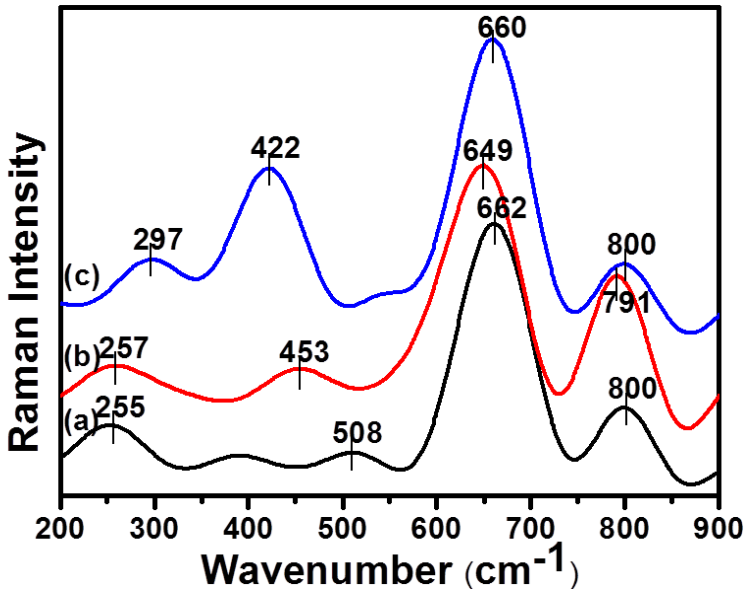

Figure 2: Raman Spectra of CSFIcalcined at (a) 800 °C (b) 900°C and (c) 1000 °C.

Spectra peaks for the sample calcined at 900 °C were observed at 257 cm^{-1}, 453 cm^{-1}, 649 cm^{-1} and 791 cm^{-1}. The large shift and increased intensity of the F_{2g} active mode of CeO_2 (453 cm^{-1}) indicates the materials have an overall structure similar to samarium doped ceria; however the separate vibrations at 649 and 791 cm^{-1} for the iron and iridium oxide metal-oxygen vibrations show that the calcination at 900 °C has not resulted in a solid solution, but the materials still have separate iron and iridium oxide phases.

At 1000 °C, Raman peaks were observed at 297, 422, 660 and 800 cm^{-1}. Comparing the samples calcined, there were red and blue shifts from the characteristic 460 cm^{-1} peak often observed for the F_{2g} mode of the CeO_2 fluorite structure [22]. The shifts with the change in

calcination temperature can be attributed to changes in the metal to oxygen bonds [25, 26]. Some authors have noted that when larger ions are substituted for Ce^{4+}, the F_2g active modes of ceria shift to lower values [23 - 26]. These changes can be used as an indication of defect sites within the ceria lattice, which may enhance the movement of oxygen anions [27].

3.3 XRD analysis

Figure 3 shows the representative XRD patterns of the cathode perovskite nanoparticles for the samples calcined at 800 °C, 900 °C and 1000 °C. The diffractogram revealed 3 phases for CeO_2 (fluorite cubic structure), Iron oxide (Fe_2O_3) hematite structure, and Iron samarium oxide ($FeSmO_2$) structure. The peaks observed for CeO_2 phase were at 2θ values of 28.56°, 32.39°, 33.17°, 47.44°, 56.55°, 59.17°, 63.28°, 69.34°, 76.77°, 79.12°, 88.38° and 95.50° indexed to 111, 110, 200, 220, 311, 222, 321, 400, 331, 420, 422 and 511 planes respectively [28]. $FeSmO_2$ structures revealed a phase of 301 at 2θ value of 69.34° [29], other peaks due to the iron oxide in the magnetite crystal phase were observed as relatively low intensity peaks at 2θ values of 63.16° and 95.15° indexed to 321 and 511 [24].

The average lattice parameter *a* is 5.4175 Å for CeO_2 phase, 5.129 Å for $FeSmO_2$ phase and 5.504 for Fe_2O_3 phase for the sample calcined at 1000 °C. The Bravais lattice is a face centred cubic (FCC) unit cell. This was calculated using the equation [24]:

$$a = \frac{\lambda}{2} \times sin \times \sqrt{h^2 + k^2 + l^2} \quad (4)$$

where, λ = X-ray wavelength and θ = 2θ value/2, *h, k, l* values are Miller indices of particular planes in the crystal. The mass of the unit cell for all samples was 1.3443×10^{-27} g for CeO_2 phase and 1.3492×10^{-27} g for Fe_2O_3 phase. This was calculated using the following equation:

$$\text{Mass of Unit Cell (M)} = \frac{(4atoms)(MolarMass)}{6.02 \times 10^{23} atoms/mol} \left[\frac{10^{-6} Mg}{g}\right]. \quad (5)$$

The density of the cell is 7.41 g/cm^3 for CeO_2 phase and 6.562 g/cm^3 for IrO_2 phase, and the following equation was used to calculate this value.

$$\text{Mass density} = \frac{mass(unit\ cell)}{Volume(unit\ cell)}. \quad (6)$$

Volume of unit cell was calculated to be 1.5984×10^{-28} cm^3 for CeO_2 phase and 0.8853×10^{-28} cm^3 for the Fe_2O_3 phase (from $v = a^3$ where a = $4R/\sqrt{2}$). The full width at half maximum (FWHM) in Table 1, increased as the calcination temperature increased. The smaller the FWHM, the larger the crystallite size. Hence, the crystallite size increased with decreasing calcination temperature from 1000 – 800 °C.

Table 1: The FWHM, Crystallite size, and Average particle size of CSFI calcined at (a) 800 °C (b) 900 °C and (c) 1000 °C.

Calcination Temperature (°C)	**Full Width at Half Maximum (FWHM) (°)**	**Crystallite Size (nm)**	**Particle Size (nm)**
800	0.1749	48.95 ± 1.4	27.41
900	0.2278	37.59 ± 0.87	22.98
1000	0.4381	19.54 ± 0.30	19.58

The varying changes in the FWHM for (111) peak reveals a change in the lattice size. In diffraction physics peak position are associated with lattice size, thus lattice expansion results in a change in peak position. The evidence of lattice expansion and the existence of large cations such as Ce^{3+} in this material [30]. In addition, once Ce^{3+} appears in the fluorite ceria structure; oxygen vacancies will be produced to sustain electrostatic stability according to the equation [30].

$$4Ce^{4+} + O^{2-} \longrightarrow 4Ce^{4+} + 2e^-/\boxdot + \frac{1}{2}O_2 \longrightarrow 2Ce^{4+} + 2Ce^{3+} + \boxdot + \frac{1}{2}O_2 \quad (7)$$

where $\boxdot$ represents an empty position (anion-vacant site) originating from the removal of O^{2-} from the lattice.

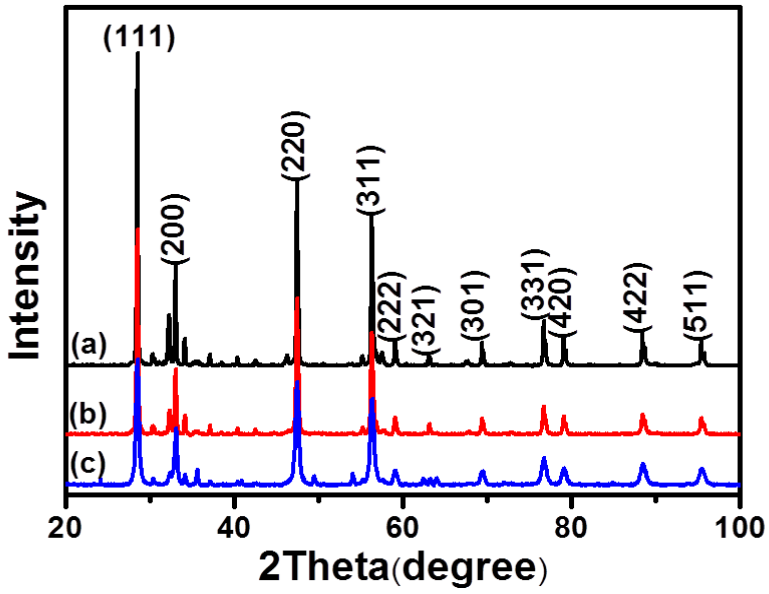

Figure 3: XRD patterns of CSFI calcined at (a) 1000 °C (b) 900 °C and (c) 800 °C.

The presence of the (111) thermodynamic phase followed by the (110) promotes the presence of oxygen vacancies, and (111) is the least active surface, followed by (100) and (110) [30]. These active surfaces promote the removal of oxygen, there by creating oxygen vacancies on the surface. The (111) plane, of the lattice expansion as per the FWHM calculations (Table 1), and Raman analysis confirm the substitution of the Ce^{4+} with Ce^{3+} in these materials, could enhance oxygen transport.

3.4 HRTEM analysis

Figure 4 presents representative transmission electron microscopy images for the samples calcined at 800 °C - 1000 °C. The images show that the materials have irregular shapes that varied in sizes with the change in calcination temperature. In diffraction physics peak position are associated with lattice size, thus lattice expansion results in a change in peak position.

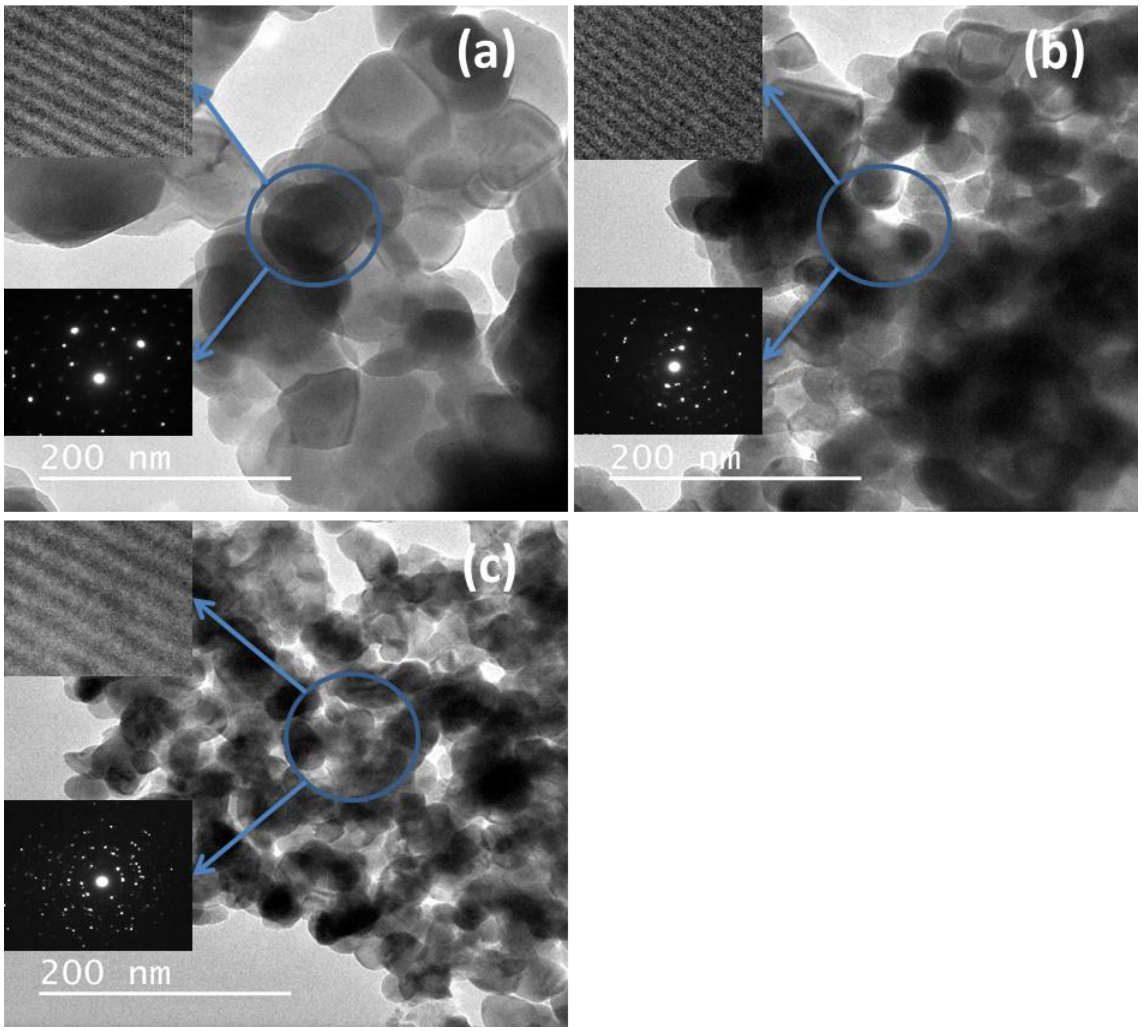

Figure 4: The HRTEM micrographs of CSFI calcined at (a) 1000 °C (b) 900 °C and (c) 800 °C.

The Lattice fringes for the samples calcined at 800 °C predominantly exposes the {111} planes of CeO_2 fluorite structure and {200} planes of $FeSmO_2$ structure for 900 °C and the {420} planes of CeO_2 structure for 1000 °C calcined samples. The selected diffraction pattern differed slightly in terms of the lattice and the arrangements of the particles.

3.5 SEM observations

The morphology of CSFI, as shown in Figure 5, showed the agglomeration of nanoparticles and the apparent voids between the particles changed with calcination temperature.

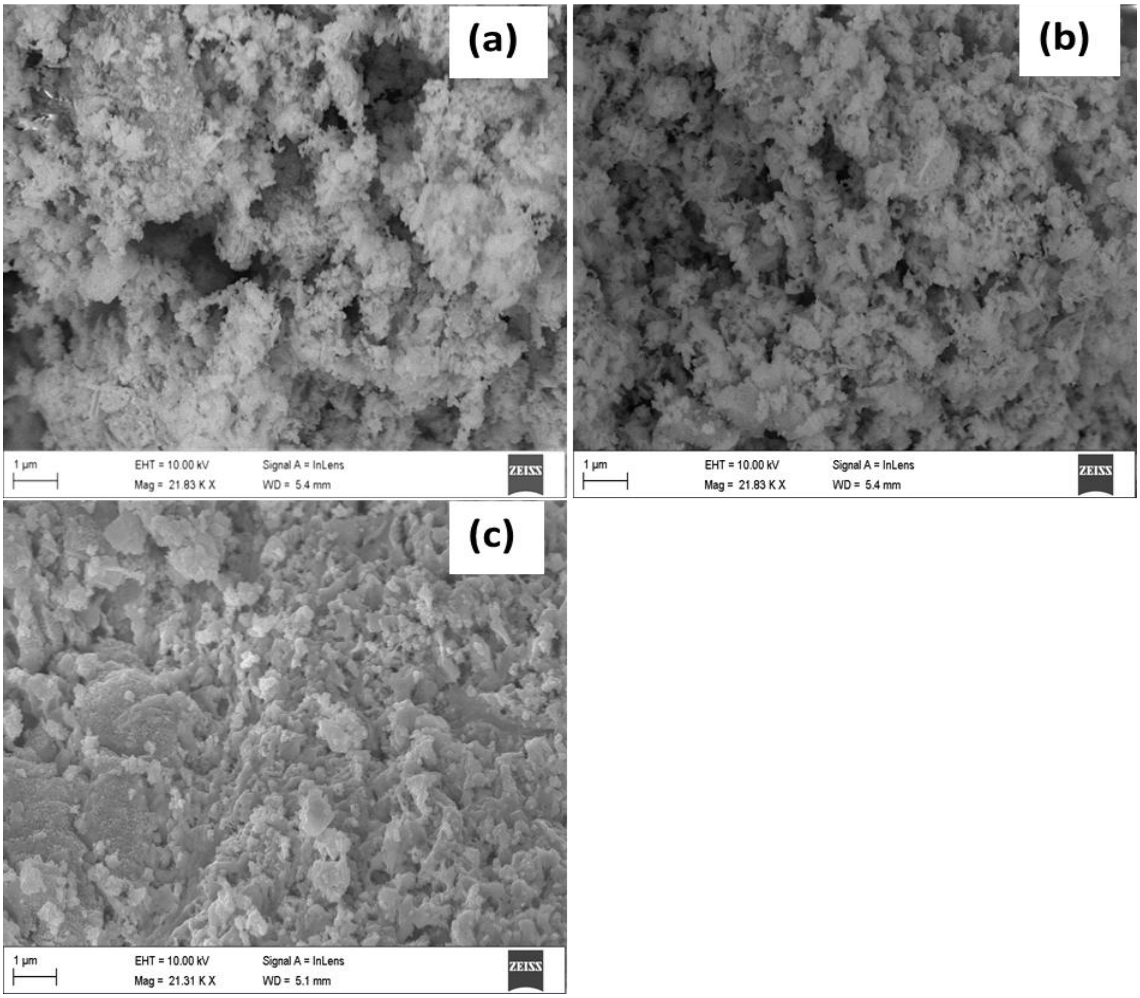

Figure 5: The SEM morphology of CSFI calcined at (a) 1000 °C (b) 900 °C and (c) 800 °C.

3.6 Thermogravimetric analysis

Thermogravimetric analysis of the samples, in air, is shown in Figure 6. In all of the sample profiles, there was a gradual weight loss from 30 - 250 °C due to desorption of carbondioxide. The samples calcined at 1000 °C showed a stable weight decrease throughout the entire process, while the samples calcined at 900 °C showed slight changes in weight loss from 300 °C – 600 °C, a slight weight increase followed by a weight decrease from 600 °C – 750 °C and a gradual weight increase from 750 °C -1000 °C. Furthermore, the samples calcined at 800 °C exhibited a weight increase from 250 °C – 550

°C followed by a gradual weight loss from 550 °C - 700 and a minimal weight increase throughout the process.

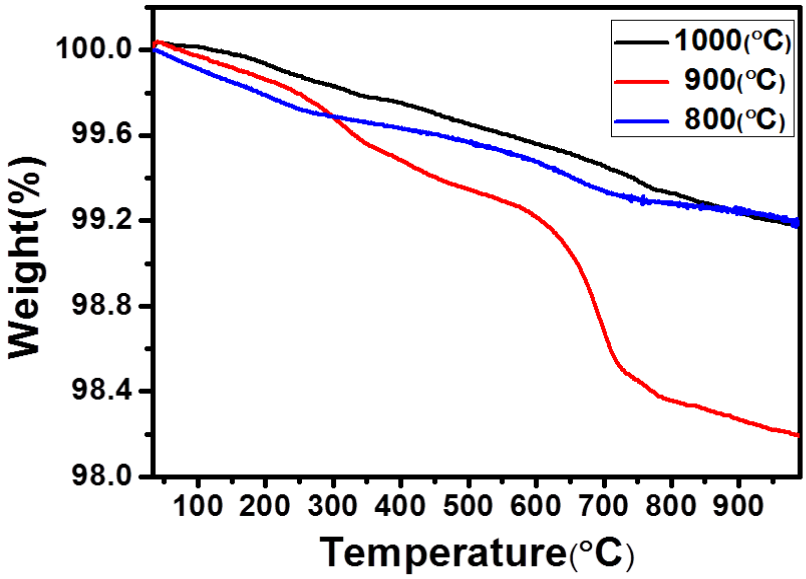

Figure 6: The thermogravimetric analysis of CSFI calcined at (a) 1000 °C (b) 900 °C and (c) 800 °C.

The weight changes of the samples were assumed to be mainly due to the removal of lattice oxygen from the surface [31, 32, 33], which can be represented by the equations [32].

$$2Fe_{fe}^{o} + O_{o}^{x} \rightarrow 2Fe_{fe}^{o} + V_{o}^{oo} + \frac{1}{2}O_2 \quad (8)$$

$$2Ir_{ir}^{o} + O_{o}^{x} \rightarrow 2Ir_{ir}^{o} + V_{o}^{oo} + \frac{1}{2}O_2 \quad (9)$$

where V_o^{oo} and O_o^x are representatives of oxide ion vacancy and oxide ions, respectively. Reduction reaction was more dominant in the samples calcined at a 1000 °C because of its steady weight decrease throughout the process. These losses result from thermal induced lattice oxygen loss caused by the increase in oxygen vacancies formation followed by a change in the valence of Ir and Fe ions from IV to III to maintain electrical neutrality. Thus

at 900 °C there is rapid loss of lattice oxygen which led to faster decomposition, than the other samples calcined at 800 °C and 1000 °C

3.7 Electrochemical Properties

The asymmetric cell comprised of NiO/SDC as anode, SDC/Na_2CO_3 as electrolyte and CSFI as cathode was tested using a Nuvant™ Powerstat 05 potentiostat and galvanostat and a Fiaxell SOFC Technologies™ open flange test set-up. Compressed air with a flow rate of 50 m^3/min and humidified hydrogen with a flow rate of 200 m^3/min was passed through the cell which was tested for 15 hrs.

3.7.1 Polarization Curve

Figure 7 shows the polarisation curves of CSFI cathode material calcined at 800 - 1000 °C. Each cell was tested in the temperature intervals of 300 - 500 °C. From Figure 7, the polarization curves revealed slight changes for the different materials and showed a linear fall in voltage with increase in current densities. This resulted from the change in resistance as current flows within the fuel cell. The drop in voltage increases as a result of kinetic and Ohmic losses within the cell. The major cause of polarisation in the system is the ohmic overpotential which result from the cell's internal resistance.It can be estimated from the effective distance between the cells components combined with the conductivity of the electrolyte [34].

Ohmic Overpotential within the cell decreased when testing temperature increased from 300 °C - 500 °C, exposing a high resistance at lower temperature as shown in Figure 7. Concentration losses were observed within the cell performance which occurs when current flows through the cell. The Concentration Overpotential increased from 300 °C - 500 °C resulting from the increase in diffusion of hydrogen ions and oxygen electrons from anode to cathode interface, and vice versa which is negligible when quality pure gases are used. The open cell voltage (OCV) values decreased with increasing measuring temperature. The OCV value was stable at 0.89 V for more than 15 hours at 500 °C, which is lower than the Nernst equation thermodynamic values. This was probably due to either gas crossover

between the composite electrolytes, thickness of the electrolyte, non-optimal pore geometry, or the presence of pin holes.

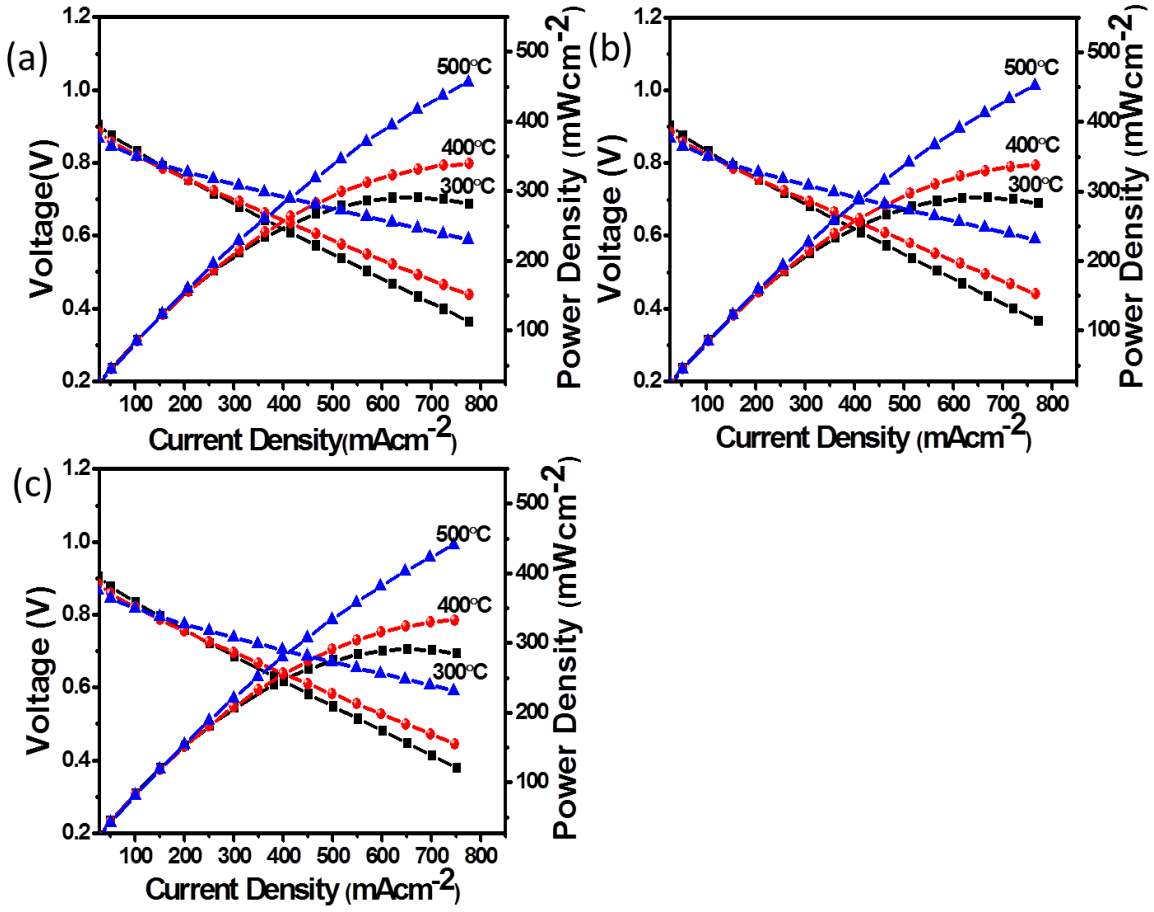

Figure 7: The polarization curve of CSFI calcined at (a) 1000 °C (b) 900 °C (c) 800 °C.

The power density of CSFI samples calcined at 800°C, 900 °C and 1000 °C, were taken at temperatures of 300 °C - 500 °C. The maximum power density at 300 °C was 308.56 mW/cm^2, 400 °C was 365.79 mW/cm^2 and 500 °C was 483.07 mW/cm^2. The maximum current densities were 776.77 mA/cm^2, 776.87 mA/cm^2 and 774.47 mA/cm^2 respectively. The maximum power density at 500 °C was exhibited by CSFI perovskite material calcined at 1000 °C with a low polarization resistance.

3.7.2 Area specific resistance

The normalised area specific resistance of the single cell in Figure 8, was calculated from the gradient of the linear portion at the centre of the I-V curve: where the Ohmic resistance is dominant. The ASR is a function of the cell design, material choice and the manufacturing or assembly processes used in producing a SOFC system.

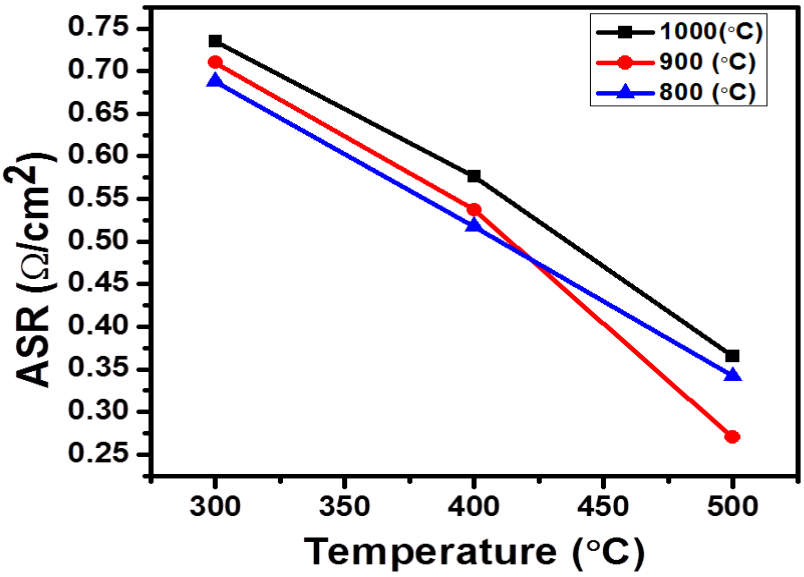

Figure 8: The Area Specific Resistance of CSFI calcined at (a) 1000 °C (b) 900 °C and (c) 800 °C.

In general the ASR decreased with increase in operating temperature, and this can be attributed to the changes observed in the material properties with an increase in calcination temperature which leads to an increase in the diffusion of oxygen due to lattice defects. The properties were determined by XRD, Raman and TGA analysis. The ionic conductivity of the cathode material also increases, which is a result of the enhanced absorbed oxygen to O^{2-} ion transitions due to the lattice defects. Previous works by Rupasov *et al.* [35] have shown that an increase in oxygen diffusion can lead to a reduction in the ASR.

It should be noted that the morphology of the material, microstructure of the electrodes, the calcination temperature and the change in porosity of the materials will affect the charge

transfer properties at the phase boundaries [36]. In addition, Park *et al.* [36], showed that samarium based materials calcined at 1000 °C were optimal in IT SOFCs, and our results show a similar trend although that SOFC tests were conducted at lower temperatures of 500 °C.

4.0 Conclusions

The physical-chemical properties of CSFI cathode materials were analysed using X-ray diffraction, Raman spectroscopy, Fourier transform infrared spectroscopy, electron microscopy, and TGA. The X-ray diffraction showed FWHM values of 0.1749 nm, 0.2289 nm and 0.4381 nm and mean crystallite sizes of 46.85 nm, 35.97 nm, 18.71 nm for the samples calcined at 800 °C, 900 °C and 1000 °C respectively. The Raman spectroscopy revealed the presence of metal oxides in the dominant perovskite phase with the presence of defect sites. The high resolution transmission electron microscopy revealed smaller particle sizes as the calcination temperature decreased. The TGA showed changes in oxygen transport with changes in the calcination temperature of the materials. The materials potential for use in SOFCs at temperatures between 300 – 500 °C for the sample calcined at 1000 °C produced the maximum power density of 483.07 mW/cm^2 at 500 °C powered for 15 hrs, and an area specific resistance of 0.342 Ω cm^2.

Acknowledgements

The authors thank the University of KwaZulu-Natal for granting access to research facilities, ESKOM-TESP and NRF THUTHUKA for their financial support.

References

1. H. Fukunaga, M. Koyama, N. Takahashi, C. Wen, K. Yamada, Reaction model of dense $Sm_{0.5}Sr_{0.5}Co_{O3}$ as SOFC cathode, Solid State Ionics. 132 (2000) 279-285.
2. T. Suzuki, M. Awano, P. Jasinski, V. Petrovsky, H.U. Anderson, Composite (La, Sr)MnO_3–YSZ cathode for SOFC, Solid State Ionics. 177 (2006) 2071-2074.

3. S.P. Jiang, W. Wang, Novel structured mixed ionic and electronic conducting cathodes of solid oxide fuel cells, Solid State Ionics. 176 (2005) 1351-1357.
4. C. Xia, W. Rauch, F. Chen, M. Liu, $Sm_{0.5}Sr_{0.5}CoO_3$ cathodes for low-temperature SOFCs, Solid State Ionics. 149 (2002) 11-19.
5. B. Wei, Z. Lu, X. Huang, S. Li, G. Ai, Z. Liu, W. Su, Electrochemical characteristics of $Ba_{0.5}Sr_{0.5}Co_{0.8}Fe_{0.2}O_{3-\delta}$–$Sm_{0.2}Ce_{0.8}O_{1.9}$ composite materials for low-temperature solid oxide fuel cell cathodes, Mater. Lett. 60 (2006) 3642 - 3646.
6. S. B. Adler, J. A. Lane, B. C. H. Steele, Electrode kinetics of porous mixed -conducting oxygen electrodes, J. Electrochem. Soc. 143 (1996) 3554-3564.
7. Z. P. Shao, S.M. Haile, A high-performance cathode for the next generation of solid-oxide fuel cells, Nature. 431 (2004) 170-173.
8. W. Zhu, Z. Lu, S. Li, B. Wei, J. Miao, X. Huang, K. Chen, N. Ai, W. Su, Study on $Ba_{0.5}Sr_{0.5}Co_{0.8}Fe_{0.2}O_{3-\delta}$–$Sm_{0.5}Sr_{0.5}CoO_{3-\delta}$ composite cathode materials for IT-SOFCs, J. Alloys Compd. 465 (2008) 274-279.
9. M. T. Colomer, B. C. H. Steele, J. A. Kilner, Structural and electrochemical properties of the $Sr_{0.8}Ce_{0.1}Fe_{0.7}Co_{0.3}O_{3-\delta}$ perovskite as cathode material for ITSOFCs, Solid State Ionics. 147 (2002) 41-48.
10. L. Zhang, R. Lan, A. Kraft, S. Tao, A stable intermediate temperature fuel cell based on doped-ceria–carbonate composite electrolyte and perovskite cathode, Electrochem. Commun. 13 (2011) 582-585.
11. X. F. Sun, R..S.Guo, J. Li, Preparation and properties of yttrium-doped $SrTiO_3$ anode materials, Ceram. Int. 34 (2008) 219-223.
12. H. Kishimoto, Y. P. Xiong, K. Yamaji, T. Horita, N. Sakai, M. E. Brito, H. Yokokawa, Stability of Ni base anode for direct hydrocarbon SOFCs, J. Chem. Eng. Jpn.40 (2007) 1178-1182.
13. N. F. P. Ribeiro, M. M. V. M. Souza, O. R. M. Neto, S. M. R. Vasconcelos, M. Schmal, Investigating the microstructure and catalytic properties of Ni/YSZ cermets as anodes for SOFC applications, Appl. Catal. A 353 (2009) 305.

14. J. Di, M. Chen, C. Wang, J. Zheng, L. Fan, B. Zhu, Samarium doped ceria–$(Li/Na)_2CO_3$ composite electrolyte and its electrochemical properties in low temperature solid oxide fuel cell, J. Power Sources 195 (2010) 4695-4699.
15. Q. L. Liu, K. A. Khor, S. H. Chan, High-performance low-temperature solid oxide fuel cell with novel BSCF cathode, J. Power Sources 161, 1(2006) 123-128.
16. X. Wang, Y. Ma, R. Raza, M. Muhammed and B. Zhu, Novel coreshell SDC/amorphous Na_2CO_3 nanocomposite electrolyte for low-temperature SOFCs, Electrochem. Commun. 10 (2008) 1617-1620.
17. L. Fan, C. Wang, M. Chen, J. Di, J. Zheng, B. Zhu, Potential low-temperature application and hybrid-ionic conducting property of ceria-carbonate composite electrolytes for solid oxide fuel cells, Int. J. Hydrogen Energy 36 (2011) 9987-9993.
18. M. Benamira, A. Ringuede, V. Albin, R. Vannier, L. Hildebrandt, C. Lagergren, M. Cassir, Gadolinia-doped ceria mixed with alkali carbonates for solid oxide fuel cell applications: I. A thermal, structural and morphological insight, J. Power Sources, 196 (2011) 5546-5554.
19. H. Okkay, M. Bayramoglu, M.F. Öksüzömer, $Ce_{0.8}Sm_{0.2}O_{1.9}$ synthesis for solid oxide fuel cell electrolyte by ultrasound assisted co-precipitation method, Ultrasonics Sonochemistry, 20 (2013) 978–983.
20. Y. Tao, J. Shao, J. Wang, W. G. Wang, Morphology control of $Ce_{0.9}Gd_{0.1}O_{1.95}$ nanopowder synthesized by sol–gel method using PVP as a surfactant, J. Alloys Compd. 484 (2009) 729-733.
21. O. N. Shebanova, P. Lazer, Raman spectroscopic study of magnetite ($FeFe_2O_4$): a new assignment for the vibrational spectrum, J. Solid State Chem. 174 (2003) 424-430.
22. M. Guo, J. Lu, Y. Wu, Y. Wang, M. Luo, UV and Visible Raman studies of oxygen vacancies in rare-earth doped ceria, Langmuir. 27 (2011) 3872-77.
23. A. V. Korotcov, Y. S. Huang, K. K. Tiong, D. S. Tsai. Raman scattering characterization of well-aligned RuO_2 and IrO_2 nanocrystals J. Raman Spectrosc. 38 (2007) 737-749.

24. C. B. Njoku, P. G. Ndungu, Synthesis and characterization of novel $Ce_{0.8}Sm_{0.2}Fe_{0.9}Ir_{0.03}Co_{0.07}O_{3-\delta}$ perovskite material and possible application as a cathode for low–intermediate temperature SOFCs, Mater. Res. Bull. 68 (2015) 100-108.

25. M. de los Reyes, K. R. Whittle, Z. Zhang, S. E. Ashbrook, M. R. Mitchell, L.-Y. Jang, G. R. Lumpkin, The pyrochlore to defect fluorite phase transition in $Y_2Sn_{2-x}Zr_xO_7$ RSC Advances 3 (2013) 5090-99.

26. Z. Wu, M. Li, J. Howe, H. M. Meyer, S. H. Overbury. Probing Defect Sites on CeO_2 Nanocrystals with Well-Defined Surface Planes by Raman Spectroscopy and O_2 Adsorption, Langmuir, 26 (2010) 16595-16606.

27. X Liu, K. Zhou, L. Wang, B. Wang, Y. Li, Oxygen Vacancy Clusters Promoting Reducibility and Activity of Ceria Nanorods, J. Am. Chem. Soc. 131 (2009) 3140-3141.

28. W. Yue, W. Zhou, Porous crystals of cubic metal oxides templated by cage-containing mesoporous silica, Journal of Materials Chemistry17 (2007) 4947-4952.

29. C. Felix, T. Maiyalagan, S. Pasupathi, B. J. Bladergroen, V. Linkov, Synthesis, characteri- sation and evaluation of IrO_2 based binary metal oxide electrocatalysts for oxygen evolution reaction, Int. J. Electrochem. Sci., 7 (2012) 12064 – 1207.

30. D. P. Rupasov, A. V. Berenov, J. A. Kilner, S. Y Istomin, E. V. Antipov, Oxygen diffusion in $Sr_{0.75}Y_{0.25}CoO_{2.62}$, Solid State Ionics., 197 (2011) 18-24.

31. A. Botea-Petcu, S. Tanasescu, V. Varazashvili, N. Lejava, T. Machaladze, M. Khundadze, F. Maxim, Thermodynamic data of $Ba_{0.6}Sr_{0.4}Co_{0.8}Fe_{0.2}O_{3-\delta}$ SOFC cathode material, Materials Research Bulletin 57 (2014) 184-189.

32. Z. Wenxia, Z. Lü, S. Li, B. Wei, J. Miao, X. Huang, K. Chen, N. Ai, W. Su, Study on $Ba_{0.5}Sr_{0.5}Co_{0.8}Fe_{0.2}O_{3-\delta}$–$Sm_{0.5}Sr_{0.5}CoO_{3-\delta}$ composite cathode materials for IT-SOFCs, J. Alloys Compd. 465 (2008) 274-279.

33. R. Mueller, H. K. Kammler, K. Wegner, S. E. Pratsinis, OH surface density of SiO_2 and TiO_2 by thermogravimetric analysis, Langmuir 19 (2003) 160-165.

34. X. Bingjun, Y. Bhawe, M. E. Davis, Spinel metal oxide-alkali carbonate-based, low-temperature thermochemical cycles for water splitting and CO_2 reduction, Chemistry of Materials 25 (2013) 1564-1571.

35. D. P. Rupasov, A. V. Berenov, J. A. Kilner, S. Y. Istomin, E. V. Antipov, Oxygen diffusion in $Sr_{0.75}Y_{0.25}CoO_{2.62}$, Solid State Ionics 197 (2011) 18-24.

36. I. Park, J. Choi, H. Lee, D. Shin, Optimization of $Sm_{0.5}Sr_{0.5}CoO_{3-\delta}$–$Sm_{0.2}Ce_{0.8}O_{2-\delta}$ composite cathodes fabricated by electrostatic slurry spray deposition, Ceram. Int. 9 (2013) 5561-5569.

CHAPTER 7

Characterisation and Electrochemical Properties of $Ce_{0.8}Sr_{0.2}Fe_{0.9}Ir_{0.04}Co_{0.06}O_{3-\delta}$ (CSFIC) Cathode Material for Application in Low Temperature SOFC

Summary

This chapter has been published in the Electrochemical Society (ECS) Transactions and has been structured according to the journal's format. This chapter has also been reformatted to incorporate further comments and corrections by the examiners

Abstract

In this study, the cathode CSFIC perovskite material has been prepared by Sol-gel technique and then tested for their characteristic application in solid oxide fuel cell. The crystal structure was tested using X-ray diffraction and the textural properties were tested using Raman spectroscopy and Fourier transform infrared spectroscopy. The morphology and microstructure was examined using scanning electron microscopy and high resolution transmission electron microscopy. The power density, current density and the DC polarization resistance were measured with a Nuvant ^{TM} potentiostat and galvanostat from Fiaxell SOFC technologies connected to the cell setup. These properties were tested for their potential application in low temperature solid oxide fuel cells from 300 to 500 °C. It exhibited a current density of 801.90 mA/cm^2, a power density of 471.59 mW/cm^2 and an area specific resistance (ASR) of 0.349 Ω cm^2.

Keywords: Solid Oxide Fuel Cell, cerium oxide, Iridium oxide, perovskites, nano-composites

1.0 Introduction

Solid oxide fuel cells (SOFCs) operating temperature has been a major interest for research in the last decade, the drive being towards the reduction of the operating temperatures. This is because of its cost and maintenance which has been of more importance. High operating temperature limits certain properties of solid oxide fuel cells [1- 4]. A major one is the Interdiffusion between the electrode and electrolyte boundaries causing sequestering layer formation. This causes strain and cracks to the cell because of the variation in the thermal expansion coefficient between the cells and densification of the electrodes.

On the other hand reducing the operating temperature of SOFCs has certain advantages; it broadens the choices for electrodes and electrolyte materials, reduces production and application cost, improves the overall lifetime and stability of the fuel cell. Several ways of reducing the operating temperature, can be achieved either by reducing the electrolyte thickness, or by using highly conductive electrolytes, such as doped ceria [5 – 9] as known by various researchers. For example Xia *et al.* [4] reported that cells operated at temperatures below 550 °C affected the performance of the cathode material especially when used with samarium doped ceria (SDC) electrolyte because their activation energy was very large.

However, this has aroused the interest of researchers to move to compounds with high ionic conductivities such as cobalt containing perovskite; which displayed high concentration of oxygen vacancy [10, 11]. Dusastre *et al* [12] reported on the effect of strontium on the interfacial resistance properties of cobalt perovskites at 590 °C. Zhang*et al.* [13] reported enhanced cathode conductivity and improved interfacial resistance less than 0.5 at 650 °C for $La_{0.6}Sr_{0.4}Co_{0.2}Fe_{0.8}O_3$ mixed with SDC-Ag. This was achieved due to an improved microstructure and better adhesion on the electrolyte. Strontium doped samarium cobaltite compounds mixed with samarium doped ceria ($Sm_{0.5}Sr_{0.5}CoO_3$-SDC) have also been reported as cathode material for low temperature and recorded an interfacial resistance of 0.18 Ω cm^2 at 600 °C with the addition of 30 % SDC phase [14]. Shao *et al.* [14] reported

$Ba_{0.5}Sr_{0.5}Co_{0.8}Fe_{0.2}O_{3-\delta}$ (BSCF) as cathode material for low temperature SOFC and it exhibited high oxygen diffusivity and high power output.

Hence, in this study, the cathode material was made with cerium because of its high oxygen ionic conduction properties and improved electrocatalytic activity. Iridium was also introduced to improve the catalytic activity and the electrical conductivity of $Ce_{0.8}Sr_{0.2}Fe_{0.9}Ir_{0.04}Co_{0.06}O_{3-\delta}$ (CSFIC) cathode material. Sol-gel technique was used to synthesize the cathode material [16, 17], as it can be used to produce ceramic oxide materials, with controlled structure and composition. It is simple, cost effective with high yield at room temperature [18, 19].

2.0 Experimental methods

2.1 Cell fabrication

The metal precursors: Strontium (III) acetylacetonate hydrate (99.9 % purity), Cerium (III) acetylacetonate hydrate, (99.9 % purity), Iron (III) acetylacetonate (97 % purity), Cobalt (II) acetylacetonate hydrate and Pluronic F-127 were purchased from Sigma-Aldrich (Pty) Ltd, South Africa. Iridium (III) acetylacetonate hydrate was purchased from Alfa Aesar UK. The materials were used as purchased and the cathode material nanoparticles are prepared by sol-gel technique with stoichiometric amounts of 0.0500 g of iridium $(acac)_3$, 0.6481 g of cerium $(acac)_3$, 0.1460 g of strontium $(acac)_3$, 0.0468 g of cobalt $(acac)_2$, and 0.5838 g of iron $(acac)_3$, were weighed out into a mixture of 50 ml and 10 ml of ethanol and deionized water respectively. The mixture was sonicated in an ultrasound bath (UMC 20, 50 kHz) for 30 mins and then heated to 80 °C to dry out the solvents on a hotplate while stirring the mixture. A solid gel was formed after 30 mins at 80 °C and was allowed to dry completely in an oven at 200 °C for 24 hours. Three different samples was made and then calcined in a muffle furnace (Kittec Squadro 1350) at temperatures of 800 °C, 900 °C and 1000 °C respectively for 10 hours at a heating rate of 2 °C/min to form perovskites.

The electrolyte material ($Ce_{0.8}Sm_{0.2}O_2/Na_2CO_3$) was also prepared by sol-gel synthesis and the stoichiometric amounts of Cerium $(acac)_3$ and Samarium $(acac)_2$ were weighed out into

50 ml of ethanol and 15 ml of deionized water. The mixture was then sonicated in an ultrasound bath (UMC 20, 50 kHz) for 30 mins and further allowed to dry on a hotplate while stirring at 80 °C for a further 30 mins. The mixture was then dried in an oven for 2 hrs at 100 °C and calcined in a muffle furnace for 4 hrs at 800 °C at a heating rate of 2 °C/min. The powder was then mixed with sodium carbonate in the ratio of 60:40 wt % electrolytes to Na_2CO_3. The electrolyte material was then combined with the cathode material to make a double layer of cylindrical pellet (disc) 13 mm in diameter and 300 μm thickness (100 μm cathode and 200 μm electrolyte). This was fabricated by uniaxial pressing the powder at 15 Ton pressure. The pellets made were then heated at 1050 °C for 2 hrs at 5 °C/min to densify the cell.

2.2 Characterization

The crystal structures of the perovskite nanocomposite were characterized using powder X-ray diffraction (XRD). The X-ray diffractogram was obtained using Bruker D8 Advance diffractometer with a Cu Kα radiation source operating at 40 kV and a wavelength of 1.5406 Å. High resolution transmission electron microscopy (HR-TEM) was used to obtain the morphology and microstructure of the perovskites. In HRTEM analysis, small amounts of the samples were poured in ethanol and sonicated for 5 mins, it was then drop-dried onto a carbon coated copper TEM grid and then examined on a JOEL 2100 HRTEM (200 kV accelerating voltage, beam current of 110 μA and a current density of 2.4 pA/cm^2).

The perovskite powders were pressed onto carbon tape coated aluminium stubs and gold coated for SEM observations on a ZEISS FEGSEM Ultra Plus. The Infrared spectra were collected on a Perkin Elmer 1200 ATR - FTIR and the Raman analysis was done on a DeltaNu advantage 532™ Raman Spectrometer (100mW Nd:YAG laser with an excitation wavelength of 532 nm). The heat stability of the cathode nanocomposite was analysed by thermogravimetric analysis using Perkin Elmer simultaneous thermal analyser STA 6000. It was heated in air at 30 ml/min from 30 °C to 1000 °C at a ramping rate of 10 °C/min.

2.3 Electrochemical characterisation

The asymmetrical cells were tested at 300 to 500 °C in 20 % deionized H_2O/H_2 mixture and air. A platinum mesh was placed on both sides of the electrode and used as a current collector. The flow of gases was controlled by flow metres and the humidified gas was bubbled through a water bottle. For each cycle the polarisation curve was collected at constant voltage and current measurements were collected from a Nuvant™ Powerstat 05 potentiostat and galvanostat, attached to the SOFC device. The SOFC device measured the polarisation resistance and the direct current (DC) conductivity of the material. The ionic conductivity was calculated using the Equation below [20]:

$$\sigma = \left[\frac{L}{RS}\right] \quad (1)$$

where, L is electrolyte thickness, S is electrode area of the electrolyte surface and R is resistance in ohms (cell resistance). The activation energy and the DC electrical conductivity were calculated using the following Arrhenius relationship [21]:

$$\sigma = \sigma^{o}\, exp\left[\frac{E_a}{kT}\right] \quad (2)$$

where, E_a is activation energy of conduction, T is Absolute temperature, σ° is pre-exponential factor and k = Boltzmann Constant.

3.0 Results and Discussion

3.1 Powder XRD analysis

Figure 3 shows the XRD diffractogram of the perovskite cathode materials calcined at 800 °C, 900 °C, and 1000 °C, exhibited 3 phases namely lattices of iron oxide (Fe_2O_3) hematite structure, cerium oxide (cerianite) structure and iron samarium oxide ($FeSmO_2$) structure with peaks observed at 2θ values of 28.56°, 32.39°, 33.17°, 39.90°, 47.44°, 56.55°, 57.88°, 59.33°, 63.16°, 68.05°, 69.34°, 76.89°, 79.27°, 88.50° and 95.15° indexed to 111, 110, 200, 211, 220, 311, 018, 222, 321, 321, 410, 400, 331, 420, 422 and 511 respectively. The

average lattice parameter a is 5.43 Å for the predominant CeO_2 phase and the Bravais lattice is face centred cubic unit cell.

The diffractogram exhibited sharper peaks and the peak intensities increased with increase in calcination temperature and decreased from the lowest to the highest 2θ values with the 111 peak as the most intense peak. This is because an increase in temperature increases the intensity of the XRD peak. The full width at half maximum (FMWH), in Table 1 showed increasing values with decrease in calcination temperature. This revealed that samples calcined at 1000 °C exhibited larger crystallite size and the sample calcined at 800 °C exhibited the smaller crystallite size. This can be confirmed on the HRTEM micrograph which showed smaller particles at 800 °C.

Table 1: The crystallite size, and average particle size of CSFIC calcined at (a) 800 °C (b) 900 °C and (c) 1000 °C.

Calcination Temperature (°C)	Crystallite Size (nm)	Average Particle Size (nm)
800	27.32 ± 0.63	20.04
900	47.104 ± 1.25	39.05
1000	64.780 ± 2.24	49.88

In recent times researchers have shown that the presence of 111 active peak is the least active surface for the removal of oxygen [22]. The presence of the 111 plane and the lattice expansions showed by the XRD analysis, proposes proof of the presence of Ce^{3+} in these materials [23]. The presence of Ce^{3+} in fluorite ceria structure produces oxygen vacancies to sustain electrostatic stability as shown in the Equation: [24]

$$4Ce^{4+} + O^{2-} \longrightarrow 4Ce^{4+} + 2e^{-}/\boxdot + \frac{1}{2}O_2 \longrightarrow 2Ce^{4+} + 2Ce^{3+} + \boxdot + \frac{1}{2}O_2 \quad (3)$$

where $\boxdot$ represents an empty position (anion-vacant site) originating from the removal of O^{2-} from the lattice. The Raman spectra revealed the presence of large size oxygen vacancy

clusters through surface defects, which promotes the transformation of Ce^{4+} to Ce^{3+} for CeO_2^- based materials.

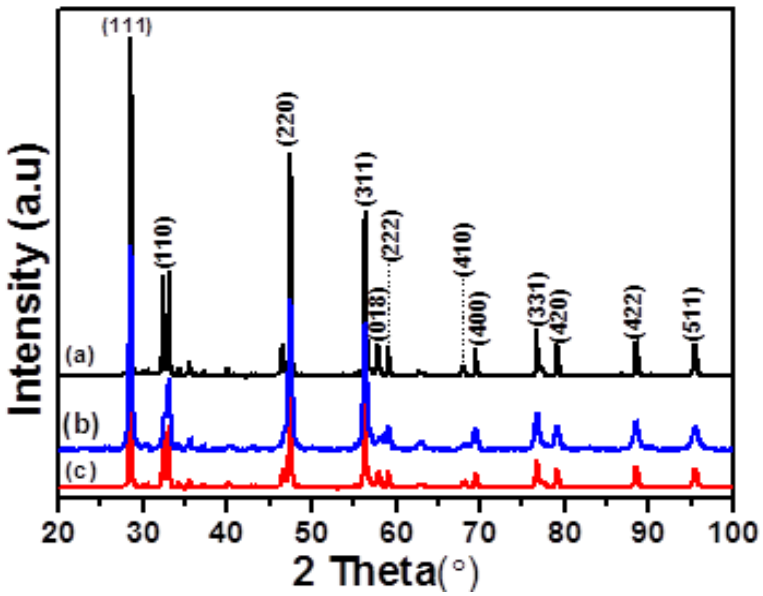

Figure 1: XRD diffractogram of CSFIC calcined at (a) 1000 °C (b) 900 °C and (c) 800 °C.

3.2 FTIR analysis

Figure 2 shows the absorbance peaks at 1446.53 – 1454.45 cm^{-1} which are attributed to C = O bonds from carbonate impurities for samarium doped ceria [25]. The bands at 1026.89 cm^{-1} and 1072.02 cm^{-1} were visible for the samples calcined at 800 °C. The wave numbers at 1031.64 cm^{-1} and 1074.39 cm^{-1} were visible for the 900 °C calcined sample, 1029.26 cm^{-1} and 1074.39 cm^{-1} were visible for 1000 °C.

These bands are attributed to the vibration of the metal (M) to oxygen bond, caused by the M-O-M stretching vibration. The variations in the peaks mentioned above are as a result of the difference in the M-O-M distances. Peaks were also evident at 419.58 cm^{-1}, 425.13 cm^{-1}, 419.58 cm^{-1} for the samples calcined at 800 °C, 900 °C and 1000 °C respectively, indicating the formation of spinel metals because these bands are common characteristics of spinel structures.

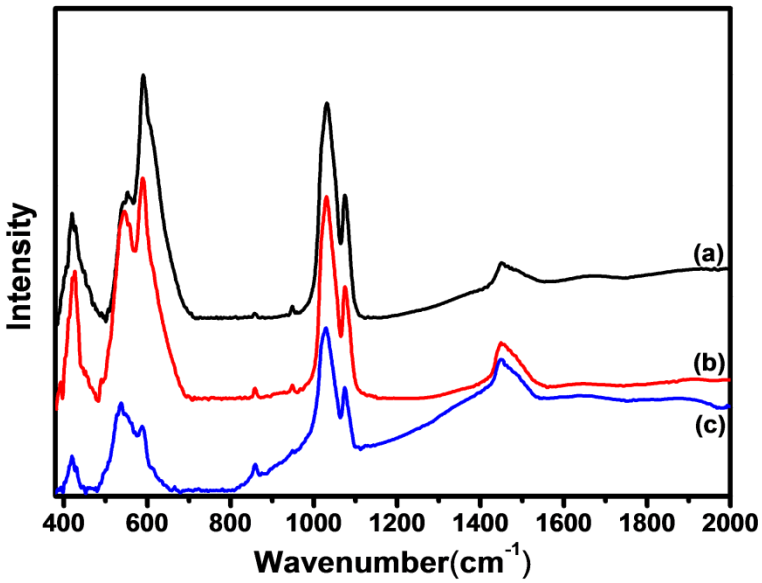

Figure 2: FTIR Spectra of CSFICcalcined at (a) 800 °C (b) 900 °C and (c) 1000 °C.

This is caused by metal~oxygen vibrations in the tetrahedral sites and the peaks observed at 534.59 cm^{-1}, 542.31 cm^{-1} and 588.24 cm^{-1}, 550.23 cm^{-1} and 590.61 cm^{-1} from 800 to 1000 °C are vibrations in the octahedral sites [26, 27]. According to Waldron [28], the vibration of unit cell of the cubic spinel can be constructed in the tetrahedral (A) sites and octahedral (B) sites. The change in band position is expected because of the difference in the $M^{+}– O_{2}–$ distances for the tetrahedral and octahedral sites. The deduction is also confirmed by XRD analysis [27].

3.3 Raman analysis

The Raman spectra of the perovskite material shown in Figure 3 showed active Raman peaks for the samples calcined at 1000 °C at 260 cm^{-1}, 381 cm^{-1}, 502 cm^{-1}, 639 cm^{-1} and 789 cm^{-1}. The peak at 260 cm^{-1} represent the E_g symmetrical bend of hematite structure [29 - 31]. The representative peak usually occurs at 245 cm^{-1}, indicating a blue shift due to a change in the iron oxide phase. 381cm^{-1} and 639 cm^{-1} peaks represent the E_g stretching modes of Fe-O magnetite structure and A_{1g} of Fe-O stretching modes of magnetite structure respectively [32]. This shows the formation of an iron oxide double crystal structure in the

material. A_{1g} symmetry mode of CeO_2 fluorite structure was observed at 789 cm^{-1} [29 - 31]. This is noticed by the intensity of the peak. The peak at 502 cm^{-1} signifies the E_g mode of IrO_2 rutile structure [33], however when IrO_2 is mixed with CeO_2 this peak occurs at 462 cm^{-1} [34] signifying the distribution of IrO_2nanocrystallites within the samarium doped ceria matrix.

The samples calcined at 900 °C displayed peaks at 251 cm^{-1} showing the E_g symmetrical bend of hematite structure. The peaks at 378 cm^{-1} and 635 cm^{-1} represent the E_g stretching modes of Fe-O magnetite structure and A_{1g} of Fe-O stretching modes of magnetite structure. Peaks at 500 cm^{-1} and 793 cm^{-1} signifies the E_g mode of IrO_2 rutile structure and A_{1g} symmetry mode of CeO_2 fluorite structure respectively. In comparison with the spectra for 1000 °C there was shift to lower values indicating a redshift.

For 800 °C, peaks were observed at 798 cm^{-1}, 658 cm^{-1}, 519 cm^{-1} and 415 cm^{-1} and 262 cm^{-1}. The peaks at 658 cm^{-1} and 415 cm^{-1} denotes the A_{1g} of Fe-O stretching modes of magnetite structure and E_g stretching modes of Fe-O magnetite structure. Peaks at 798 cm^{-1} represent A_{1g} symmetry mode of CeO_2 fluorite structure. The peaks at 519 cm^{-1} and 262 cm^{-1} represents the E_g mode of IrO_2 rutile structure and E_g symmetrical bend of hematite structure respectively. When compared to the peaks for the sample calcined at 900 °C, there was a shift to higher values. These variations occurred with the change in calcination temperature. This is because the ordering level of the samples increased with increasing calcination temperatures and the lattice becomes more perfect, leading to the change in the position of the defect sites.

Furthermore, lowering of the peak intensities and the broadening of the peaks observed also were as a result of the change in the calcination temperature and the presence of the infiltrated metals in the CeO_2 based material. This lowers the symmetry of the Ce-O bond, which also corresponds to the decreasing concentration of the CeO_2-type complex in the sample. The surface defects present in these spectra, show linear clusters of oxygen vacancies formed at the calcination temperatures used [35].

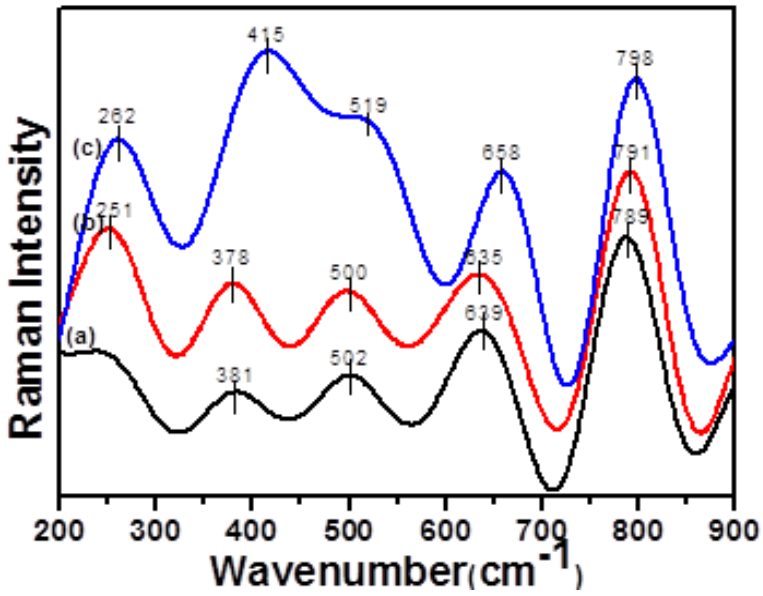

Figure 3: Raman spectra of CSFIC calcined at (a) 1000 °C (b) 900 °C and (c) 800 °C.

It has been reported that the presence of surface defect, such as large size oxygen vacancy clusters, would promote the transformation of Ce^{4+} to Ce^{3+} for CeO_2-based materials [36].This enhances the catalytic effects of the CeO_2 based materials.

3.4 HRTEM observations

Figure 4 reveals the micrograph of the samples calcined at 800 °C - 1000 °C. The nano crystals revealed irregular shapes that varied in sizes with the change in calcination temperature. The Lattice fringes for the samples calcined at 800 °C predominantly exposes the {111} planes of CeO_2 fluorite structure and {200} planes of $FeSmO_2$ structure for 900 °C and the {420} planes of CeO_2 structure for 1000 °C calcined samples. The presence of {111} planes reveals the presence of the formation of oxygen vacancy, which corresponds to the theoretical prediction [36] that the vacancies formation energy follows the order of {110} < {100} < {111}.The low magnification image exposes dark spots predicting the presence of defect sites as shown in Raman spectra [38]. The selected diffraction pattern differed slightly in terms of the lattice and the arrangements of the particles.

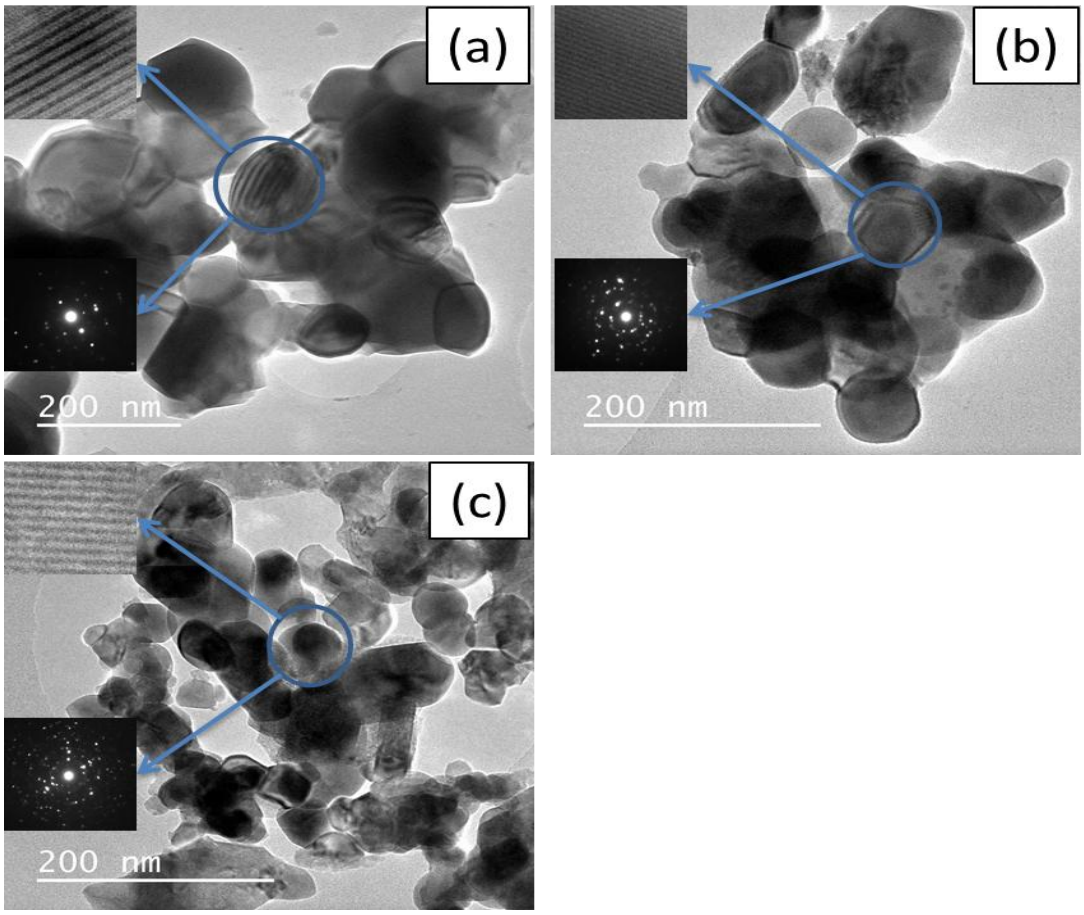

Figure 4: The HRTEM micrograph of CSFIC calcined at (a) 1000 °C (b) 900 °C and (c) 800 °C.

3.5 SEM observations

Figure 5 shows that the morphology of the cathode material revealing particles of different sizes, assumed to be nanoparticles in agglomerate formation. The surfactant used increased the agglomeration separation of the particles leading to bigger pore spaces, which decreased as the calcination temperature decreased. These pore spaces formed allow the diffusion of gases through the electrodes. The bigger the pore sizes the faster the rate of diffusion which enhances the performance of the cathode material. This corroborates with

the HRTEM micrograph which revealed smaller particle sizes as the calcination temperature decreased.

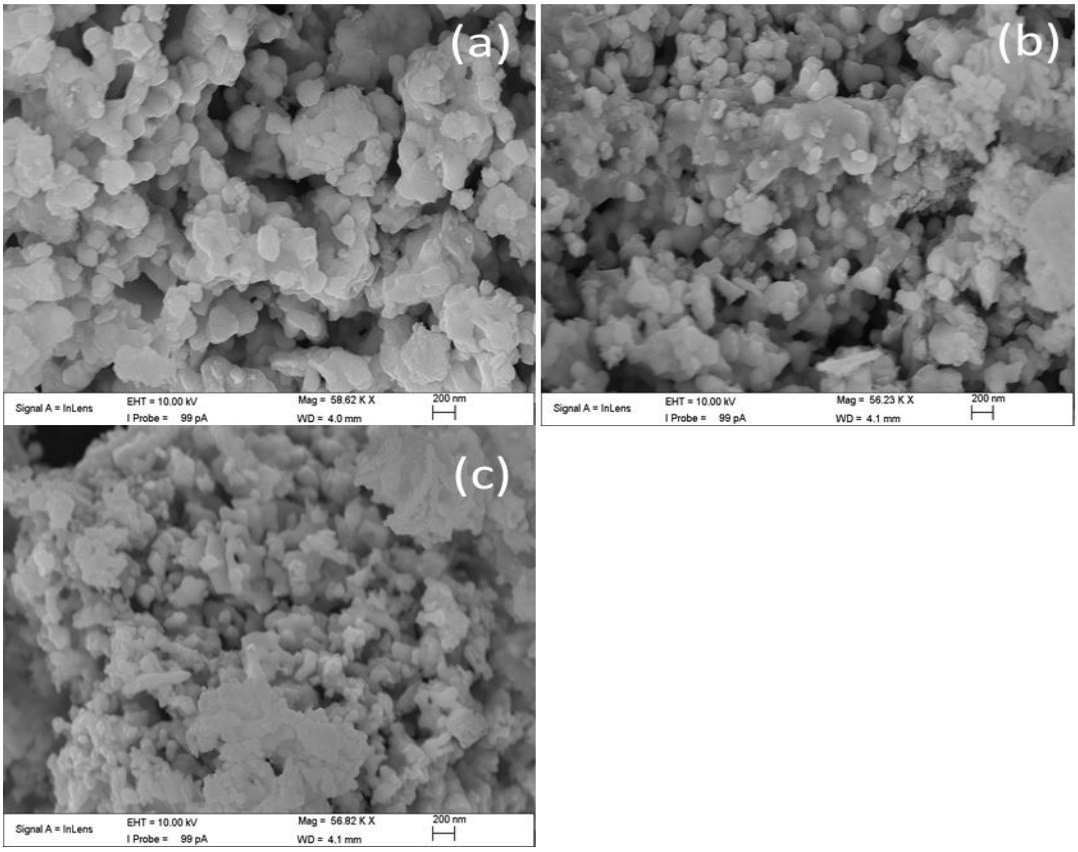

Figure 5: SEM morphology of CSFIC calcined at (a) 1000 °C (b) 900 °C and (c) 800 °C.

3.6 Thermogravimetric analysis

Figure 6 shows that the thermogravimetric analysis of the sample calcined at 1000 °C. Showed a gradual weight loss from 30 °C - 250 °C due to desorption of carbondioxide occurs. A gradual weight loss was observed from 30 °C – 250 °C then a minimal weight increase from 250 °C to 400 °C and a weight loss from 400 °C – 1000 °C for the sample calcined at 900 °C. The sample calcined at 800 °C showed a different routine from the other samples, there was a gradual weight loss from 35 °C to 250 °C due to desorption of

physically absorbed water, then a weight increase from 250 °C – 550 °C , a gradual weight loss from 550 °C - 750 °C and a small weight increase throughout the process.

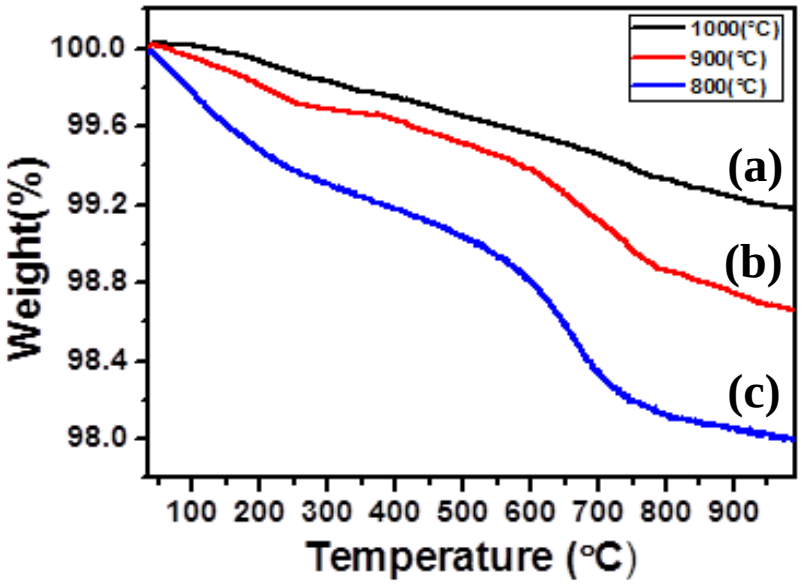

Figure 6: The thermogravimetric analysis of CSFIC calcined at (a) 1000 °C (b) 900 °C and (c) 800 °C.

The weight changes of the samples were assumed to be mainly due to the behaviour of lattice oxygen as indicated by the Equations [39]:

$$2\mathrm{Fe}_{fe}^{oo} + O_O^X \longrightarrow 2\mathrm{Fe}_{fe}^{x} + V_o^{oo} \quad (4)$$

$$2\mathrm{Co}_{co}^{oo} + O_O^X \longrightarrow 2\mathrm{Co}_{co} + V_o^{oo} + \frac{1}{2}\mathrm{O}_2 \quad (5)$$

where V_o^{oo} and O_o^x represent oxide ion vacancy and oxide ions, respectively. Reduction reaction was more dominant in the samples calcined at a 1000 °C because of its gradual weight loss [40] throughout the process. This is as a result of thermal induced lattice oxygen loss caused by the increase in oxygen vacancies formation complemented by a change in the valence of Co and Fe ions from IV to III to maintain electrical neutrality. This causes a shift in the equilibrium positions of equations 4 and 5 to the right accompanied by a weight reduction. Furthermore, the starting temperature for lattice oxygen loss was earlier

in the samples calcined at 1000 °C and decreased to the samples calcined at 800 °C. The weight losses also increased with decrease in the calcination temperature of the material. This means that the calcination temperature reduces the temperature of the thermal reduction; hence lattice O_2 becomes more active at lower temperature. In conclusion the samples showed high thermal stability and thermal reduction of the materials started occurring at lower temperatures and faster with limited weight loss at higher calcination temperatures; hence the material is suitable for low temperature SOFC.

3.7 Electrochemical properties

The symmetrical cells were tested using a Kittec SQUADRO muffle furnace and a Nuvant potentiostat and galvanostat was used to measure the current and voltage. 50 m^3/min of compressed air and 200 m^3/min of humidified hydrogen mixed with 4 – 20 % water was passed through the cell and it was tested for 15 hrs.

3.7.1 Polarisation curve

Figure 7 shows the electrochemical property of $Ce_{0.8}Sr_{0.2}Fe_{0.9}Ir_{0.04}Co_{0.06}O_{3-\delta}$ cathode material. The polarization properties were tested in air and humidified hydrogen (H_2 + 10% H_2O) as fuel at temperature intervals of 300 – 500 °C. The thickness of the electrolyte was 0.03 mm, the cathode material was 0.02 mm and the anode was 0.045 mm. The polarization curves exhibited a linear fall in voltage characteristics as the current density increased. This development is due to the resistance to current flow, which denotes that an increase in current causes an increase in the voltage drop.

The OCV values of the tested cells decreased from 300 – 500 °C and were stable at 0.86 V for more than 15 hrs at 500 °C for all calcined samples. This value is lower than the Nernst equation thermodynamic values, which are possible by 2 reasons, reduction in hydrogen pressure at the anode and electrolyte interface by the anode materials. Crossover of gases flowing through the composite electrolyte because of change in temperature. These could leave residual pores and leakages through the connected pore in the cathode/SDC electrolyte layer.

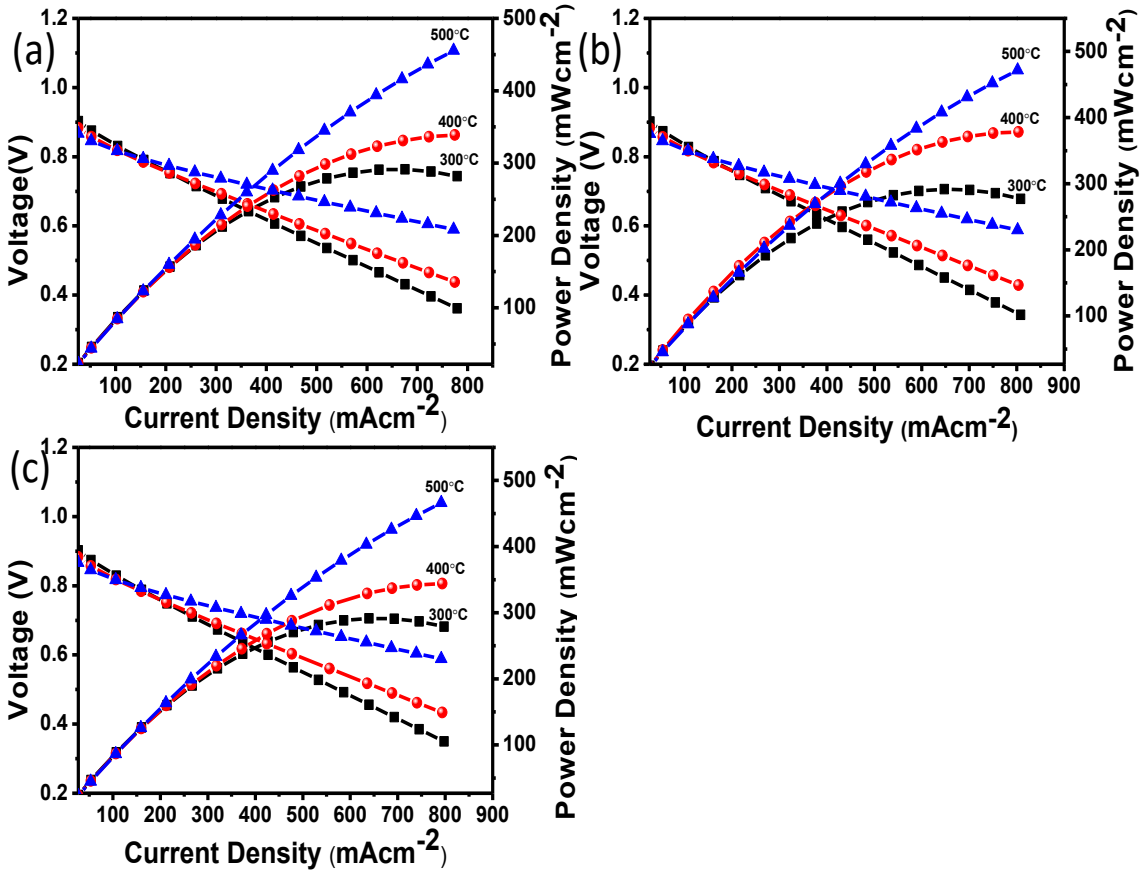

Figure 7: The polarization curve of CSFIC calcined at (a) 1000 °C (b) 900 °C (c) 800 °C measured at 300, 400 and 500 °C.

The linear fall reduced from 300 – 500 °C, which was instigated by these reasons. Increase in ohmic and concentration losses from the internal resistance of the cell, which are produced by the effective distance between the cell components and its ionic conductivity. As the measuring temperature increased from 300 - 500 °C the ionic conductivity increased, this influenced the reduction of adsorbed molecular oxygen to O_2 ions and improves the diffusion of these ions to the electrode/electrolyte interface. The increase in temperature increased the diffusion of the ions to and fro the electrodes, the discharge of the ions to form hydrogen atoms and oxygen atoms on the surface of the electrode and the formation of water molecules. The increase in the overall rate of the diffusion process reduces polarisation losses/resistance; hence, the losses were smaller at 500 °C.

3.7.2 Area Specific Resistance

Figure 8 shows the normalised area specific resistance (ASR) of the cell. This is calculated from the gradient of the linear fall, at the centre of the polarisation curve, where the ohmic resistance is dominant. This is reported as a plot of cell potential against current density.

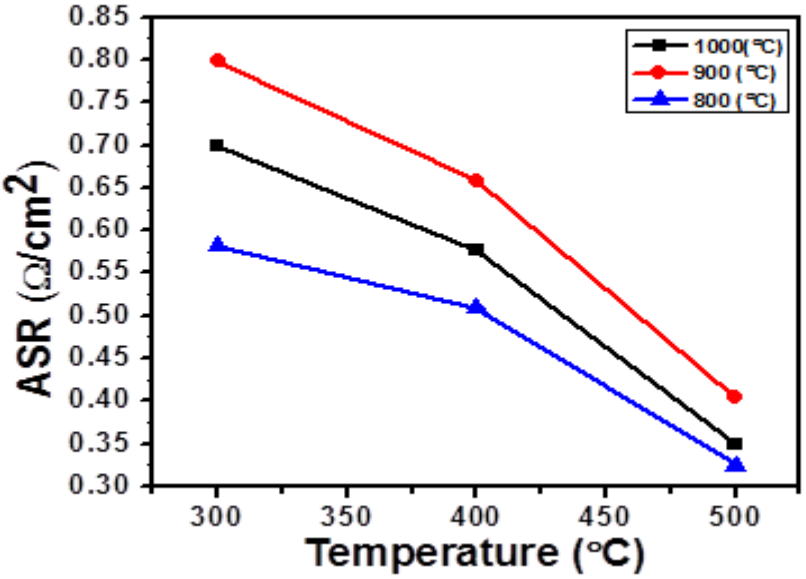

Figure 8: The Area Specific Resistance of CSFIC at (a) 1000 °C (b) 900 °C and (c) 800 °C.

The ASR values when measured at 500 °C showed varying changes of 0.324 Ω cm^2 for the samples calcined at 800°C, 0.403 Ω cm^2 for 900°C and 0.349 Ω cm^2 for 1000 °C. This is a function of the cell design, material choice and manufacturing technique. The ASR reduced with increasing measuring temperature and reduced slightly with decreasing calcination temperature. Subsequently increase in temperature changes the material properties and leads to an increased oxygen loss from the lattice and increasing the total overall diffusion processes thereby reducing polarisation resistance.

The power density displayed maximum values of 291.72 mW/cm^2 at 300 °C, 344.72 mW/cm^2 at 400 °C and 471.59 mW/cm^2 at 500 °C. The maximum power densities were displayed by the samples calcined at 900 °C and the power density increased with

increasing measuring temperature. This resulted from increase in ionic conductivity at higher temperature and higher ionic conductivity increases the voltage. The product of the voltage and its current density increases the power density.

4.0 Conclusions

The performance of the cathode composite material CSFIC was investigated by X-ray diffraction, IR spectroscopy, Fourier transform infrared spectroscopy, thermogravimetric analysis and the electrochemical properties. The XRD diffractogram exhibited FWHM value of 0.127 nm, 0.174 nm and 0.299 nm and mean crystallite sizes of 64.78 nm, 47.10 nm, and 27.32 nm for 1000 °C, 900 °C and 800 °C respectively. This implies that the crystallite size and particle sizes increased with increasing calcination temperature as shown on the micrograph. The thermogravimetric analysis confirmed that the material is stable when heated to 1000 °C. The samples decreased in weight as the calcination temperature increased. The sample calcined at 900 °C produced the highest power density of 471.59 mW/cm^2 and a current density of 801.9 mA/cm^2 at 500 °C powered for 15 hours, and an area specific resistance of 0.349 Ω cm^2. The properties exhibited revealed that the material is a promising cathode material for low temperature solid oxide fuel cell.

Acknowledgements

The authors thank the University of KwaZulu-Natal, for a conducive environment, ESKOM - TESP and NRF THUTUKA for their financial support.

References

1. Fukunaga, H., Koyama, M., Takahashi, N., Wen, C. and Yamada, K., 2000. Reaction model of dense $Sm_{0.5}Sr_{0.5}CoO_3$ as SOFC cathode. *Solid State Ionics*, *132*(3), pp.279-285.
2. Suzuki, T., Awano, M., Jasinski, P., Petrovsky, V. and Anderson, H.U., 2006. Composite (La, Sr) MnO_3–YSZ cathode for SOFC. *Solid State Ionics*, *177*(19), pp.2071-2074.

3. Jiang, S.P. and Wang, W., 2005. Novel structured mixed ionic and electronic conducting cathodes of solid oxide fuel cells. *Solid State Ionics*, *176*(15), pp.1351-1357.
4. Xia, C., Rauch, W., Chen, F. and Liu, M., 2002. $Sm_{0.5}Sr_{0.5}CoO_3$ cathodes for low-temperature SOFCs. *Solid State Ionics, 149*(1), pp.11-19.
5. Will, J., Mitterdorfer, A., Kleinlogel, C., Perednis, D. and Gauckler, L.J., 2000. Fabrication of thin electrolytes for second-generation solid oxide fuel cells. *Solid State Ionics*, *131*(1), pp.79-96.
6. Mogensen, M., Sammes, N.M. and Tompsett, G.A., 2000. Physical, chemical and electrochemical properties of pure and doped ceria. *Solid State Ionics*, *129*(1), pp.63-94.
7. Xia, C. and Liu, M., 2001. A simple and cost-effective approach to fabrication of dense ceramic membranes on porous substrates. *Journal of the American Ceramic Society*, *84*(8), pp.1903-1905.
8. Xia, C., Lang, Y. and Meng, G., 2004. Recent advances to the development of low-temperature solid oxide fuel cells. *Fuel Cells*, *4*(1-2), pp.41-47.
9. Xia, C. and Liu, M., 2001. Low-temperature SOFCs based on $Gd_{0.1}Ce_{0.9}O_{1.95}$ fabricated by dry pressing. *Solid State Ionics*, *144*(3), pp.249-255.
10. Steele, B.C.H., 2000. Appraisal of $Ce_{1-y}Gd_yO_{2-y/2}$ electrolytes for IT-SOFC operation at 500 °C. *Solid state ionics*, *129*(1), pp.95-110.
11. Maguire, E., Gharbage, B., Marques, F. M. B. and Labrincha, J. A., 2000. Cathode materials for intermediate temperature SOFCs. *Solid State Ionics*, *127*(3), pp.329-335.
12. Dusastre, V. and Kilner, J. A., 1999. Optimisation of composite cathodes for intermediate temperature SOFC applications. *Solid State Ionics*, *126*(1), pp.163-174.
13. Zhang, J. D., Ji, Y., Gao, H. B., He, T. M., Liu, J., 2005. Composite cathode $La_{0.6}Sr_{0.4}Co_{0.2}Fe_{0.8}O_3$-$Sm_{0.1}Ce_{0.9}O_{1.95}$-Ag for intermediate temperature solid oxide fuel cells. *Journal of Alloys and Compounds*, *395*(1-2), pp.322-325.

14. Shao, Z. and Haile, S. M., 2004. A high-performance cathode for the next generation of solid-oxide fuel cells. *Nature*, *431*(7005), pp.170-173.
15. Sharma, M. and Jeevanandam, P., 2011. Synthesis of magnesium oxide particles with stacks of plate's morphology. *Journal of Alloys and Compounds*, *509*(30), pp.7881-7885.
16. Lou, Z., Peng, J., Dai, N., Qiao, J., Yan, Y., Wang, Z., Wang, J. and Sun, K., 2012. High performance $La_3Ni_2O_7$ cathode prepared by a facile sol–gel method for intermediate temperature solid oxide fuel cells. *Electrochemistry Communications*, *22*, pp.97-100.
17. M. S. Mastuli, N. S. Ansaria, M. A. Nawawia, A. Maria, Effects of Cationic Surfactant in sol-gel synthesis of nano-sized magnesium oxide". APCBEE Procedia, 3, 93 – 98 (2012).
18. Lou, Z., Qiao, J., Yan, Y., Peng, J., Wang, Z., Jiang, T. and Sun, K., 2012. Synthesis and characterization of aluminum-doped perovskites as cathode materials for intermediate temperature solid oxide fuel cells. *International Journal of Hydrogen Energy*, *37*(15), pp.11345-11350.
19. C. B. Njoku, P. G. Ndungu, Effect of non-ionic, anionic and cationic surfactants on the sol gel synthesis of IrO/$Ce_{0.8}Sm_{0.2}O_2$ nanocomposite for solid oxide fuel cell application, Journal of Fuel Cell Science and Technology, 11 (2014) 101 - 109.
20. Okkay, H., Bayramoglu, M. and Öksüzömer, M. F., 2013. $Ce_{0.8}Sm_{0.2}O_{1.9}$ synthesis for solid oxide fuel cell electrolyte by ultrasound assisted co-precipitation method. *Ultrasonics Sonochemistry*, *20*(3), pp.978-983.
21. Tsunekawa, S., Ishikawa, K., Li, Z. Q., Kawazoe, Y. and Kasuya, A., 2000. Origin of anomalous lattice expansion in oxide nanoparticles. *Physical Review Letters*, *85*(16), p.3440.
22. Fu, Q., Saltsburg, H. and Flytzani-Stephanopoulos, M., 2003. Active nonmetallic Au and Pt species on ceria-based water-gas shift catalysts. *Science*, *301*(5635), pp.935-938.

23. Wu, Z., Li, M., Howe, J., Meyer III, H. M. and Overbury, S. H., 2010. Probing defect sites on CeO_2 nanocrystals with well-defined surface planes by Raman spectroscopy and O_2 Adsorption†. *Langmuir*, *26*(21), pp.16595-16606.
24. Liu, X., Zhou, K., Wang, L., Wang, B. and Li, Y., 2009. Oxygen vacancy clusters promoting reducibility and activity of ceria nanorods. *Journal of the American Chemical Society*, *131*(9), pp.3140-3141.
25. Shen, C. and Shaw, L.L., 2010. FTIR analysis of the hydrolysis rate in the sol–gel formation of gadolinia-doped ceria with acetylacetonate precursors. *Journal of Sol-gel Science and Technology*, *53*(3), pp.571-577.
26. Xu, B., Bhawe, Y. and Davis, M. E., 2013. Spinel Metal Oxide-Alkali Carbonate-Based, Low-Temperature Thermochemical Cycles for Water Splitting and CO2 Reduction. *Chemistry of Materials*, *25*(9), pp.1564-1571.
27. Liu, X., Zhou, K., Wang, L., Wang, B. and Li, Y., 2009. Oxygen vacancy clusters promoting reducibility and activity of ceria nanorods. *Journal of the American Chemical Society*, *131*(9), pp.3140-3141.
28. R. D. Waldron, Infrared spectra of ferrites, Phys. Rev., 1955, 99, 1727-1735.
29. M. A. Legodi, Raman Spectroscopy Applied to Iron Oxide Pigments from Waste Materials and Earthenware Archaeological Objects, University of Pretoria etd – Legodi, M A (2008).
30. Shebanova, O. N. and Lazor, P., 2003. Raman spectroscopic study of magnetite (Fe_2O_4): a new assignment for the vibrational spectrum. *Journal of Solid State Chemistry*, *174*(2), pp.424-430.
31. Witke, K., Götze, J., Robler, R., Dietrich, D. and Marx, G., 2004. Raman and cathode luminescence spectroscopic investigations on Permian fossil wood from Chemnitz, a contribution to the study of the permineralisation process. *Spectrochimica Acta Part A: Molecular and Biomolecular Spectroscopy*, *60*(12), pp.2903-2912.
32. Hanesch, M., 2009. Raman spectroscopy of iron oxides and (oxy) hydroxides at low laser power and possible applications in environmental magnetic studies. *Geophysical Journal International*, *177*(3), pp.941-948.

33. Chaubey, N., Wani, B. N., Bharadwaj, S. R. and Chattopadhyaya, M. C., 2013. Physicochemical properties of rare earth doped ceria $Ce_{0.9}Ln_{0.1}O_{1.95}$ (Ln = Nd, Sm, Gd) as an electrolyte material for IT-SOFC/SOEC. *Solid State Sciences*, *20*, pp.135-141.
34. Kuntaiah, K., Sudarsanam, P., Reddy, B. M. and Vinu, A., 2013. Nanocrystalline $Ce_{1-x}Sm_xO_{2-\delta}$ (x = 0.4) solid solutions: structural characterization versus CO oxidation. *RSC Advances*, *3*(21), pp.7953-7962.
35. Li, L., Chen, F., Lu, J. Q. and Luo, M. F., 2011. Study of Defect Sites in $Ce_{1-x}M_xO_{2-\delta}$ (x = 0.2) Solid Solutions Using Raman Spectroscopy. *The Journal of Physical Chemistry A*, *115*(27), pp.7972-7977.
36. Korotcov, A. V., Huang, Y. S., Tiong, K. K. and Tsai, D. S., 2007. Raman scattering characterization of well-aligned RuO_2 and IrO_2 nanocrystals. *Journal of Raman Spectroscopy*, *38*(6), pp.737-749.
37. Lin, J., Li, L., Huang, Y., Zhang, W., Wang, X., Wang, A. and Zhang, T., 2011. In situ calorimetric study: structural effects on adsorption and catalytic performances for CO oxidation over Ir-in-CeO_2 and Ir-on-CeO_2 catalysts. *The Journal of Physical Chemistry C*, *115*(33), pp.16509-16517.
38. Esch, F., Fabris, S., Zhou, L., Montini, T., Africh, C., Fornasiero, P., Comelli, G. and Rosei, R., 2005. Electron localization determines defect formation on ceria substrates. *Science*, *309*(5735), pp.752-755.
39. Shao, Z., Xiong, G., Tong, J., Dong, H. and Yang, W., 2001. Ba effect in doped Sr $(Co_{0.8}Fe_{0.2})O_{3-\delta}$ on the phase structure and oxygen permeation properties of the dense ceramic membranes. *Separation and Purification Technology*, *25*(1), pp.419-429.
40. Shuyan, L., Zhe, L., Xiqiang, H., Bo W., Wenhui, S., 2007. Electrical and thermal properties of $(Ba_{0.5}Sr_{0.5})_{1-x}Sm_xCo_{0.8}Fe_{0.2}O_{3-\delta}$ perovskite oxides, *Solid State Ionics* 178.pp. 417–422.

CHAPTER 8

Effects of surfactant on the performance of samarium doped ceria ($Ce_{0.8}Sm_{0.2}O_2$) perovskites as electrolyte for low temperature SOFC application

Summary

This chapter has been formatted in paper format to incorporate further comments and corrections by the examiners

Abstract

In our current work, we have adapted sol-gel technique that takes advantage of the structural directing properties, and templating characteristics of Pluronic F-127 surfactant to produce porous samarium doped ceria (SDC) nanoparticles. The electrolyte material was calcined at 800 °C, the crystalline nanostructures and microstructures were characterized by X-ray diffraction spectroscopy and high resolution transmission electron microscopy. Textural characteristics and morphology of the particles were characterized by nitrogen sorption at 77.5 K and scanning electron microscopy. The electrochemical properties were characterised by using Kittec Squadro SOFC testing equipment with air and hydrogen as gases used. Our results show that the nature of the surfactant influenced the particle morphology, pore diameter, pore size, crystallite size, surface area and the electrochemical properties.

Key words: Solid oxide fuel cell, Cerium, Samarium, Surfactant, Air, Sol-gel technique

1.0 Introduction

Sol-gel technique is a unique and adaptable technique frequently used to produce ceramic oxide materials and perovskite materials with controlled structure [1, 2]. These materials are produced by two methods, the hydrolysis of the metal alkoxide precursor and its condensation [3] and aggregation of aqueous colloidal dispersions, containing discrete particles which lead to formation of materials with tailored microstructure [4, 5]. The addition of surfactants in synthesizing metal oxides at ambient temperatures leads to production of composite materials that are homogeneously distributed throughout the resulting matrix and controls. The interfacial tension between the non-polar and polar phases and thus control the droplet sizes [6]. This causes changes in the physical characteristics such as density, pore size, nanostructure of the oxides produced and restrictionsin aggregation of metallic nanoparticles into matrices by sol–gel processing [7]. The materials can also be tailored by controlling the sol–gel reaction kinetics and the relative rates of hydrolysis and condensation [8 - 12].

$Ce_{0.8}Sm_{0.2}O_2$ (SDC) has been considered as a suitable electrolyte that can operate effectively at temperatures below 700 °C. At these temperatures they possess high ionic conductivity in air, have superb redox properties and contain high density of surface oxygen vacancies, resulting from the population of mixed valence states [13 - 16]. They also possess better chemical compatibility with high performance cathode materials [17 - 19]. Operating at low temperatures the electrolyte is susceptible to reduction on the anode side and grain boundary resistance is a significant impediment to ionic conductivity [20]. Hence surfactant can be used to improve its performance at these temperatures.

The surfactant used in this experiment is Pluronic F-127, which has been proven to provide better stabilization of the micelle walls, reduction in the inter-droplet exchange, resulting in the production of smaller particles, smaller crystals and the avoidance of the aggregation of the metallic nanoparticles into matrices [6]. Pluronic F-127 was added in different masses of (2 to 5 g) to SDC electrolyte to confirm its effect on the electrolyte material. This surfactant-assisted technique may provide an electrolyte material with appropriate pore

diameter, high surface areas and a better access to the active sites [21 – 23]. The support has a fundamental role in determining the nature, number of active sites and the activity of the catalyst.

2.0 Experimental Methods

2.1 Starting materials

The surfactant Pluronic F-127, ceria acetylacetonate hydrate (98 % purity) and samarium acetylacetonate hydrate (97 % purity) were purchased from sigma aldrich chemicals USA. The chemical reagents were used as acquired from their commercial sources without further purification.

2.2 Preparation of $Ce_{0.8}Sm_{0.2}O_2$ with surfactant

The synthesis was carried out by adding 0.7200 g of cerium acac and 0.3250 g of samarium acac to 50ml of ethanol and 15ml of deionized water as the solvent. The mixture was stirred in anultrasonic bath (UMC 20 Ultrasonic cleaner, 50 kHz and 220 W) for 30 mins. The mass of 2 to 5 g of Pluronic F-127 was added to each of the mixture. The mixtures were stirred using a magnetic stirrer on a hot plate for 30 mins at a temperature of 80 °C, to form a sol. The hydrolysis, condensation and solvent evaporation was very rapid and therefore the collapse of the gel network was also rapid as a result of the surfactant. The sol was left to dry in an oven for 24hrs and then calcined using a muffle furnace (Kittec Squadro 1350) at 800 °C for 4 hrs.

2.3 Preparation of $Ce_{0.8}Sm_{0.2}O_2$ without surfactant

0.7200 g of cerium acac and 0.3250 g of samarium acac was added to 50 ml of ethanol and 15 ml of deionized water as solvents. The mixture was sonicated for 30 mins using an ultrasonic bath (UMC 20 Ultrasonic cleaner, 50 kHz and 220 W). The mixture was stirred using a magnetic stirrer on a hot plate for 2 hrs at 80°C, to form a sol. The hydrolysis and condensation occurred slowly and the solvent evaporation was sluggish. The gel formed was allowed to dry at atmospheric temperature for 4 hrs at 150 °C and then calcined using a

muffle furnace (Kittec squadro SQ11) at 800 °C for 4 hrs. A summary of the process is stated in table 1.

Table 1: Summary of the synthesis processes of $Ce_{0.8}Sm_{0.2}O_2$ and Pluronic F-127.

Surfactant Name	Sample ID	Mass of Sample (g)
No Surfactant	SDC 1	No surfactant
Pluronic F127	SDC 2	2g
Pluronic F127	SDC 3	3g
Pluronic F127	SDC 4	4g
Pluronic F127	SDC 5	5g

2.4 Characterization

X-ray diffractometer (XRD) (Phillips PW 3710, 30 kV voltage and 35 mA current, Cu-Kα radiation 1.5406 Å wavelength) was used to analyze the crystallite structure, crystal size, lattice spacing and the phase present in the powder. The XRD diffractogram were recorded in the interval of $20° \leq 2\theta \leq 90°$ at a scan speed of 2 °/ min. The mean crystallite size 'D' was calculated using the Scherrer equation:

$$D = \frac{0.9\lambda}{\beta cos\theta} \quad (1)$$

where λ is the X-ray wavelength (1.5406 Å), β is the full width at half maximum of the diffraction line and θ is the diffraction angle.

Fourier transform infrared spectroscopy (Perkin Elmer 1200 ATR- FTIR) was used to perform the infrared spectra analysis. Raman spectroscopy was analysed with DeltaNu advantage 532™ spectrometer (100 mW Nd:YAG laser with an excitation wavelength of 532 nm). The JOEL 2100 HRTEM (200 kV accelerating voltage, beam current of 110 µA and a current density of 2.4 pA/cm^2) was used to analyse the lattice fringes, low magnification and diffraction patterns in the material. The morphology and grain size of samarium doped ceria powder was investigated with ZEISS FEGSEM Ultra Plus scanning

electron microscopy and the samples were coated with gold before the examination. Nitrogen adsorption and desorption (BET) was examined in a Micromeritics Tristar II 3020 V1.03 to find the surface area and porosity. For nitrogen desorption and absorption the samples were degassed using the vacuum degasser (Micromeritics VacPrep 061 sample Degas system) for 1 hr at 90 °C thenincreased to 200 °C to run overnight. The samples were then put in the BET instrument using Nitrogen at 77 K, to carry out the process.

2.5 Single cell fabrication

The cells were prepared by moulding the materials using a 20 Ton press and a 1.3 cm die kit. The press was made from strong steel and the die kit was made from stainless steel. For the SSFC material, 0.1435 g of the sample was placed into the die kit mould and 15 Tons of pressure was then applied using the 20 Ton press. 0.1545 g of NiO-SDC was used to make the anode and 0.2100 g of SDC- surfactant was used to prepare the electrolyte using the same method. The discs had a total active area of 1.327 cm^2. The single cell discs was made up of three layers with the electrolyte in between the anode and the cathode, then heat treated to 500 °C for 2 hrs at a steady heating rate of 5 °C/min, The electrolyte was estimated to be 100 µm thick, the cathode was 100 µm thick and the anode was 100 µm thick.

2.6 Electrochemical characterisation

The symmetrical cells were tested at 400 to 500 °C in 20 % H_2O/H_2 mixture and in air (O_2). Platinum mesh was placed on both electrodes which are used as a current and voltage collector. The gases (H_2O/H_2 and O_2) were passed through a pipe into the cell and it was controlled using flow metres. H_2 gas was passed through a gas bubbler to humidify the gas. For each cycle of the polarisation curve, the voltage was kept constant and current was measured. The current measurement was collected with a Nuvant™ Powerstat 05 potentiostat and galvanostat, attached to the SOFC device.

The ionic conductivity was calculated using these equations [24, 25]:

$$\sigma = \frac{l}{RS} \tag{2}$$

where, l is the electrolyte thickness, S is the electrode area of the electrolyte surface and R is resistance in ohms (cell resistance).

The activation energy and the DC electrical conductivity can be calculated using the Arrhenius relationship [25]:

$$\sigma = \sigma^{\circ}\exp\left[-\frac{E_a}{kT}\right] \tag{3}$$

where, E_a is the activation energy of conduction, T is the absolute temperature, σ^o is the pre-exponential factor and k is the Boltzmann constant.

3.0 Results and discussion

3.1 Powder XRD analysis

The XRD results of samarium doped ceria (SDC) can be seen in **Figure 1**. This confirms the structural pattern for SDC. The addition of surfactants in the sol-gel process caused changes to the structural pattern by increasing its intensity. The diffractogram shows only one main peak and other smaller peaks that decreased in peak intensity from left to right as the angle 2θ increased, with very sharp peaks.

The structure system was cubic corresponding to a FCC lattice and the diffracted peaks were located at 2θ values of 28.88°, 33.43°, 47.75°, 56.56°, 59.29°, 69.54°, 76.76°, 79.12° and 88.32° that were indexed as (111), (200), (220), (311), (222), (400), (331), (420), (JCPDS file NO. 00-034-0394). The average crystallite sizes were 3.63 nm, 5.46 nm, 13.55 nm, 15.95 nm and 17.50 nm for SDC1 to SDC5 respectively which was calculated from Scherrer equation using the most intense peak as shown in Table 2. This confirms that the

sample is crystalline, the peak intensities increased with increase in the surfactant mass which also had a proportionate effect on the crystallite sizes.

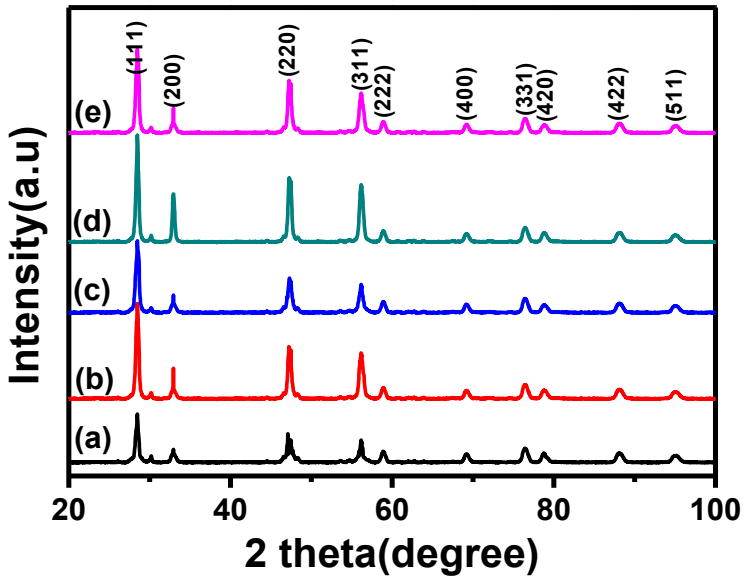

Figure 1: XRD diffractogram of (a) SDC1 (b) SDC2 (c) SDC3 (d) SDC4 and (e) SDC5 calcined at 800 °C for 4 hours.

For the SDC samples after calcination, the average lattice parameter a is 5.411 Å, and was calculated by using the equation [26].

$$a = \frac{\lambda}{2} \times \sin\theta \times \sqrt{h^2 + k^2 + l^2} \quad (4)$$

where, λ is the average X-ray wavelength, θ is 2θ value/2, h,k,l are Miller indices of particular planes in crystal.

The lattice parameter of the SDC material confirmed the lattice parameter of CeO_2 (JCPDS file NO. 00-034-0394) which confirms the formation of the SDC compound. The mass of the unit cell for all samples was 1.1572 x 10^{-27} g, and this was calculated using the equation:

$$\text{Mass of Unit Cell (M)} = \frac{(4atoms)(MolarMass)}{6.02\times10^{23}atoms/mol}\left[\frac{10^{-6}Mg}{g}\right] \quad (5)$$

The volume mass of the unit cell was 7.303 g/cm^3, and the following equation was used to calculate this value:

$$\text{Volume mass} = \frac{mass(unit\ cell)}{Volume(unit\ cell)} \quad (6)$$

Volume mass of unit cell was calculated to be 1.5845 x 10^{-28} cm^3 (From$v = a^3$ where a = $4R/\sqrt{2}$)

Table 2: The difference in crystallite size of SDC 1, SDC2, SDC 3, SDC 4 and SDC 5.

Sample ID	FWHM (°)	Crystallite Sizes (nm)
SDC 1	2.255	3.637 ± 0.043
SDC 2	1.501	5.461 ± 0.066
SDC 3	0.605	13.550 ± 0.191
SDC4	0.514	15.950 ± 0.238
SDC5	1.092	7.509 ± 0.094

3.2 Raman analysis

Figure 2 shows the Raman spectra of SDC solid solutions exhibiting Raman peaks at 472 cm^{-1} and 565 cm^{-1}. The band peak at 472 cm^{-1} represents F_{2g} vibrational mode Sm_2O_3 and the other peak at 565 cm^{-1} is assigned to MO_8- type (M = Sm) complex [27 – 30]. It has been reported that the presence of SmO_8^-type complex could be related to the different radius between Sm^{4+} (0.084 nm) and Ce^{4+} (0.097 nm), since the valence state of Sm is +4 [31].

The band at 565 cm^{-1} could also be assigned to oxygen vacancy and the emergence of this band results from the different oxidation state of the dopant compared to that of Ce^{4+} and the different ionic radius of the dopant compared to that of Ce^{4+}. Therefore, it was also observed that the vibrational bands at 472 cm^{-1} increased with increase in the mass of the surfactants added to the material. This is because the ordering level of the samples

increases with increasing surfactant and the lattice becomes more perfect, leading to the declining concentration of the defect sites.

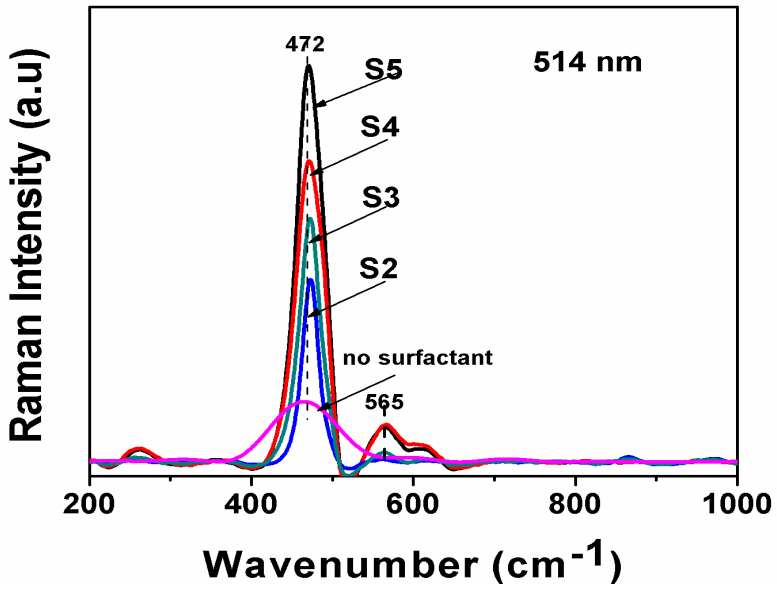

Figure 2: Raman spectra of (a) SDC 1 (b) SDC 2 (c) SDC 3 (d) SDC 4 and (e) SDC 5 calcined at 800 °C for 4 hours.

3.3 HRTEM analysis

Figure 3 shows the lattice fringes and low magnification of SDC mixed with surfactants. The microstructure shows that it is crystalline with the evidence of large visible particles. The representative images showed the microstructure for all samples, which reveal slight differences such as specific irregular shaped particles and varying crystalline shapes. We note that there are differences in the powdered crystals as observed in the XRD data in terms of the crystal sizes.

The lattice distance between the fringes for SDC 1 was 0.183 nm indexed to (220), SDC 2 is 0.157 nm indexed to (222), SDDC 3 is 0.202 nm indexed to (220), SDC 4 is 0.207 nm indexed to (211) and SDC 5 is 0.190 nm indexed to (220). These lattice parameters are linked to the XRD as SmO_2 structure and CeO_2 (fluorite) structures. The presence of CeO_2

fluorite structure on the HRTEM as shown in the XRD reveals a concentration of O_2 vacancies on the surface. The presence of oxygen (O_2) vacancies influences oxygen ion diffusion paths through the electrolyte. The selected area electron diffraction patterns differed slightly in terms of the lattice and arrangements of the particles, showing slight scattering and disorder of the lattice, thus displaying a decrease in crystallinity as the surfactants added to the electrolyte decreased.

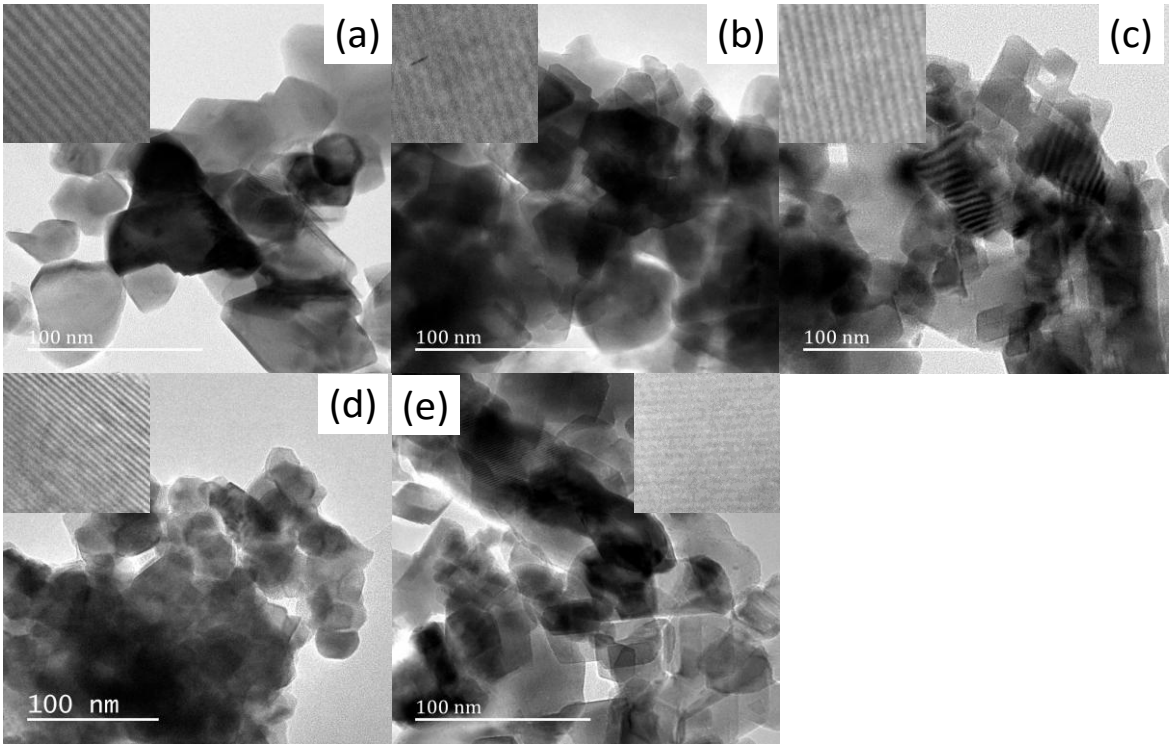

Figure 3: Low magnification and lattice fringe of the High Resolution TEM for (a.) SDC1 (b).SDC 2 (c).SDC3 (d).SDC 4 and (e).SDC 5 Calcined at 800 °C for 4 hours.

3.4 SEM analysis

Figure 4 show images of SDC prepared using Pluronic F-127 as surfactant, the figure reveal that particles prepared with Pluronic F-127 exposed a low conglomeration but a wide size distribution. The SEM image for all the materials synthesized, showed an accumulation of metal acacs bonded together to form agglomerates. These particles are held together by the strong and weak bonds that exist between the metal acacs. The particles were separated

as a result of the addition of surfactants, forming loosely coherent secondary loose particles. The morphology showed the formation of holes or pore spaces on the material layer. These pore spaces increased and were obvious as the amount of surfactants added to the material increased.

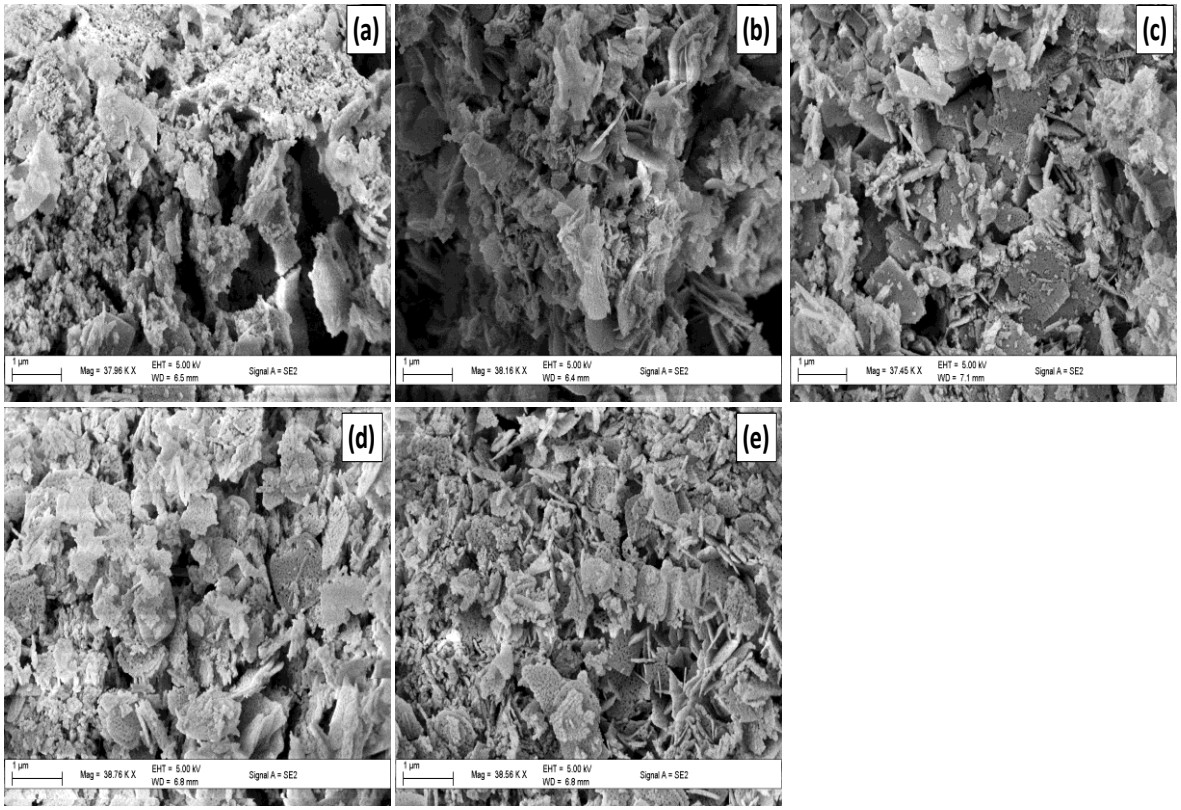

Figure 4: SEM morphology of (a) SDC 1 (b) SDC 2 (c) SDC 3 (d) SDC 4 and (e) SDC 5 calcined at 800 °C for 4 hours.

The material prepared without surfactant showed a breaking of the bonds between the tiny particles to form bigger separated particles that are loosely packed. These particles bonded with other loosely packed particles grew asymmetrically and formed agglomerates. The formation of fine particles using this method is usually prominent for its large surface to volume ratio, higher adsorption capacity and enhanced chemical reactivity.

3.5 Surface area analysis (BET)

The nitrogen desorption of the materials were observed as follows; SDC1 exhibited the lowest surface area of 5.535 m^2/g, the highest pore size value of 39.950 nm and a low pore volume of 0.0948 cm^3/g. SDC 2 isotherm plot as shown in the figure revealed that the samples are macroporous material, the surface area observed was 17.846 m^2/g, a pore size of 25.404 nm and the pore volume was 0.1325 cm^3/g. SDC 3 exhibited a higher surface area of 18.634 m^2/g, a pore size of 26.366 nm and a pore volume of 0.1421 cm^3/g. The surface area for SDC 4 was 19.044 m^2/g, the pore size was 27.131 nm and exhibited a pore volume of 0.1441 cm^3/g. The surface area for SDC 5 showed the highest surface area of 20.821 m^2/g, the pore size value was 25.759 nm and the pore volume showed 0.155 cm^3/g.

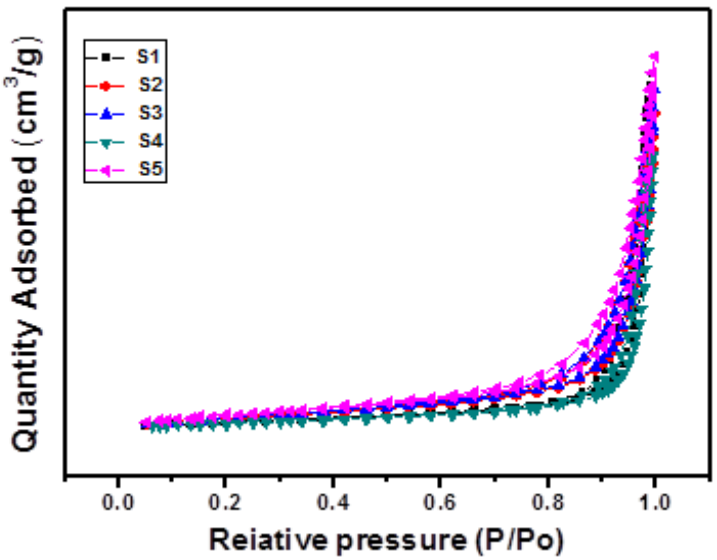

Figure 5: Nitrogen desorption Isotherm plot of (a) SDC 1 (b) SDC 2 (c) SDC 3 (d) SDC 4 and (e) SDC 5 calcined at 800 °C for 4 hours.

The materials in general, showed an increase in the surface area of the material as the mass of the surfactant used increased, the pore volume and pore size also increased. In totality the observations show that the addition of varying amounts of surfactants caused a vast increase in surface area, pore size and pore volume of the material when compared to the

materials without surfactant confirming a change in the structural properties of the material with an increasing change in the mass of surfactants.

Table 3: The surface area, pore diameter and pore volume of SDC1, SDC 2, SDC 3, SDC 4 and SDC 5.

Sample ID	Pluronic F-127 Used	Surface area m^2/g	Pore diameter (nm)	Pore volume (cm^3/g)
SDC 1	No surfactant	5.535	39.950	0.0948
SDC 2	2 g	17.846	25.404	0.1325
SDC 3	3 g	18.634	26.366	0.1421
SDC 4	4 g	19.044	26.856	0.1441
SDC 5	5 g	20.821	25.759	0.1557

3.6 Electrochemical properties

The symmetrical cell was tested by using a muffle furnace made by Kittec Squadro and a Nuvant potentiostat and galvanostat. These instruments were used as measuring instruments for the collection of the current and voltage data. 50 m^3/min of compressed air and 200 m^3/min of humidified hydrogen gas mixed with 20 % H_2O was passed through pipes into the cell and it was tested for 15 hrs.

3.6.1 Polarisation graph

Figure 6 illustrates the electrochemical property of $Ce_{0.8}Sm_{0.2}O_{2,}$ prepared using Pluronic F-127 as surfactants. The polarization properties were tested using air at the cathode side and humidified hydrogen (H_2 + 20 % H_2O) as fuel gas at the anode side. The cathode material used for testing was $Sm_{0.8}Sr_{0.2}Fe_{0.8}Co_{0.2}$ perovskite with a thickness of 100 μm and the anode used was NiO/SDC which was 100 μm thick and the electrolyte was 150 μm thick. The symmetric cell was measured within the temperature intervals of 400 – 500 °C.

The polarization graph displayed tendencies showing a linear fall in voltage with increase in the current density. This resulted from the resistance to current flow, confirming that an increase in current is directly proportional to an increase in voltage. The open circuit

voltage (OCV) showed stability for over 15 hrs at 500 °C and showed different values for OCV. The OCV values were less than the Nernst thermodynamic values because of two reasons: hydrogen pressure reduction at the anode/electrolyte interface by the anode materials and the gas crossover flowing through the electrolyte because of the change in temperature.

The voltage showed a linear fall with corresponding increase in the current density in the polarisation graph. The linear fall was activated by these reasons: increase in the Ohmic and concentration losses from the internal resistance of the cell, which was produced by the ionic conductivity and the effective distance between the cell components. Change in the ionic conductivity can be influenced by the reduction of adsorbed molecular oxygen to O_2 ions which improves the diffusion of these ions to the electrode/electrolyte interface. The increase in the overall rate of the diffusion process reduces polarisation losses and resistance; hence, low polarisation losses are observed at 400 °C.

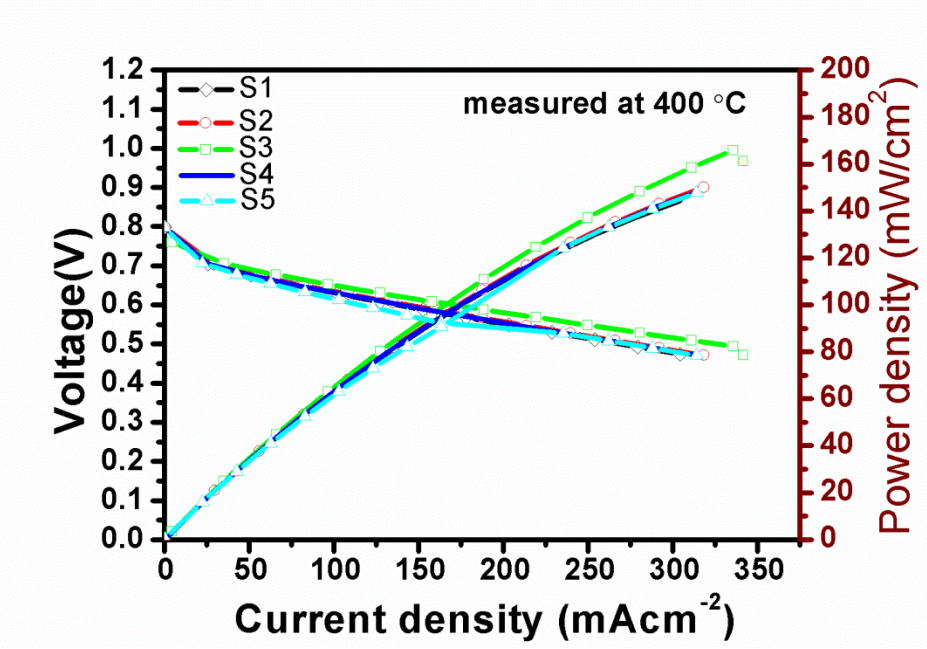

Figure 6: The polarization graph of (a) SDC 1 (b) SDC 2 (c) SDC 3 (d) SDC 4 and (e).SDC 5 calcined at 800 °C for 4 hours.

The maximum power density for the SDC-surfactant samples calcined at 800 °C with different wt % are shown in Figure 7. The power densities were measured at 400 °C and 500 °C and SDC 3 presented the maximum power density of 140.61 mW/cm^2 at 500 °C and 161.24 mW/cm^2 at 400 °C. Therefore, at each test temperature, the SDC 3 sample showed the largest power density; however the electrolyte presented a better performance at lower temperature. These results could have some implication for application, depicting that the electrolytes made, can perform better at 400 °C than 500 °C and it exhibits a moderate power output from a non-ideal single cell. Improvements can be achieved by using thin electrolyte and suitable cathode and anode materials, using tape casting or dip coating methodologies to control and optimize adhesion between the layers.

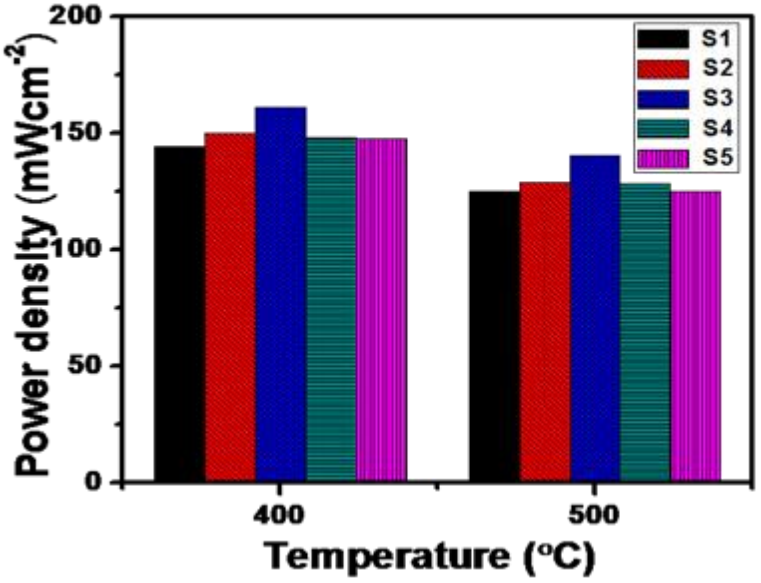

Figure 7: The Power density graph of (a) SDC 1 (b).SDC 2 (c).SDC 3 (d).SDC 4 and (e).SDC 5 calcined at 800 °C for 4 hours.

3.6.2 Area Specific Resistance

The area specific resistance (ASR) can be calculated from the gradient, at the centre of the linear fall representing the voltage to current graph of the IV curve where ohmic resistance

is dominant. The design of the cell's electrodes, electrolyte properties and the assembly process used to make the single cell determines the ASR [31].

Figure 8 shows the ASR values for electrolytes with surfactant, the graph illustrates a linear fall in resistance as the temperature increased. This can be connected to changes in material compositions and increased oxygen loss from the lattice. Sample SDC 3 showed the lowest ASR values and SDC 5 showed the highest value at 400 °C. Which could be attributed to an increase in oxygen loss from the SDC 3 sample than SDC 5 sample, due to increase in the mass of surfactant blocking the pores and thereby limiting oxygen ion transfer. Also reduction in the ASR values at 500 °C can be triggered by the intensification of oxygen diffusion resulting from the conversion of absorbed oxygen to O_2 ions [32]. The modification in porosity, surface area, pore volume, and morphology also influences the movement of O_2 ions at the triple phase boundary. The low ASR values by SDC 3 sample can also be attributed to their competence to transfer O_2 ions faster than other electrolytes at the triple phase boundary (TPB) [33].

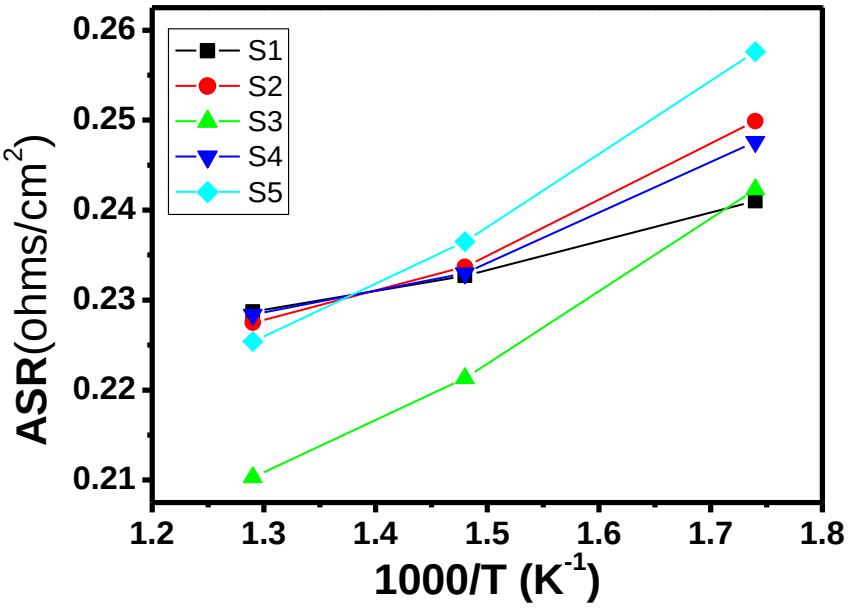

Figure 8: The Arrhenius plot of the ASR of (a) SDC 1 (b) SDC 2 (c) SDC 3 (d) SDC 4 and (e) SDC 5 calcined at 800 °C for 4 Hours measured from 300 – 500 °C.

4.0 Conclusions

Pluronic F-127 surfactant was mixed with SDC to improve its ability to perform better than conventional SDC in this experiment. The crystal structure was investigated by X-ray diffraction and the structural properties were investigated by Raman spectroscopy. The morphology, microstructure and textural characteristics were investigated by SEM, HRTEM and BET respectively. The electrochemical properties was investigated using a potentiostat and galvanostat. The XRD revealed an increase in the crystallite sizes of the materials with surfactant when compared to the material without surfactant. Nitrogen desorption analysis showed that the surface area and porosity of the material increased with increasing mass of surfactant when compared to the ordinary SDC. The Raman spectra displayed a high structural stability and high oxygen vacancy concentration. SDC combined with 3 g of surfactant produced the highest power density of 161.24 mW/cm^2 and a current density of 325.90 mA/cm^2 at 400 °C powered for 15 hrs. When compared to contemporary SDC without surfactant, it produced a power density of 144.289 mW/cm^2 at 400 °C. This describes that the electrolyte material works best with the addition of surfactant and also works best at lower temperatures. The properties reveal that the electrolyte material mixed with surfactant can be used as a promising electrolyte for low temperature solid oxide fuel cell.

Acknowledgements

The authors thank the University of KwaZulu-Natal, for granting access to research facilities for my research, ESKOM-TESP and NRF THUTUKA for their financial support.

References

[1] M. Sharma, J. Peng, Synthesis of magnesium oxide particles with stacks of plate's morphology, J.Alloys Compd. 509 (2011) 7881 - 7885.

[2] M. S. Mastuli., N. S. Ansaria, M. A. Nawawia, A. Maria, Effects of cationic surfactant in sol-gel synthesis of nano-sized magnesium oxide. APCBEE Procedia, 3 (2012) 93 – 98.

[3] L. Zhongliang, J. N. Dai, J. Qiao, Y. Yan, Z. Wang, J. Wang, K. Sun, High performance $La_3Ni_2O_7$ cathode prepared by a facile sol–gel method for intermediate temperature solid oxide fuel cells, Electro. Comm. 22 (2012)97-100.

[4] N. I. Ermokhina, V. A.Nevinsky, P. A. Manorik, V. G. Ilyin, N. N. Shcherbatyuk, D. O. Klymchyuk, A. M. Puziy, Synthesis of large pore mesoporousnano crystalline TiO_2 microspheres, Materials Letters, 75 (2012) 68 – 70.

[5] K. T. Parada , G. V. A. A. Mantilla , M. A. Valenzuela, E. Hernández, Synthesis and characterization of Ni/Ce–SiO_2 and Co/Ce–TiO_2 catalysts for methane decomposition, Fuel 110 (2013) 70 – 75.

[6] S. K. Das, A. K. Sinha, A. Bhaumik, Self-assembled mesoporous zirconia and sulfated zirconia nanoparticles synthesized by triblock copolymer as template, J. Phys. Chem. 113 (2009) 8918 – 8923.

[7] J. Milewski, A. Miller, Influences of the type and thickness of electrolyte on solid oxide fuel cell hybrid system performance, Journal of Fuel Cell Science and Technology 3(4) (2006) 396 – 402.

[8] S. B. Adler, Factors governing oxygen reduction in solid oxide fuel cell cathodes, Chem. Rev. 104 (2004) 4791 – 4843.

[9] A. V. Vikar, J. Chen, C. W. Tanner, J. W. Kim, The role of electrode microstructure on activation and concentration polarizations in solid oxide fuel cells, Solid State Ionics 131 (2000)189 –198.

[10] E. P. Murray, M. J. Sever, S. A. Barnett, Electrochemical performance of (La,Sr)(Co,Fe)O_3– (Ce,Gd)O_3 composite cathodes, Solid State Ionics 148 (2002) 27 – 34.

[11] W. Guo, J. Liu, C. Jin, H. Gao, Y. Zhang, Electrochemical evaluation of $La_{0.6}Sr_{0.4}Co_{0.8}Fe_{0.2}O_{3-\delta}$–$La_{0.9}Sr_{0.1}Ga_{0.8}Mg_{0.2}O_{3-\delta}$ composite cathodes for $La_{0.9}Sr_{0.1}Ga_{0.8}Mg_{0.2}O_{3-\delta}$ electrolyte SOFCs, J. Alloys Compd. 473 (2008) 43 – 47.

[12] F. Qiang, K. N. Sun, N. Zhang, X. D. Zhu, X. D. Lee, D. R. Zhou, Characterization of electrical properties of GDC doped A-Site deficient LSCF based composite cathode using impedance spectroscopy, J. Power Sources, 168 (2007) 338 – 345.

[13] R. W. Tarnuzzer, J. Colon, S. Patil, S. Seal, Vacancy engineered ceria nanostructures for protection from radiation-induced cellular damage, Nano letters, 5 (2005) 2573-2577.

[14] T. Pirmohamed, J. M. Dowding, S. Singh, B. Wasserman, E. Heckert, A. S. Karakoti, J. E. S. King, W. T. Self, Nanoceria exhibit redox state-dependent catalase mimetic activity, Chemical communications, 46 (2010) 2736-2738.

[15] E. G. Heckert, A. S. Karakoti, S. Seal, W. T. Self, The role of cerium redox state in the SOD mimetic activity of nanoceria, Biomaterials, 29 (2008) 2705-2709.

[16] D. A. Andersson, S. I. Simak, B. Johansson, I. A. Abrikosov, N. V. Skorodumova, Modeling of CeO_2, Ce_2O_3 and CeO_{2-x} in the LDA+ U formalism, Physical Review B, 75 (2007) 035109.

[17] W. G. Wang, M. Mogensen, High-performance lanthanum ferrite based cathode for SOFC, Solid State Ionics, 176 (2005) 457-462.

[18] X. Xu, C. Xia, G. Xiao, D. Peng, Fabrication and performance of functionally graded cathodes for IT-SOFCs based on doped ceria electrolytes, Solid State Ionics, 176 (2005) 1513-1520.

[19] Z. Bi, M. Cheng, Y. Dong, H. Wu, Y. She, B. Yi, Electrochemical evaluation of $La_{0.6}Sr_{0.4}CoO_3$–$La_{0.45}Ce_{0.55}O_2$ composite cathodes for anode-supported $La_{0.45}Ce_{0.55}O_2$–$La_{0.9}Sr_{0.1}Ga_{0.8}Mg_{0.2}O_{2.85}$ bilayer electrolyte solid oxide fuel cells, Solid State Ionics, 176 (2005) 655-661.

[20] J. M. Ralph, J. A. Kilner, B. C. H. Steele, Improving Gd-doped ceria electrolytes for low temperature solid oxide fuel cells," New Materials for batteries and fuel cells. Proc. Symp. San Francisco, 14 (1999) 309-3257.

[21] P. Blennow, J. Heljm, T. Klemens, S. Ramousse, A. Kromp, A. Leonide, A. Weber, Manufacturing and characterization of metal-supported solid oxide fuel cells, Journal of Power Sources, 196 (2011) 7117– 7125.

[22] C. Shen, L. L. Shaw, FTIR analysis of the hydrolysis rate in the sol–gel formation of gadolinia-doped ceria with acetylacetonate precursors, J. Sol-gel Sci Technol., 53 (2010) 571 – 577.

[23] M. C. Brasil, E. V. Benvenutti, J. R. Gregorio, A. E. Gerbase, Iron acetylacetonate complex anchored on silica xerogel polymer. React. Funct. Polym., 63 (2005) 135 – 141.

[24] C. B. Njoku, P. G. Ndungu, Effect of non-ionic, anionic and cationic surfactants on the sol gel synthesis of IrO/$Ce_{0.8}Sm_{0.2}O_2$ nanocomposite for solid oxide fuel cell application, Journal of fuel cell science and technology, 11 (2014) 101 - 109.

[25] H. Okkay, M. Bayramoglu, M. F Öksüzömer, $Ce_{0.8}Sm_{0.2}O_{1.9}$ synthesis for solid oxide fuel cell electrolyte by ultrasound assisted co-precipitation method, Ultrasonics Sonochemistry, 20 (2013) 978 – 983.

[26] N. Chaubey, B. N. Wani, S. R. Bharadwaj, M. C. Chattopadhyaya, Physicochemical properties of rare earth doped ceria $Ce_{0.9}Ln_{0.1}O_{1.95}$ (Ln = Nd, Sm, Gd) as an electrolyte material for IT SOFC/SOEC, Solid State Sciences, 20 (2013) 135 - 141.

[27] K. Kuntaiah, P. Sudarsanam, B. M. Reddy, A. Vinu, Nanocrystalline $Ce_{1-x}Sm_xO_{2-\delta}$ (x = 0.4) solid solutions: structural characterization versus CO oxidation, RSC Advances, 3 (2013) 7953 - 7962.

[28] L. Li, F. Chen, J. Q. Lu, M. F. Luo, Study of defect sites in $Ce_{1-x}M_xO_{2-\delta}$ (x = 0.2) solid solutions using Raman spectroscopy, Journal of Physical Chemistry A, 115 (2011) 7972 - 7977.

[29] A. M. Torres-Huerta, J. R. Vargas-García, M. A. Domínguez-Crespo, Preparation and characterization of IrO_2 –YSZ nanocomposite electrodes by MOCVD, Solid State Ionics, 178 (2007) 1608 - 1616.

[30] E. Barsoukov, J. R. Macdonald, Impedance spectroscopy, theory, experiment and applications 2nd Edition (2005) John Wiley & Sons,Inc., Hoboken, New Jersey.

[31] C. B. Njoku, P. G. Ndungu, Synthesis and characterization of novel $Ce_{0.8}Sm_{0.2}$ $Fe_{0.9}Ir_{0.03}Co_{0.07}O_{3-\delta}$ perovskite material and possible application as a cathode for low–intermediate temperature SOFCs, Materials Research Bulletin, 68 (2015) 100-108.

[32] Z. Wenxia, Z. Lü, S. Li, B. Wei, J. Miao, X. Huang, K. Chen, N. Ai, W. Su, Study on $Ba_{0.5}Sr_{0.5}Co_{0.8}Fe_{0.2}O_{3-\delta}$–$Sm_{0.5}Sr_{0.5}CoO_{3-\delta}$ composite cathode materials for IT-SOFCs, Journal of Alloys and Compounds, 465 (2008) 274-279.

[33] F. Esch, S. Fabris, L. Zhou, T. Montini, C. Africh, P. Fornasiero, R. Rosei, Electron localization determines defect formation on ceria substrates, Science, 309 (2005) 752-755.

CHAPTER 9

Comparative study of the properties of $Ce_{1-X}Sm_XO_2$ (x = 0.1 - 0.4), $Ce_{0.8}Sm_{0.2}O_2/Na_2CO_3$, $Ce_{0.8}Sm_{0.2}O_2/ LiCO_3$ and $Ce_{0.8}Sm_{0.2}O_2 / Na_2CO_3/LiCO_3$ electrolytes for application in low temperature SOFC

Summary

This chapter has been formatted in paper format to incorporate further comments and corrections by the examiners

Abstract

The study utilized sol-gel technique to prepare the electrolytes $Ce_{1-x}Sm_xO_2$ compositions (x = 0.1 - 0.4), $Ce_{0.8}Sm_{0.2}O_2/Na_2CO_3$, $Ce_{0.8}Sm_{0.2}O_2/LiCO_3$ and $Ce_{0.8}Sm_{0.2}O_2/ Na_2CO_3/LiCO_3$ composite electrolyte materials, which were calcined at 800 °C. The powders were characterized using X-ray diffraction, Raman spectroscopy, high resolution transmission electron microscopy and scanning electron microscopy. The electrochemical properties were investigated using an open flange test set-up made by Fiaxell Company, Nuvant™ Powerstat-05 potentiostat and galvanostat used to measure the current density and voltage. Particle sizes and crystallite sizes varied with electrolyte compositions and the microstructure became more compact with the addition of the sodium carbonate and lithium carbonate composites to the electrolyte. $Ce_{0.8}Sm_{0.2}O_2$ / $Na_2CO_3/LiCO_3$ electrolyte composites generated the highest current density and power density, hence can be said to perform better at low temperature conditions.

Key words: Solid Oxide Fuel Cell, Cerium, Samarium, Electrolytes, Current density.

1.0 Introduction

Solid oxide fuel cell is an innovative technological device for the generation of electricity, because of its high efficiency, low emission of pollutants and fuel flexibility. SOFCs that operate at high temperatures usually at 1000 °C use yttria stabilized zirconia (YSZ) as electrolytes [1]. In reducing the operating temperatures of SOFCs, doped ceria have been extensively studied as electrolytes and samarium doped ceria is considered to be one of the most promising electrolytes for SOFCs operating below 650 °C [2 - 6]. Doped ceria is a promising electrolyte since it works best at low temperatures, because of its high ionic conductivity at low temperatures and high electronic conduction at low oxygen partial pressure resulting from the partial reduction of Ce^{4+} to Ce^{3+} [7 - 9].

Doped ceria nanoparticles possess excellent redox properties and contain a high density of surface oxygen vacancies, resulting from the population of mixed valence states [10 - 13]. They also possess better chemical compatibility with high performance cathode materials [14 - 16]. The ionic transport through doped ceria electrolyte depends on several factors. The vacancy contraction profiles through the electrolyte affects the leak current and the electrode polarizations, which closes the circle by affecting the vacancy concentration profile. This disadvantage is solved by improving its mixed ionic and electronic properties by varying the doping level, temperature and oxygen activation [17 - 19].

Furthermore, reports show that composite electrolytes work even more effectively at reduced temperatures. These composite electrolytes generally contain two phases, which are a combination of doped ceria solid solution and salt or oxide phase, usually insulating phase, such as a mixture of Li_2CO_3 or Na_2CO_3 or solid phase like Na_2CO_3 and some oxides below the molten point. Addition of carbonates to SDC performs several crucial functions. It enhances significantly the ionic conductivity of the electrolyte, improves the thermal stability of the nanostructure and increases the cell's OCV significantly compared to typical SDC single cells. In addition, the softening of amorphous Na_2CO_3 could improve densification of solid electrolyte layer to prevent any gas leakage [20]. The sol-gel technique was adapted to synthesize the electrolytes with different doping concentrations

and the composite electrolytes. This technique is a less complicated synthesis procedure. It is cost effective and produces perovskite that are of high purity, are homogenous, have better active sites and regular particle sizes and morphology.

In this study we intend to achieve a comparative study between samarium doped ceria and the composite electrolytes, since it has been demonstrated that interface of the composite electrolyte provides a better channel for ionic transport.

2.0 Experimental Methods

2.1. Synthesis of electrolyte material

Samarium doped ceria (SDC) perovskites was synthesized using the following metal precursors, samarium (III) acetylacetonate hydrate (99.9 %), cerium (III) acetylacetonate hydrate, (99.9 % purity), sodium carbonate (Na_2CO_3) and lithium carbonate ($LiCO_3$) were purchased from Sigma-Aldrich (Pty) Ltd, South Africa. These chemicals were used without further purification.

The synthesis procedure was carried out by weighing, 1.3102 g of cerium (III) acetylacetonate hydrate and 0.4640 g of samarium (III) acetylacetonate hydrate for $Ce_{0.8}Sm_{0.2}O_2$ electrolyte composition. Other electrolyte compositions were weighed out in their stoichiometric ratios. Each composition was then added to a mixture of 50 ml of ethanol and 15 ml of deionized water. The mixture was sonicated for 30 mins in an ultrasound bath (UMC 20, ultrasonic cleaner 50 kHz). The solution formed was then placed on a hot plate and heated upto 80 °C while stirring at 180 rpm for 30 mins. The samples were then dried for 5 hours at room temperature, and then calcined in a muffle furnace (Kittec Squadro SQ11) for up to 800 °C at a heating rate of 2 °C/min for 4 hrs. This process was repeated for other compositions.

To synthesize SDC and salt compositions, 0.200 g of samarium (III) acetylacetonate and 0.534 g of cerium (III) acetylacetonate was mixed in a solution of 50 ml ethanol and 15 ml of deionized water. This was then placed in an ultrasound bath to completely mix the samples. After 30 mins, the solution was then placed on a hotplate and heated up to 80 °C

while stirring for 20 mins. The samples were allowed to dry for 5 hours at room temperature then calcined for 4 hours at 800 °C at 2 °C/min ramping rate in a muffle furnace. Samarium doped ceria (SDC) material formed was hand mixed separately with sodium carbonate (Na_2CO_3) and lithium carbonate ($LiCO_3$) in a mass ratio of 60:40 % to form SDC/Na_2CO_3 and SDC/$LiCO_3$ electrolyte respectively as shown in Table 1. SDC material was also hand mixed with the same mass ratios of Na_2CO_3 and $LiCO_3$ (60:20:20 %) to form SDC/Na_2CO_3/$LiCO_3$ electrolyte shown in Table 1.

Table1: Summary of the Electrolyte compositions of $Ce_{1-x}Sm_xO_2$ (x = 0.1 - 0.4), composite electrolyte and Sample ID.

Electrolyte Compositions	Sample ID
$Ce_{0.7}Sm_{0.3}O_2$	E 1
$Ce_{0.9}Sm_{0.1}O_2$	E 2
$Ce_{0.8}Sm_{0.2}O_2/LiCO_3$	E 3
$Ce_{0.8}Sm_{0.2}O_2$	E 4
$Ce_{0.6}Sm_{0.4}O_2$	E 5
$Ce_{0.8}Sm_{0.2}O_2/Na_2CO_3$	E6
$Ce_{0.8}Sm_{0.2}O_2$/ $LiCO_3$/ Na_2CO_3	E7

2.2. Characterization

The crystal structure of the electrolyte nanocomposite was characterized using powder X-ray diffraction (XRD). The XRD patterns were obtained using Brucker D8 Advance diffractometer with a Cu Kα radiation source operating at 40 kV and a wavelength of 1.5406 Å. The XRD diffractogram was recorded in the interval of $20° \leq 2\theta \leq 85°$ at a scan speed of 2 °C/min. The mean crystallite sizes 'D' was calculated using the Scherrer equation:

$$D = \frac{0.9\lambda}{\beta cos\theta} \quad (1)$$

where λ is the X-ray wavelength (1.5406 Å), β is the full width at half maximum of the diffraction line and θ is the diffraction angle.

The microstructure of the material was characterized by high resolution transmission electron microscopy (HR-TEM). The HR-TEM analysis was done by pouring small amounts of the samples into ethanol to mix, using an ultrasound bath. It was then drop-dried onto a carbon coated copper TEM grid, and then examined on a JOEL 2100 HRTEM (200 kV accelerating voltage, beam current of 110 µA and current density of 2.4 pA/cm^2). The structural properties were characterised using Raman spectroscopy. The Raman analysis was done on a DeltaNu advantage 532™ Raman Spectrometer (100 mWNd: YAG laser with an excitation wavelength of 532 nm). The morphology was characterized using scanning electron microscopy (SEM). The electrolyte powders were pressed onto carbon tape pasted on an aluminium stubs and gold coated for SEM observations on a ZEISS FEGSEM Ultra Plus. Nitrogen adsorption and desorption (BET) was examined in a Micromeritics Tristar II 3020 V1.03 to find the surface area and porosity. For nitrogen desorption and absorption, the samples were degassed using the vacuum degasser (Micromeritics VacPrep 061 sample Degas system) for 1 hr at 90 °C, it was then increased to 200 °C and allowed to run overnight. The samples were then put in the BET instrument using Nitrogen at 77 K, to carry out the process.

2.3. Single Cell fabrication

The button cells were prepared by moulding the materials into a disc using a 20 Ton press and a 1.3 cm die kit. For each cell 0.2300 g electrolyte material of 0.2000 g $Sm_{0.8}Sr_{0.2}Fe_{0.8}Co_{0.2}$ (SSFC) cathode material and 0.3500 g of NiO/SDC anode material was pressed together in the press to form a 3 layered single button cell, for each electrolyte sample. The cell discs were then heat treated to 350 °C for 2 hrs at a steady heating rate of 5 °C/min sandwiched in a ceramic blanket. The button cell has a total active area of 1.327 cm^2 and the cell was 350 µm thick.

2.4. Electrochemical Performance test

To test the electrochemical properties, the button cell was positioned between the nickel foam mesh on the anode side. Platinum mesh on the cathode side, this was then placed in

the open flange test set-up from Fiaxell SOFC Technologies™. This set-up was designed for the cell sizes, and the meshes were used as contact components, with the cell, to act as a combined current, voltage collector and gas distributor. The test-bed was placed in a muffle furnace (Kittec Squadro SQ11) and linked to appropriate gas tight fittings for the delivery of the gases to the cell. The current and the voltage from the cells were measured with a Nuvant™ Powerstat 05 potentiostat and galvanostat. Polarization curves were recorded between 400 to 500 °C with a fuel gas consisting of humidified hydrogen (4 – 20 % water) on the anode side and air on the cathode side.

3.0 Results and discussions

3.1 Powder XRD analysis

Figure 1 shows the XRD results of the crystalline structure for the electrolytes nanoparticles. The diffractogram shows a main peak and smaller peaks that decreased in intensity from left to right as the angle 2θ values increased, with very sharp peaks. The structure system was cubic corresponding to FCC lattice and the diffracted peaks were located at 2θ values of 28.88°, 33.43°, 47.75°, 56.56°, 59.29°, 69.54°, 76.76°, 79.12°, 88.04° and 94.98° which were indexed as (111), (200), (220), (311), (222), (400), (331), (420), (422) and (511) (JCPDS file NO. 00-034-0394). The peak intensities varied for the electrolytes, resulting in average crystallite sizes of 45.90 nm, 38.87 nm, 15.60 nm, 15.94 nm, 13.42 nm, 18.10 nm and 15.94 nm for E1 to E7 respectively which was calculated from Scherrer equation using the most intense peak.

This showed that the different compositions had an effect on the sizes of the crystals. The single phase electrolyte exhibited bigger crystallite sizes with the conventional doped ceria compositions E4 and E5 showing smaller crystallite sizes. The composite electrolyte E3, E6 and E7 also exhibited smaller crystallite sizes. This is because, when molten phase of salts is added to conventional SDC it reduces the texture and coarseness of the material by introducing the smoother and smaller crystalline nature of the salt. The smaller crystallite size of the sample improves the ability of the material to densify and prevent any gas leakage.

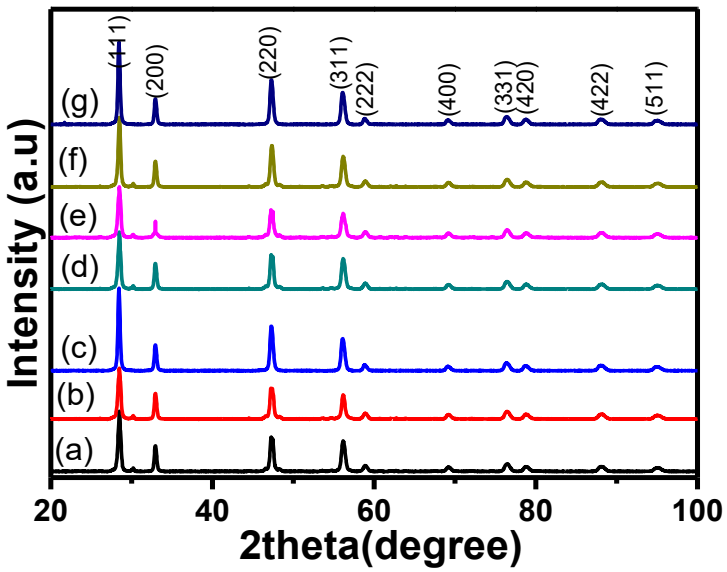

Figure 1: XRD pattern of (a) E1 (b) E2 (c) E3 (d) E4 (e) E5 (f) E6 and (g) E7 calcined at 800 °C for 4 hrs.

3.2 Raman analysis

Figure 2 shows the Raman spectra for SDC investigated, one major peak was seen at 470 - 474 cm^{-1} which represents the F_{2g} symmetry mode of CeO_2 fluorite phase. Peak shifts were observed for the different spectra resulting from different compositions of metals in the perovskites leading to changes in metal to oxygen bonding. The full width at half maximum (FWHM) for the different Raman spectra were observed and these are represented as 92 cm^{-1}, 40 cm^{-1}, 36 cm^{-1}, 36 cm^{-1}, 58 cm^{-1}, 37 cm^{-1} and 36 cm^{-1} for the E1 - E7 SDC compositions, respectively. Shifts in FWHM values were seen, which are attributed to defects in nanomaterials and defects being created by inclusion of salts to the SDC materials [21].

The relative peak intensity I_D/I_{F2g} ratio displayed differences which are dependent on compositions of the materials. Single SDC perovskites showed high intensity ratio than the mixture of the SDC and salts.

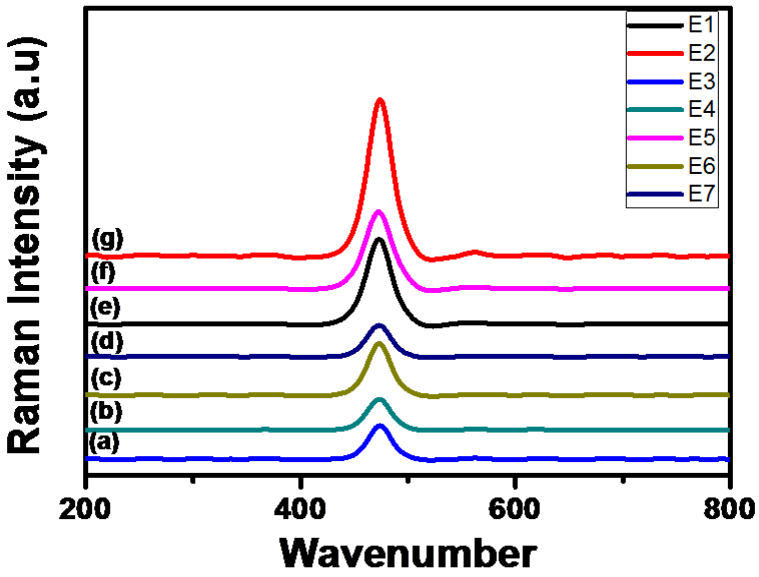

Figure 2: Raman spectra of (a) E1 (b) E2 (c) E3 (d) E4 (e) E5 (f) E6 and (g) E7 calcined at 800 °C for 4 hrs.

This implies that adding of salts lowers the intensity ratio of the spectra.The changes can alsobe attributed to stress and change of defect sites in CeO_2 [22]. Researchers have found that the presence of surface defects such as large size oxygen vacancy clusters promote the transformation from Ce^{4+} to Ce^{3+} of CeO_2 based material [23, 24]. The presence of Ce^{3+} in the fluorite ceria structure produces oxygen vacancies to sustain electrostatic stability according to equation (2) [25]. This creates a pathway for an improved ionic conductivity of oxygen in SDC/salt electrolyte.

$$4Ce^{4+} + O^{2-} \longrightarrow 4Ce^{4+} + 2e^{-}/\boxdot + \frac{1}{2}O_2 \longrightarrow 2Ce^{4+} + 2Ce^{3+} + \boxdot + \frac{1}{2}O_2 \qquad (2)$$

where $\boxdot$ represents an empty position, anion vacant site originating from the removal of O^{2-} from the surface.

3.3 HRTEM observations

Figure 3 reveals the microstructure of the electrolytes made from different compositions and SDC/salt compositions. The nanocrystals revealed irregular shapes that varied in sizes with the change in composition of the samples. The lattice distance between the fringes for electrolyte composites E1 is 0.25 nm indexed to (200), E2 is 0.207 nm indexed to (220), E3 is 0.175 nm indexed to (311), E4 is 0.207 nm indexed to (211), E5 is 0.201 nm indexed to (122), E6 is 0.190 nm indexed to (220) and E7 is 0.175 nm indexed to (311) which predominantly exposes the (200) planes of CeO_2 fluorite structure and (122) planes of $FeSmO_2$ structure for samarium oxide in the composites and the (311) planes of SDC structure for the electrolyte samples [26].

The variability in lattice distance can be due to the addition of salts to SDC which changes the surface morphology by a reconstruction in SDC structure. It could also be attributed to the varying compositions of the SDC material and the structural compatibility between the different materials. The low magnification image exposes dark spots predicting the presence of defects sites as shown in the Raman spectra. The selected diffraction pattern differed slightly in terms of the lattice and the arrangements of the particles. The lattice parameters can be linked to the XRD diffractogram exposing the active planes in the pattern.

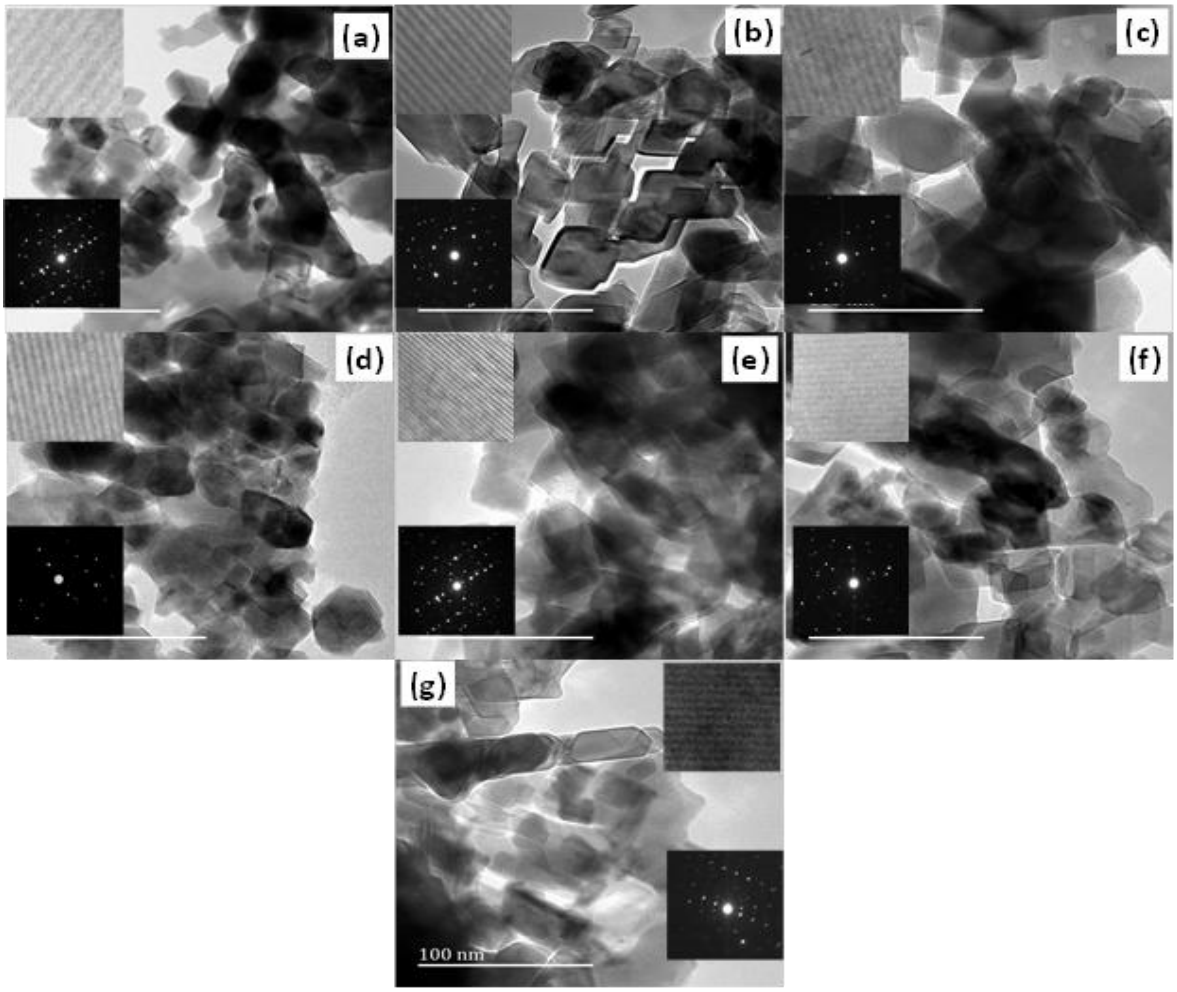

Figure 3: HRTEM micrograph of (a) E1 (b) E2 (c) E3 (d) E4 (e) E5 (f) E6 and (g) E7 calcined at 800 ℃ for 4 hrs.

3.4 SEM Observations

The morphologies of electrolytes as shown in Figure 4 show that the metals accumulate together in agglomerate formation with large pore sizes in existence between the particles. The morphologies display fine particle combinations and agglomerate formation with pore spaces that vary with the different compositions of the electrolytes and SDC mixed with salt. This agrees with the HRTEM micrographs, which also show particle size reduction for the different electrolytes.

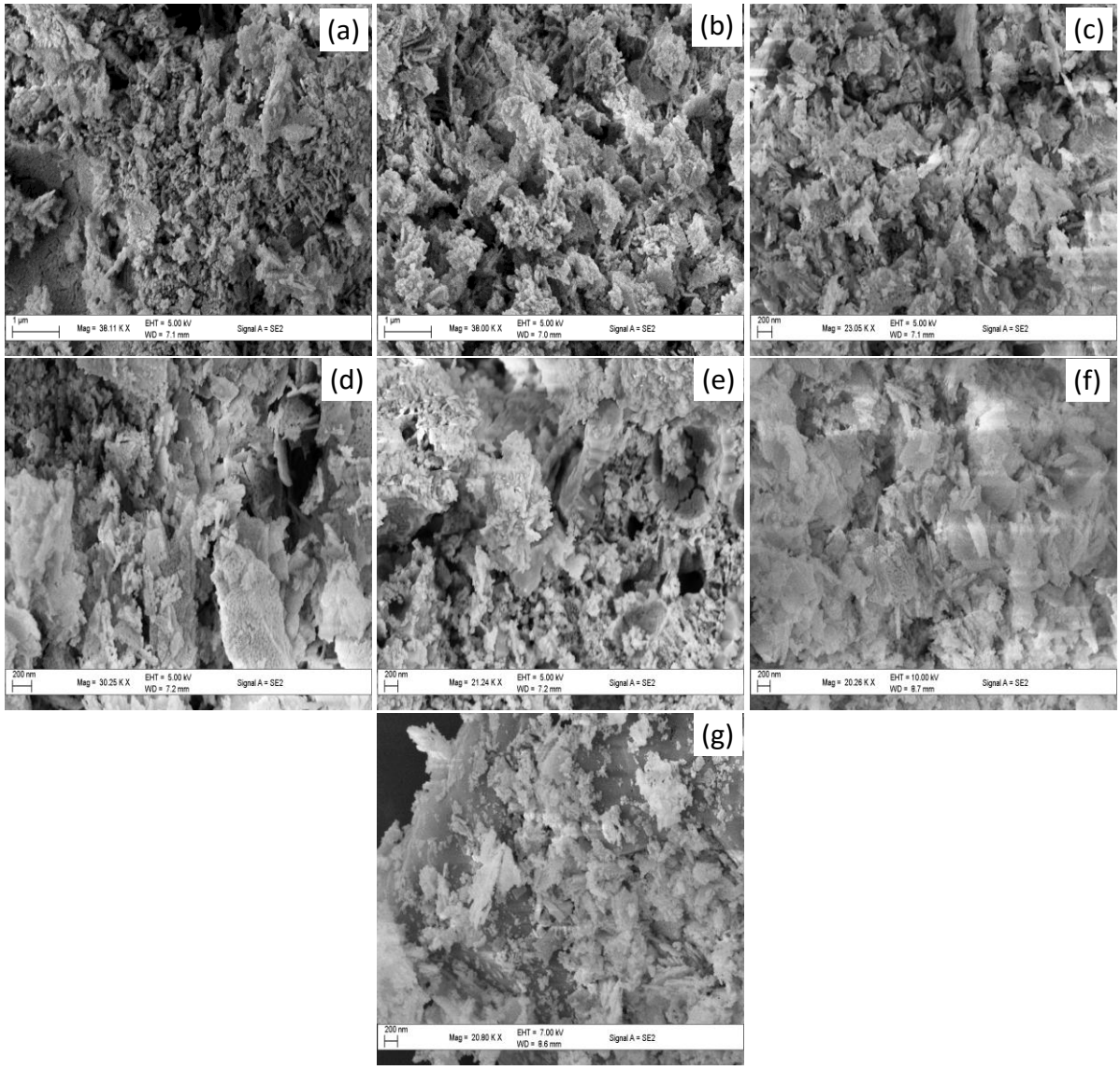

Figure 4: SEM morphology of (a) E1 (b) E2 (c) E3 (d) E4 (e) E5 (f) E6 and (g) E7 calcined at 800 °C for 4 hrs.

3.5 Nitrogen desorption /absorption Analysis

Figure 5 shows the isotherm plot of the different electrolyte compositions. Nitrogen desorption analysis examines the textural properties of materials which are shown in Table 2. The isotherm plot revealed the materials to be type III isotherm, revealing macroporous materials, which are observed from the diameter of the spherical pores and distance

between opposite walls in case of slit pores. These sizes reveal that the pores were large enough for vehicular transport of ions and electrons.

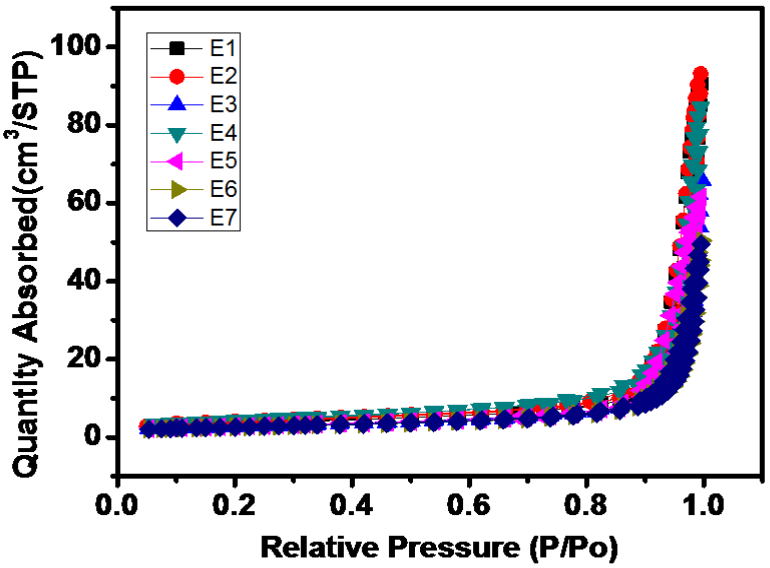

Figure 5: Nitrogen desorption Isotherm plot of (a) E1 (b) E2 (c) E3 (d) E4 (e) E5 (f) E6 and (g) E7 calcined at 800 °C for 4 hrs.

Table 2: Surface Area, Pore diameter and Pore Volume of Electrolytes E1, E2, E3, E4, E5, E6 and E7.

Sample ID	Surface area m^2/g	Pore diameter (nm)	Pore volume (cm^3/g)
E 1	12.641	39.306	0.1437
E 2	13.426	40.011	0.1466
E 3	9.537	43.430	0.102
E 4	15.407	35.560	0.1325
E 5	9.936	32.829	0.0985
E 6	8.939	37.906	0.0786
E 7	9.032	37.012	0.0774

Figure 6 shows the particle size distribution of the electrolyte materials which reveals them as macroporous materials. The nature of the size distribution also reveals an efficient transport of oxygen and hydrogen to and from the active sites.

Furthermore, the materials in general, showed an increase in the surface area, the pore volume and pore size of the single electrolyte material compared with the electrolyte materials mixed with salt. In totality the observations show that the addition of salts to electrolyte caused a vast reduction in the surface area, pore size and pore volume of the materials. This confirms changes inthe textural properties of materials with varying electrolyte compositions and SDC material combined with salts. The reduction in surface area and particle size distribution portrayed by the SDC/salt electrolyte poses an advantage in oxygen ion transport, because smaller pore sizes limits leakages and blockages at the active sites.

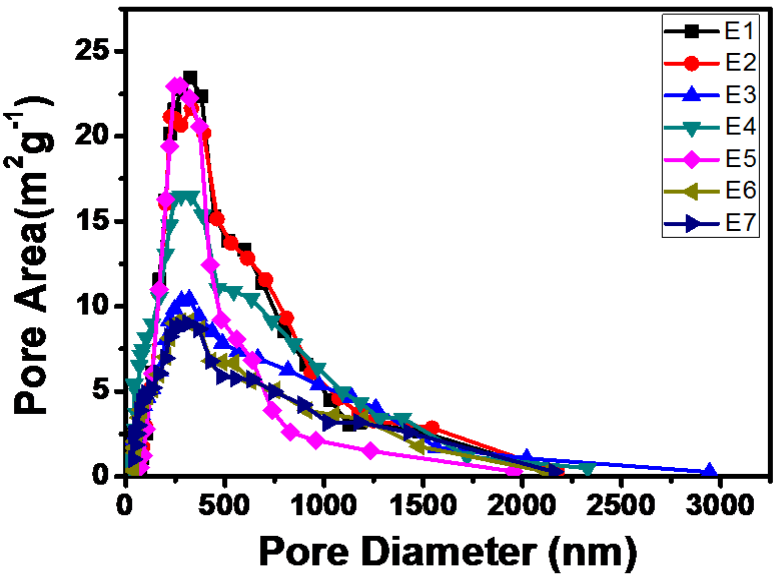

Figure 6: Nitrogen desorption pore size distribution of (a) E1 (b) E2 (c) E3 (d) E4 (e) E5 (f) E6 and (g) E7 calcined at 800 °C for 4 hrs.

3.6.0 Electrochemical properties

The assymmetrical cell was measured by placing the cell between two platinum meshes of 15 mm each, mounted on an open flange set-up. This was then placed on a muffle furnace and connected to a potentiostat and galvanostat. 50 m^3/min of air and 200 m^3/min of hydrogen gas mixed with 20 % H_2O was supplied to both sides of the electrolyte cells. Measurements were conducted at 400 - 500 °C and tested for 15 hrs using a 3-probe setup.

3.6.1 Polarisation Curve

Figure 7 shows the polarisation curve of the different electrolytes made with cerium and samarium oxides. The polarization properties were tested using air at the cathode side and humidified hydrogen (H_2 + 20 % H_2O) as fuel gas at the anode side. The cathode material used for testing was $Sm_{0.8}Sr_{0.2}Fe_{0.8}Co_{0.2}$ (SSFC) perovskite with a thickness of 100 μm, the anode (NiO/SDC) was 150 μm thick and the electrolyte was 100 μm thick.

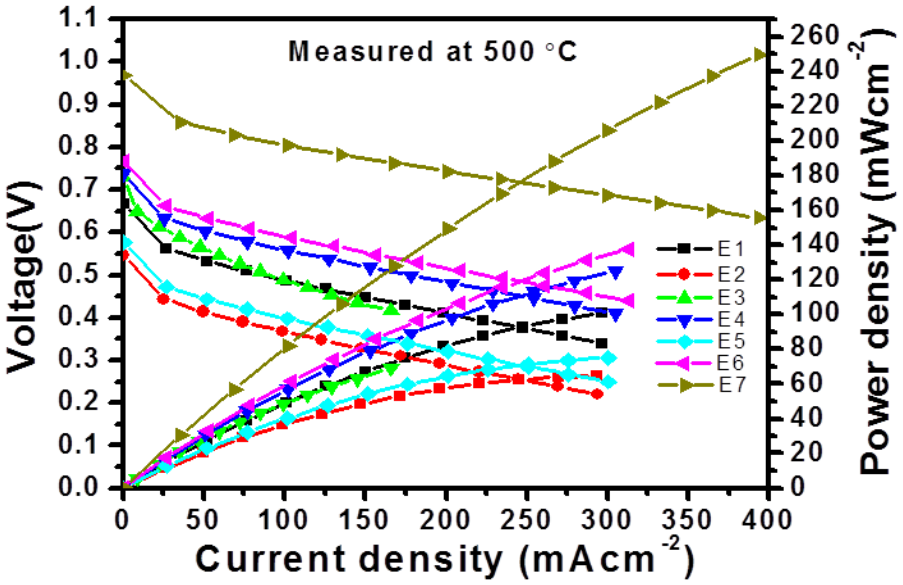

Figure 7: The Polarisation graph of (a) E1 (b) E2 (c) E3 (d) E4 (e) E5 (f) E6 and (g) E7 calcined at 800 °C for 4 hrs.

The polarization graph exhibit tendencies showing a linear fall in voltage with an increase in current density. This result in resistance to current flow depiction, an increase in current is directly proportional to an increase in voltage. The maximum current density differed for the different electrolytes which produced values of 300.48 mA/cm^2, 293.80 mA/cm^2, 165.90 mA/cm^2, 304.46 mA/cm^2, 300.28 mA/cm^2, and 313.73 mA/cm^2 and 374.39 mA/cm^2 displayed for electrolytes E1 – E7 respectively. The electrolytes displayed different open circuit voltages (OCVs) of 0.62 V, 0.45 V, 0.76 V, 0.70 V, 0.54 V, 0.74 V and 0.94 V for E1, E2, E3, E4, E5, E6 and E7 respectively and showed stability for over 15 hrs at 500 °C. The Open circuit voltage (OCV) values were less than the Nernst thermodynamic values because of the following reason namely, the hydrogen pressure reduction at the anode/electrolyte interface by the anode materials and the gas crossover flowing through the electrolyte because of the change in temperature.

The SDC/salt composites E7, E6 and E3 exhibited higher OCV values than the single SDC E1, E5 and E2 which showed low OCV values. We observed that the single electrolyte E4 ($Ce_{0.8}Sm_{0.2}$) showed an equivalent high OCV which may account for the reason it is the most popular SDC electrolyte used. The increase in OCV for SDC/salt composites may be as a result of the reduction of gas leakages from the cell, because of its compatibility and densification.

The linear fall in the polarisation graph was activated by these reasons: increase in the ohmic and concentration losses from the internal resistance of the cell. This was produced by the ionic conductivity and the effective distance between the cell components. Increase in the ionic conductivity influences the reduction of adsorbed molecular oxygen to O_2 ions and improves the diffusion of these ions to the electrode/electrolyte interface [27]. The increase in ionic conductivity of the electrolytes increases the diffusion of the ions to and from the electrodes. The increase in the overall rate of the diffusion process reduces polarisation losses and resistance; hence, the difference in the current density at 500 °C.

3.6.2 Power density

Figure 8 shows the maximum power density for the different SDC compositions calcined at 800°C. The maximum power densities obtained are 100.85 mW/cm^2, 64.66 mW/cm^2, 69.17 mW/cm^2, 124.98 mW/cm^2, 75.01 mW/cm^2, 137.72 mW/cm^2 and 249.63 mW/cm^2 for electrolytes E1 - E7 respectively, measured at 500 °C. The power density was calculated from the product of the current density and its corresponding voltage.

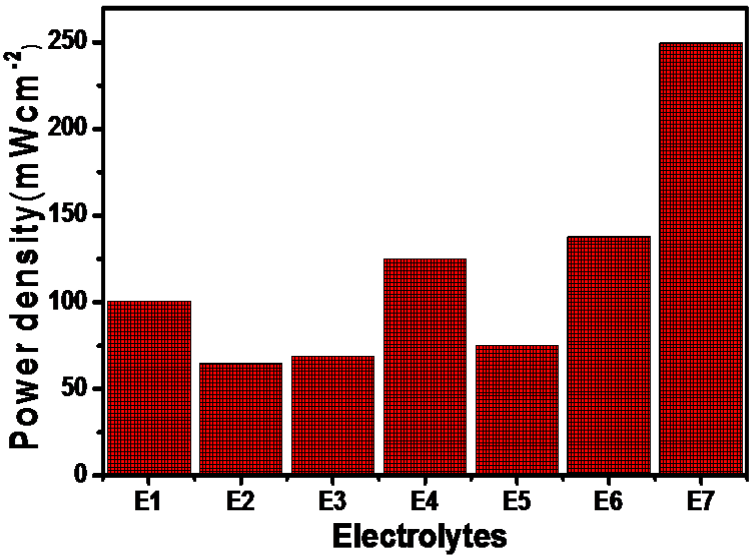

Figure 8: The Power Density plot of (a) E1 (b) E2 (c) E3 (d) E4 (e) E5 (f) E6 and (g) E7 calcined at 800 °C for 4 hrs measured at 500 °C.

Each electrolyte produced a different power density; sample E7 showed the largest power density. However the electrolyte exhibited a better performance because of its high current density and voltage. Another key implication from our results shows that the addition of salt to SDC electrolyte improves the performance of the electrolyte. Change in the composition of the electrolytes also causes an improvement in the power output from a non-ideal single cell.

3.6.3 Area specific resistance

Figure 9 shows the normalized area specific resistance (ASR) of the single cell calculated from the slope of the substantial linear portion (in the centre) of the I-V curve, where the ohmic resistance is dominant. The ASR is directly related to the design of the cell's anode, electrolyte and cathode properties and the assembly process used to make the single cell [28].

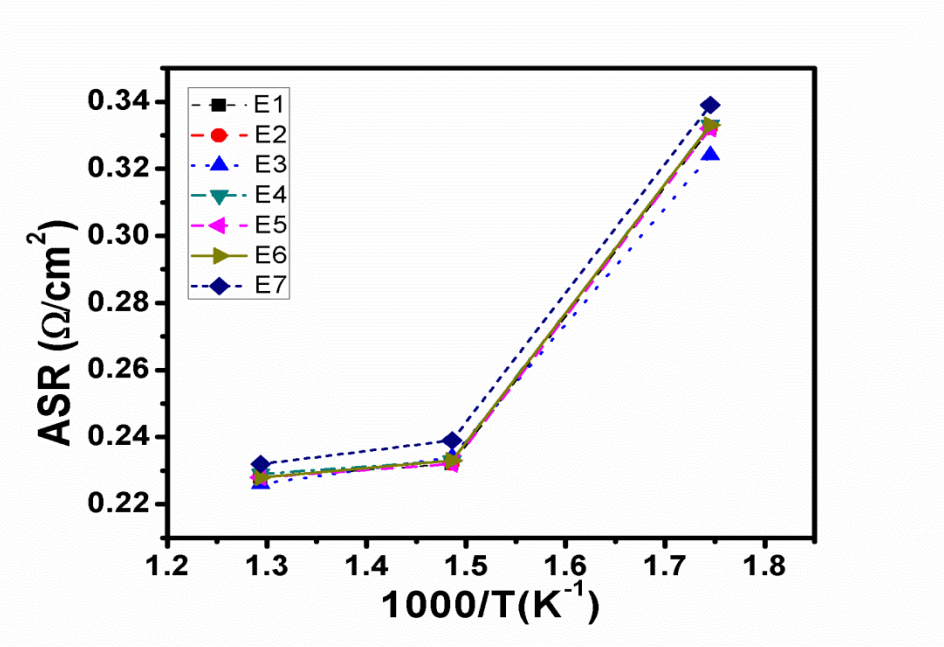

Figure 9: The Arrhenius plot of the ASR of (a) E1 (b) E2 (c) E3 (d) E4 (e) E5 (f) E6 and (g) E7 calcined at 800 °C for 4 hrs measured from 300 – 500 °C.

It is interesting to note that the different compositions of the electrolyte used, have little effect at 300 °C then there was a sharp drop from 300 to 400 °C and then slightly stable at 500 °C except for E1 and E3. This can be attributed to the compositions of the electrolytes which may suggest at 300 °C, SDC may not be a suitable electrolyte. However, the disparity in the ASR of the different electrolytes can be connected to changes in the material compositions and increased oxygen loss from the lattice. As mixed ionic conductors, oxygen reduction occurs at the triple phase boundary of the electrolytes which results from the increase in ionic conductivity of the various electrolytes. Reduction in the

ASR at 500 °C can be caused by increase in oxygen diffusion which results from the transformation of absorbed oxygen to O_2 ions [29]. The change in porosity, surface area, pore volume, the variation in the compositions of the electrolytes and the overall morphology also affects the movement of the O_2 ions at the triple phase boundary. The SDC/salt composite displayed low ASR values which can be attributed to their abilities to transport O_2 ions faster than the other electrolytes at the TPB [30].

4.0 Conclusions

SDC electrolyte was combined with salts (Na_2CO_3, $LiCO_3$) in this experiment and the crystal structure was investigated by X-ray diffraction. The textural properties were investigated by nitrogen adsorption/desorption analysis. The microstructure and morphology were tested by SEM analysis and HRTEM analysis respectively. The electrochemical properties were investigated using a Nuvant^{TM} potentiostat and galvanostat. The XRD diffractogram exhibited mean crystallite sizes of 45.90 nm, 38.87 nm, 15.60 nm, 15.94 nm, 13.42 nm, 18.10 nm and 15.58 nm for E1 – E7 respectively. This implies that the crystallite sizes varied with the different compositions made and SDC/salt electrolyte generated small crystals because of the nature of the salt. The SDC material alone generated a higher surface area than SDC combined with salts, depicting that the addition of salts increases the compatibility of the electrolyte. The microstructure of the SDC revealed smaller particles that are separated but the microstructure of SDC/salt composites revealed agglomerated large particles. The electrolyte composite E7 which is a combination of two salts and SDC, generated the highest power density of 249.63 mW/cm^2 and a current density of 325.90 mA/cm^2 at 500 °C powered for 15 hrs. When compared with the contemporary SDC without surfactant that produced a power density of at 500 °C showing that SDC/salt composites work best than the SDC material alone at lower temperatures. The properties exhibited revealed that the material is a promising electrolyte for low temperature solid oxide fuel cell.

Acknowledgements

The authors thank the University of KwaZulu-Natal, ESKOM-TESP and NRF THUTUKA for their financial support.

References

1. Hibino, T., Hashimoto, A., Yano, M., Suzuki, M., Yoshida, S. I., & Sano, M. (2002). High performance anodes for SOFCs operating in methane-air mixture at reduced temperatures. *Journal of the Electrochemical Society*, *149*(2), A133-A136.

2. Singhal, S. C. (2000). Advances in solid oxide fuel cell technology. *Solid state ionics*, *135*(1), 305-313.

3. Steele, B. C. H. (2000). Appraisal of $Ce_{1-y}Gd_yO_{2-y/2}$ electrolytes for IT-SOFC operation at 500 C. *Solid state ionics*, *129* (1), 95-110.

4. Mogensen, M., Sammes, N. M., & Tompsett, G. A. (2000). Physical, chemical and electrochemical properties of pure and doped ceria. *Solid State Ionics*, *129*(1), 63-94.

5. Sahibzada, M., Steele, B. C., Hellgardt, K., Barth, D., Effendi, A., Mantzavinos, D., & Metcalfe, I. S. (2000). Intermediate temperature solid oxide fuel cells operated with methanol fuels. *Chemical Engineering Science*, *55*(16), 3077-3083.

6. Xia, C., & Liu, M. (2002). Microstructures, conductivities, and electrochemical properties of $Ce_{0.9}Gd_{0.1}O_2$ and GDC–Ni anodes for low-temperature SOFCs. *Solid State Ionics*, *152*, 423-430.

7. Huang, J., Yang, L., Gao, R., Mao, Z., & Wang, C. (2006). A high-performance ceramic fuel cell with samarium doped ceria–carbonate composite electrolyte at low temperatures. *Electrochemistry communications*, *8*(5), 785-789.

8. Wang, X., Li, X., Zhang, L., Yoon, Y., Weber, P. K., Wang, H., Guo, J., & Dai, H. (2009). N-doping of graphene through electrothermal reactions with ammonia. *Science*, *324*(5928), 768-771.

9. Matsui, T., Inaba, M., Mineshige, A., & Ogumi, Z. (2005). Electrochemical properties of ceria-based oxides for use in intermediate-temperature SOFCs. Solid State Ionics, 176(7), 647-654.

10. Tarnuzzer, R. W., Colon, J., Patil, S., & Seal, S. (2005). Vacancy engineered ceria nanostructures for protection from radiation-induced cellular damage. *Nano letters*, *5*(12), 2573-2577.

11. Pirmohamed, T., Dowding, J. M., Singh, S., Wasserman, B., Heckert, E., Karakoti, A. S., King, J. E.S., & Self, W. T. (2010). Nanoceria exhibit redox state-dependent catalase mimetic activity. *Chemical communications*, *46*(16), 2736-2738.

12. Heckert, E. G., Karakoti, A. S., Seal, S., & Self, W. T. (2008). The role of cerium redox state in the SOD mimetic activity of nanoceria. *Biomaterials*, *29*(18), 2705-2709.

13. Andersson, D. A., Simak, S. I., Johansson, B., Abrikosov, I. A., & Skorodumova, N. V. (2007). Modeling of CeO_2, Ce_2O_3, and CeO_{2-x} in the LDA+ U formalism. *Physical Review B*, *75*(3), 035109.

14. Wang, W. G., & Mogensen, M. (2005). High-performance lanthanum-ferrite-based cathode for SOFC. *Solid State Ionics*, *176*(5), 457-462.

15. Xu, X., Xia, C., Xiao, G., & Peng, D. (2005). Fabrication and performance of functionally graded cathodes for IT-SOFCs based on doped ceria electrolytes. *Solid State Ionics*, *176*(17), 1513-1520.

16. Bi, Z., Cheng, M., Dong, Y., Wu, H., She, Y., & Yi, B. (2005). Electrochemical evaluation of $La_{0.6}Sr_{0.4}CoO_3$–$La_{0.45}Ce_{0.55}O_2$ composite cathodes for anode-supported $La_{0.45}Ce_{0.55}O_2$–$La_{0.9}Sr_{0.1}Ga_{0.8}Mg_{0.2}O_{2.85}$ bilayer electrolyte solid oxide fuel cells. *Solid State Ionics*, *176*(7), 655-661.

17. Wang, X., Ma, Y., Li, S., Zhu, B., & Muhammed, M. (2012). SDC/Na_2CO_3 nanocomposite: new freeze drying based synthesis and application as electrolyte in low-temperature solid oxide fuel cells. *International journal of hydrogen energy*, *37*(24), 19380-19387.

18. Hibino, T., Hashimoto, A., Asano, K., Yano, M., Suzuki, M., & Sano, M. (2002). An intermediate-temperature solid oxide fuel cell providing higher performance with hydrocarbons than with hydrogen. *Electrochemical and solid-state letters*, *5*(11), A242-A244.

19. Zha, S., Moore, A., Abernathy, H., & Liu, M. (2004). GDC-based low-temperature SOFCs powered by hydrocarbon fuels. *Journal of the Electrochemical Society*, *151*(8), A1128-A1133.

20. Li, L., Chen, F., Lu, J. Q., & Luo, M. F. (2011). Study of Defect Sites in $Ce_{1-x}M_x$

$O_{2-\delta}$ (x= 0.2) Solid Solutions Using Raman Spectroscopy. *The Journal of Physical Chemistry A*, *115*(27), 7972-7977.

21. Lin, J., Li, L., Huang, Y., Zhang, W., Wang, X., Wang, A., & Zhang, T. (2011). In situ calorimetric study: structural effects on adsorption and catalytic performances for CO oxidation over Ir-in-CeO_2 and Ir-on-CeO_2 catalysts. *The Journal of Physical Chemistry C*, *115*(33), 16509-16517.

22. Liu, X., Zhou, K., Wang, L., Wang, B., & Li, Y. (2009). Oxygen vacancy clusters promoting reducibility and activity of ceria nanorods. *Journal of the American Chemical Society*, *131*(9), 3140-3141.

23. Tsunekawa, S., Ishikawa, K., Li, Z. Q., Kawazoe, Y., & Kasuya, A. (2000). Origin of anomalous lattice expansion in oxide nanoparticles. *Physical Review Letters*, *85*(16), 3440.

24. Martínez-Arias, A., Gamarra, D., Fernández-García, M., Wang, X. Q., Hanson, J. C., & Rodriguez, J. A. (2006). Comparative study on redox properties of nanosized CeO_2 and CuO/CeO_2 under CO/O_2. *Journal of Catalysis*, *240*(1), 1-7.

25. Abdulsattar, M. A. (2011). Ab initio large unit cell calculations of the electronic structure of diamond nanocrystals. *Solid State Sciences*, *13*(5), 843-849.

26. Leone, P., Lanzini, A., Santarelli, M., Calì, M., Sagnelli, F., Boulanger, A., & Zitella, P. (2010). Methane-free biogas for direct feeding of solid oxide fuel cells. *Journal of Power Sources*, *195*(1), 239-248.

27. Yang, S. Q., Chen, T., Wang, Y., Peng, Z., & Wang, W. G. (2013). Electrochemical analysis of an anode-supported SOFC. *Int. J. Electrochem. Sci*, *8*(2), 2330-2344.

28. Njoku, C. B., & Ndungu, P. G. (2015). Synthesis and characterization of novel $Ce_{0.8}Sm_{0.2}Fe_{0.9}Ir_{0.03}Co_{0.07}O_{3-\delta}$ perovskite material and possible application as a cathode for low–intermediate temperature SOFCs. *Materials Research Bulletin*, *68*, 100-108.

29. Zhu, W., Lü, Z., Li, S., Wei, B., Miao, J., Huang, X., Ai, N., & Su, W. (2008). Study on $Ba_{0.5}Sr_{0.5}Co_{0.8}Fe_{0.2}O_{3-\delta}$–$Sm_{0.5}Sr_{0.5}CoO_{3-\delta}$ composite cathode materials for IT-SOFCs. *Journal of Alloys and Compounds*, *465*(1), 274-279.

30. Esch, F., Fabris, S., Zhou, L., Montini, T., Africh, C., Fornasiero, P., & Rosei, R. (2005). Electron localization determines defect formation on ceria substrates. *Science*, *309*(5735), 752-755.

CHAPTER 10

Conclusions and Future work

1.0 Conclusions

In conclusion, sol-gel technique was applied to make nanocomposite materials that have been successfully applied to design and develop cathodes, anodes and electrolytes with enhanced properties for low-temperature SOFC in this thesis.

Moreover, the templating characteristics of non-ionic, cationic and anionic surfactants were utilized to produce porous IrO/SDC nanocomposite as electrodes. The addition ofsurfactants to the material caused a reduction in the crystallite sizes, resulting from an increase in the XRD peak intensities and a high full width at half maximum value. The surface area increased in the materials where F127, CTAB, PEG surfactants were added and reduced with SDS and P123 compared with the sample without surfactant. The morphology and microstructure of the materialal so changed from surfactant to surfactant with varying porosity, spherical particle shapes and particle sizes, but the material with SDS revealed a rectangular particle shape, resulting from a complete coalescing of the substituent materials. Overall, the nature of the surfactant influenced the particle morphology, pore diameter, crystallite size, surface area and the electrochemical properties of the electrode material.

A cathode material produced was $Ce_{0.8}Sm_{0.2}Ir_yCo_{1-y}O_{3-\delta}$ perovskite, the material was then characterised using powder XRD patterns which revealed only samarium doped ceria and iridium oxide phases but no cobalt oxide phase. The Raman data revealed the formation of complex oxides with perovskite, pyrochlore and defective fluorite phases. The morphology and microstructure showed an agglomerate formation with irregular particles varying in sizes with increasing calcination temperature. There were some small differences between the different compositions as shown by the electrochemical properties with the sample y = 0.03 composition calcined at 800 °C having the highest power density of 287.6 mW/cm^2 at 500 °C, and the sample with y = 0.04 calcined at 1000 °C having a maximum power density of 222.7 mW/cm^2 at 500 °C.

Furthermore, Iron oxide was added to $Ce_{0.8}Sm_{0.2}Ir_yCo_{1-y}O_{3-\delta}$ perovskite to form this $Ce_{0.8}Sm_{0.2}Fe_{0.9}Ir_{0.03}Co_{0.07}O_{3-\delta}$ (CSFIC) perovskite. Results revealed via Raman spectroscopy

showed that the different calcination temperatures affected the characteristic vibration modes of samarium doped ceria and iridium oxide in the material and magnetite vibrational modes were also observed at higher temperatures. FTIR spectra revealed that carbon impurities were present at 800 °C calcination temperature. An increase in calcination temperature caused a shift with the mid-range FTIR peaks indicating changes in the metal – oxygen – metal bonds. XRD analysis confirmed the presence of Ce^{3+} and oxygen vacancies within the samples and the TGA analysis further confirmed that the concentration of oxygen vacancies differed with calcination temperatures. The presence of oxygen vacancies improved the performance of the cathode material, which exhibited an increased performance with a maximum power density of 400.15 mW/cm^2 at 500 °C.

Samarium oxide was then substituted in the A site of the cathode material with strontium oxide and cobalt oxide was removed to investigate its performance. The XRD showed the formation of an oxygen vacancy disordered perovskite oxide with a cubic lattice symmetry. The FTIR, TGA and Raman displayed a high structural stability, high thermal expansion and high oxygen vacancy concentration. The cathode material showed a superior electrocatalytic activity and relatively low electrical conductivity when compared with the cobalt based mixed conducting cathode which may be attributed to the Sr substitution and showed favourable long term stability. The single perovskite formed was $Ce_{0.8}Sr_{0.2}Fe_{0.9}Ir_{0.1}O_{3-\delta}$ (CSFI) which produced a maximum power density of 483.07 mW/cm^2 and an area specific resistance (ASR) of 0.342 Ω cm^2.

The experiment was further conducted with the addition of cobalt oxide because of its active catalytic activity for the electrolytic evolution of oxygen, thus investigating its effect on the performance of $Ce_{0.8}Sr_{0.2}Fe_{0.9}Ir_{0.04}Co_{0.06}$ (CSFIC) cathode. The Raman and XRD showed the formation of oxygen vacancy with modulated crystallite sizes. It also displayed high structural stability, high thermal expansion as shown by the TGA, high oxygen vacancy concentration which was observed by the defects in the Raman. The cathode material showed a relatively high electrocatalytic activity and demonstrated long term stability under testing conditions but its performance was lower than the cobalt free cathode. It generated a maximum power density of 471.59 mW/cm^2 when measured at 500 °C and a relatively low ASR.

Finally, SDC was synthesized by sol gel technique with the addition of varying masses of (2 g – 5 g) of Pluronic F-127 surfactant, to improve its performance by modulating its particle

sizes and porosity. The morphology and microstructure of the materials, changed with increasing mass of the surfactant with varying porosity, change in the particle sizes and spherical and irregular particle shapes shown in the micrographs. The XRD revealed an increase in the crystallite sizes of the materials with surfactant when compared to the material without surfactant. Nitrogen desorption analysis showed that the surface area and the pore sizes of the material increased with increasing mass of surfactant when compared to the ordinary SDC. The electrolyte exhibited long term stability with a power density of 161.24 mW/cm^2 at 500 °C for SDC with 3 g of surfactant when compared with a power density of 140.61 mW/cm^2 generated by SDC electrolyte without surfactant. Thus concluding that controlling the particle sizes and porosity can increase the performance of SDC electrolyte.

SDC was then used as the core material in the synthesis of SDC/Na_2CO_3 and SDC/$LiCO_3$ nanocomposite for its application as electrolytes in LTSOFC. The ionic conductivity of the electrolyte was significantly enhanced and the thermal stability of the nanostructure was also improved. Introduction of carbonate supressed the electronic conductivity of SDC effectively, which was evidenced from the open-circuit voltage (OCV) of the cells based on the SDC-carbonate electrolyte. The OCV values were significantly higher than the typical SDC single cell compositions. The addition of the softening properties of the salts improved the densification of the solid electrolyte layer thus preventinggas leakage, which was also evidenced by the increase in OCV. The SDC-salt electrolyte produced a better electrochemical performance with a power density of 249.63 mW/cm^2 when compared to the power density of 124.98 mW/cm^2 produced by SDC single cell. This conclusion shows that the performance SDC can be improved by the addition of salts (Na_2CO_3) and a combination of (Na_2CO_3/$LiCO_3$) for LTSOFCs.

2.0 Future work

Further investigation needs to be done on three parts of this work regarding the improvement of electrolyte and electrode materials for LTSOFC application. Further investigative studies would be done on electrochemical properties like electrochemical impedance spectroscopy (EIS) and resistivity measurements. Detailed investigative study needs to be done for CuO-SDC material as anode, such as explicit EIS measurement for interfacial polarisation of its performance mechanism. Further studies can be carried out on the combination of the individual cathode materials made in this study with existing cathode materials. The materials

should then be examined for its morphology, structural properties, textural properties and electrochemical performance using thorough EIS measurements for impedance and interfacial polarisations. Intergranular resistance might be obtained using impedance measurements (grain resistance). Investigation of the problems associated with electrode poisoning during long term stability testing of low temperature SOFC.

Furthermore, improving the performance of nanocomposite electrolyte (SDC-salt), more attention should be paid on the nano effects of the nanocomposites. The focus should be on the particle size and morphology of host particle SDC and how it affects the properties of the nanocomposite. Thin film technique might also be employed to make the electrolyte pellets which will reduce resistance and improve the power density output. Modelling simulations of the interfacial conduction mechanism could be established based on current experimental work and theoretical calculations can also be employed.